

MONASH UNIVERSITY



Doctoral Thesis

**Viscous biochemical samples: its
characteristics and transportation issues**

Author:

Supervisor:

Co. Supervisor:

Alifa Afiah Ahmad Zahidi

Associate Prof. Tuck Wah Ng

Dr. Brandon H. Cheong

BE Aerospace (Hons)

A thesis submitted for the degree of Doctor of Philosophy at Monash

University in 2019

Laboratory for Optics and Applied Mechanics

Department of Mechanical and Aerospace Engineering

MONASH UNIVERSITY

Faculty of Engineering

Department of Mechanical and Aerospace Engineering

Laboratory for Optics and Applied Mechanics

Doctor of Philosophy

**Viscous biochemical samples: its characteristics and
transportation issues**

22 May 2019

by Alifa Afiah Ahmad Zahidi

COPYRIGHT NOTICE

© Alifa Afiah Ahmad Zahidi (2019).

I certify that I have made all reasonable efforts to secure copyright permissions for third-party content included in this thesis and have not knowingly added copyright content to my work without the owner's permission.

ABSTRACT

This work was conducted to investigate relevant issues associated with the transportation and application of viscous biochemical samples under challenging environmental conditions. The scope of the research was divided into three categories which involved the investigation of stability of viscous liquids during transport, the factors affecting such liquid processing and finally exploring some applications in using viscous liquids. The results from this work showed that viscous liquid such as glycerol of 50% concentration is sufficient to provide thermal stability as it was able to eliminate turbidity effects arising from heating of BSA samples. Furthermore, the understanding obtained on the mechanics and behaviour of these liquids under various types of perturbation could aid in future designs of a more autonomous, robust and stable system for transport. This work also describes the test conducted under different stability conditions where viscous droplet was tested on an inclined surface, and different impact conditions. The separation of droplet behaviour under impact conditions showed the feasibility of improved liquid mixing. The use of widely familiar and established microplate assay format could potentially be maintained in transport through either standard or transparency type microplates.

If standard microplates are used, methods to overcome edge effect have been demonstrated by applying two-temperature heating modes where 304 K is applied at the side compared to 310 K applied at the bottom to achieve a more uniform temperature distribution. The transparency microplate option is advantageous as the architecture eliminates the occurrence of edge effect altogether. The main advantage gained in using viscous liquids also lies in the ability to conduct preliminary open field investigations that allows specimens to be examined on site. This work discusses the ability of 30% water-glycerol concentration to capture and immobilize *Drosophila* flies without harming the specimen. Furthermore, the functions of this glycerol concentration can also be extended to the creation of liquid lens incorporated to a smart phone that allows magnification of collected samples. However, it was found that there are random occurrences of bubble presence when dispensing viscous liquids from tips

which may affect the reliability of its use as liquid lens or immobilizing mediums. The experimental setup using gravitational impact in this work would allow for inspection and intervention of this problem before it is used as liquid lens or immobilizing mediums. Finally, it was found mixing and centrifugation of milk and blood samples could be done en-route while transport and could possibly improve the timeliness and cost factors to achieve optimal medical care for people living in remote areas.

STATEMENT OF ORIGINALITY

I, Alifa Afiah Ahmad Zahidi, hereby declare that this thesis titled, 'Viscous biochemical samples: its characteristics and transportation issues' and the work presented in it contains no material which has been accepted for the award of any other degree or diploma at any university or equivalent institution and that, to the best of my knowledge and belief, this thesis contains no material previously published or written by another person, except where due reference is made in the text of the thesis.

X

Alifa Afiah Ahmad Zahidi

Date: 22/05/2019

PUBLICATIONS DURING ENROLMENT

1. **AHMAD ZAHIDI, A. A.**, SALLEH, K. M., SAMARASINGHE, S. K., CHUNG, D. C. K., DANTARAYANARA, U., UDDIN, M. H., LIEW, O. W. & NG, T. W. 2019. Behaviour of sessile drops revealed in ‘car crash’ like impact. *Colloids and Surfaces A: Physicochemical and Engineering Aspects*, 579, 123661.
2. **AHMAD ZAHIDI, A. A.**, CHUNG, D. C. K., KATARIYA, M., LIEW, O. W. & NG, T. W. 2019. Living specimens under field immobilization and smartphone microscopic observation. *Microscopy Research and Technique*, 0.
3. **ZAHIDI, A. A. A.**, LAU, C. Y., KATARIYA M., LIEW, O. W. & NG, T. W. 2017. Characteristics of drops on flat microplating surfaces from controlled upward longitudinal impact. *Colloids and Surfaces A: Physicochemical and Engineering Aspects*, 522, 74-82.
4. **ZAHIDI, A. A. A.**, CHEONG, B. H.-P., HUYNH, S. H., VUONG, T., LIEW, O. W. & NG, T. W. 2015. Glycerol–water sessile drop elongation on PTFE inclines in relation to biochemical applications. *Colloids and Surfaces A: Physicochemical and Engineering Aspects*, 486, 21-28.
5. LAU, C. Y., **ZAHIDI, A. A. A.**, LIEW, O. W. & NG, T. W. 2015. A direct heating model to overcome the edge effect in microplates. *Journal of Pharmaceutical and Biomedical Analysis*, 102, 199-202.
6. HUYNH, S. H., **ZAHIDI, A. A. A.**, MURADOGLU, M., CHEONG, B. H.-P. & NG, T. W. 2015. Plastron-Mediated Growth of Captive Bubbles on Superhydrophobic Surfaces. *Langmuir*, 31, 6695-6703.
7. CHUNG, D. C. K., KATARIYA, M., **AHMAD ZAHIDI, A. A.**, LAU, C. Y., LIEW, O. W. & NG, T. W. 2019. Antibody drop based handling with near-superhydrophobic mesh substrates overcomes condensation sticking. *Materials Science and Engineering: C*, 96, 599-605.
8. CHUNG, D. C. K., HUYNH, S. H., **AHMAD ZAHIDI, A. A.**, LIEW, O. W. & NG, T. W. 2018. Simultaneous Multidrop Creation with Superhydrophobic Wells for Field Environmental Sensing of Nanoparticles. *ACS Omega*, 3, 9310-9317.
9. KATARIYA, M., CHUNG, D. C. K., MINIFE, T., GUPTA, H., **ZAHIDI, A. A. A.**, LIEW, O. W. & NG, T. W. 2018. Drone inflight mixing of biochemical samples. *Analytical Biochemistry*, 545, 1-3.
10. CHONG, M.L.H., CHENG, M., KATARIYA M., MURADOGLU M., CHEONG, B.H.-P., **ZAHIDI, A. A. A.**, YU, Y., LIEW, O.W., NG, T.W. 2015. Liquid body resonance while contacting a rotating superhydrophobic surface. *The European Physical Journal E*, 38, 119.
11. KATARIYA, M., CHUNG, D. C. K., MINIFIE, T., GUPTA, H., **ZAHIDI, A. A. A.**, LIEW, O. W. & NG, T. W. 2018. Note: Biochemical samples centrifuged in-flight on drones. *Review of Scientific Instruments*, 89, 106102.

ACKNOWLEDGEMENTS

This research was supported by an Australian Government Research Training Program (RTP) Scholarship. I would like to thank Majlis Amanah Rakyat Malaysia for providing me with scholarship for my stipend. Thank you for the funding support from the Australian Research Council through DP120100583. This work was performed in part of the Melbourne Centre for Nanofabrication (MCN) in the Victorian Node of the Australian National Fabrication Facility (ANFF). The assistance of H. Uddin, Melbourne Centre for Nanofabrication, in obtaining the optical profilometry traces and topography imaging of the PTFE surface and stainless-steel tip is appreciated. Information provided by the Victorian Institute of Invertebrate Sciences is also appreciated. I would like to thank D. Li and Z. Xiong, Department of Chemical Engineering, University of Melbourne for providing the PVA samples. Discussions with Y.T. Png, Pel-Air Aviation Pty Ltd are appreciated.

I would like to thank my supervisors Associate Professor Tuck Ng and Dr. Brandon Cheong, who have treated me fairly, with unyielding patience, provided me with unlimited amount of guidance and advice, showed confidence in my work and encouraged me to flourish my skills to become a better researcher. I am thankful to my colleagues, Dwayne, Sewminda, Mayur and Tristan for the informative discussions, ground-breaking ideas and impeccable company.

Finally, I am eternally grateful to my mother and father; Rosita and Zahidi, my sister and brothers; Asma, Tirmizi and Sidqi, my closest friends; Nadhirah, Hazirah, Arina, Hanim, Sofiyya, Sophie, Ameera, Shafeeqa, Nina, Alia, Aina, Manissa, Athirah, Sakinah, Syahieza, Fatin, Syazwani, Naurah, Amin, Ariff, Anwar, Sufyan and of course, my fiancé; Abdul for providing unconditional love, strength, motivation and support throughout the years of completing this research. They are the people whom without which I would not have survived the tremendous amount of stress and anxiety that I faced while completing this journey.

CONTENTS

COPYRIGHT NOTICE.....	III
ABSTRACT	IV
STATEMENT OF ORIGINALITY	VI
PUBLICATIONS DURING ENROLMENT	VII
ACKNOWLEDGEMENTS.....	VIII
CONTENTS	IX
LIST OF FIGURES.....	XIII
LIST OF TABLES.....	XXI
1 INTRODUCTION	1
1.1 RESEARCH MOTIVATION	1
1.2 RESEARCH OBJECTIVES	2
1.3 THESIS OVERVIEW.....	3
2 LITERATURE REVIEW.....	4
2.1 VISCOUS LIQUIDS	4
2.1.1 <i>Properties of Viscous Liquids.....</i>	<i>4</i>
2.1.2 <i>Introduction to Biochemical Viscous Liquids.....</i>	<i>5</i>
2.1.3 <i>Applications in Biomedical Industry.....</i>	<i>9</i>
2.2 LIQUID PHENOMENON & CHARACTERISTICS.....	11
2.2.1 <i>Wetting Phenomenon & Contact Angles.....</i>	<i>11</i>
2.2.2 <i>Surface Tension, Surface Energy & Young's Equation.....</i>	<i>13</i>
2.2.3 <i>Hydrophilic and Hydrophobic Surface.....</i>	<i>15</i>
2.3 LIQUID HANDLING	17
2.3.1 <i>1-60 μL (drop).....</i>	<i>17</i>
2.3.2 <i>25-350 μL (standard microplate).....</i>	<i>18</i>
2.4 EFFECTS ON LIQUID.....	19
2.4.1 <i>Heating (incubation).....</i>	<i>19</i>
2.4.2 <i>Evaporation.....</i>	<i>20</i>
2.4.3 <i>Edge Effect.....</i>	<i>21</i>
2.5 LIQUID DISPENSING.....	21
2.5.1 <i>Methods of Dispensing</i>	<i>21</i>
2.5.2 <i>Bubble Formation.....</i>	<i>22</i>

Table of Contents

2.6	UNMANNED AERIAL VEHICLE (UAV) IN BIOMEDICAL INDUSTRY.....	22
3	LIQUID STABILITY STUDIES.....	24
3.1	INTRODUCTION.....	24
3.2	DROP ELONGATION ON INCLINED SURFACE.....	24
3.2.1	<i>Introduction.....</i>	<i>24</i>
3.2.2	<i>Materials and Methodology.....</i>	<i>27</i>
3.2.3	<i>Results & Discussion.....</i>	<i>30</i>
3.2.4	<i>Conclusion.....</i>	<i>38</i>
3.3	DROP CHARACTERISTICS UNDER UPWARDS LONGITUDINAL IMPACT.....	39
3.3.1	<i>Introduction.....</i>	<i>39</i>
3.3.2	<i>Materials and Methodology.....</i>	<i>40</i>
3.3.3	<i>Results & Discussion.....</i>	<i>44</i>
3.3.4	<i>Conclusion.....</i>	<i>57</i>
3.4	DROP CHARACTERISTICS UNDER CAR CRASH-LIKE IMPACT.....	58
3.4.1	<i>Introduction.....</i>	<i>58</i>
3.4.2	<i>Materials and Methodology.....</i>	<i>59</i>
3.4.3	<i>Results & Discussion.....</i>	<i>61</i>
3.4.4	<i>Conclusion.....</i>	<i>70</i>
3.5	DROP DISLODGE MENT FROM GRAVITATIONAL IMPACT.....	70
3.5.1	<i>Introduction.....</i>	<i>70</i>
3.5.2	<i>Materials and Methodology.....</i>	<i>76</i>
3.5.3	<i>Results & Discussion.....</i>	<i>77</i>
3.5.4	<i>Conclusion.....</i>	<i>81</i>
3.6	CHAPTER SUMMARY.....	82
4	LIQUID PROCESSING FACTORS.....	84
4.1	INTRODUCTION.....	84
4.2	EDGE EFFECT (MICROPLATING).....	84
4.2.1	<i>Introduction.....</i>	<i>84</i>
4.2.2	<i>Materials and Methodology.....</i>	<i>87</i>
4.2.3	<i>Results & Discussion.....</i>	<i>88</i>
4.2.4	<i>Conclusion.....</i>	<i>92</i>
4.3	BUBBLE FORMATION (DISPENSING).....	93
4.3.1	<i>Introduction.....</i>	<i>93</i>
4.3.2	<i>Materials and Methodology.....</i>	<i>93</i>
4.3.3	<i>Results & Discussion.....</i>	<i>94</i>
4.3.4	<i>Conclusion.....</i>	<i>95</i>
4.4	CHAPTER SUMMARY.....	95

Table of Contents

5	APPLICATIONS OF VISCOUS LIQUIDS	97
5.1	INTRODUCTION	97
5.2	FIELD IMMOBILISATION (WATER-GLYCEROL)	97
5.2.1	<i>Introduction</i>	97
5.2.2	<i>Materials and Methodology</i>	98
5.2.3	<i>Results & Discussion</i>	99
5.2.4	<i>Conclusion</i>	100
5.3	SMART PHONE MICROSCOPY (WATER-GLYCEROL)	100
5.3.1	<i>Introduction</i>	100
5.3.2	<i>Materials and Methodology</i>	104
5.3.3	<i>Results & Discussion</i>	104
5.3.4	<i>Conclusion</i>	106
5.4	REAGENT MIXING WITH UAV (WATER-GLYCEROL).....	107
5.4.1	<i>Introduction</i>	107
5.4.2	<i>Materials and Methodology</i>	109
5.4.3	<i>Results & Discussion</i>	109
5.4.4	<i>Conclusion</i>	111
5.5	CENTRIFUGATION WITH UAV (BLOOD-MILK)	112
5.5.1	<i>Introduction</i>	112
5.5.2	<i>Materials and Methodology</i>	113
5.5.3	<i>Results & Discussion</i>	115
5.5.4	<i>Conclusion</i>	118
5.6	OPTICAL CHARACTERIZATION IN THE THERMAL IMMOBILISATION OF BSA.....	118
5.6.1	<i>Introduction</i>	118
5.6.2	<i>Materials and Methodology</i>	120
5.6.3	<i>Results & Discussion</i>	121
5.6.4	<i>Conclusion</i>	123
5.7	CHAPTER SUMMARY.....	123
6	OVERALL CONCLUSIONS	125
	REFERENCES	127
	APPENDICES	155
	APPENDIX A	155
	APPENDIX B	163
	APPENDIX C	172
	APPENDIX D	180

Table of Contents

APPENDIX E.....	187
APPENDIX F.....	191
APPENDIX G	194

LIST OF FIGURES

1. Figure 1: Behaviour of non-Newtonian fluids.
2. Figure 2: Various wetting behaviour of droplets on surfaces.
3. Figure 3: Measurement of contact angle of droplets on surfaces.
4. Figure 4: Hydrophilic and Hydrophobic contact angles on surfaces.
5. Figure 5: Interfacial boundaries of solid, liquid, and gas phase governing surface tension.
6. Figure 6: Comparison of contact angles on Wenzel and Cassie-Baxter Models.
7. Figure 7: Standard 96 well microplate with cover.
8. Figure 8: The placement of a drop on a horizontal surface (a) having an equilibrium contact angle θ with initial width, l_o based on a semi-spherical shape. When tilted at an angle α to the horizontal (b), the drop will assume an advancing, θ_a and receding, θ_r contact angles. It is often the case that the drop will breach at the advancing ahead of the receding contact line. Consequently, the drop experiences elongation of front contact line one direction such that $l > l_o$. The situation is different when the drop is compressed (c) and extended (d), where it will solely exhibit advancing and receding contact angles respectively with no elongation of front contact line.
9. Figure 9: The experimental setup to observe the drop behaviour from zero incline up to detachment. This method of using a rotary stage with a through hole, and positioning the drop at the gimbal point, allows for the drop to rotate through a wide range of inclines, and eliminates the need to reposition the camera each time. The inset pictures show the setup without the camera and light source set up, as well as an example image of the drop recorded.
10. Figure 10: Typical area topographic scan (a) from an area on the PTFE substrate using optical profilometry. No anisotropy in the topographic distributions were revealed from the scans taken for the horizontal (b) and vertical (c) line sections.
11. Figure 11: Plots shows the distributions of equilibrium contact angle (on horizontal position i.e. before inclination), the slip angle (inclined angle when drop detaches

List of Figures

from surface), as well as advancing and receding contact angles (at the point just before detachment). These values were recorded for water-glycerol mixtures (ranging from 0-100% glycerol) on PTFE substrate that was slowly tilted up to the point of detachment. The slip angle distributions were irregular and cannot be correlated to the advancing and receding contact angles. Advancing and receding contact angles tend to decrease with increasing concentration of glycerol in the mixture. The error bars indicate one standard deviation from 5 readings.

12. Figure 12: Plots of l/l_0 ratios with varying water-glycerol concentration where drops are placed on PTFE surface. The distribution shows similar trends to the slip angles in Figure 11. This indicates a relationship between the extent of elongation of the drop and its capacity resist detachment as the inclination of PTFE surface is slowly increased. The error bars indicate one standard deviation from 5 readings.
13. Figure 13: Traces of the advancing and receding contact angles of a water drop with various tilting of the incline. The inset gives the case with 30% glycerol in a mixture with water. In all cases, the contact angle does not provide information on the propensity of the drop to slip or to deform on the incline prior to slipping.
14. Figure 14: Traces of the length of drop with progressive change in the tilt angle of incline for a drop of water and a mixture containing 30% glycerol. A two-stage elongation process is observed for the drops. The inset provides a plot of the sine of α in relation to the change in α , which provides a scaling of progressive force due to gravity acting on the drop.
15. Figure 15: Traces of the (a) advancing contact angle when a drop of 50% glycerol liquid mixture on PTFE substrate was slowly compressed, and the (b) receding contact angle when it was slowly extended with time.
16. Figure 16: Schematic description of the setup to conduct the experiments in which a pair of identical solenoids activated simultaneously actuate a gantry containing a substrate with drop dispensed on it. With diffuse illumination from the rear, high speed camera video sequences of the drop as it was raised and stopped suddenly could be recorded for analysis.
17. Figure 17: Plot of displacement versus time for two stroke settings of the solenoid used in the experiment. A higher stroke produced higher maximum velocities (from gradient of plot) prior to impact.

List of Figures

18. Figure 18: Type I drop behaviour upon impact for 10% water-glycerol (V/V) where no necking occurred nor separation of the liquid body were observed.
19. Figure 19: Type II drop behaviour upon impact for 10% water-glycerol (V/V) where necking occurred but no separation of the liquid body was observed.
20. Figure 20: Type III drop behaviour upon impact for 10% water-glycerol (V/V) where separation of the liquid body was observed.
21. Figure 21: Region plot of the types of drop behaviour observed with varied solenoid stroke settings and percentage of glycerol in the water-glycerol mixture (V/V) tested on a non-scribed substrate. The type of behaviour was chosen from the most prevalent one observed out of 10 recordings at each stroke and glycerol percentage setting.
22. Figure 22: Region plot of the types of drop behaviour observed with varied solenoid stroke settings and percentage of glycerol in the water-glycerol mixture (V/V) tested on a circularly scribed substrate. The type of behaviour was chosen after taking the most prevalent one observed out of 10 recordings at each stroke and glycerol percentage setting.
23. Figure 23: The cross-section topography of the scribed region of the substrate. There is clear presence of a groove due to the cutter used, with structures resembling parapets and scarps on either side. These were not symmetrical.
24. Figure 24: Traces of the width of a water drop with time on both non-scribed and scribed substrates. The widths were normalized to their initial values (non-scribed = 2.3 mm, scribed = 2.5 mm) which were taken from the point of impact ($t = 0$ s) under stroke setting 4. In both cases, oscillations in the width after impact are used by the liquid body to dissipate energy. For the non-scribed case, the diameter of the scribed well is the minimum to which the drop could reduce its width to.
25. Figure 25: Traces of the height of a water drop with time on both non-scribed and scribed substrates. The heights were normalized to their initial values (non-scribed = 7.2 mm, scribed = 6.86 mm) taken from the point of impact ($t = 0$ s) using stroke setting 4. The trends on both surfaces were similar though the droplet non-scribed surface exhibited Type 1 behaviour but Type II behaviour were observed for the scribed surface.

List of Figures

26. Figure 26: Traces of the contact angle of the drop with time on the non-scribed and scribed substrates taken from the point of impact ($t = 0$ s) using stroke setting 4. The contact angle exhibited greater receding angles (up to 30° reduction from the original angle) compared to the non-scribed substrate (15° from original angle).
27. Figure 27: Graded meshes of drop coalescence behaviour under finite element analysis, in which the (A) liquid and (B) gaseous phases are depicted. The dense meshes enable the interaction changes to be well described.
28. Figure 28: Representation of sequence of simulation results of flow field generated (A) to (D) when two of liquid bodies began to merge. x and y in (A) describe the original shapes and positions of the two liquid bodies. The circulation flow strength was investigated in the selected region z .
29. Figure 29: The circulation flow strength developed in the region z in Figure 28(A) traced with time where the positive values are counter-clockwise flow. An initial high positive peak was observed followed by a cycle of positive and negative values implying good liquid mixing.
30. Figure 30: Sequence of high-speed camera images of the coalescence phase (A) to (D) in the Type III behaviour. They show the merging liquid shape to experimentally corresponded with the simulation images results of Figure 28 (A) to (D).
31. Figure 31: Sequence of images showing the separated globular portion not merging together with the main liquid body on rare occasions.
32. Figure 32: Experimental setup devised to replicate “car crash” investigations of sessile drops. The drops were deposited on substrates attached to the slider before it was moved at constant speed until it collided with the block. A high-speed camera was used to record the video sequence.
33. Figure 33: Illustration of (A) a sessile drop on a horizontal substrate with an axis-symmetric shape of contact angle θ . When the substrate was (B) inclined, the droplet shapes into advancing line AL and receding line RL with advancing contact angle θ_a and receding contact angle θ_r respectively.
34. Figure 34: Invariant displacements of the advancing (AL) and receding (RL) contact lines from a reference point on the rigid substrate, $L_a(0)$ and $L_r(0)$ respectively, up to point of impact as (A) a substrate with sessile drop was moved

List of Figures

(in the direction of the arrow). After impact (B), the behaviour of the droplet response was described by the changes in L_a , L_r , θ_a , and θ_r with time.

35. Figure 35: The (A) displacement versus time trace of the slider before impact. The small spread of speeds (B) extracted from 10 repeated experiments show consistent values were achieved.
36. Figure 36: High-speed image sequence (from top to bottom) recorded for (A) water, and (B) 70% water-glycerol (V/V) droplets under sidelong impact (direction according to blue arrow). The second image onwards depicts impact with the block. There was a clear difference in parameters (displacement and contact angle) at the advancing (left) and receding (right) contact points for the two sets of images.
37. Figure 37: Phase-space plots of the left (orange) and right (blue) contact angles and positions upon impact for different concentrations of water-glycerol mixture. The start positions were marked and circles and crosses were marked for end positions.
38. Figure 38: Phase-space plots of the left (orange) and right (blue) contact angles and positions upon impact for different concentrations of water-polyvinyl alcohol mixture. The start positions were marked and circles and crosses were marked for end positions.
39. Figure 39: Plots of Bond, Weber, and Ohnesorge numbers for both of water-glycerol and water-PVA mixtures of varied concentration. Only Ohnesorge numbers correlated to the results.
40. Figure 40: A resting pendant drop allows the angle ϕ to undertake a range of possible values as drop volume increases until the maximum condition is reached where $\sin \phi = 1$ and any further addition of liquid will result in drop detachment. As the tip begins its motion, three conditions occur from left to right. When tip is accelerating downwards (left), the opposing airflow creates an upward lifting force on the drop. When the downward moving tip is stopped abruptly due to impact (centre), the impact force resulting from the sudden deceleration creates a downward-acting momentum force that causes deformation towards an almost oblate spheroidal shape (with diameters L_1 and L_2) before detachment of the drop from the tip. After detachment, the drop continues to experience an upward-acting drag force exerted by the laminar airflow around it as it falls downward (right) until it finally reaches the solid substrate.

List of Figures

41. Figure 41: Gantry design setup attached with a steel tip that is able to stably suspend pendant drop. The gantry was raised to a height of 9.5mm and released. The video sequences of the drop motion during gantry movement and stopped abruptly due to impact was recorded using a high-speed camera. The diffuse illumination improves contrast for recording.
42. Figure 42: Plot (A) of displacement versus time trace of tip and thus the gantry (based on rigid body assumption). The velocity at the point of impact to be determined from the gradient. The sequence (B) of high-speed images (from left to right) show changes in the morphology of a drop initially stably maintained at the dispensing tip and then accelerated downwards by gravity to an abrupt stop before reaching terminal velocity. The resulting impact force triggers detachment of the drop from the tip where it resumes its flattened spherical shape.
43. Figure 43: The plots (A) of L_1/L_2 against volume of the drop and the corresponding surface energy developed at time just before detachment from the tip. After drop detachment, plots (B) of mean drop velocity v (vertical axis on the left) against volume at time just before contact with the substrate (average taken from 5 readings). Using these values, the first and third terms in Equation (20) can be calculated and plotted (vertical axis on the right).
44. Figure 44: Illustration of liquid residence in a (a) standard microplate well, and (b) transparency microplate well.
45. Figure 45: Results of the steady-state temperature distribution for finite element simulation in a (a) standard microplate with direct heating at the bottom, (b) standard microplate with direct heating at the bottom and sides, (c) transparency microplate with direct heating at the bottom.
46. Figure 46: Average liquid temperature plots in a well at the centre and corner at different liquid filling ratios (height of liquid / height of well) of a standard microplate (a) directly heated only at the bottom at 310K, (b) directly heated at the bottom and sides at 310K, and (c) directly heated at the bottom at 310K and the sides at 304K.
47. Figure 47: Distribution of temperature at different wells along the length of a transparency microplate, which show strong uniformity from centre to the edge.

List of Figures

48. Figure 48: The presence of (A) air bubbles entrained in a pendant drop during liquid dispensation. These bubbles will degrade the image quality of the liquid lens. Imaging results (B) from optical profilometry of the tip do not reveal material accretion that would affect liquid pinning or facilitate bubble formation.
49. Figure 49: Images of a *Drosophila* sample immobilized in a microplate well using varying concentrations of water-glycerol mixtures. 30% (w/v) concentration was found sufficient for effective immobilization of live *Drosophila* flies.
50. Figure 50: Sessile drop (A) placed on top of the lens of a smartphone creates a compound lens system with key parameters that increases magnification. Plots of $fV^{-1/3}$ and fa^{-1} (B) against θ showing that the focal length can be manipulating by keeping either values V or a as constant. This indicates that magnification adjustment can be achieved.
51. Figure 51: Images of the test chart obtained (A) without, and with (B) liquid lens of 1 μL and 4 μL created using different volumes dispensed onto a scribed transparent substrate of 3 mm diameter.
52. Figure 52: Images of a *Drosophila* sample immobilized in a microplate well, recorded with liquid lens incorporated to a smartphone.
53. Figure 53: The quadcopter (A) affixed with 3D printed vial holder that is able to house up to four vials for transport. Before transport (B), the vial comprising of water (stained blue) and glycerol (stained red) showed clear segregation between liquid mediums, which was confirmed by the quantitative red, green, and blue colour distribution as derived from the line profile (dashed line). Uniform mixing was achieved upon transport and flipping on the quadcopter (C). Under transport conditions without flipping, the result shown in (B) was obtained.
54. Figure 54: The propellers of the quadcopter (A) were adapted with stainless-steel tube and hinge affixed by strong adhesive on them (B) to allow en-route centrifugation of samples in capillary tubes. After the capillary tube was inserted into the stainless-steel tube (C), a bent rod that acts as a latch was moved to secure the capillary tube in place.
55. Figure 55: A non-homogeneous milk sample in a capillary tube when centrifuged developed a cream layer. Line plots were taken along the dashed red lines to

List of Figures

analyse the cream layer. The separation is indicated by the positions marked x' and x'' and became sufficiently distinct after 30 minutes centrifugation.

56. Figure 56: A human blood sample in a capillary tube when centrifuged developed separation into regions containing red blood cells, buffy coat, and plasma. Although analysis of line plots taken along the dashed white lines indicate separation becomes sufficiently distinct after only 2 minutes centrifugation, it was necessary to extend the centrifuge time longer to ensure that a complete process was achieved.
57. Figure 57: Calculations of the packed cell volume (PCV) as a function of centrifugation time from 5 blood samples. It can be seen that centrifugation of at least 8 minutes is needed to complete the separation process.
58. Figure 58: The experimental setup to examine the optical behaviour of BSA in water-glycerol mixtures. Both samples were added to a cuvette and were illuminated using broadband light. An optical fibre connected to a spectrometer was used to collect the transmitted light.
59. Figure 59: Plots of the absorbance changes in BSA dissolved in solutions containing varying water-glycerol compositions when heated from 25 °C to 95 °C. When aggregation occurs in response to temperature, the sample undergoes significant absorbance (at 600 nm) increase (see points grouped by dashed box). The inset graph indicates the heating rate of the samples

LIST OF TABLES

1. Table 1: Listing of viscosity and surface tensions of water-glycerol mixtures used.
2. Table 2: The list of maximum velocity and impact momentum obtained using the different stroke settings (increasing stroke lengths) on the solenoid.
3. Table 3: Water properties that are invariant with temperature.
4. Table 4: Water properties dependent on temperature.

1 INTRODUCTION

1.1 Research Motivation

The biomedical, biotechnology and biochemistry sectors conduct extensive research on a variety of cells and living organisms. Biochemical samples such as proteins, hormones, nucleosides and enzymes are known to be sensitive and unstable, making them liable to damage, denature or aggregation depending on the modes of perturbation (temperature, pH, hydrostatic pressure, salinity) [1-3]. Many of the biochemical samples are commonly stored via freezing or centrifugation [4] and transported via pneumatic systems [5], courier or mail. Hence, the transfer and handling of biochemical samples must be done with complete care to overcome problems associated with viability. Due to the potential damage to biochemical samples, this research aims to create a safe and stable system that allows for storage and transport of small volumes of biochemical samples in environments that are more challenging. A familiar way to increase stability of biochemical samples during storage and transport is by using aqueous solutions, additives and stabilizing effectors [6, 7]. Some methods of heuristic algorithms may be used to improve operational efficiency of blood supply chain [8]. An area of interest is in investigating the potential of viscous liquid mediums in the role of securing the stability, containment from contamination and maintaining conformation of biochemical samples. The use of viscous liquids to preserve the quality of samples using UAV can be a promising future for effective transportation that can overcome time constraints.

This offers versatility in studies into the behaviour of sessile drops for cooling or subjected freezing, which have important application industrial implications. New prospects for investigations of drops subjected to evaporation and freezing are also expected. Microfluidic technology has existed since over a decade and there is high levels of interest in its application in biochemical analysis [9, 10]. Current research in microfluidics is moving towards adopting alternative approaches that are easier to integrate and scale. A common problem in closed continuous flow devices is the dependence of flow at a location on the flow of an entire system. The use of discrete,

independently controllable sample volumes [11], specifically with drops on open surfaces [12-14], is a promising option. It provides an advantage of repeating basic sets of operations, that allows one unit of fluid to be precisely moved over one unit of distance, thus facilitating the use of hierarchical and modular approaches that lead to flexible and scalable system architectures with high fault tolerance. Additionally, systems can be reconfigured to change functionality since the sample volumes can be controlled independently.

1.2 Research Objectives

The overall aim of the research was to enable transportation of biochemical samples in challenging environments. Hence, the research objectives can be broken down to the following:

1. Mode of transportation:

- To investigate the efficiency of liquid transport in droplet form and in microplate assay format.
- To investigate the influence of edge effect and thermal stability of microplates on transported samples.

2. Medium for transportation:

- To investigate the factors affecting stability conditions of viscous liquids during transport.
- To investigate the potential of viscous liquids in preserving biochemical samples/living specimens.
- To investigate and reduce/eliminate bubble formation phenomenon for viscous fluids.

1.3 Thesis Overview

This thesis consists of six main chapters:

Chapter 2 begins with a background of literature resources that are related to the research

Chapter 3 details the experimentation on liquid stability under various physical conditions. It is divided into 5 subchapters that demonstrates each experimentation.

Chapter 4 outlines the liquid processing factors and its application problems. This is divided into two subchapters discussing edge effect on microplates as well as bubble formation in dispensing viscous liquids from tips.

Chapter 5 introduces the useful applications of viscous liquids in biomedical experimentation. It is divided into 5 subchapters specifying field immobilization of *Drosophila Melanogaster*, smart phone microscopy using glycerol, reagent mixing and centrifugation using Unmanned Aerial Vehicles (UAV) and optical thermal immobilization using Bovine Serum Albumins.

Chapter 6 explains the overall conclusions for this research.

Appendices includes detailed plots, tables and calculation as well as articles associating the work forming this thesis.

2 LITERATURE REVIEW

2.1 Viscous Liquids

2.1.1 Properties of Viscous Liquids

Viscosity is defined as the measure of resistance to fluid flow. It is correlated to the thickness of a fluid. The dynamic viscosity is often used to describe resistance of shear flows and is given in the form of shear stress divided by the shear rate in Equation (1). In addition, the kinematic viscosity is defined as the ratio of dynamic viscosity to the liquid density in Equation (2).

$$\mu = \frac{\tau}{\frac{\partial u}{\partial y}} \quad (1)$$

Where μ is dynamic viscosity,

τ is shear stress,

and $\partial u/\partial y$ is shear rate.

$$\nu = \frac{\mu}{\rho} \quad (2)$$

Where ν is kinematic viscosity,

μ is dynamic viscosity,

and ρ is density.

Newtonian fluids are explained as fluids that obey the Newton laws of viscosity. They are fluids of simple molecular formula and low molecular structure such as water. Non-Newtonian fluids are the opposite and consist of complex molecular structure such as molten polymers. Liquids are deemed to be viscous when they have viscosities greater than water (0.89 mPa.s). Examples of viscous liquids are oil, glycerine and honey. Viscous liquids are generally used in the study of fluid flows [15]. Moreover, studies have shown that viscosity is able to increase liquid strength and stability [16-18].

2.1.2 Introduction to Biochemical Viscous Liquids

2.1.2.1 Glycerol

Glycerol (Glycerine) is a colourless and odourless and viscous liquid having a sweet taste [19]. It is an alcohol compound consisting of three hydroxyl group that enables them to be soluble in water. It is widely used in the pharmaceutical, cosmetics and food industry. It is by-product of biodiesel industry and exhibits interesting thermal properties enabling it to perform useful functions [20]. Glycerol is useful for its bioconversion to high value compounds through microbial fermentation [21]. It is able to act as catalysts and buffers in chemical reactions [22-24]. Furthermore, glycerol based copolymers represent a new kind of thermoresponsive polymers and is useful as switchable bioinert surface coatings [25]. Glycerol exhibits good optical properties [26] which makes it suitable for analysis using optical sensing devices. Due to its chemical composition, glycerol is known to be biocompatible with living cells and have been used for clinical treatments over the years [27]. Glycerol is also osmotically active and was found to give better performance as hyper-hydration agents in hot and humid conditions [28]. Due to its solubility with water, current researches involve the use of water-glycerol mixtures for enhancing protein stability.

For example, water-glycerol mixture of specific concentrations were found to inhibit thermal activation and aggregation of enzymes by stabilizing the structure of the enzyme [29]. The presence of hydroxyl group in glycerol enables it to fix proteins by

rigidifying the matrix structure through hydrogen bonding [30]. Glycerol is able to eliminate the hydrophobic effects arising from the changes in the structure of water and as a result stabilizes the protein [31]. With the presence of glycerol in aqueous solutions, proteins need to use more free energy to unfold [32]. The strength and magnitude of protein-protein interaction is increased with increasing glycerol concentration and decreasing temperature via preferential interaction effect [33]. Even a small amount of glycerol was able to stabilize lysozyme in low water content of trehalose solutions [34]. In larger scale proteins, a larger amount of glycerol is required to activate protein mobility [35]. Therefore, the use of glycerol for preservation of biochemical samples is feasible. Water-glycerol mixtures are routinely used to preserve the functionality of biological molecules during cooling and thawing processes, and to suppress intracellular ice formation, which can be harmful to cells and tissues [36, 37]. Besides that, Triton X-114, also a highly viscous liquid, can be used to purify proteins. There have been reports of glycerol being successfully used to lower the aggregation temperature of Triton X-114 [38].

2.1.2.2 Bovine Serum Albumin

Bovine Serum Albumin (BSA) is a type of serum albumin protein derived from milk and exhibits viscous properties. Different concentrations of BSA introduce different levels of viscosity. At low concentrations, viscosity is primarily influenced by the electroviscous effects whereas at high concentrations, the viscosity is governed by the short-range attractive interactions [39]. The intrinsic viscosity of BSA reduces with increasing temperature [40]. Due to its stable and non-reactive nature, BSA is commonly used for biochemical applications. Typically, BSA is used as blocking agents. Recently, BSA have been used as a reducing agent to create fluorescent gold nanoclusters due to its distinctive nanostructure [41]. It is also useful for measuring viscosity of small liquid volumes such as a single living cell [42]. The photostability of dyes and fluorescence properties can be enhanced using BSA which is crucial for use in bioimaging applications [43]. However, BSA can heavily coagulate when exposed

to heat. Greater aggregations of BSA occur with higher concentrations used under prolonged heating [44].

2.1.2.3 Blood Composition

Blood is a crucial source of antidotes and vaccines in the medical industry. It consists of erythrocytes (red blood cells), leukocytes (white blood cells), platelets and plasma which play vital roles in clinical diagnostics [45]. Blood is classified as a non-Newtonian (pseudoplastic) fluid and its viscosity behaviour is generally described where the rate of change of shear stress to shear rate is not proportional and that it requires more force to move blood at lower speeds than at faster speeds [46]. The general Power Law model for non-Newtonian fluids is given by Equation (3). Pseudoplastic behaviours have $n < 1$ values and is illustrated in Figure 1.

$$\tau = K \left(\frac{\partial u}{\partial y} \right)^n \quad (3)$$

Where τ is shear stress,

K is flow consistency index,

$\partial u / \partial y$ is shear rate,

and n is flow behaviour index.

Classification of NonNewtonian Fluids

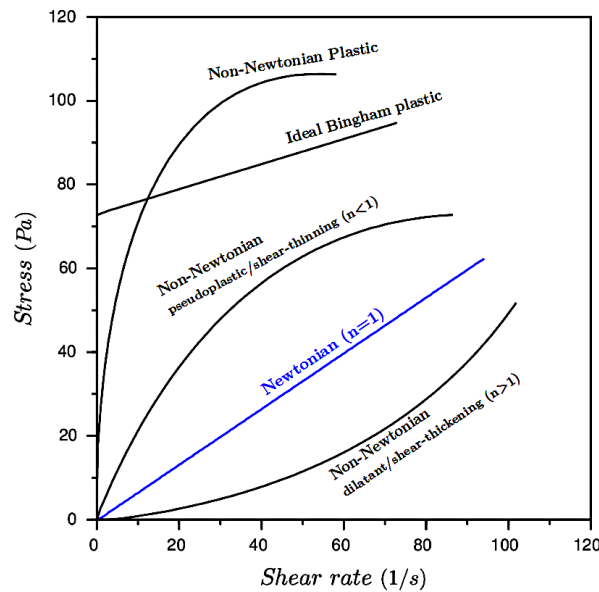


Figure 1: Behaviour of non-Newtonian fluids.¹

Blood viscosity plays a vital function in blood flow therefore, increasing interest in monitoring blood viscosity has developed in the medical field. For example, high blood viscosity can cause delays in artery dilation and increases arterial stiffness hence increasing cardiovascular risks [47]. There are many factors influencing blood viscosity. An advancement in accuracy of blood viscosity measurement is the development of micro-viscometer that has the ability to measure viscosity over multirange of shear rates in a single flow rate as blood viscosity is highly dependent on shear rates [48] and some use electrical impedance techniques [49]. The increase in accuracy of viscosity measurement will help improve regulation of blood viscosity methods [50]. Advanced diagnosis of body status can be done from monitoring the levels of erythrocytes and leukocytes which can be separated from whole blood using centrifugation methods [51-53]. However the isolation must be done under minimal physical or chemical stress to avoid altering profiles of isolated cells [54]. Another method that can be used to lower blood viscosity besides medications such as aspirin is by applying magnetic fields to the erythrocytes [55].

¹ Sourced from: https://www.simscale.com/docs/_images/NonNewtonian01.png

2.1.2.4 Milk

Milk, is one of the important sources of protein and calcium in daily consumption. Concentrated milk solutions, also exhibits non-Newtonian liquid behaviours [56]. The viscosity of milk has been used as a measure to research the effect of interaction of milk proteins during thermal processing [57]. Therefore, understanding the fluidic behaviour of milk is necessary to improve production in the food industry. A problem found was that storage of concentrated milk at 50°C exceeding four hours can alter viscosity and these effects were irreversible [58]. The viscosity of milk protein concentrates (MPC) can be reduced by manipulating pH using citric acid and calcium ion (Ca^{2+}) activity which helps increase stability of thermal processing [59]. High intensity ultrasound technology can be used to reduce concentrated skim milk viscosity and control the age thickening process [60]. In production of cheese, milk coagulation is a significant process to ensure high quality product which is influenced by the pH, temperature and also the compositions of casein and fat in the milk [61].

2.1.3 Applications in Biomedical Industry

In biomedical application for targeting drug delivery, it was found that large specific absorption rate was produced for magnetic nanoparticles assembled in viscous liquids [62]. The applications for viscosity have expanded in the field of biology where it was found to influence the flow measurements of liquid feeding insects [63]. In other cases, viscosity has been used as a mode to describe the instability of liquid under the influence of an electric field [64]. Therefore, the use of viscous liquids as a medium for transportation is viable. However, viscosity is at a disadvantage when used as micro cantilever sensors in viscous liquid media. Studies have been conducted to overcome this effect [65].

Viscous liquids below glass transition behave like solids but its solidity depends on the solidity length scale [66]. This makes it useful for facilitating transport by

increasing liquid stability. In addition, viscous liquids can increase bubble stability by defining bubble break up and coalescence rates [67]. This was found useful in the context of gas-liquid reactions for waste processing and treatments. The energy dissipation rates of viscous fluids can be used to improve quality and efficiency of micro-mixing [68]. Redox reactions can be controlled by the viscosity of liquids as they were found to increase the activation energy of the redox reaction with increasing activation energy of viscosity [69].

2.1.3.1 Particle Trapping Using Viscous Liquids

Airborne particle trapping is an important application in the medical and agricultural industry. A simple universal technique of collecting airborne biological particles is by placing sticky liquids on to glass slides. The size, amount and efficiency of trapping relies on the gravitational sedimentation or impact of particles on vertical surfaces via air current [70]. Viscosity plays an important role in allowing adhesion [71]. Highly viscous fluids ensure slower evaporation which aids in bio-adhesion [72]. It has been proven that viscous forces show great significance in influencing filtration efficiencies in liquid media [73]. These properties allow particle trapping using viscous liquid mediums. In biotechnology research, viscous liquids are used for trapping spores and micro-organisms [74, 75].

The common liquids used for particle trapping exhibit high viscosity as well as sticky characteristics. Examples of these liquids are petroleum jelly, glycerine jelly or silicon grease [76-78]. However, in order to achieve the high efficiency of adhesion for a mounting medium, a suitable balance between viscosity and liquid concentration and a certain combination of liquid mixture is required [79, 80]. It is speculated that the capture efficiency to adsorb semi volatile organic species and/or retain particulate aerosols is enhanced by glycerol coatings [81]. The efficiency of particle trapping also depends on the sizes of the trapped particles [82]. The many different devices used for particle trapping are described in Chapter 3 of [70] but the most commercially used is the Burkard traps. These devices are heavy, bulky, and stationary, requires an electric pump/motor to operate and only cover a limited radius.

2.2 Liquid Phenomenon & Characteristics

2.2.1 Wetting Phenomenon & Contact Angles

Wetting is an important factor when dealing with liquids on solid surfaces. This can be defined as the ability of a fluid to spread readily and uniformly over a surface of another fluid or solid. The theory suggested by Wenzel is that wetting includes three interfacial boundary surfaces whereby a solid-liquid interface replaces solid-air interface with an extension of liquid-air interface [83]. This is called the triple phase contact line. Many have applied the use of contact angle and hysteresis to measure the degree of wetting on a particular surface [84-87]. The hysteresis angle, θ_H is the difference between the advancing and receding angles (i.e. $\theta_A - \theta_R$) and is considered more accurate when studying the motions of drops on surfaces [88]. Advancing contact angle is the maximum angle achieved when the volume of the liquid increases and moves the triple contact line forward towards the solid-gas interface whereas the receding contact angle is the minimum angle achieved when the volume of the liquid decreases moving the triple contact line backwards towards the solid-liquid interface [89].

The wetting behaviour and contact angle of droplets are illustrated in Figure 2 and Figure 3. Studies from [90] showed that the equilibrium and static advancing/receding contact angles can be calculated from disjoining/conjoining pressure isotherms. Some use surface tension and surface energy to relate to the wetting phenomenon [91, 92]. Furthermore, wetting involves defining hydrophilic and hydrophobic surfaces [93-95] as illustrated in Figure 4. It was found that the roughening of surfaces intensified wetting or dewetting characteristics of liquids on surfaces [83]. Others show that it is possible to characterise and understand the stability of a liquid based on its wetting behaviour [96-98].

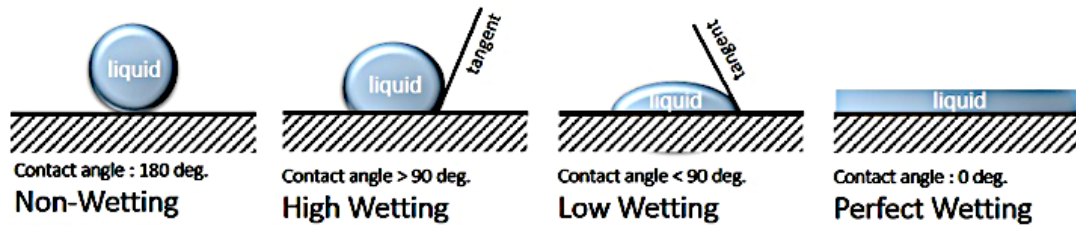


Figure 2: Various wetting behaviour of droplets on surfaces.²

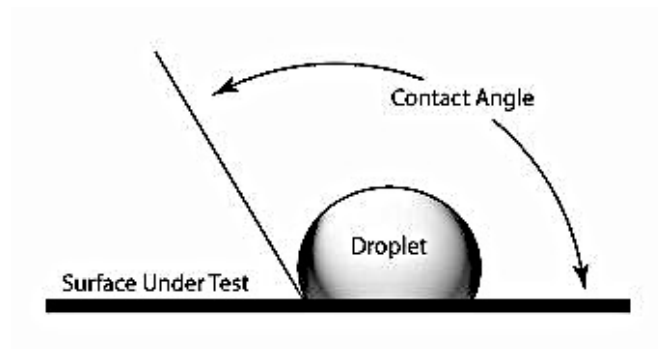


Figure 3: Measurement of contact angle of droplets on surfaces.³

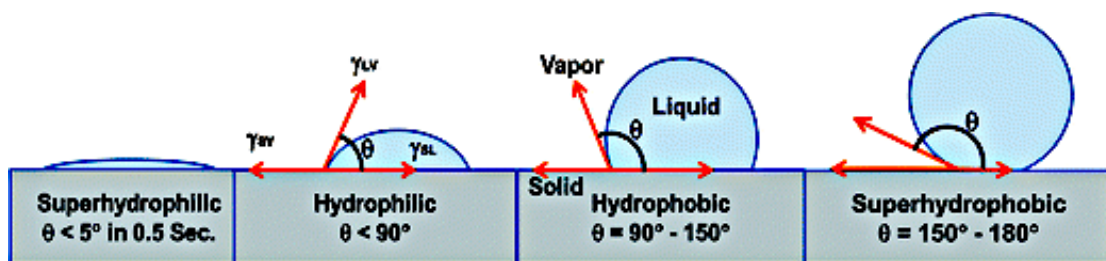


Figure 4: Hydrophilic and Hydrophobic contact angles on surfaces [99].

The understanding of wetting phenomenon is of particular interest in various biological and microfluidic fields as well as nanotechnology [100-102]. Several studies have also reported on the effect of viscosity on the wetting characteristics [103-105].

² Sourced from: <http://www.cscscientific.com/csc-scientific-blog/initiation-to-contact-angle>

³ Sourced from: <https://techblog.ctgclean.com/2011/08/is-it-clean-oil-and-hydrophobic-films-contact-angle-and-beyond/>

However, an increasing concern is that when conducting scientific experiments in the smaller scales, the wetting of liquids causes some remnants or residue to be left behind during liquid transfer or mixing, which may result in volume losses/wastage leading to contamination and reading inaccuracies especially when dealing with optical sensing measurements and microfluidic devices [106].

2.2.2 Surface Tension, Surface Energy & Young's Equation

Surface tension and surface energy are parameters that can be used for investigating the wetting of liquids on surfaces. The definitions from [107] describes surface tension as a property of liquid that opposes deformation or distortion when the liquid membrane is stretched and is denoted by γ . The unbalanced forces acting on the liquid molecules at the liquid interface creates surface tension [89]. These unbalanced forces arise from cohesion and adhesion of liquid molecules. Cohesive forces are attractive forces between those of the same substance/molecules whereas adhesive forces are the attractive force between different substances/molecules. Therefore, this property accounts for the ability of a liquid to control its shape.

For example, as explained in [89] the strong cohesive forces between water molecules (due to strong Hydrogen bonds) compared to the weak forces in air molecules (due to Van der Waals interaction) results in an inward pressure that minimizes the surface area and is responsible for creating a droplet shape. Whereas the strong adhesive forces between water molecules on a glass surface causes the water to spread creating wetting as mentioned in Section 2.1.1. The concept of surface energy is described as the amount of work done required to distort a liquid to increase its surface area by an amount ∂A [107]. The relations of surface tension to surface energy is shown in Equation (4).

$$\delta W = \gamma \cdot \partial A \quad (4)$$

Chapter 2: Literature Review

Where W is the surface energy,

γ is the surface tension,

and ∂A is the surface area.

The relation between surface tension and three interfacial boundaries of solid, liquid, and gas phase are simplified in the Young's Equation as shown in Equation (5). This equation provides a method for prediction of contact angle of droplets on surfaces.

$$\gamma_{SG} = \gamma_{SL} + \gamma_{LG} \cos \theta \quad (5)$$

Where γ_{SG} is the surface tension of solid-gas interface,

γ_{SL} is the surface tension of solid-liquid interface,

γ_{LG} is the surface tension of liquid-gas interface,

and θ is the contact angle.

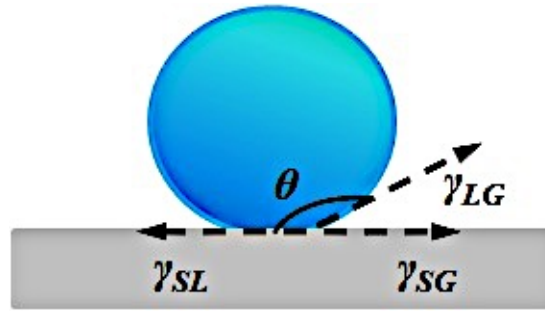


Figure 5: Interfacial boundaries of solid, liquid, and gas phase governing surface tension.⁴

There are a few factors that can affect/control the surface tension and contact angle. Surface tension can vary with temperature and also by adding surfactants, while contact angles can change due to electrowetting effect (i.e. applying electric field) and also through evaporation that may decrease the volume of the liquid [89].

2.2.3 Hydrophilic and Hydrophobic Surface

Hydrophilic surfaces are surfaces that have strong attraction to water i.e. encourages wetting. In contrast, hydrophobic surfaces repel water. Hydrophilic surfaces have contact angles less than 90° and hydrophobic surfaces have angles greater than 90°. Extremely wetting or non-wetting surfaces are called superhydrophilic and superhydrophobic surfaces where the angles are less than 5° and more than 150° respectively [108].

Hydrophilic surfaces are useful in applications that require high wettability and surface polarity such as electrochemical energy storage systems like Li-Ion or Sulphur batteries [109]. In the biomedical industry, superhydrophobic surfaces can help suppress protein adsorption, inhibit bacterial adsorption, prevent blood coagulation, support in handling microplate diagnostics and also control drug delivery [110]. The ability of superhydrophobic surfaces to retain air during under water immersion, results

⁴ Sourced from: <http://www.mecheng.iisc.ernet.in/~bobji/Hydrophobic/hydrophobic2.html>

in drag reduction of underwater vessels like submarines [111]. Both superhydrophobic and superhydrophilic surfaces can be useful for self-cleaning and anti-fogging applications [108].

Naturally existing superhydrophobic surfaces are those of plants leaves (e.g. Lotus leaves, taro leaves, India canna leaves) and insects (e.g. butterfly, dragonfly, water striders) [112]. The increasing interest in these surfaces have encouraged man-made fabrication. Surface geometry and surface chemistry is an important factor in creating hydrophobic surfaces. Two criteria necessary to create a superhydrophobic surface are that the surface must have low surface energy and should be roughened [111]. Surface wetting is commonly modelled using the Wenzel state [83] and Cassie Baxter state [113]. The difference in these two states is that the droplet is in direct contact with the roughened surface in Wenzel state but in the Cassie-Baxter state, the droplet is in contact with the peaks of the rugged surface and the air pockets in between them as shown in Figure 6 [114]. However, it was found that these two models do not account for the pinning effect [115].

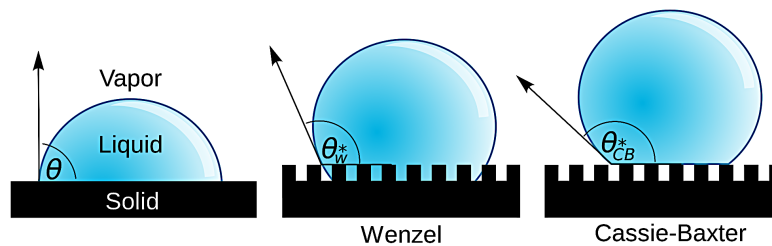


Figure 6: Comparison of contact angles on Wenzel and Cassie-Baxter Models.⁵

There are various methods of preparing hydrophobic surfaces. One of the methods included laser ablation by creating micro-patterns and can be done without altering surface chemistry of the substrate [116]. Some other methods include electrospinning process [117], modification of hierarchical structures through Silane

⁵ Sourced from: https://commons.wikimedia.org/wiki/File:Contact_angle_microstates.svg

coating [118], induced phase separation [119], as well as plasma [120] and sol-gel [121] processing. A technique that can be used to increase hydrophilicity is from an investigation conducted by Prakash et al. that introduces a combination of nanoparticle coating and UV irradiation which resulted in 0° contact angle [122].

Tang et al. discovered that hydrophobic robustness can be improved by micro-rolling grate onto titanium strips followed by the layering of Ti (C,N) on top using laser carbonitriding method [123]. In this case, Titanium was chosen due to its impressive chemical and physical properties. A recent study by Yilbas et al. showed that a surface wetting property can be controlled to exhibit both hydrophilic and hydrophobic behaviours [124]. In addition, a hydrophilic and hydrophobic hybrid surface can be created using oxidation and pyrolysis of nanocarbons where the surface retains hydrophilic characteristics [109]. Superhydrophobic surfaces like any other material are susceptible to wear and tear. Therefore, Tian et al. proposed a standardization method for testing durability of superhydrophobic material via linear abrasion [125].

2.3 Liquid Handling

2.3.1 1-60 μ L (drop)

Investigations on droplet mechanics are important for microfluidic applications and lab on chip devices. Thus, it is imperative to control droplet handling. Cira et al. showed that droplet movement can be controlled using evaporation-induced surface tension gradient [126]. Shemesh et al. demonstrated a method to generate stationary nanodroplet assays that can be useful for monitoring cellular processes of long timescales [127]. Studies on fine droplets are important in pneumatic spray applications where spray drift of pesticides cause pollution to the environment [128]. There are various types of methods in handling micro liquids. A common method in segmented flow microfluidics is dispensing droplets in an immiscible carrier liquid such as water in oil droplets that are generated using T-junction channels [129]. A study conducted by Leibacher et al. showed that bulk acoustic wave (BAW) acoustophoresis method can be used for droplet fusion, sorting and medium exchanges [130]. In digital

microfluidics (DMF), droplets can be moved using dielectrowetting, dielectrophoretic and magnetic-based techniques [131]. Moreover, the use of liquid marbles can avoid fluids leaks and easily move the droplet across surfaces due to small contact with substrate [132].

2.3.2 25-350 μL (standard microplate)

Microplates (Microtiter plates) have become a standard tool in optical sensing, analytical research and clinical diagnostic screening [133, 134]. Its multi-well design replaces the use of small test tubes and is most advantageous when dealing with samples of small volumes. Microplates promote the use of less reagents during experimentation. A focus for microplate advancement has been to find more effective methods to dispense and manage the testing of increasingly smaller liquid volumes where poor well filling is a known problem [135]. An approach of using scribed transparency-based microplates has been shown to overcome this problem [136, 137]. It is useful especially in cell culturing applications where it provides high throughput quantitation [138]. Common well densities for microplates are 96, 384 and 1536 wells on each plate. The 96 well density is the most frequently used in biochemical industry and is illustrated in Figure 7. These microplates are designed for compatibility with readers that are used to analyse characteristics of samples. Microplates are manufactured with different colours and material to suit the desired application. For example, opaque plates in black and white are used for luminance and fluorescence assays to enhance its detectability whereas translucent plates are used so that compound volumes and colours are visible [139].



Figure 7: Standard 96 well microplate with cover.⁶

2.4 Effects on Liquid

2.4.1 Heating (incubation)

Cell culturing is commonly used for research in the biomedical and biotechnology fields. Microfluidics technology in cell culturing allow for controllability, parallelization, automation, excellent imaging properties from a single cell level to tissues [140]. The parameters necessary to promote cell growth is its culturing media. The medium conditions can be manipulated by creating a specific defined medium containing nutrients suitable for the cell and also by adding a buffering systems to control pH [141-143]. Another important condition is to maintain optimal

⁶ Sourced from: <https://www.stemcell.com/corning-96-well-round-bottom-microplate.html>

temperature conditions that can replicate natural cell environment [144] which can be done via incubation [145]. However, studies show that higher incubation temperature results in slow cell growth [146]. Another problem related to incubation is evaporation of liquid media [147]. This can be countered by controlling the relative humidity [148] or by covering culture vessels [149]. Other methods involve using hydrophobic membranes which permits use of dry incubators [150] or adding silicone oil to the samples [149].

2.4.2 Evaporation

Evaporation of liquids is an important factor especially in the study of micro volume droplets. The applications include inkjet printing [151], spray cooling [152] and surface coating [153]. The problem when dealing with small volume droplets is that it easily evaporates resulting in loss of volume and inconsistency and inaccuracy in experimental analysis [149, 154]. There are two modes of evaporation which are called the constant contact angle (CCA) and the constant contact radius (CCR) [155] and there are cases where these modes are combined [156]. On rough surfaces, these modes occur randomly depending on surface morphology but may undergo specific mode based on proper design of the surface [157]. For example, roughened laser patterned substrate can be used to control the contact line pinning during evaporation [158]. The behaviour of droplets of azeotropic liquid mixtures during evaporation depends on the composition of the mixtures. Rowan et al. showed a gradual decrease contact angle over time with excess composition of 1-propanol whereas an unstable behaviour of contact angle was observed with excess water composition [159]. Other physical changes observed is the loss of mass of droplets as evaporation progresses with time [160]. One of the factors affecting rate of evaporation is relative humidity. An increase in humidity can reduce the rate of evaporation, resulting in low droplet contact angles due to greater spreading [161].

2.4.3 Edge Effect

Extended incubation of cell-based assays results in evaporation of culture media. This reduces the consistency of assay and also viability of cultured cells. It was reported that the evaporation of samples vary from inner wells to outer wells of the microplate array [162]. The outer edge shows greater evaporation rate [147]. The temperature of the outer edge of the microplate is found higher than the inside wells [163]. This was concluded to occur due to the heat conduction on the side walls of the outer wells [164] and the liquid film attached to the walls of the well act as an additional mass transfer area [165]. This suggests use of transparency microplates due to the air presence between liquid and solid walls resulting in insusceptibility to this effect [164]. Other studies show that pre-incubation at room temperature can help reduce this effect [166]. The latest design by Thermo Fisher Scientific that incorporated a built-in fluid reservoir surrounding the 96 well-plate was able to encounter this problem [167].

2.5 Liquid Dispensing

2.5.1 Methods of Dispensing

Two different displacement systems are used for dispensing liquids namely air and liquid. The traditional hand-held pipettes use air displacement where the air is pushed by internal plungers [168]. In contrast, liquid displacement uses working fluid where the fluid is controlled by a solenoid valve [168]. More sophisticated technology involve use of piezoelectric pulse generators, pneumatic pulse generators and electromagnetic force pulse [169]. Felton explains that handling extremely small volumes of liquids will be disadvantageous as air compressibility may lead to dispensing errors. He further explains that a downside to liquid displacement systems is that the flow rates may be influenced by temperature fluctuations and that corrective measures cannot be implemented due to it being an open loop system. Another issue when dealing with very small volumes of liquids is transferring the liquid from tip to surface without contact. This contact will likely lead to loss of volume or contamination. Creating electrostatic potential between pipette tips and the target

surface can counter this issue [170]. Viscous liquids can cause large errors when dispensing nano to micro scale volume because of its high resistance to flow. The time taken for it to rise in the tip is slow and unknown and liquid tends to stay attached to tip wall resulting in loss of volume or creating air bubbles inside the tip. It is found that positive displacement pipettes can be used to counter this as the piston is in direct contact with liquid sample eliminating the air cushion [171].

2.5.2 Bubble Formation

In liquids, bubbles can be naturally occurring or intentionally induced to perform certain functions. Multiple studies on bubble dynamics were conducted in viscous liquids [172-177]. Manipulating the temperature and pressure in a three phase fluidized bed system consisting of gas-liquid-solid allows the bubble dynamics to be controlled [178]. It is possible to form larger sized bubbles by dispensing via the plastron layer existing on superhydrophobic surfaces [179]. Bubbles are used as to aid operation of electromechanical actuators [180, 181]. Moreover, microbubbles are used as agents to enhance contrast in ultrasound imaging [182]. Although this phenomenon might be beneficial to some applications, it may give disadvantages to many other industries. For example, bubble formation may significantly decrease operational efficiency in coagulation-flocculation and filtration [183]. Bubble formation also degrades the mechanical properties of final composite material during Liquid Composite Moulding (LCM) [184]. Presence of bubbles may also cause reading inaccuracies for the analysis of assays using optical sensing devices. Viscosity is a contributing factor to bubble formation and its sizes [185].

2.6 Unmanned Aerial Vehicle (UAV) in Biomedical Industry

An Unmanned Aerial Vehicle (UAV) was firstly designed to perform military reconnaissance for warfare [186]. Now, UAV is well known for its commercial use in photography and cinematography. Other applications involve using UAV for

surveillance and navigation [187], and even search and rescue missions [188]. The design of UAV has expanded with many advantageous features such as broadcasting, autonomous/remote piloting, light weight, manoeuvrability, autonomous sensing, and long board endurance [189-192]. These favourable features allow us to reduce labour and have raised the possibility for the use of UAV for easy access and coverage in the rural sectors. In the recent years, the applications of UAV have vastly expanded in the sectors of agriculture to estimate biomass and perform forest inventory [193-195]. Zarco-Tejada et al. used UAV to obtain high resolution hyperspectral imagery for estimation of carotenoid contents in leaves covering multiple vineyards [196]. UAVs provide a quicker method for crop monitoring of pests [197]. A recent breakthrough in precision agriculture is using low altitude remote sensing aboard UAVs for weed management [198]. Therefore, the use of UAV in biochemical industry is most advantageous.

3 LIQUID STABILITY STUDIES

3.1 Introduction

During transport, liquids are sensitive to surrounding perturbations. When dealing with droplet movement, it is necessary to examine the different factors underlying droplet mechanics and its reaction to various perturbations before designing a system that can increase and maintain stability during transport. This chapter presents the investigations on liquid stability under different conditions. Section 3.2 presents the investigations on droplet elongation on an inclined surface. This is followed by studies on droplet behaviour under impact presented in Sections 3.3 and 3.4 where the investigations were conducted using upward longitudinal impact and horizontal forward car crash-like impact respectively. Lastly, droplet dislodgement behaviour from gravitational impact is presented in Section 3.5.

3.2 Drop Elongation on Inclined Surface

3.2.1 Introduction

A type of perturbation that a droplet may experience during transport is inclination. In this section, the results for the experiment in which elongation of drops on inclined Polytetrafluoroethylene (PTFE) surface are discussed. This experiment focuses on the stability and behaviour of droplet under this perturbation. Many analytical, experimental and numerical studies have explored drop motion on inclined surfaces. Young's equation from Equation (5) is extensively used to account for this to dictate the contact angle. The droplet is able to exhibit both advancing and receding contact angles while it is static (see Figure 8b). Numerous complex mathematical models have been devised to account for this effect [199, 200]. However, this is different to cases where the drop is under axis-symmetric compression (Figure 8c) or extension (Figure 8d), exhibiting exclusive advancing or receding angles respectively.

It is found that the front contact line breaches first when a drop placed on a surface subjected to increasing and gradual inclination relative to the horizontal [201, 202]. Hence, the drop is able to extend in one direction (i.e. only extending the front contact line) before total drop detachment from the surface can be achieved from a high enough incline (see Figure 8b). To some extent, such a behaviour is akin to a pendant drop dripping from a faucet [203]. This experiment is useful to predict the ability of droplet to withstand the degree of inclination of the surface, especially on surfaces that are weakly wetting which will provide insights in the design stage of a droplet transport system. Glycerol has higher viscosity ($\sim 1.4 \text{ Pa}\cdot\text{s}$) compared to water ($\sim 0.001 \text{ Pa}\cdot\text{s}$), which may cause clogging when used for applications involving closed channel microfluidic devices. However, application in droplet form on open surfaces may overcome these problems.

From the models developed in [199, 200], there is validity in monitoring the contact angle but this cannot be concluded from experiments. In this section, tests on water-glycerol mixture drops dispensed on a hydrophobic PTFE surface (equilibrium contact angle $> 90^\circ$) were conducted in two parts. In part 1 of the experiments, the drop was quasi-statically tilted until it was able to displace from the surface. The contact angle behaviour was compared to part 2 of the experiments where the drops were subjected to compression and extension.

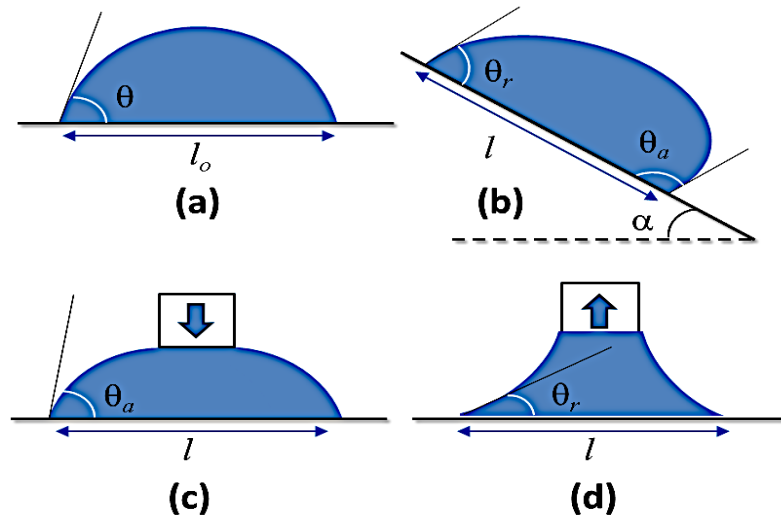


Figure 8: The placement of a drop on a horizontal surface (a) having an equilibrium contact angle θ with initial width, l_o based on a semi-spherical shape. When tilted at an angle α to the horizontal (b), the drop will assume an advancing, θ_a and receding, θ_r contact angles. It is often the case that the drop will breach at the advancing ahead of the receding contact line. Consequently, the drop experiences elongation of front contact line one direction such that $l > l_o$. The situation is different when the drop is compressed (c) and extended (d), where it will solely exhibit advancing and receding contact angles respectively with no elongation of front contact line.

A droplet on solid surface spreads due to the interfacial energies in the system, which are the surface-liquid, (γ_{SL}), surface-gas, (γ_{SG}) and the liquid-gas, (γ_{LG}) interfacial tensions. In this process, the flat area in contact between the drop and the surface, A_{SL} , increases, while the substrate surface area that is exposed to air, A_{SG} , decreases. From this, it is possible to assume that $\partial A_{SL} = -\partial A_{SG}$. However, changes to the liquid-to-gas area, A_{LG} may vary depending on droplet development. The spreading will stop when equilibrium is reached such that the work done by spreading δ_w goes to zero. It is also necessary to include the contribution of work done by change in total volume of liquid ∂V as well as the Laplace pressure change ΔP between the inside and outside of the drop. Hence, from Equation (4), it will be possible to express the whole process as

$$\delta w = \gamma_{LG} \partial A_{LG} + \gamma_{SL} \partial A_{SL} + \gamma_{SG} \partial A_{SG} + \partial V \Delta P \quad (6)$$

The liquid can generally be taken as incompressible. Therefore, $\partial V = 0$ so Equation (6) can then be simplified to

$$\delta w = \gamma_{LG} \partial A_{LG} + (\gamma_{SL} - \gamma_{SG}) \partial A_{SL} \quad (7)$$

If the drop is tilted quasi-statically on an incline, the incremental work done is accounted by the gravitational acceleration, g such that the elongation drop is displaced through its centre of mass by Δx in which

$$\rho V g (\sin \alpha) \Delta x = \gamma_{LG} \partial A_{LG} + (\gamma_{SL} - \gamma_{SG}) \partial A_{SL} \quad (8)$$

Where ρ is the fluid density,
and V is its volume.

3.2.2 Materials and Methodology

Materials

A hydrophobic PTFE block was used as a substrate. An optical profiler (Bruker Contour GT-I) was used to verify the characteristics of the substrate surface. The profiler employs phase-shifting and/or vertical scanning interferometry to resolve the topology of complex 3D structures. The technique is able to marry precision z-axis

control with interference-based techniques to resolve features from the angstrom to millimetre scale.

Water-Glycerol mixtures ranging from 0 – 100% glycerol concentration by volume, were prepared by adding glycerol (Sigma Aldrich, G5516) to Milli-Q water. These solutions were prepared in a polypropylene centrifuge tubes and mixed to homogeneity using a vortex mixer (Proscitech EVM80). The mixtures were allowed to settle for 1 hour before use. For all experiments associated with drop on an incline, the temperature and relative humidity ranges were 20 °C to 22 °C, and 50% to 56% respectively.

Methods

Part 1: Drop on Incline Experimentation

An opto-mechanical rotary stage setup (Edmund Optics, 52-572) with 1° resolution was adapted to permit a drop to be located on the PTFE substrate to correspond to the gimbal position as illustrated Figure 9. This eliminates the need to move the camera when different amounts of tilts were applied and also to allow the substrate to tilt over a large angular range. A bright LED lamp with diffuser was used to provide the lighting for recording. A video camera attached to an InfiniVar CFM-2/S microscope lens was used to image the drop. A manual pipette (VITLAB, 1641000) was used to accurately dispense a 10 µL volume of the mixture on the substrate surface. The stage was tilted at intervals of 1°. In between each tilt, a delay of 30 seconds was introduced to permit the drop to acquire a quasi-static equilibrium state. Six readings were recorded for each drop concentration to confirm the drop characteristics. Since the images recorded had high contrast, post-processing operations were not performed on them. The geometrical values of the drop (angles and lengths) were derived using the software Tracker (<https://www.cabrillo.edu/~dbrown/tracker/>).

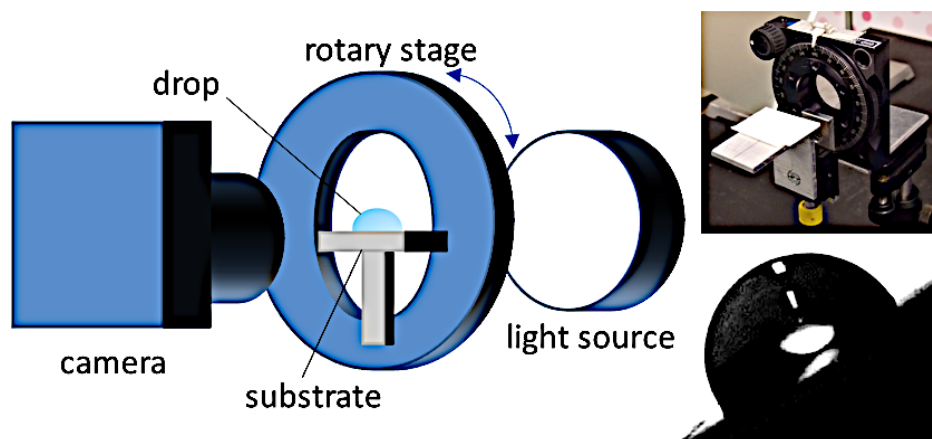


Figure 9: The experimental setup to observe the drop behaviour from zero incline up to detachment. This method of using a rotary stage with a through hole, and positioning the drop at the gimbal point, allows for the drop to rotate through a wide range of inclines, and eliminates the need to reposition the camera each time. The inset pictures show the setup without the camera and light source set up, as well as an example image of the drop recorded.

Part 2: Drop Compression and Extension Experimentation

In this set of experiments, a manual pipette (VITLAB, 1641000) was used to accurately dispense a 10 μL volume of the mixture on the substrate surface. To examine compression, a solid stainless-steel rod of diameter 1.270 mm was then lowered slowly at a speed of 0.00001 mm/s onto the centre of drop towards the substrate. The video was recorded to establish the contact angle development. To examine extension, the same stainless steel was lowered until it just contacted the centre of drop. It was then raised slowly away from the substrate. The video was again recorded to establish the contact angle development using Tracker.

3.2.3 Results & Discussion

Part 1: Drop on Incline Experimentation

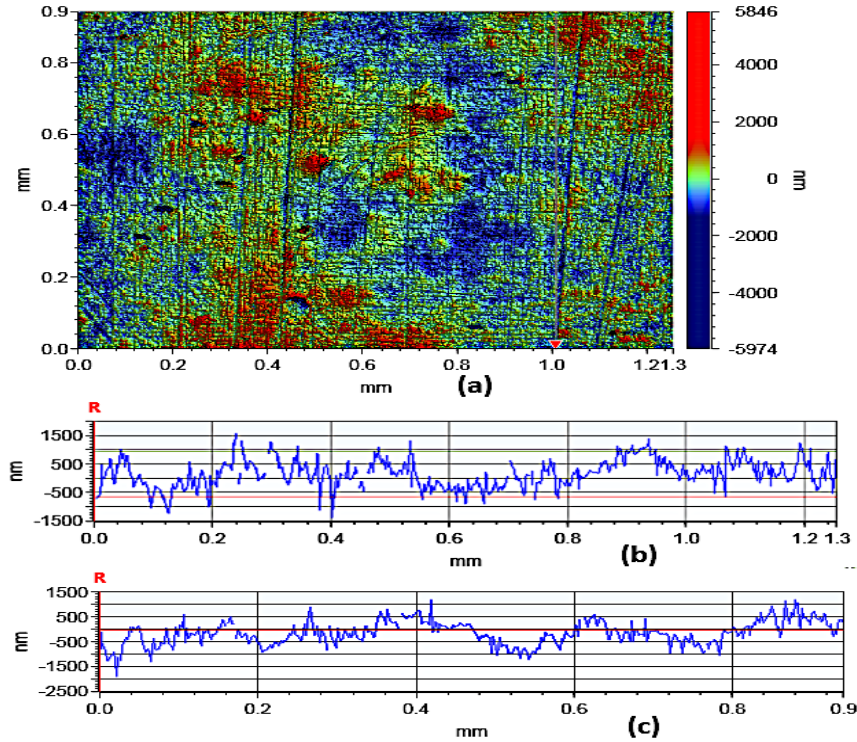


Figure 10: Typical area topographic scan (a) from an area on the PTFE substrate using optical profilometry. No anisotropy in the topographic distributions were revealed from the scans taken for the horizontal (b) and vertical (c) line sections.

There were no unusual structures noticeable from the optical profilometry scans conducted on the PTFE substrate used (Figure 10). In addition, no anisotropy was found that would suggest that there would be directional influences on the drop, in terms of surface wetting behaviour. From a typical scan comprising 298512 data sampling points, the peak-to-peak value and root mean squared roughness parameters were measured to be $11.819 \mu\text{m}$ and $0.571 \mu\text{m}$, respectively.

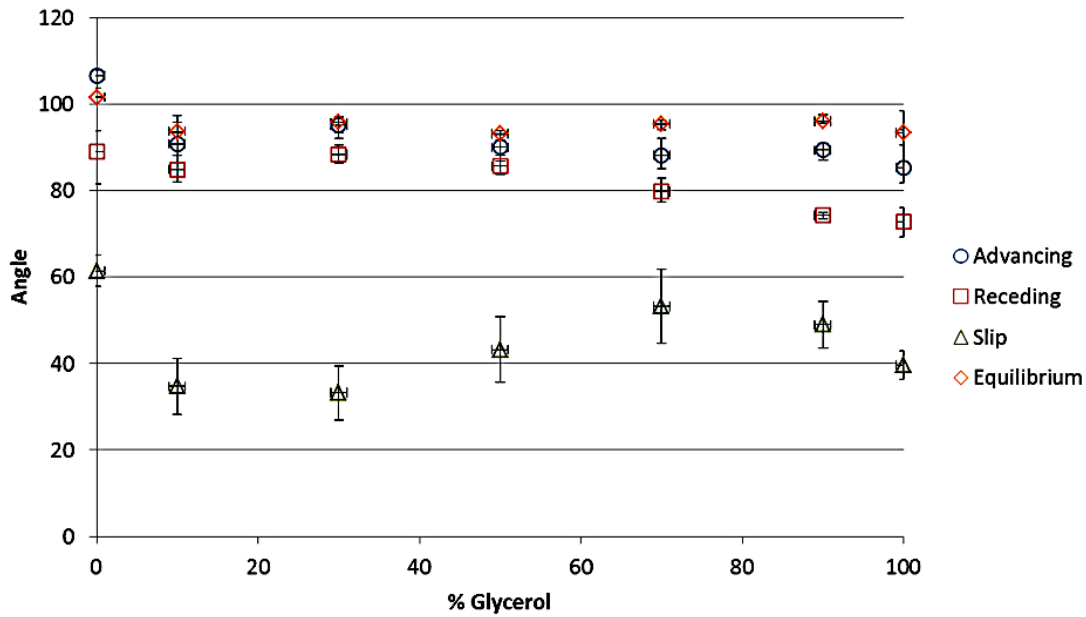


Figure 11: Plots shows the distributions of equilibrium contact angle (on horizontal position i.e. before inclination), the slip angle (inclined angle when drop detaches from surface), as well as advancing and receding contact angles (at the point just before detachment). These values were recorded for water-glycerol mixtures (ranging from 0-100% glycerol) on PTFE substrate that was slowly tilted up to the point of detachment. The slip angle distributions were irregular and cannot be correlated to the advancing and receding contact angles. Advancing and receding contact angles tend to decrease with increasing concentration of glycerol in the mixture. The error bars indicate one standard deviation from 5 readings.

From the plots given in Figure 11, it can be seen that the equilibrium contact angle (at zero incline) distribution was relatively similar regardless of the mixture composition. The trend of the advancing contact angle is seen larger than the receding contact angle. These angles were measured when the surface reached an inclined angle just before droplet begins its detachment from the surface. This describes the hysteresis that is frequently used to express the ability of drops to stay on inclines. However, the level of hysteresis does not show any influence on the slip angle, defined as the inclined angle where the drop completely detaches from the surface. Another observation is that the advancing contact angles are generally smaller than the equilibrium contact angle.

The ability of the drop to breach its front contact line first explains this contact angle behaviour [201, 202]. With the rear contact line still pinned to the surface, the drop is able to undergo a transient elongation. In solid mechanics, this elongation is

classified as plastic since the drop will not resume its original length even if the inclined surface was returned to its horizontal. Flow dominated effects can be omitted as the surface was tilted in a quasi-static manner. The droplet undergoes a relaxation due to this elongation, thus assuming smaller advancing angles compared to equilibrium contact angles.

The slip angle trends in Figure 11 indicates a complex relationship between the adhesion forces of mixture-dependent composition of glycerol and water to the PTFE surface. This relationship is likely governed by the capacity of PTFE surface structure to retain bubbles on the surface. PTFE surfaces are hydrophobic and manufactured with micro and nanostructures, and these surfaces have the capacity to be highly non-wetting and develop very high equilibrium contact angles ($> 120^\circ$) to characterise them as superhydrophobic (SH) [204, 205]. SH surfaces develop a stable thin film of air called a plastron when they are immersed in water, [206, 207]. It is suggested that much larger volumes of sessile bubbles are able to exist on the SH surfaces due to these plastrons [208]. It is likely that regions of non-visible surface air entrapment may continue to exist on non-SH PTFE even when the larger bubbles dissipate through diffusion [201]. In aqueous solutions, glycerol is able to make the solution more compact by disrupting the hydrogen-bonded structure of water [209].

Molecular dynamics simulations conducted on water-glycerol liquid mixtures with higher weight percentages of glycerol, revealed heterogenous systems where surrounding water molecules were found to have a large influence on the populations of glycerol conformational isomers (or conformers) [210]. Although the local structure of water in the mixture may be similar to its structure pure state, the glycerol structure can exist in three different forms; as molecules occurring in an environment reflective of pure glycerol, as monomers solvated by water, and as mixtures of H-bonded clusters connected in a 3-D glycerol H-bond network with water molecules. It is possible that complex wetting characteristics resulted from the interaction of droplet with the PTFE surface due to the presence of these micro-heterogeneities in the water-glycerol mixture. This led to the extent of air bubble entrapment on the surface. The interaction of these air bubbles with the contact line affects the ability to keep the drop from detaching.

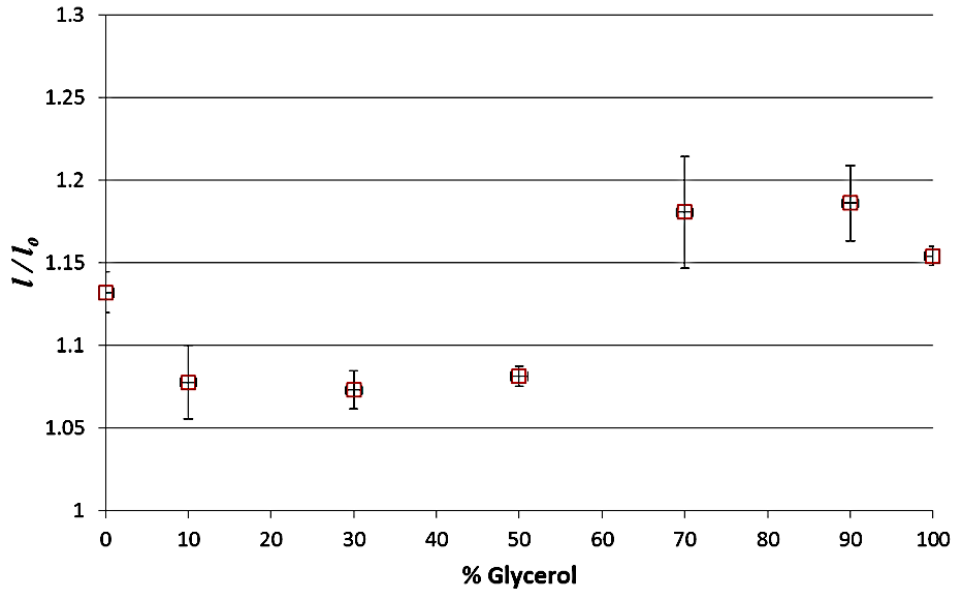


Figure 12: Plots of l/l_0 ratios with varying water-glycerol concentration where drops are placed on PTFE surface. The distribution shows similar trends to the slip angles in Figure 11. This indicates a relationship between the extent of elongation of the drop and its capacity resist detachment as the inclination of PTFE surface is slowly increased. The error bars indicate one standard deviation from 5 readings.

It will be useful to be able to relate the slip angle to a physical parameter of the drop. Hence, the distributions of l/l_0 ratios (at the point of detachment of the drop) in relation to the water-glycerol mixture was plotted as shown in Figure 12. It is observed that these show a similar trend to slip angles presented in Figure 11. The readiness of the PTFE surface to randomly trap air bubbles on surfaces can account for the large spread in values of the slip angles and l/l_0 ratios. Tracing the important parameters of the drop with increase in inclined angle from the beginning up to the point of detachment from the surface provides a better understanding of the correlation between slip angle and l/l_0 ratio. This is shown in Figure 13 where the advancing and receding contact angles were traced from zero incline up to detachment with two concentrations; one with water and another with 30% glycerol concentration (inset). From the plots, there is no indication that can correlate the contact angles to the ability of drops to either elongate or detach from the surface. This implies that contact angles are only representations of the drop process of undertaking different shapes in order to best minimize its surface energy in response to the increasing perturbation by gravity.

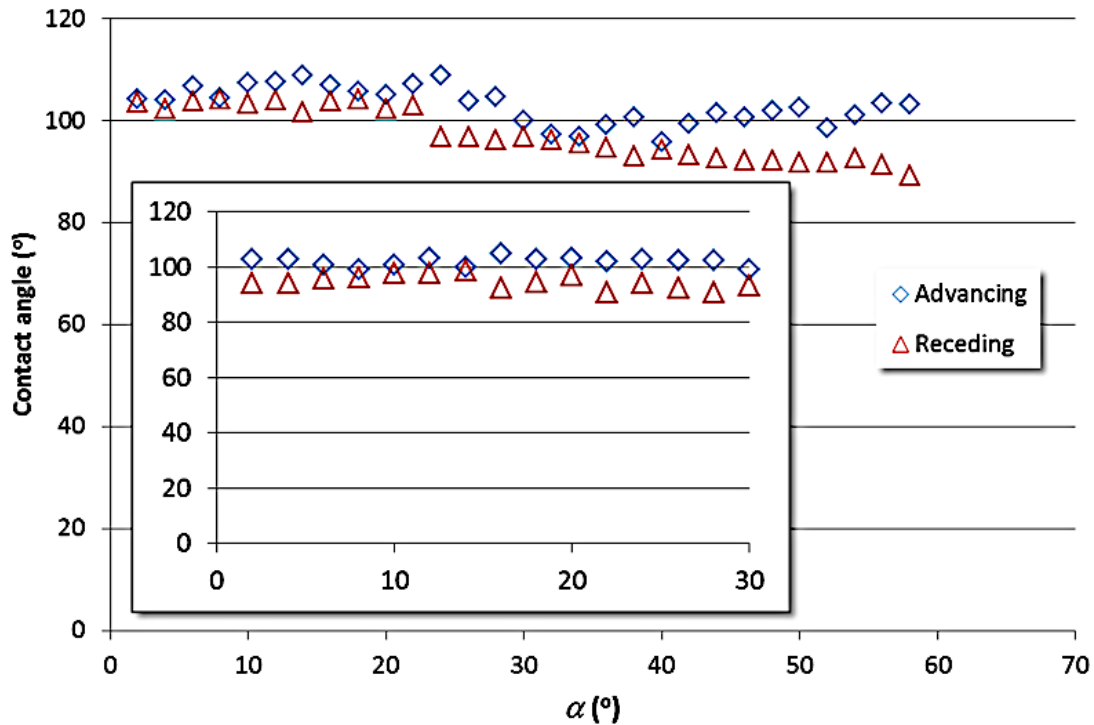


Figure 13: Traces of the advancing and receding contact angles of a water drop with various tilting of the incline. The inset gives the case with 30% glycerol in a mixture with water. In all cases, the contact angle does not provide information on the propensity of the drop to slip or to deform on the incline prior to slipping.

Conversely, a different result was seen from tracing the length of the drops (see Figure 14). It was found that a two-stage manifestation of elongation occurred in both pure water and with 30% glycerol. The gravitational force, is a function of sin of the tilt angle, α (see inset of Figure 14). Thus, a sudden change in the gravitational force acting on the drop cannot correlate with the droplet behaviour. This suggests that in the initial stage, the drop was extending as single body but the drop was attempting to initiate a process of splitting into two in the second stage. In the second stage, the extension rate is intensified due to the front end of the liquid body having a greater motive force compared with the rear end that wishes to remain attached to the surface. Before detachment, the droplet is able to withstand the limited surface energy change. Due to the limited surface energy change that the drop is able to withstand which prevents it from rupture resulting in formation of daughter droplet at the rear end and remain attached the surface. To an extent, the mechanics is comparable to a liquid bridge that is quasi-statically stretched [211] or evaporated [212] between two solid

surfaces. In particular, the ability of the liquid body to displace has been seen when one of the surfaces is a nozzle where that liquid contained in it could be “pulled” out [213]. This situation is similar to the behaviour of drops undergoing frustrated attempts to separate which is typically encountered in highly dynamical conditions but typically on surfaces that have low adhesion forces [214, 215]. This is expected as the droplet then has higher freedom to undergo shape adjustments more readily. Still, the drop does not proceed to rupture immediately. This is due to a reverse process where drops have a tendency to coalesce even when attempting to separate [216].

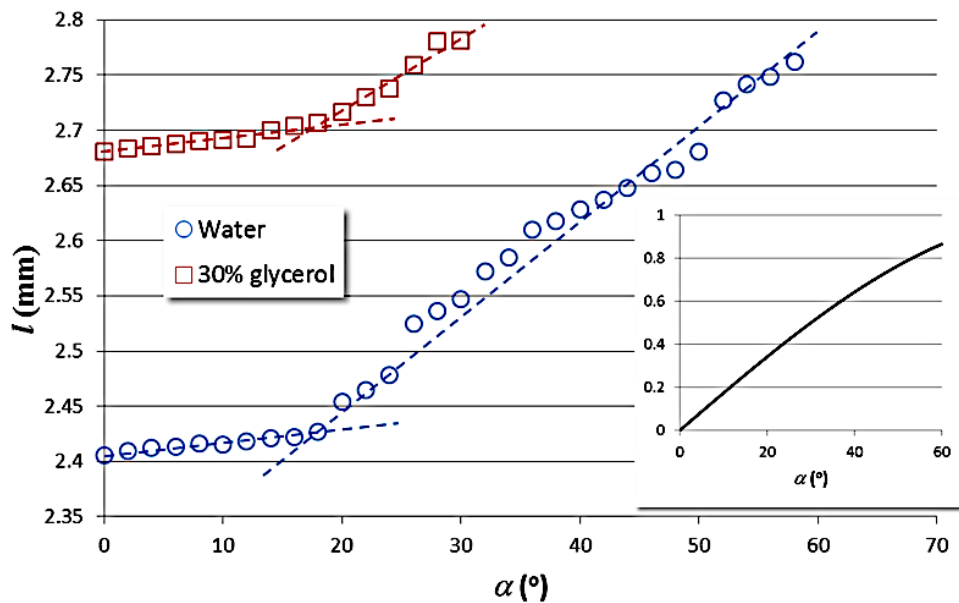


Figure 14: Traces of the length of drop with progressive change in the tilt angle of incline for a drop of water and a mixture containing 30% glycerol. A two-stage elongation process is observed for the drops. The inset provides a plot of the sine of α in relation to the change in α , which provides a scaling of progressive force due to gravity acting on the drop.

To consider the energetics involved, Δx in Equation (8) corresponds to the can be assumed to correspond to change in l , then a large portion of work done by the drop to account for the energy change due to gravitational increase can be supported by ∂A_{SL} . This assumption is reasonable since hydrophilic surfaces have more shape extensions

compared to hydrophobic surfaces, where corners can develop and lead to pinching [217]. Since hydrophobic surfaces restrains the shape deformations more, ∂A_{SV} is more limited, thus allowing ∂A_{SL} to dominate during the attempts to energetically adjust to the energy supplied by gravity. This limited extent of ∂A_{SG} allows the drop to develop advancing contact angles are near equilibrium values, since it requires less work to reach the limiting condition at the front contact line.

Part 2: Drop Compression and Extension Experimentation

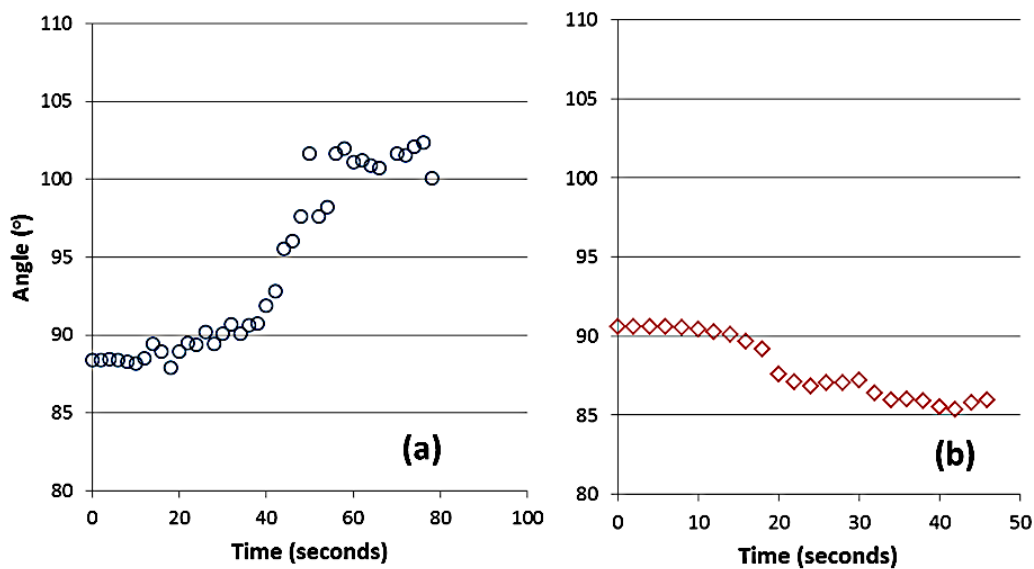


Figure 15: Traces of the (a) advancing contact angle when a drop of 50% glycerol liquid mixture on PTFE substrate was slowly compressed, and the (b) receding contact angle when it was slowly extended with time.

Figure 15 shows the changes of contact angle with time for a liquid drop that was compressed and extended respectively. During the compression process in (a), the contact angle increases to an advancing state before reaching a limiting value of $\sim 102^\circ$. During the extension process in (b), the contact angle reduces to a receding state before arriving at a limiting value of $\sim 85^\circ$. Both these behaviours are similar to those in

previous studies using non-wetting surfaces [218]. Hence, this shows that the behaviour of drops on the incline are not influenced by surface or liquid characteristics, but by the means of minimizing its energy on the surface. The conditions of the droplet on an incline is different to that under compression or extension as the three-phase contact line is more unbalanced on an incline. Using the contact length of the drop to adapt to this unbalance effect will not be significant when the surface is wetting, as the higher adhesion forces will restrict the front contact line extension whilst allowing the drop to undergo angular distortion instead that is seen through the contact angle changes. In contrast, low adhesion forces on a weak wetting surface allows for contact length extension and thus does not require any angular distortion to adapt to change in energy. The results in Figure 15 also deduce that the somewhat invariant contact angle trends in Figure 13 are not caused by measurements inaccuracies.

Superhydrophobic surfaces may be feasible for liquid transfer with reduced sample loss (i.e. from low levels of adhesions) and contamination in biochemical analysis. Nevertheless, the control of drop movement will expectedly be challenging in systems that involve tilting especially during sample transport unless these surfaces can be designed with shapes that provide gravitational potential wells and movement can only be achieved by external perturbation. To create a practical system, the surface requires regions that are both hydrophobic and superhydrophobic. The understanding of the manner of drop elongation can be used to match the hydrophobic region to the extent of extension within the first stage. Following that, a consistent tilt angle to drop detachment may be achieved regardless of the mixture composition thus easing design for automation of the system. Besides possessing low evaporation characteristics, drop movement using water-glycerol mixtures is useful in transport due to their protein stabilizing properties in biochemical processes such as protein crystallization and pharmaceutical protein formulation [219] due to its ability to preserve protein stability and functionality [220]. It is worth noting that once drop movement commences, mass and heat transfer can be facilitated due to the wall shear stresses developing [221]. Moreover, the other advantages offered in the use of glycerol as the medium for which will be explained in Sections 5.1 and 5.3.

3.2.4 Conclusion

The equilibrium contact angle (with zero incline) distribution on a PTFE surface was found to be relatively similar with various water-glycerol mixture compositions but the slip angle showed a more complicated trend. This is likely governed by the capacity of the surface to retain bubbles on it. In aqueous solutions, glycerol has the ability to disrupt the hydrogen-bonded structure of water, thereby making the glycerol structure able to develop micro-heterogeneities. This suggests the wetting characteristics to be determined by the interaction of fluid with both the solid as well as the air entrapped within the surface microstructures. When tilted to the extent just before total detachment from the surface, the drop was found to breach its front contact line first. This showed that the contact angle hysteresis does not have any influence on the slip angle, in fact the advancing contact angle values were smaller than the equilibrium contact angle. Alternatively, the l/l_0 ratios calculated at the point of detachment of the drop mimic the trends seen for slip angles. When the length of the drops was traced from zero incline up to detachment, a two-stage elongation was found. This behaviour could not be attributed to the sudden change in the gravitational force acting on the drops. This implied that the drop was initially extending as single body, but then attempted to initiate a process of splitting into two. Through considering the energetics involved, it could be concluded that ∂A_{SL} was main factor used by the drop adjust to the energy supplied by gravity but ∂A_{SG} was limited. Results from comparative experiments for drop under compression and extension eliminate the possibility that specific characteristics associated with the liquid and solid could be responsible for this behaviour. This understanding of drop mechanics will be useful when designing for automation of systems during transport as a constant inclined angle can be achieved to prevent droplet movement regardless of its mixture concentration.

Results of this work were reported in the paper (ZAHIDI, A. A. A., CHEONG, B. H. P., HUYNH, S. H., VUONG, T., LIEW, O. W. & NG, T. W. 2015. Glycerol-water sessile drop elongation on PTFE inclines in relation to biochemical applications. *Colloids and Surfaces a-Physicochemical and Engineering Aspects*, 486, 21-28) attached in Appendix A.

3.3 Drop Characteristics Under Upwards Longitudinal Impact

3.3.1 Introduction

Scribed transparency-based microplates have been demonstrated to be able to withstand sidelong impact without liquid sample spilling or displacement despite their seemingly less robust architecture in terms of handling stability [222]. An effect of this sidelong impact is the capillary waves were found to travel towards the contact line at the opposite end. Through heightened pinning from the scribed edges on the surface, the amplitude of the wave could increase and multiply its resistance to spreading given that the advancing contact angle condition was not exceeded [222]. These capillary waves serve to dissipate the mechanical energy supplied to the system. Nevertheless, the extent of these perturbations is unable to offer strong bulk mixing of the liquid sample.

There are driving forces that can cause sessile drops to exhibit resonance. In such case, it may be possible for bulk mixing and even particle assembly to occur [223] but a highly precise equipment is required to provide a driving excitation to match the sessile drop's resonant frequency. However, if stochastic excitation is introduced such that it falls within the range the resonant frequency resides in, it is possible for the system to be set into resonance. This has been seen in drops (i) rolling down a surface with asperities lithographically produced using fibrils of well-defined lengths, cross-sections and spacing [224], (ii) placed on a stationary tip coming in contact with a rotating SH drum, such that resonance is maintained primarily from stochastic stick-slip events between the liquid and SH surface [225], and (iii) dispensed on substrates that are created to have a circular hydrophilic region bound by superhydrophobicity so that they exhibited high contact angles, and then translated by a linear stepper actuator [226]. Still, the extent of mechanical energy transferred from actuation of the liquid body will facilitate enhanced diffusion but is not sufficient to result in significant bulk mixing.

In this section, the results for the experiment in which sessile drops were accelerated upwards and then stopped suddenly to create a longitudinal impact effect

are discussed. This experiment examines on the stability and behaviour of droplet under this perturbation and also the capability of the system to be used as a mixing tool during transport. This experiment contrasts sharply with previous studies made of drops released from heights and then impacted on solid substrates [227-230]. The tests were conducted using water-glycerol mixtures of varying volumes. The range of behaviours exhibited were categorized up to point of liquid body separation. The effects arising from the scribed or non-scribed structure of the transparency were analysed. In the event of the liquid body detachment, numerical simulation was used to identify the liquid flow characteristics in order to deduce the extent of coalescent mixing.

3.3.2 Materials and Methodology

Materials

Water-glycerol mixtures (0 – 70% v/v) of 40 μ L volume were used as test liquid drop samples. The values of surface tension and viscosity in relation to the mixtures used is shown in Table 1. Cellulose acetate film of 0.5 mm thickness was used as the substrate. To create the scribed substrates, samples wells were scribed on the substrate with a diameter 6.96 mm (similar to standard 96-well microplate well diameter). This was done by placing the cellulose acetate film in a desktop cutter plotter (Wentai, JK361) which had a 90° cutting tip. The force of the needle on the cutter plotter was chosen to ensure that the transparency was not completely cut through which was set to 500 N for best results. Also, a speed of 50 mm/s was chosen so that the accuracy of the shape of the design was well preserved.

Table 1: Listing of viscosity and surface tensions of water-glycerol mixtures used.

Glycerol mixture % (V/V)	Viscosity (Ns/m ²) at 20°C	Surface tension (N/m) at 20°C
0	0.001790	0.0728
10	0.002564	0.0717
20	0.003900	0.0707
30	0.006371	0.0697
40	0.011331	0.0688
50	0.022363	0.0679
60	0.050223	0.0670
70	0.13286	0.0662

A rectangular 50 x 50 mm aluminium channel of 2.5 mm thickness with a depth of 20 mm was used to construct the gantry. The light weight and rigid feature of Aluminium made it a suitable choice for the setup. The scribed substrate was characterized using a 3D optical profilometer (Bruker, Veeco-Wyko) based on a non-contact GT-1 interferometric system. The instrument was placed on a pneumatic vibration-isolation table (Newport) which was fitted with active high attenuation isolation and calibrated using step height standards (Bruker, Veeco). The instrument uses phase-shifting and/or vertical scanning interferometry to resolve the topology of structures. Imaging was obtained using both low and high magnifications to ensure optimal scanning results.

Methods

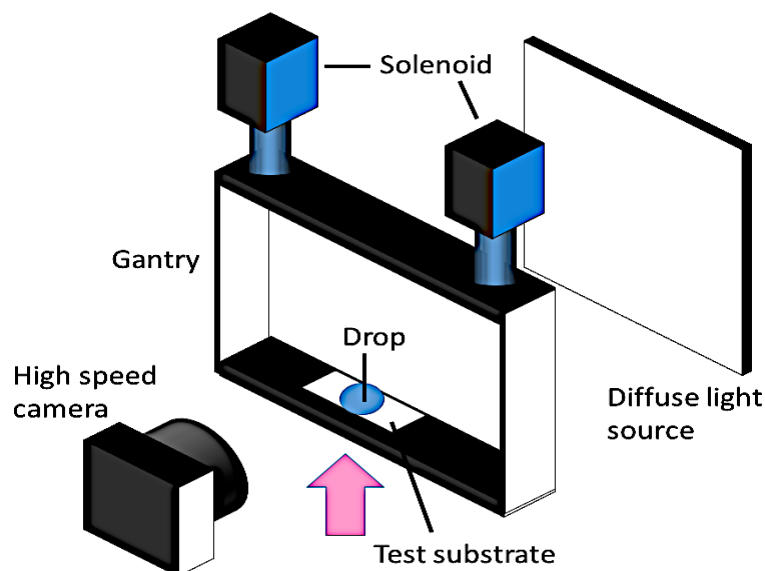


Figure 16: Schematic description of the setup to conduct the experiments in which a pair of identical solenoids activated simultaneously actuate a gantry containing a substrate with drop dispensed on it. With diffuse illumination from the rear, high speed camera video sequences of the drop as it was raised and stopped suddenly could be recorded for analysis.

The experimental setup is shown in Figure 16. Two pull-only solenoids (Techbrands, SS0902) were used to move a gantry uniformly upwards powered by a 12 Volt DC power supply that provided electrical current to them simultaneously via a latching switch. The test substrate was attached to the bottom surface of the gantry. Various volumes of liquids were dispensed on the test substrate using a manual pipette (Eppendorf). Background illumination was provided by a diffused light source to obtain good contrast images on a high-speed camera as the solenoid moves the gantry upwards and stops abruptly (impact) at the end of each stroke. Different impact effects were achieved by adjusting the stroke movement of the solenoid to specific values.

The gantry movement in relation to the stroke of the solenoids was characterised prior to conducting the experiments with drops. This was done by tracking a selected position on the gantry using the video sequences recorded using the high-speed camera

from the beginning up to the moment where the gantry movement stopped. This allowed the impact momentum to be calculated. The maximum value is limited by the pulling power of solenoids actuators and the frame rate of the high-speed camera. If the frame sampling rate is not rapid enough, the accuracy for obtaining higher impact momentums will be limited. All parameters associated with the drop following impact were obtained from the high-speed video sequences. They were derived by selecting specific locations on an initial image followed by frame-by-frame software processing (Tracker).

Numerical simulations were used to investigate the capacity of drop mixing. They were based on the finite element method and performed using COMSOL Multiphysics 5.0 based on the geometries of two typical drop sizes coming together. It is useful to develop models that can support interconnected physical phenomena. The model needed to simulate a two phase flow (the flow of liquid and flow of the surrounding air) using the level-set method [231, 232] to simulate the merging and deformation of the droplets. A two-dimensional mesh model was used as it will sufficiently account for an axis-symmetry coalescence. To define the boundary conditions, the bottom boundary was assumed to be a wetted wall with a contact angle of 90° , the boundary tangent to the axis symmetry surrounding the droplet was assumed to be an outlet for the air flow and the top boundary was assumed to be a free inlet for airflow. The total elements used in this simulation ranged from 1.31×10^5 to 3.34×10^5 , in which the minimum and maximum element sizes of the fluid phase were 1.31×10^{-5} and 3.31×10^{-5} respectively. The absolute tolerances on every model were 5×10^{-4} to minimize errors. These conditions were arrived from a mesh convergence process conducted. This was also used to confirm that the results obtained were not a product of under-resolved geometries.

3.3.3 Results & Discussion

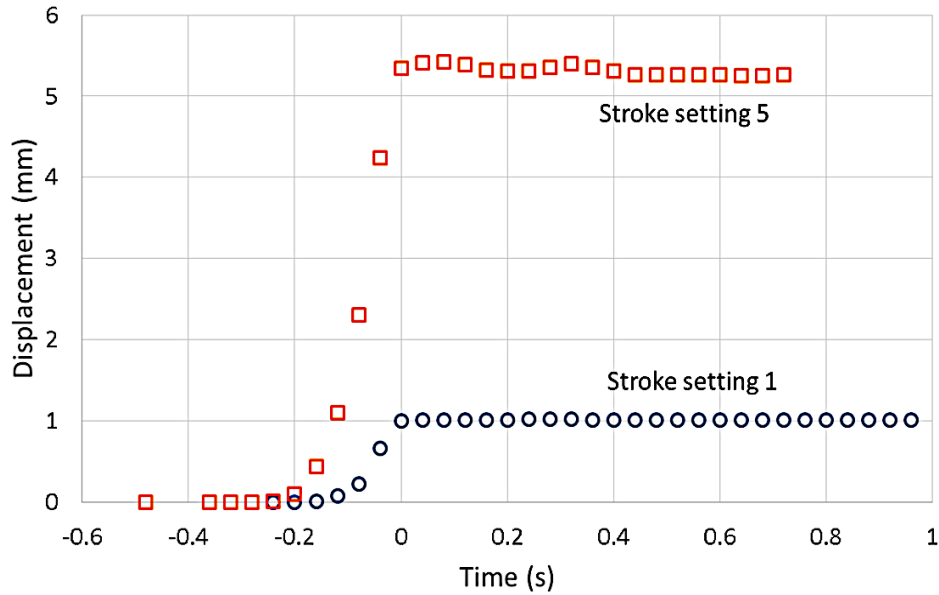


Figure 17: Plot of displacement versus time for two stroke settings of the solenoid used in the experiment. A higher stroke produced higher maximum velocities (from gradient of plot) prior to impact.

The displacement versus time was traced for two stroke setting (stroke lengths) on the solenoid and shown in Figure 17. The maximum velocities were calculated from the gradient of the plots were generally higher with longer strokes but the relationship is non-linear. The total mass of the moving parts was weighed 0.1062 kg. The momentum of impact was calculated from Equation (9) and are listed in Table 2.

$$p = mv \tag{9}$$

Where p is momentum at impact,

m is mass of moving parts,

v is maximum velocity.

Table 2: The list of maximum velocity and impact momentum obtained using the different stroke settings (increasing stroke lengths) on the solenoid.

Stroke Setting	Maximum Velocity (mm/s)	Impact Momentum (Ns x 10 ⁻³)
1	12.00	1.28
2	20.00	2.13
3	33.60	3.57
4	35.70	3.79
5	40.55	4.31

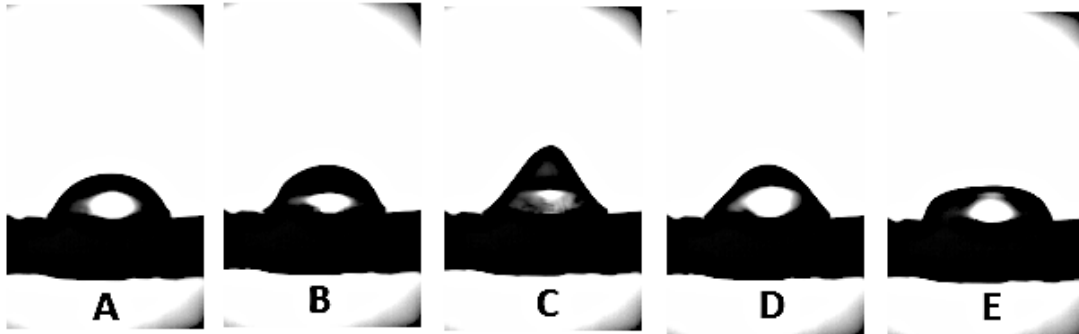


Figure 18: Type I drop behaviour upon impact for 10% water-glycerol (V/V) where no necking occurred nor separation of the liquid body were observed.

Three types of droplet behaviour were observed after impact. In Figure 18, the droplet is categorized as Type 1 where it undergoes some axial extension after impact, but behaves as one single body throughout. The drop began with an original semi-spherical shape (A), then continues to extend and forms a cone-like shape (C) at its highest extension and assumes a pancake-like shape (E) before returning to its original shape.

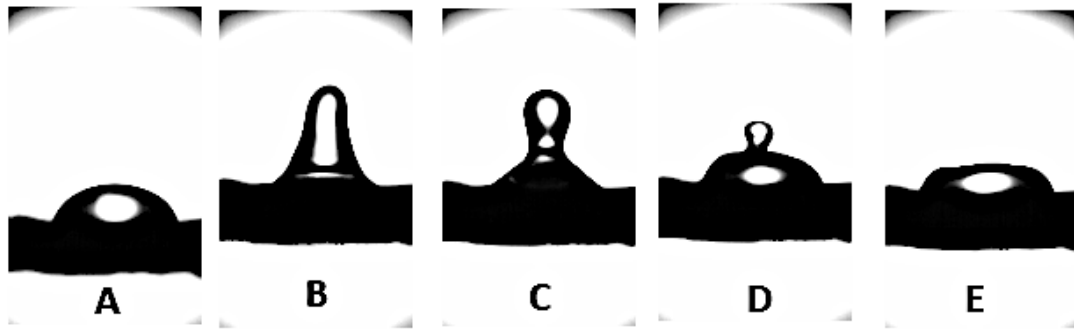


Figure 19: Type II drop behaviour upon impact for 10% water-glycerol (V/V) where necking occurred but no separation of the liquid body was observed.

Figure 19 characterizes the Type II behaviour where the drop experiences greater axial (B). However, due to its inability to further continue with extension, it begins to experience some instability [233], where the upper section forms a globular shape and develops a necking region that acts as a liquid bridge connecting the upper portion to the main body (C). Next, the upper drop portion collapses downward onto the main liquid body with reduced globular and neck region (D). Finally, the globular and neck region completely disappears and the drop assumes the initial pancake-like shape (E) similar to the observation in Type I behaviour before returning to its original shape (A).

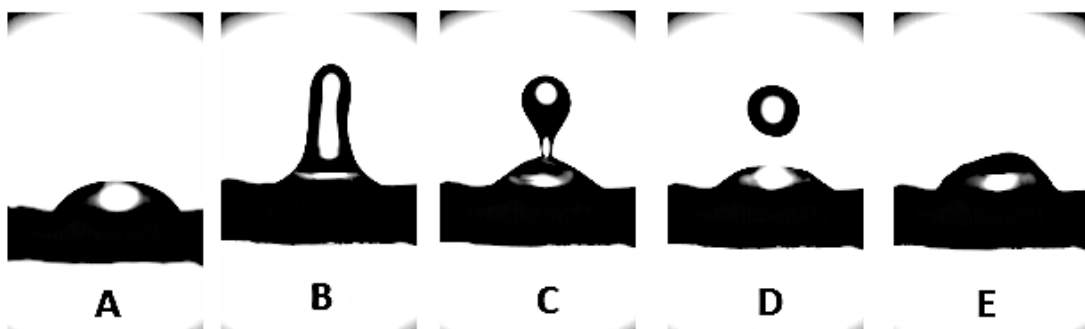


Figure 20: Type III drop behaviour upon impact for 10% water-glycerol (V/V) where separation of the liquid body was observed.

In Type III behaviour (see Figure 20), it was observed that drop separation occurred wherein the wavelength caused by the perturbation exceeds its circumference. Here, the drop experiences an even greater extension and narrowing of the neck region connecting the upper globule portion with the main body (B and C). Subsequently, two separate bodies were formed as a result of complete pinching off at the narrow neck region which detaches the upper globular region. The upper liquid body forms a sphere whereas the bottom liquid body resumes a semi-spherical shape (D). The upper portion then falls back onto and merges with the bottom to reform a single liquid body (E).

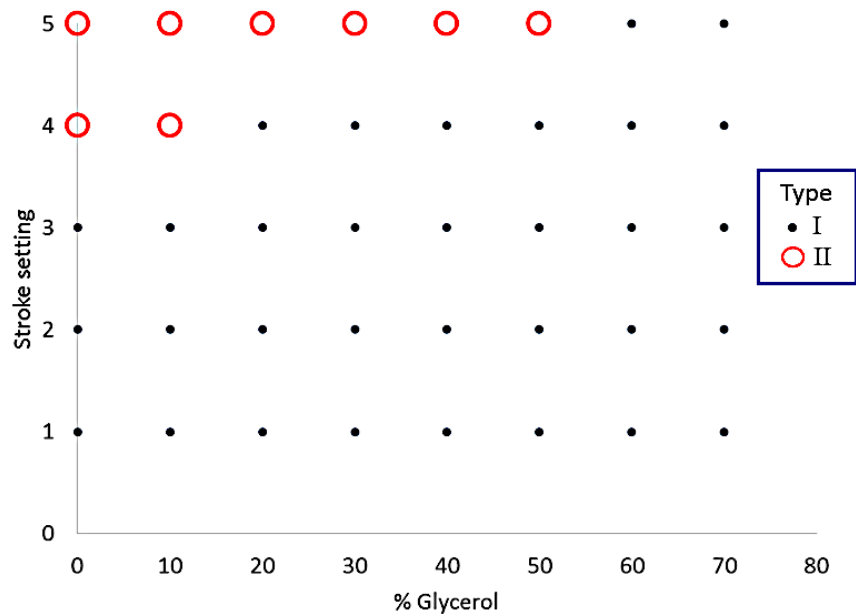


Figure 21: Region plot of the types of drop behaviour observed with varied solenoid stroke settings and percentage of glycerol in the water-glycerol mixture (V/V) tested on a non-scribed substrate. The type of behaviour was chosen from the most prevalent one observed out of 10 recordings at each stroke and glycerol percentage setting.

From Figure 21, only Types I and II behaviours were observed on non-scribed surface, with Type II emerging when higher stroke setting was used. This can be explained by the droplet trying to adjust to a smaller cross-sectional width, thus being able to approach the Rayleigh instability condition more readily. At higher glycerol percentage in the mixture, the viscosity of the mixture becomes higher results in enhanced energy dissipation and any perturbations are rapidly damped from the thread. Hence, there is lower tendency for formation of Type II behaviour at higher water-glycerol mixtures.

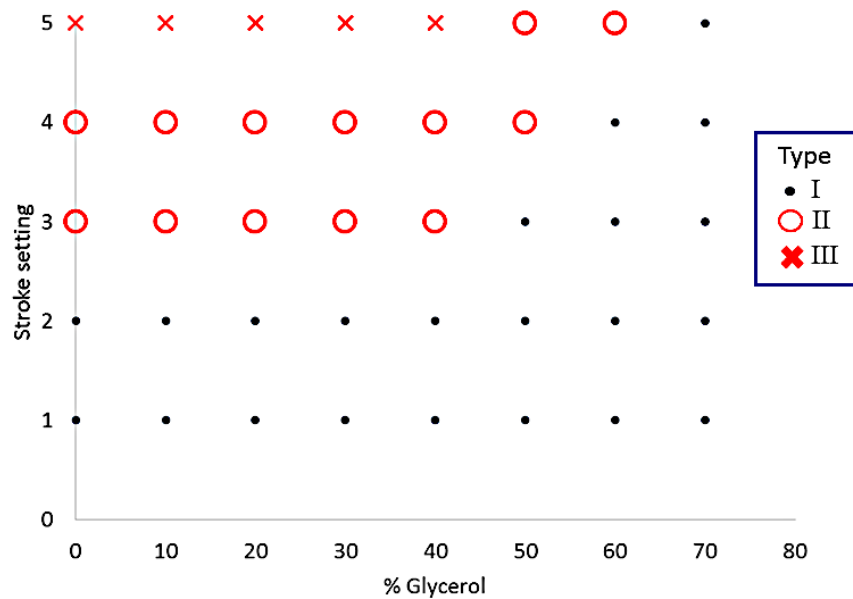


Figure 22: Region plot of the types of drop behaviour observed with varied solenoid stroke settings and percentage of glycerol in the water-glycerol mixture (V/V) tested on a circularly scribed substrate. The type of behaviour was chosen after taking the most prevalent one observed out of 10 recordings at each stroke and glycerol percentage setting.

In contrast, all three types of drop behaviour were observed when tested on the circularly scribed substrate (see Figure 22). Since the composition of the substrate used was the same, and all test conditions were unchanged, it is obvious that the liquid pinning action that arose from the scribed surface structure at the three-phase contact line caused liquid body to become readily unstable. Inspection of the topography of the scribed region reveals the formation of grooves whereby the inability to remove substrate material resulted in structures resembling parapets and scarps (see Figure 23). These structures are not symmetrical which might affect the directional pinning of three-phase contact lines.

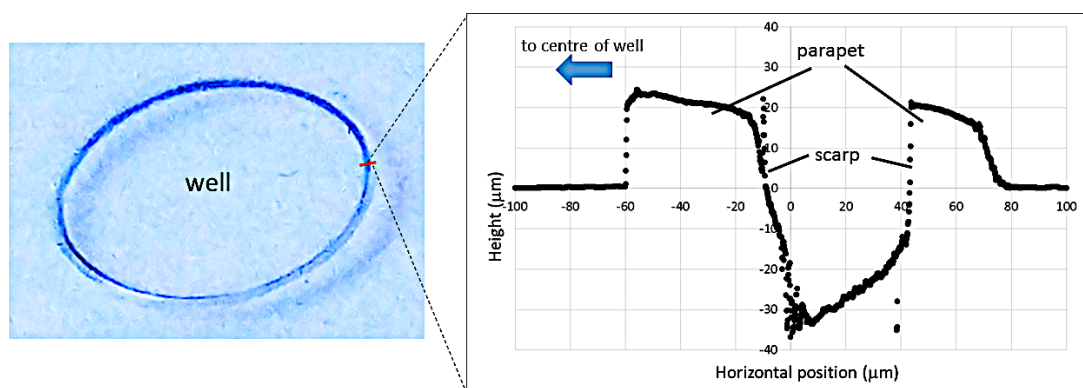


Figure 23: The cross-section topography of the scribed region of the substrate. There is clear presence of a groove due to the cutter used, with structures resembling parapets and scarps on either side. These were not symmetrical.

An attempt to describe the physics explaining this phenomenon is to compare the time evolution traces of key parameters of the drop. Figure 24 gives the situation for the normalized (to the value prior to motion) width of the drop. In both the non-scribed and scribed substrates, there was width increase at the phase just before impact. This is a result from the deceleration forces that caused the drop to flatten out. As soon as impact occurred, the width then starts to shrink as a mechanism to allow the liquid

body to harness the momentum transferred from the gantry and try to propel itself upwards. Following this, a series of oscillations in the width is observed, which is the mechanism used by the liquid body to dissipate the mechanical energy. These are the result of capillary waves formed that typically accompany severe free-surface deformations in drops when they impact on surfaces [222, 234]. It is important to note that when tested on the scribed surface, the width does not reduce beyond the width of the well which suggests a stronger pinning effect at the three-phase contact line as the liquid tries to shrink towards the centre of the well. Although, the extent of this pinning is not as strong to restrain the increase of the width over the diameter of the scribed well. This is due to the asymmetrical geometry of the scribed groove, where the less steep scarp further from the centre of the well (see Figure 23) and provides a lower pinning strength on the three-phase contact lines as the width extends.

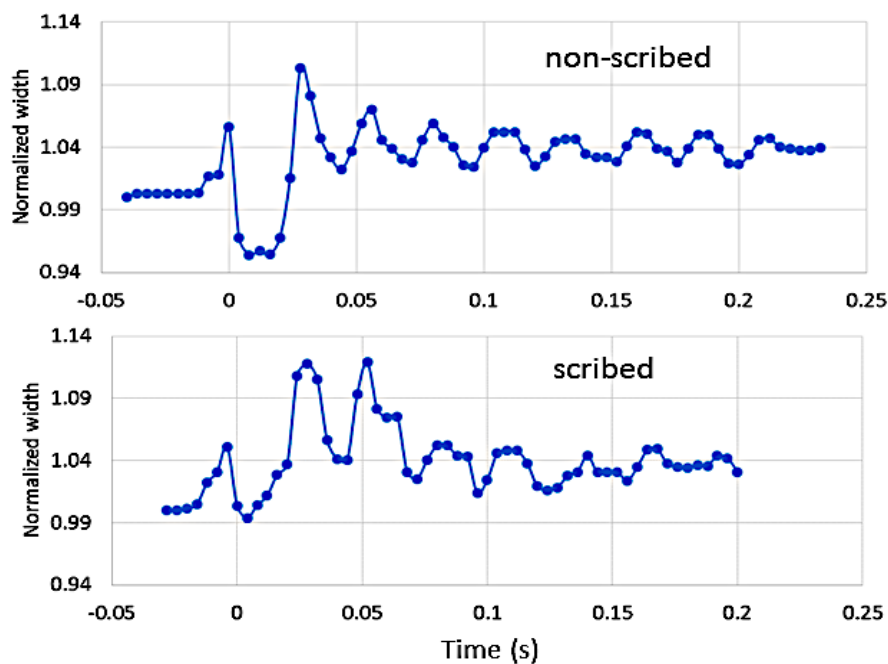


Figure 24: Traces of the width of a water drop with time on both non-scribed and scribed substrates. The widths were normalized to their initial values (non-scribed = 2.3 mm, scribed = 2.5 mm) which were taken from the point of impact ($t = 0$ s) under stroke setting 4. In both cases, oscillations in the width after impact are used by the liquid body to dissipate energy. For the non-scribed case, the diameter of the scribed well is the minimum to which the drop could reduce its width to.

Initially, the height of the drop on the scribed surface (= 2.5 mm) was slightly higher than on the non-scribed surface (= 2.3 mm). This is expected due to the width constraint on scribed surface. During the deceleration phase prior to impact, the drop in both cases experiences a reduction in height (Figure 25) to accommodate its increase in width. Upon impact, a sudden increase in height was observed, followed by its decrease and then cycles of height fluctuations behind tapering off. Similar to the case of width, this mechanism is used by the liquid body to dissipate mechanical energy. The maximum height achieved on both surfaces is approximately the same, though the drop tested on non-scribed surface experienced Type I behaviour but the drop tested on the scribed surface exhibited Type II behaviour. This implies the height achieved is only dependent on the upward momentum transferred from the impact, while the changes in shape is governed by method to use surface tension to redistribute the mass within the body.

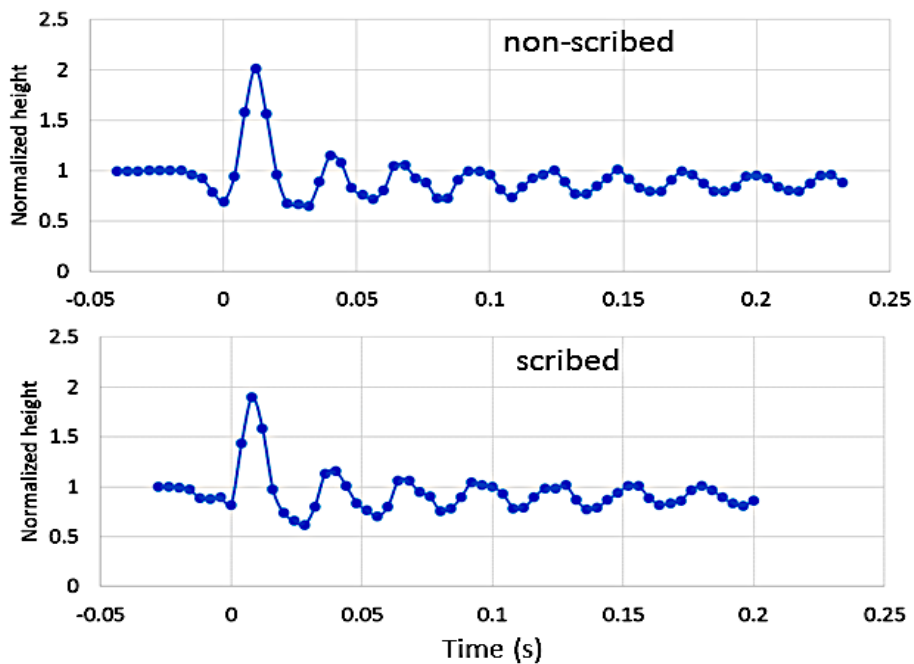


Figure 25: Traces of the height of a water drop with time on both non-scribed and scribed substrates. The heights were normalized to their initial values (non-scribed = 7.2 mm, scribed = 6.86 mm) taken from the point of impact ($t = 0$ s) using stroke setting 4. The trends on both surfaces were similar though the droplet non-scribed surface exhibited Type I behaviour but Type II behaviour were observed for the scribed surface.

It would be also be useful to compare the traces of the contact angle with time (see Figure 26). The initial contact angle for scribed surface ($= 80^\circ$) is generally higher than the non-scribed surface ($= 55^\circ$) due to the restriction in width if the former. The contact angle increases for a short fraction of time (~ 8 ms) at point of impact before the drop begins to adjust its height (Figure 25) and width (Figure 24). This implies that the drop uses contact angle change as the first response for adjusting the mechanical energy changes. As the liquid body extends, the contact angle moves to a receding state, which is responsible for maintaining adhesion to the substrate. Moreover, the contact angle is able to recede to a greater extent (by 20°) on the scribed surface compared to the non-scribed surface (by 15°). This is a result from the strong contact line pinning offered by the parapet and steep scarp surrounding the scribed groove. On the non-scribed surface, contact angle oscillations are quickly suppressed as the drop is able to adjust its width and height more readily. The development of Type III behaviour is due to the liquid body being able to achieve a lower receding contact angle on the scribed surface, the higher adhesion effect on its main body together with the ability of the drop to form greater necking at high stroke setting, thus allowing complete detachment of upper globular portion. This behaviour should be avoided at best.

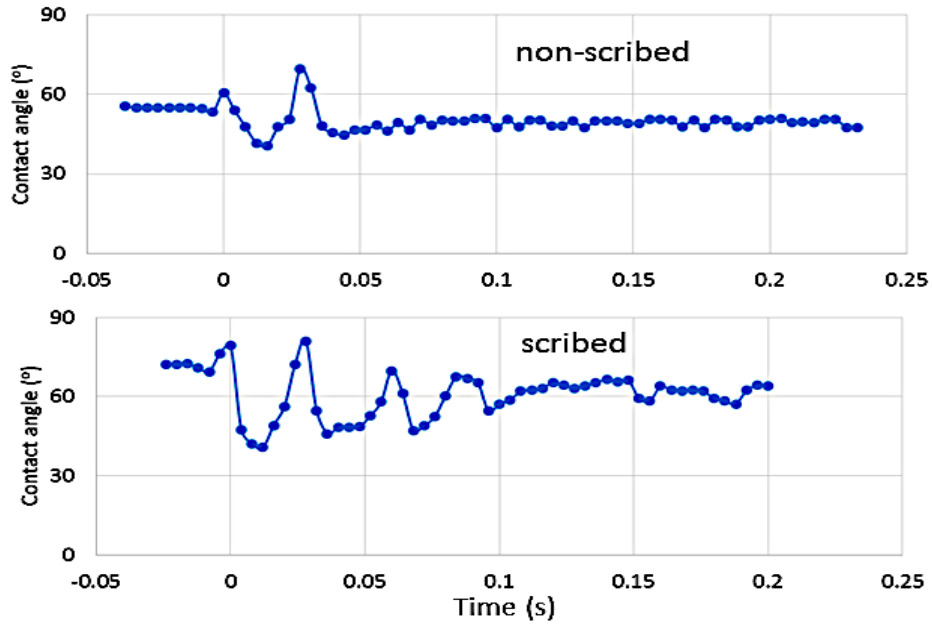


Figure 26: Traces of the contact angle of the drop with time on the non-scribed and scribed substrates taken from the point of impact ($t = 0$ s) using stroke setting 4. The contact angle exhibited greater receding angles (up to 30° reduction from the original angle) compared to the non-scribed substrate (15° from original angle).

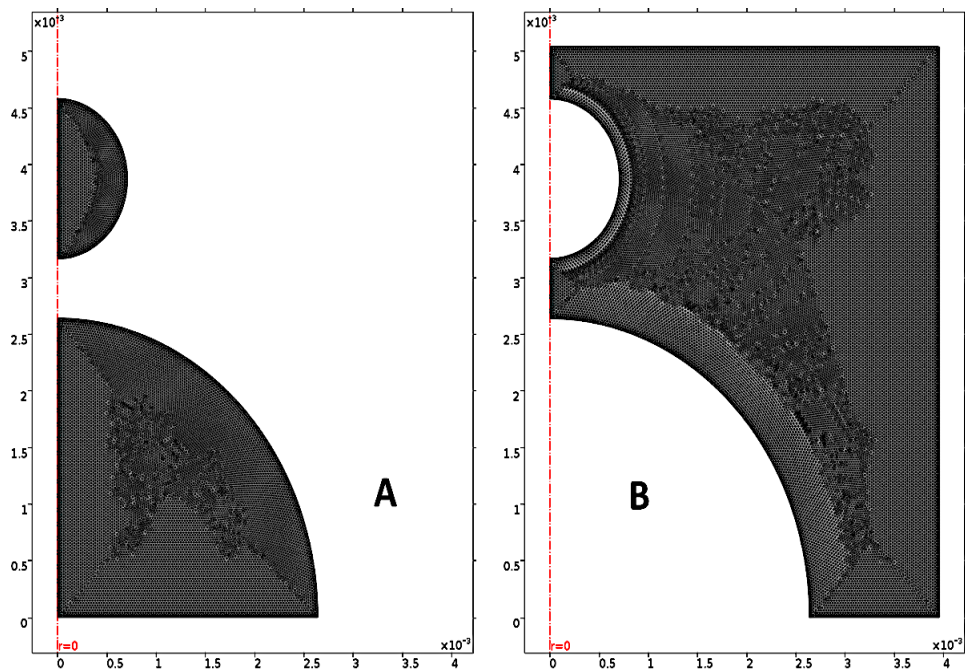


Figure 27: Graded meshes of drop coalescence behaviour under finite element analysis, in which the (A) liquid and (B) gaseous phases are depicted. The dense meshes enable the interaction changes to be well described.

The platform movement characteristics is repeatable which suggests the prospect to use the method for enhanced mixing when the two liquid bodies coalesce. Finite element modelling may provide a better understanding. Using only half the drops for simulation helped reduce the computational time. The graded mesh models of the two liquid bodies for the liquid phase (A) and for the gaseous phase (B) are illustrated in Figure 27. To track the spatial changes, the meshing densities were kept high and roughly constant throughout. Figure 28A to D demonstrates the different stages of flow as a result of coalescence of the upper portion and the main liquid body. As the two bodies merged and expanded, the flow unifies at approximately 67 ms from start into a downwards and outwards position. This produces a capillary wave that rebounds about 78 ms that creates an inward flow. Around 79 ms, circulation emerges whilst the merged drop begins to regain its height at 0.83 ms. This is followed by a downward flow that reappear as drop height reduces. The capillary wave then develops a back and forth motion, forming circulation.

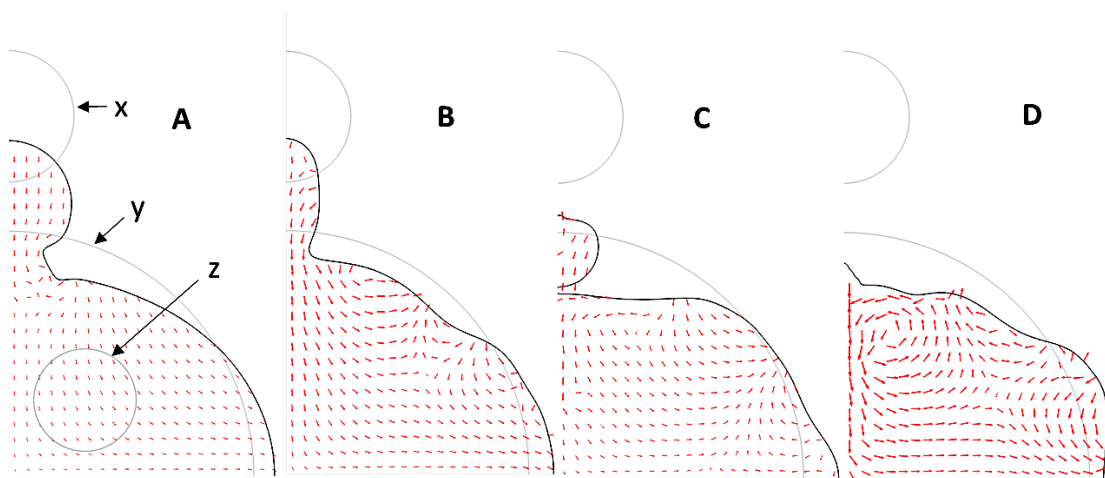


Figure 28: Representation of sequence of simulation results of flow field generated (A) to (D) when two of liquid bodies began to merge. x and y in (A) describe the original shapes and positions of the two liquid bodies. The circulation flow strength was investigated in the selected region z.

Throughout this merging process, circulations develop in the merged liquid body which suggests good mixing [235-237]. To investigate the circulations further, the

magnitude of circulatory flows was traced in the selected region z (shown in Figure 28A) calculated from Equation (10).

$$C = \oint V \cdot dl \quad (10)$$

Where V is the velocity,

and dl the differential length.

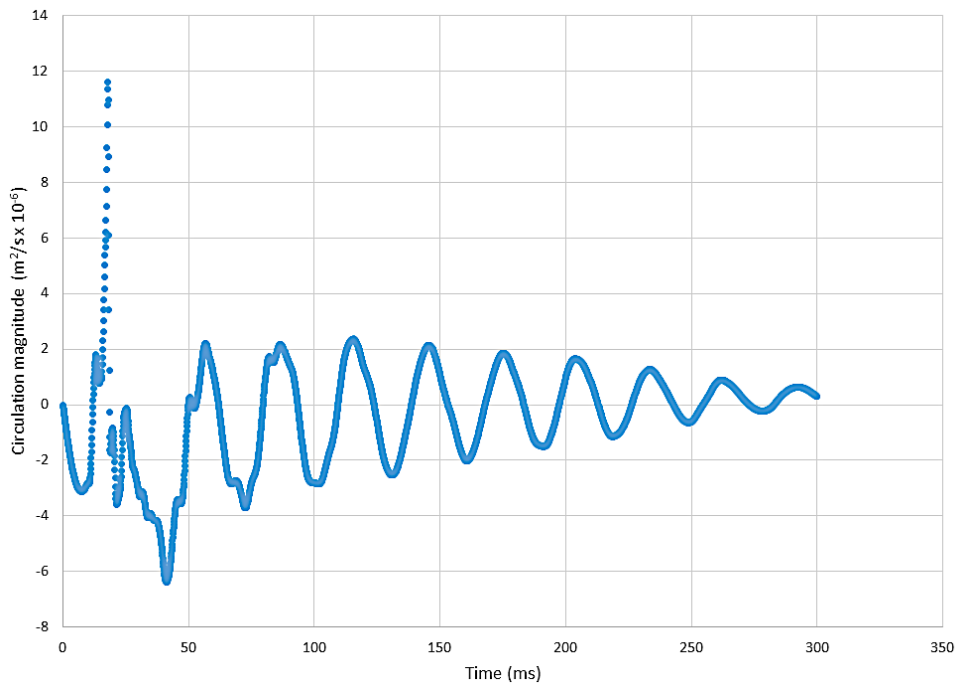


Figure 29: The circulation flow strength developed in the region z in Figure 28(A) traced with time where the positive values are counter-clockwise flow. An initial high positive peak was observed followed by a cycle of positive and negative values implying good liquid mixing.

The plots in Figure 29 shows an initial high positive peak (anti-clockwise circulation) followed by a cyclical trend of positive and negative values, which indicates that the circulation interchanges between the clockwise and anti-clockwise flows. This process is achievable without moving physical contacts in different directions [235] or create any reversals in flow [237] which suggests the prospects of enhanced mixing. Furthermore, the multiple centres of circulation (see Figure 28A – D) of the liquid body can occur throughout the coalescence process. It would be difficult to locate the exact locations of these centres. Nevertheless, the spatial shifting indicates that the mixing is not centred at a particular location but distributes across the whole liquid body. Although it is unclear if there is possibility of achieving a uniform mixing throughout, still the process should considerably achieve an overall mixing.

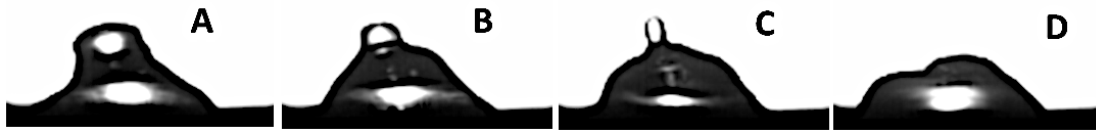


Figure 30: Sequence of high-speed camera images of the coalescence phase (A) to (D) in the Type III behaviour. They show the merging liquid shape to experimentally corresponded with the simulation images results of Figure 28 (A) to (D).

The modelling can be assumed correct as the shape changes observed at specific phases of coalescence corresponds to the trends of the experimental results (Figure 30) despite the slight skew to the left. However, it is possible for this process to produce unpredicted outcomes. For example, in a rare case, it was found that the two separated bodies were able to bounce off each other instead of merging (Figure 31). Since the coalescence occurs following the receding process, it is obvious that the pinning characteristics influences the dynamics of main liquid body (sticking with the substrate). Subsequently, this should then strongly influence the coalescence between the separated globular portion and the main liquid body. Unfortunately, the limitations of the existing experimental setup cannot verify the inability to completely control the symmetry of coalescence of the liquid bodies (Figure 30). An alternative cause for the non-coalescence behaviour may result from formation of an increasingly compressed

entrapped air film between the two liquid bodies preventing coalescence regardless their motions towards each other. Though, this has only occurred with highly viscous vibrated liquids [238]. In addition, a stable development of collision can result in non-coalescence. Some previous studies showed that there are parameter spaces (i.e. interaction velocity, drop deformation, interfacial tension, etc.) where hydrodynamic effects can stabilize collisions that are intrinsically unstable [239]. This indicates that it is possible to integrate a control schemes that can eliminate occurrence of non-coalescence.

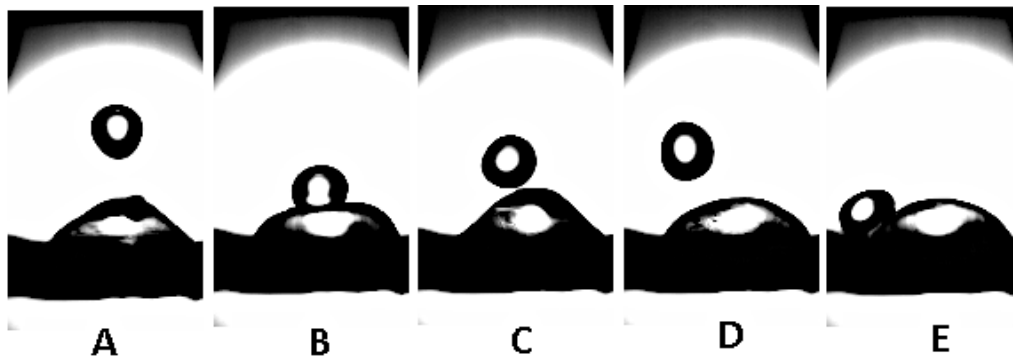


Figure 31: Sequence of images showing the separated globular portion not merging together with the main liquid body on rare occasions.

3.3.4 Conclusion

A method to cause sessile drops, based on water-glycerol mixtures at 40 μL volume, deposited on solid substrates, to accelerate upwards and then stopped suddenly to create a longitudinal impact effect was devised. At impact momentums of up to $4.31 \times 10^{-3} \text{ Ns}$, three categories of drop behaviour were discovered where Type 1 and II were observed when tested on non-scribed substrate where all behaviours were observed when tested on scribed substrate. Unlike the non-scribed surface, the drop was found to be able to separate (Type III) on scribed surfaced regarding it as unstable. This is explained by the ability of the contact angle on the scribed substrate to be able to recede more compared with the non-scribed substrate. With stronger adhesion of the main liquid body to the substrate, greater necking could occur allowing for complete pinching off of the upper globular portion. Droplet on the non-scribed surface has

greater ability to adjust its width, height and contact angle parameters to redistribute the mechanical energy absorbed from impact. Instead of finding Type III behaviour as unstable and disadvantageous, numerical simulations of the separated drops coalescing together showed circulations that change direction with time. This suggest feasibility of improved mixing during transportation if the experimentation could be integrated with control schemes.

Results of this work were reported in the paper (AHMAD ZAHIDI, A. A., LAU, C. Y., KATARIYA, M., LIEW, O. W. & NG, T. W. 2017. Characteristics of drops on flat microplating surfaces from controlled upward longitudinal impact. *Colloids and Surfaces A: Physicochemical and Engineering Aspects*, 522, 74-82) attached in Appendix B.

3.4 Drop Characteristics Under Car Crash-Like Impact

3.4.1 Introduction

It is important to investigate the ability of liquid to stay on or to be displaced from surfaces, especially during transport. In nature, many animals use bursts of shaking to expel water from surfaces. This helps to prevent the onset of hypothermia in the cold for mammals as water has thermal conductivity of about 25 times higher than that of air [240, 241], and to inhibit the pathogen growth on the skin [242, 243]. The availability of drops on surfaces to dissipate heat through evaporation influences the capability of extractors, heat exchangers, and condensers to reduce energy requirements [244, 245]. It is found that displaced drops, can allow for propagation and colonization of bacteria in new environments covering extensive areas [246].

Studies shown that airflow can be used to shed single sessile drops on surfaces [247, 248]. Droplets and formation of icicles on vehicle window surfaces when at low temperature can hinder vision. The availability of self-cleaning superhydrophobic surfaces helps eliminate these problems with emerging new applications for sessile drops [13, 249] but most surfaces are non-superhydrophobic. Thus, sidelong impact

proposes another method to shed sessile drops. This has been found relevant in investigations of the ability of pinned drops in maintaining positional stability despite inadvertent collisions [222]. A more controlled and better means to characterize the ability of sessile drops to remain stably on surfaces can be devised from this impact method. This experiment will also facilitate investigations for the use of polymer solutions that possess interesting self-healing [250-252] and electro-optical properties [253]. It can also provide insight for applications of water-glycerol systems to handle biological samples [254, 255] and to vary the density and viscosity of liquids for tests [256-258].

3.4.2 Materials and Methodology

Materials

Solutions of Glycerol (Sigma, G9012-1L) and PVA (Sigma, 9002-89-5) were obtained from commercial sources to prepared for testing. Varying mixture concentrations were prepared with appropriate volumes of glycerol and PVA with deionized (DI) water in plastic centrifuge tubes. These tubes were placed in a vortex mixer (VELP Scientifica, Wizard IR) for 2 minutes to achieve uniform mixing. The mixture was allowed to settle for at least 1 hour before use. A slider mechanism (

Figure 32) of travel length 860 mm was 3D printed using standard metal components.

Methods

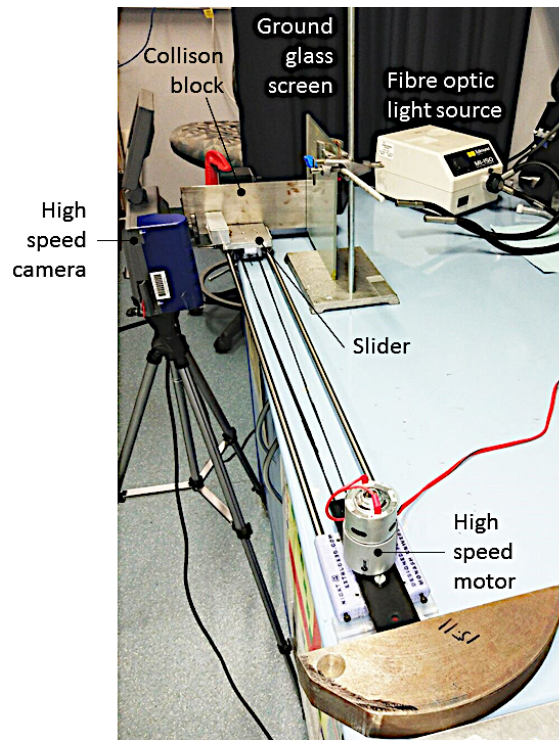


Figure 32: Experimental setup devised to replicate “car crash” investigations of sessile drops. The drops were deposited on substrates attached to the slider before it was moved at constant speed until it collided with the block. A high-speed camera was used to record the video sequence.

A high-speed direct current (DC) motor supplied electricity to a motorized belt drive enables the movement of the slider. Clamps were used to secure the setup to the table. A ground glass microscopic slide of thickness 1.02 mm was affixed to the slider using strong adhesive. It was positioned to ensure that the thickness and trailing edge were both visible for scaling and positional referencing purposes respectively when extracting the information from the video sequence of high-speed camera. The slider was made to translate at a constant speed until it collided with a heavy block where it reached a complete stop. A high-speed camera (Fastec) operating at 1000 frames per second was used to record the video sequence of the sidelong impact. A fibre optic light source that was diffused via a ground glass screen at the opposite end of the camera to provide higher quality imaging. To maintain a consistent transport speed of the slider prior to impact, the motor was driven using the same amount of voltage and current for

all tests. An initial test was conducted with ten repetitions without liquid drops to confirm this. When tested with liquid drops, 15 μL of varying compositions of water-glycerol (0 - 100% v/v) and water-PVA (0 - 10% v/v) were dispensed onto the microscope slide using a manual pipette (Eppendorf). The slide was sanitized with alcohol and dried by heating before each test to ensure there was no remaining residues from the previous test.

3.4.3 Results & Discussion

A previous study was conducted where sidelong impact was attained using a swinging pendulum setup [222]. However, for the object to receive a purely sidelong force component, the striker must hit the object at the lowest point of the pendulum but the consistency of this is difficult to maintain in practice. Therefore, a more reliable method would be to design a setup that mimics a “car crash” test. This can be done via moving an object linearly to reach a pre-determined speed before it is brought to an abrupt stop due to collision with a stationary obstacle. A table-top version of this setup was developed and the impact behaviour of water-glycerol and water-polyvinyl alcohol (PVA) sessile drops deposited on a glass substrate were investigated. The viscosity and density of both the liquids can be varied by altering their compositions.

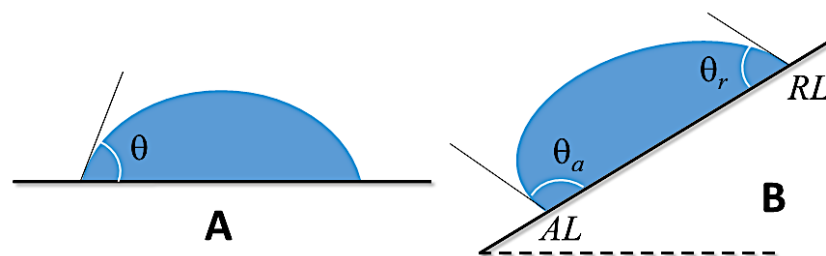


Figure 33: Illustration of (A) a sessile drop on a horizontal substrate with an axis-symmetric shape of contact angle θ . When the substrate was (B) inclined, the droplet shapes into advancing line AL and receding line RL with advancing contact angle θ_a and receding contact angle θ_r respectively.

A drop on a horizontal surface (Figure 33A) that is in equilibrium is governed by laws of Laplace and Young where the three-phase contact line is governed by Equation (5). The theoretical thermodynamic contact angle is based on very clean environmental conditions but mechanical pinning [259] or adhesion hysteresis [260] could occur in real conditions. Hence, the droplet can exhibit a range of contact angles that can exist suggesting more than one value for γ_{SL} [261]. To support this, a droplet placed on an incline (Figure 33B) exhibits both advancing and receding contact lines and angles. For known values of advancing and receding contact angles, the values of interfacial energy of the solid-liquid phase corresponds to these different angles [262]. This explains the energy dissipation occurring as a results of liquid travel in a capillary tube [263]. It is found that besides exhibiting varied contact angles, the movement of contact line of bubbles is dependent on the inflation or deflation based on contentions of adhesion hysteresis [264].

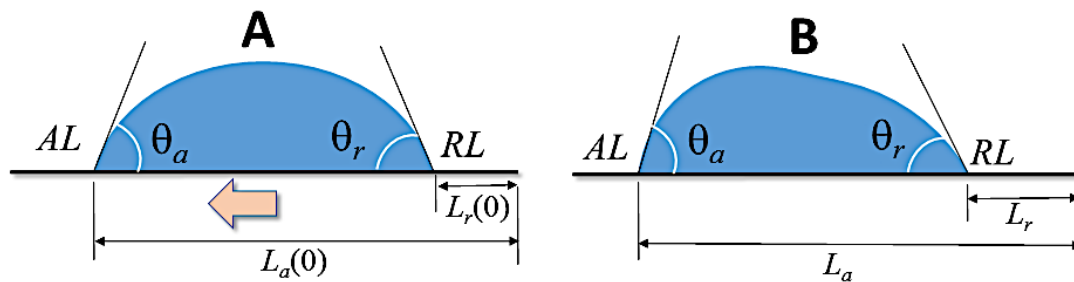


Figure 34: Invariant displacements of the advancing (AL) and receding (RL) contact lines from a reference point on the rigid substrate, $L_a(0)$ and $L_r(0)$ respectively, up to point of impact as (A) a substrate with sessile drop was moved (in the direction of the arrow). After impact (B), the behaviour of the droplet response was described by the changes in L_a , L_r , θ_a , and θ_r with time.

A drop on a moving substrate (Figure 34A) will experience similar drag effect to the air flowing towards a drop on a stationary substrate. It can be assumed that this effect is small, if the rate of displacement of the substrate is moderate and if there is adequate adhesion to the substrate. When the substrate is brought to an abrupt stop after impact, the drop experiences a change in momentum and develops energy dissipation mechanisms to adjust to this. To accommodate to this, the drop has the ability to

undergo changes in contact angles as well as the movement of its contact line [265, 266]. The energetics associated with the contact line movement can be estimated provided that the extent of adhesion on the surface is not significant. An example of such surface would be superhydrophobic surfaces. Although, the deformed liquid body would require a three-dimensional shape of the liquid body to complete the energetic calculations. Since the liquid body undergoes significant free-form deformation, it will be difficult to collect the measured data.

The analysis in this experiment is based on a simpler approach that considers the contact angles and displacements corresponding to advancing (*AL*) and receding (*RL*) contact line (Figure 34A and B). It has been shown that surface energy can be characterized using contact angles when the propensity of drops to move is altered albeit while they are still stationary [267]. Prior to impact (Figure 34A), the displacements of contact line with corresponding contact angles, θ_a and θ_r were reasonably constant. There were changes in the parameters after impact (Figure 34B). Although it is convenient to track the changes in θ_a and θ_r , the displacements of *AL* and *RL* should be determined from a reference point on the rigid reference. These were obtained with the progress of time t after impact described in Equations (11) and (12).

$$\delta_a(t) = L_a(t) - L_a(0) \quad (11)$$

$$\delta_r(t) = L_r(t) - L_r(0) \quad (12)$$

The displacements and contact angles of *AL* and *RL* were two fundamental parameters used by the liquid body to dissipate energy. It is useful to illustrate the parameters in a phase space plot. Phase-space diagrams have been used to describe dynamical systems in numerous mathematical and physics problems where every point

contains the distinctive state of the properties that define how the behaviour of the system. For example, it has been used to characterize signals from real systems subjected to chaos [268] or driven by Brownian perturbations [269].

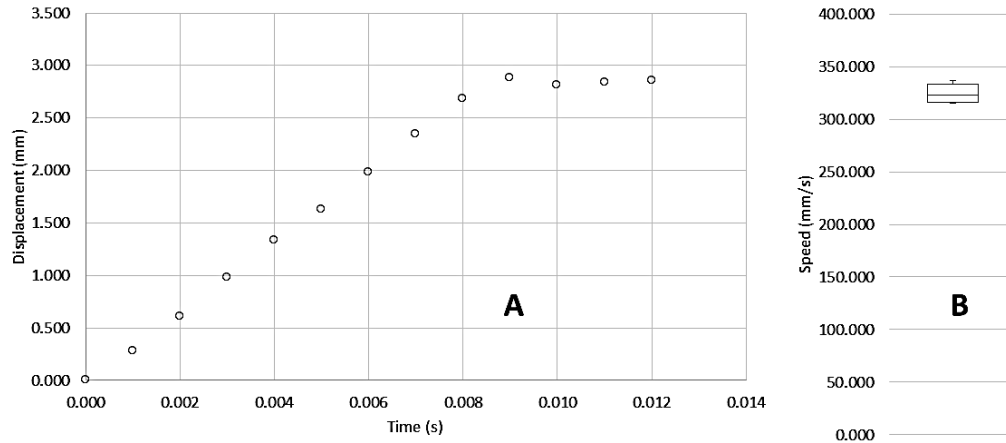


Figure 35: The (A) displacement versus time trace of the slider before impact. The small spread of speeds (B) extracted from 10 repeated experiments show consistent values were achieved.

The displacement of the slider was traced with time as shown in Figure 35A. Prior to impact, a constant gradient is shown from the graph which indicates a constant velocity. Upon impact, the slider is shown to be brought to an abrupt halt (gradient = 0). A small spread in the box plot (Figure 35 B) taken from 10 readings indicate consistent velocity. The average speed calculated prior to impact was 0.323 m/s.

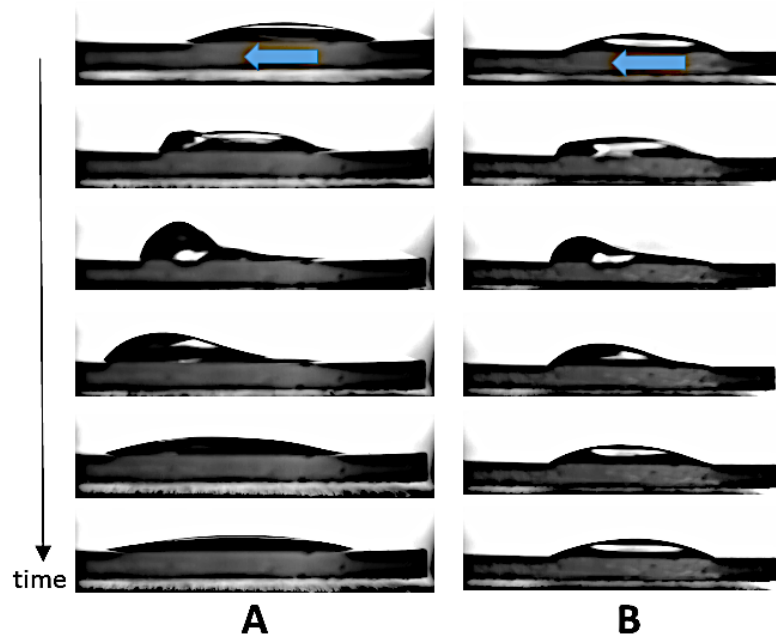


Figure 36: High-speed image sequence (from top to bottom) recorded for (A) water, and (B) 70% water-glycerol (V/V) droplets under sidelong impact (direction according to blue arrow). The second image onwards depicts impact with the block. There was a clear difference in parameters (displacement and contact angle) at the advancing (left) and receding (right) contact points for the two sets of images.

The sequence of images of the drops, leading to and after the impact for water (Figure 36A) and 70% water-glycerol mixture (Figure 36B), revealed clear differences. Firstly, there were no changes to the position and shape for both of the drops prior to impact. This indicated that the air flow in the experiments (arising from slider movement) was slow enough that it did not cause any significant deformation on the drops. Upon impact (from the second image onwards), the contact angles at the left three-phase contact lines moved into advancing state and the right moved into receding state. Monitoring the values of contact angles would be sufficient provided that there is no displacement for left and right three-phase contact line. However, the images revealed that there was displacement after impact. This suggest that the droplet uses displacement as a method to dissipate the energy absorbed from impact. Comparing the displacement and the contact angle changes of the drop together should provide better insights into the processes used for energy dissipation. This is feasible as the nature of collision of the slider with the block was restricted to only one axis (in the direction of the slider).

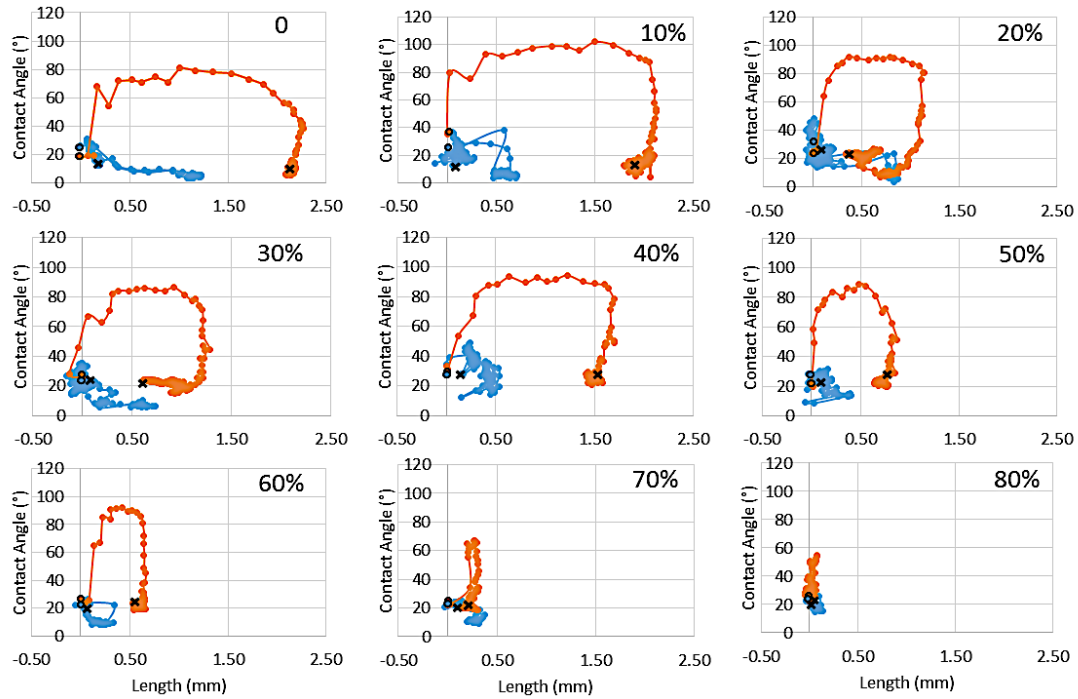


Figure 37: Phase-space plots of the left (orange) and right (blue) contact angles and positions upon impact for different concentrations of water-glycerol mixture. The start positions were marked and circles and crosses were marked for end positions.

The phase-space plots for contact angles versus displacement of the left (*AL*) and right (*RL*) three-phase contact lines of different concentrations of water-glycerol mixtures upon impact are given in Figure 37. It was observed that the trace of *AL* (indicated in orange) for water showed a large increase in its contact angle as well as its displacement. The contact angle eventually restored close to its initial equilibrium condition but this did not occur with its displacement. In contrast, the traces of *RL* (indicated in blue) showed minimal reductions in the contact angle but significant increase in displacement, although not as much compared to *AL*. It is noteworthy that the *RL* line could be restored relatively close to its original position. The displacement of *RL* was extremely reduced with increasing glycerol composition and was eventually unchanged at 50% composition. The displacement of *AL* behaved in the same manner with increasing glycerol composition but displacement was only unchanged after 60% composition while contact angle continued to vary even after 80% composition. This

implies that it is more convenient for the drop to alter its contact angles to adapt to energy changes compared to contact line movement. Although change in contact angle is quite uniform, some extent of position restoration of *AL* is exhibited at 20% and 30% compositions was noticed. The random nature of local pinning strengths can ascribe to this. *RL* is less susceptible to changes in contact angle and displacement compared to *AL*. This follows the behaviour of droplets gradually tilted on inclined surfaces that are influenced by gravity, where the advancing contact line has been shown to breach more readily than the receding contact line [256, 270]. It was observed that the value of contact angle in *AL* was limited to below 100°. This can be attributed to the overall constant heterogeneity of the surface which influences value [271].

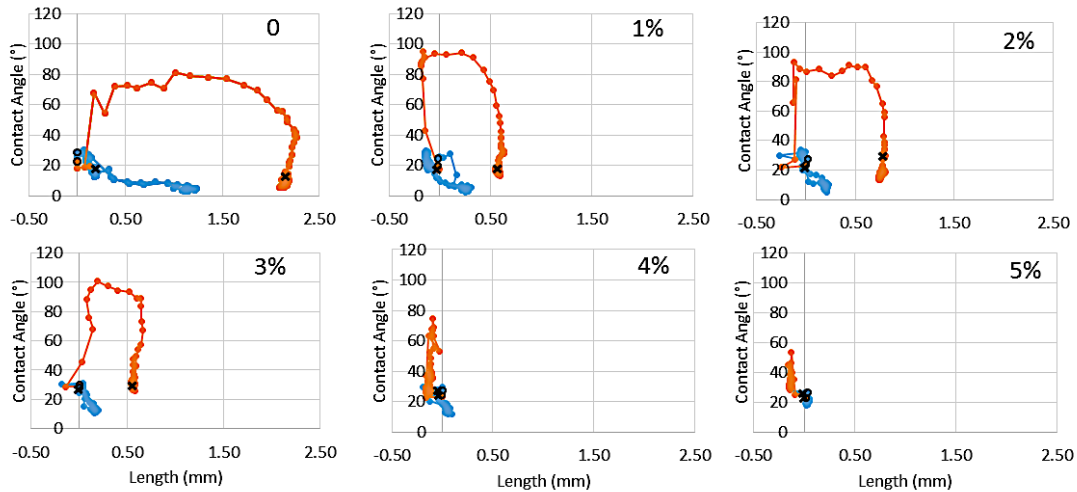


Figure 38: Phase-space plots of the left (orange) and right (blue) contact angles and positions upon impact for different concentrations of water-polyvinyl alcohol mixture. The start positions were marked and circles and crosses were marked for end positions.

The behaviour with water-PVA mixtures (Figure 38) follows the trend of water-glycerol mixtures. It was observed that higher concentrations of PVA reduced the changes in contact angles and displacement of *RL* and *AL*. Due to the similarity in the behaviours of both mixtures in the phase-space plots, it will be useful to investigate if they are scaled by non-dimensional parameters such as the Bond (Bo), Weber (We) or Ohnesorge numbers (Oh) given by Equations (13),(14),(15) respectively.

$$Bo = \frac{(\rho_L - \rho_V)gw^2}{\gamma} \quad (13)$$

$$We = \frac{\rho_L w v^2}{\gamma} \quad (14)$$

$$Oh = \frac{\mu}{\sqrt{\gamma w \rho_L}} \quad (15)$$

Where ρ is the density (of the liquid or gaseous phase),

γ is the viscosity,

g is the gravitational acceleration,

v is the velocity of the slider just before impact,

and w the characteristic length (the contact length of the liquid drop with the solid substrate just before impact).

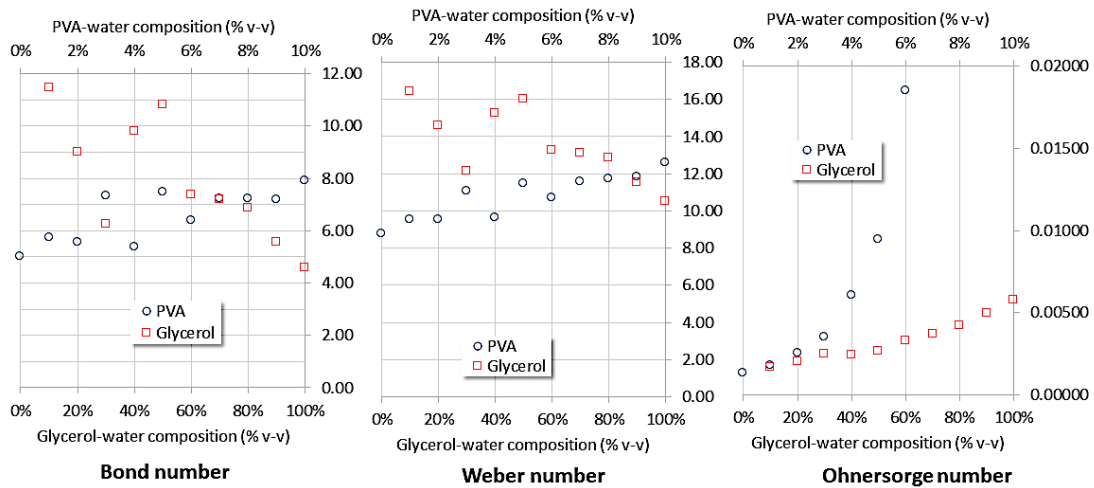


Figure 39: Plots of Bond, Weber, and Ohnesorge numbers for both of water-glycerol and water-PVA mixtures of varied concentration. Only Ohnesorge numbers correlated to the results.

From the plots of these parameters corresponding to the compositions of mixtures (Figure 39), it was observed that only the Ohnesorge number trends correlate with the experimental results. This particular dimensionless parameter relates viscous forces to inertial and surface tension forces which suggests that viscosity of the fluid governs the ability of the drop to resist perturbation from impact (i.e. the higher the viscosity the lower the changes in contact angle and displacement in *AL* and *RL*). Minimal changes were observed when $Oh \sim 0.005$, which corresponded to 90% and 5% glycerol and PVA concentration. This value is significantly smaller than the values used for creating jets in inkjet printing (permissible only when $0.1 < Oh < 1$) [272]. Viscosity can be estimated using inkjet printing [273] but is only possible when jetting has occurred. The use of this experimental approach proposes the same function without meeting the jetting requirements. It is plausible to devise more economical setups (e.g. lasers and photodiodes) that eliminate high speed imaging for characterization as the drops are more static. It is noteworthy altering the impact speed will alter the range of viscosity in which the phase-space trajectories can occur. It is important to note that if two or more sessile drops were placed on the substrate, the forces applied on each upon impact will be exactly the same. In contrast, the drops upstream will experience different forces than those downstream when applying airflows over sessile drops. This

experiment offers potential investigations into the behaviour of sessile drops for cooling or subject to freezing, which are important in industrial applications.

3.4.4 Conclusion

This experimental approach here has been shown to maintain constant speeds prior to impact. The displacement right and left contact point lines of a sessile drop occurred along only one axis. This allowed for phase-space trajectories to be plotted to describe the behaviour for both water-glycerol (0 – 100% vv) and water-PVA mixtures (0 – 10%). The droplet undergoes changes in contact angles more readily compared to displacement to dissipate energy absorbed from impact. The droplet behaviour from the experiment only correlates to the Ohnesorge number was found proposing a feasibility of this method to be used for determining fluid viscosity. It suggested that resistance to perturbation from impact is governed by viscosity of liquid.

Results of this work were reported in the paper (**AHMAD ZAHIDI, A. A., SALLEH, K. M., SAMARASINGHE, S. K., CHUNG, D. C. K., DANTARAYANARA, U., UDDIN, M. H., LIEW, O. W. & NG, T. W.** 2019. Behaviour of sessile drops revealed in ‘car crash’ like impact. *Colloids and Surfaces A: Physicochemical and Engineering Aspects*, 579, 123661) attached in Appendix C.

3.5 Drop Dislodgement from Gravitational Impact

3.5.1 Introduction

There has been a wide interests in the study of shapes of pendant drops [274, 275]. Similar to sessile drops, surface tension of different liquid systems can be determined using pendant shapes [276]. Despite having similar equations describing the two drop shapes, opposing body of forces are exerted on them causing different effects. Sessile drops tend to spread and flatten while pendant drops tend to elongate downwards where the pendant drop formation undergoes several developmental stages.

Stationary Phase

For a pendant drop that with sufficiently small volume, it is able to maintain attached to the dispensing tip of inner radius r . The angle ϕ , is the intersections of the tip profile and the plane of the tip edge that can assume a range of values. In the initial stage, bifurcation of the liquid body occurs as it elongates with slowly increasing drop size. A liquid bridge is developed from a necking region connecting the dispensing tip to the lower spherical region of the pendant drop. The rate of volume increase in the spherical region cannot exceed the volume increase at the neck region to maintain drop stability. A simple force balance can be made when $\sin \phi = 1$ at the threshold volume V_{max} where three dominant components involved which can be described in Equation (16). These components consist of the surface tension force (acting upwards) that attempts to minimize energy as the drop assumes a spherical form, followed by the gravitational force (acting downwards) on the drop that tends to distort the spherical shape, and the force due to the pressures at the plane of the tip opening (acting downwards). Equation (17) describes the pressures at the tip.

$$2\pi r\gamma_{LG} - V_{max}(\rho_L - \rho_G)g - \pi r^2(P_L - P_G) = 0 \quad (16)$$

Where γ_{LG} is surface tension of liquid-gas interface,

r is inner radius of the tip,

g is gravitational acceleration,

ρ_L and ρ_G are densities of the liquid and gas phase respectively,

and P_L and P_G pressures of the liquid and gas phase at the tip.

$$P_L - P_G = \frac{2\gamma_{LG}}{R} - h(\rho_L - \rho_G)g \quad (17)$$

Where R is radius of curvature of the drop surface,

and h is height of the drop.

The third term on the left-hand side of Equation (16) tends to be small since the other two terms on the right-hand side of Equation (17) act in opposition to each other. Thus, from this assumption, we can approximate V_{max} via Equation (18).

$$V_{max} \approx \frac{2\pi r \gamma_{LV}}{(\rho_L - \rho_V)g} \quad (18)$$

This relationship suggests that the maximum drop volume that can be maintained on the tip reduces with finer tips (smaller values of r) i.e. drops will detach at smaller volumes. As the motion of tip begins, three conditions are illustrated in Figure 40 (from left to right) and explained in the next respective sections.

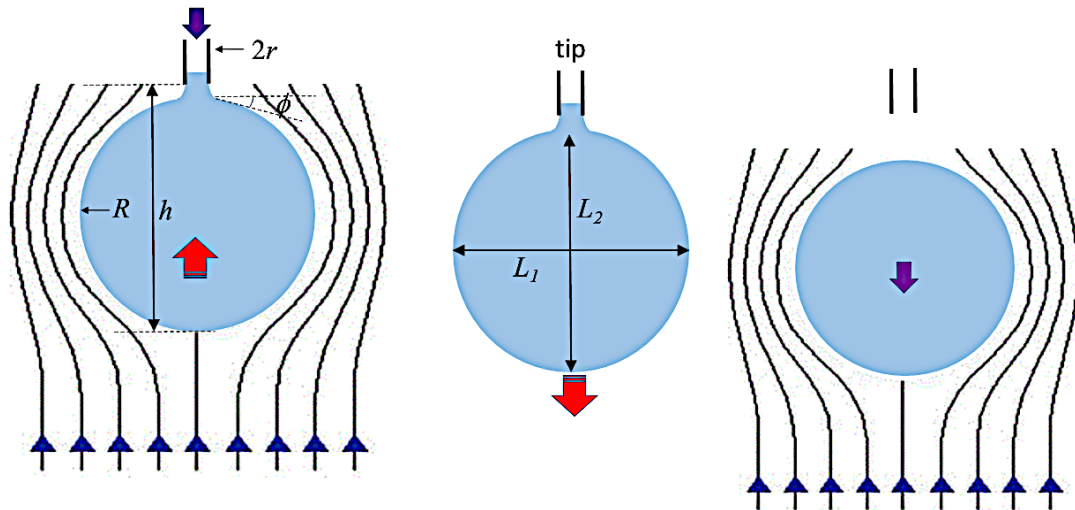


Figure 40: A resting pendant drop allows the angle ϕ to undertake a range of possible values as drop volume increases until the maximum condition is reached where $\sin \phi = 1$ and any further addition of liquid will result in drop detachment. As the tip begins its motion, three conditions occur from left to right. When tip is accelerating downwards (left), the opposing airflow creates an upward lifting force on the drop. When the downward moving tip is stopped abruptly due to impact (centre), the impact force resulting from the sudden deceleration creates a downward-acting momentum force that causes deformation towards an almost oblate spheroidal shape (with diameters L_1 and L_2) before detachment of the drop from the tip. After detachment, the drop continues to experience an upward-acting drag force exerted by the laminar airflow around it as it falls downward (right) until it finally reaches the solid substrate.

Downward Movement Applied to the Dispensing Tip

The orifice of the tip was dispensed and steadily pinned with a pendant drop below its critical detachment volume. The tip was applied with a downward force allowing it to move along with the pendant drop in the direction of gravity. During this process, an upward acting force exerted by the drag force on the drop moving through air acts to keep the drop attached to the tip. Hence, the drop can be stably suspended on the tip if the axis of the tip and drop remains aligned.

Abrupt Deceleration of Tip

When the moving tip was decelerated to a complete stop abruptly (from impact), an upward-acting impact force will be exerted on the tip with equal and opposite impact force exerted on the drop. This provides the drop with sufficient energy to detach from the tip as it is able to overcome the retention force due to pinning effects. This energy transference is reflected in the manner of its deformation from an estimated spherical to oblate spheroid shape [225, 277]. The surface energy developed can be approximated using Equation (19) from [277]. When the shape is spherical (i.e. $L_1 = L_2$), E_s is minimized. If other parameters remain constant, E_s scaled according the size of the drop to second power.

$$E_s = \frac{\gamma_{LG}\pi K L_1^2}{2} \left(K + \frac{\sin^{-1}\varepsilon}{\varepsilon} \right) \quad (19)$$

Given that $K = \frac{L_1}{L_2}$ and $\varepsilon = (1 - K^2)^{\frac{1}{2}}$

Drop Falling

Drops falling through air have been studied in the last century [278]. The surface tension acts to minimize the surface area of a given drop volume and the gravitational force which exerts an elongating effect on the drop is responsible for the overall spherical shape adopted by a hanging drop. However, droplet deformations occur when the drops fall at high velocities as the inertial friction can exceed surface tension forces [279]. The equation describing the motion of a spherical drop can be expressed as Equation (20) from [280]. The drag coefficient is related to the Reynold's number given by Equation (21).

$$\frac{dv}{dt} - \frac{(\rho_L - \rho_G)g}{\rho_L} + \frac{3\rho_G v^2 C_d}{8R\rho_L} = 0 \quad (20)$$

Where v is the instantaneous velocity,

C_d is the drag coefficient,

ρ_L and ρ_V are the densities of the liquid and surrounding gas respectively,

and R is the drop radius.

$$Re = \frac{2R\rho_G v}{\eta_V} \quad (21)$$

Where η_V is the dynamic viscosity.

C_d assumes values to that of a falling solid sphere [279]. To achieve terminal velocity, the spherical drop must travel a sufficient distance and the force of air resistance balances the force of gravity where dv/dt in Equation (20) goes to zero. The drop will pose a non-zero value for dv/dt when it impacts the substrate surface if the terminal velocity cannot be achieved. The drop impact dynamics are influenced by values of v and dv/dt of the drop just before impact with the substrate surface.

3.5.2 Materials and Methodology

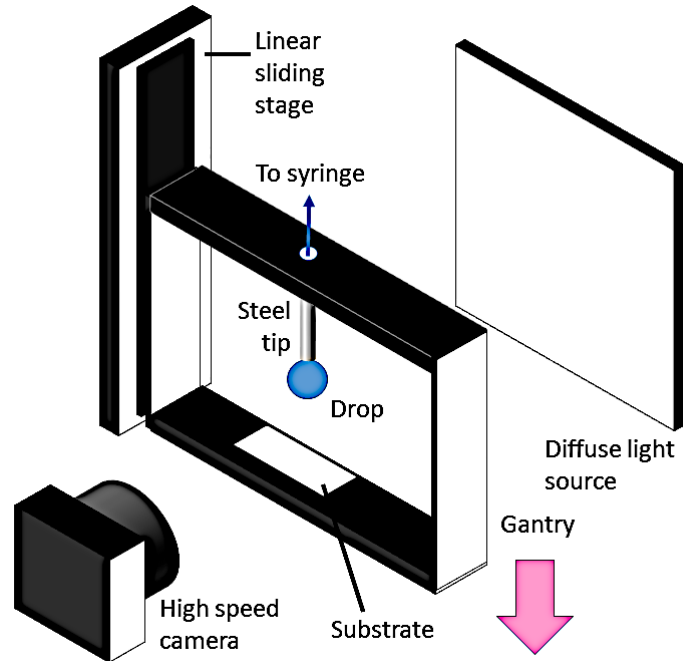


Figure 41: Gantry design setup attached with a steel tip that is able to stably suspend pendant drop. The gantry was raised to a height of 9.5mm and released. The video sequences of the drop motion during gantry movement and stopped abruptly due to impact was recorded using a high-speed camera. The diffuse illumination improves contrast for recording.

The experimental setup is illustrated in Figure 41. A rectangular 50 x 50 mm aluminium channel of 2.5 mm thickness with a depth of 20 mm was sawed off to create the gantry. It was then attached to a linear sliding stage. The test substrate was attached to the bottom surface of the gantry. A pendant drop of specific volumes of liquid were created by delivering liquid via a flexible hose from a syringe pump to a 23-gauge stainless steel tip (with flat end) via syringe. The gantry design included a diffused light source to improve background illumination to obtain good contrast images from a high-speed camera (Fastec Imaging, Troubleshooter TS1000ME). The gantry was raised to a constant height at 9.5mm and released which was able to supply a fixed impact force that dislodges the drop from the tip. The momentum generated by the gantry system was characterized prior to conducting the experiments with drops attached to the tip. This was done by tracking the video sequence recording of the falling positions of the

gantry from start until just before impact that were recorded using the high-speed camera. The mass of all the moveable parts was measured and found to be 0.4 kg. The momentum, p of the impact was determined using Equation (22).

$$p = mv \tag{22}$$

Where m is mass of moving parts,

and v is velocity just before impact.

3.5.3 Results & Discussion

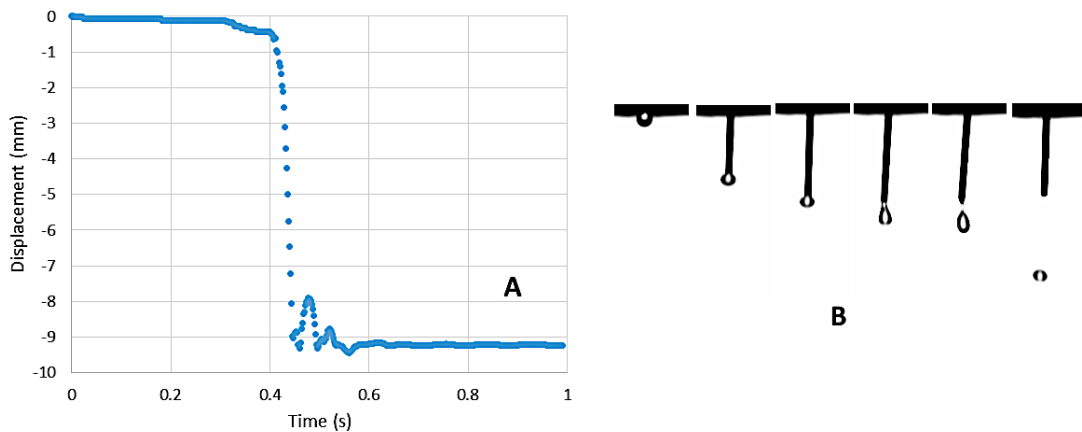


Figure 42: Plot (A) of displacement versus time trace of tip and thus the gantry (based on rigid body assumption). The velocity at the point of impact to be determined from the gradient. The sequence (B) of high-speed images (from left to right) show changes in the morphology of a drop initially stably maintained at the dispensing tip and then accelerated downwards by gravity to an abrupt stop before reaching terminal velocity. The resulting impact force triggers detachment of the drop from the tip where it resumes its flattened spherical shape.

Pendant drops of 30% water-glycerol mixture with volumes ranging from 1 to 15 μL were stably maintained on the stationary tip. A gravitational force was applied

by gantry displacement. From Equation (18), the calculated theoretical maximum drop volume that can be sustained on the tip was 26.8 μL . Understanding this relationship between parameters governing V_{max} aids the design of devices. Gravity was the sole dominant force involved as seen from the trace of gantry displacement with time (Figure 42A) and that air resistance can be neglected. The fall velocity was found to be 366 mm/s determined from the gradient at the point of impact. The theoretical fall velocity was found to be 373 mm/s calculated based on Newton's law from Equation (23).

$$v = u + gt \quad (23)$$

Where v is the fall velocity,

u is the initial velocity (= 0mm/s)

g is the gravitational acceleration (=9.81m/s)

and t is the fall time (=0.038s from trace of gantry).

The close values between experimentally and theoretically-derived velocities suggested that airflow drag did not show significant influence on the movement of the gantry. Considering the mass of all the moving parts, the momentum at the point of impact was found to be 0.1464 N/s calculated from Equation (22). When gantry was raised and initially released from a constant height (Figure 42B), the dispensing tip and spherical drop moves downward in tandem where the drop forms a flattened shape as expected due to the compression from the upward-acting force of the laminar air flow illustrated in Figure 40 (left). At point of impact, the change in drop shape during detachment resembles the characteristics of a pendant drop that is generated from slow flowrates and pinched-off from a stationary tip due to its own weight [281].

A comparison of these two cases can be made. In the case of continuous liquid delivery to a stationary tip, the pendant drop is able to accommodate greater deformation due to higher axial momentum resulting from higher liquid velocity (despite flowrate being kept constant), assuming the drop forms a more cusp like initial shape and advances to an elongated shape. In this case, the drop stability is governed by two dominant opposing forces; the increasing gravitational force arising from increasing drop mass which initiates drop detachment and the surface tension forces that is responsible in pinning the drop to the tip. This results in the volume of the drop at pinch-off remains relatively constant. In contrast, when using the experimental setup here, drop detachment is the result of the momentum transferred to the drop due to impact since volume of the pendant drop was kept constant.

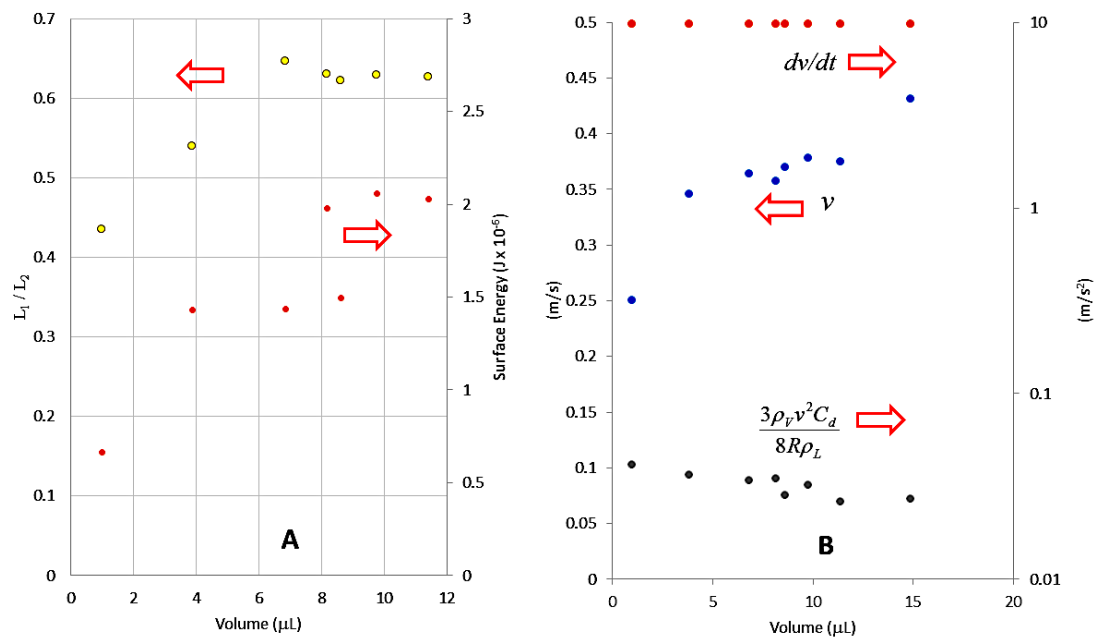


Figure 43: The plots (A) of L_1/L_2 against volume of the drop and the corresponding surface energy developed at time just before detachment from the tip. After drop detachment, plots (B) of mean drop velocity v (vertical axis on the left) against volume at time just before contact with the substrate (average taken from 5 readings). Using these values, the first and third terms in Equation (20) can be calculated and plotted (vertical axis on the right).

The plot in Figure 43A shows the change towards oblate spheroidal shape is more noticeable with larger volumes are used. It should be noted that the Bond number is $O(1)$. Even though the momentum available from the impact was kept constant, gravitational forces (although smaller than the influence of surface tension forces) may still be responsible for this trend. Based on Equation (19), the surface energies (see Figure 43A) show the similar trend to L_1/L_2 with volume but are amplified due to the scaled-up effect of dimensional length. This will possibly influence the downward velocity of the drop at the point of detachment, which cannot possess non-zero values (i.e. velocity should begin with zero after impact).

For pendant drops suspended on a stationary tip that are generated by applying a continuous liquid flow, the study from Scheele and Meister [282] shows that the calculation for droplet volume is dependent on complex empirical equations that includes the radius of the tip, surface tension of the liquid and the delivery flowrate. However, there is high potential for satellite or daughter drop formation using this method of dispensing which results in sample loss and volume inconsistency. It is possible to avoid this by using air plugs to partition the liquid into separate discrete volumes before delivery [283]. Unfortunately, this alternative creates possibility of air entrainment into the drop during dispensation, which then affects imaging fidelity. The method of experimentation using gantry setup has the favourable characteristics that does not produce neither daughter drops nor air entrainment into drops.

The pendant drop forms a spherical shape soon after detachment (see Figure 42B). This suggests adherence to the differential relationship from Equation (20). A better insight to drop characteristics can be obtained by considering the condition at time just before contact with the substrate. Firstly, greater instantaneous velocity (see Figure 43B) is seen with increasing drop volume. The Reynolds number followed by the drag coefficient, C_d could be determined from the drop dynamics modelled by Beard [280] using experimentally-derived velocity and volume values. The values of dv/dt calculated from Equation (20), are invariant against drop volume and almost equal to gravitational acceleration. This provides decent evidence that the drop has not achieved its terminal velocity and that the contribution of drag (third term in Equation (20)) is small at this stage. The plot in Figure 43B shows that drag is confirmed to be roughly

$O(10^2)$ smaller than dv/dt . These results imply that $v \neq 0$ upon detachment since the drops do not achieve similar velocity just before contact with the substrate. This suggests that the impact provides momentum that is not only responsible for the drop detachment but also the initial non-zero velocity value upon detachment. Considering that the attachment force to the tip to be constant relative to drop volume, the elastic energy stored will be proportional to the amount of drop elongation prior to detachment (see Figure 43A). The kinetic energy arising from inertial energy transfer after detachment is believed to provide the drop with its initial velocity upon detachment. This proposed mechanism is supported by the trend for velocity (Figure 43B) and surface energy at the point of detachment (Figure 43A) with volume.

3.5.4 Conclusion

This proposed experimental setup with moving gantry released from a constant height to an abrupt stop (impact) shows favourable characteristics that does not produce neither daughter drops nor air entrainment into drops. The gravitational forces may be responsible for the more prominent oblate spheroid shape with increasing drop volume. In addition, the surface energy trend follows to that of L_1/L_2 with volume but are amplified due to the scaled-up effect of dimensional length. The drop does not achieve its terminal velocity just before impact with substrate and that the contribution of drag is small since the values of dv/dt is close to gravitational acceleration. The impact provides momentum that is not only responsible for the drop detachment but also the initial non-zero velocity value upon detachment. The understanding of the relationship between parameters governing V_{\max} aids the design of devices during liquid transport.

Results of this work were reported in the paper (AHMAD ZAHIDI, A. A., CHUNG, D. C. K., KATARIYA, M., LIEW, O. W. & NG, T. W. 2019. Living specimens under field immobilization and smartphone microscopic observation. *Microscopy Research and Technique*, 0) attached in Appendix D.

3.6 Chapter Summary

When transporting biochemical samples, they will be subjected to various types of perturbations. This chapter demonstrated results from liquid stability investigations. Glycerol was chosen as the test sample to investigate its characteristics and behaviour under inclined conditions and also three varying impact conditions (upward longitudinal, car crash-like, and gravitational). From investigations for drops on surface under inclined conditions, the results revealed that the wetting characteristics was influenced by the interaction of fluid with both the solid as well as the air entrapped within the surface microstructures and the contact angle hysteresis does not have any influence on the slip angle.

In the case of drops under upward longitudinal impact, there were there distinctive behaviours observed when tested on both scribed and non-scribed transparency microplates. It was found that the drops tend to be more unstable with scribed surface due to the extra pinning offered by the scribed groove restricting the means to adapt to energy changes. Type III behaviour where the droplet separated was observed with the scribed surface undesired for transport. Although this condition should be avoided, it was found that it could provide feasibility of improved mixing during transportation which is later continued in Section 5.4.

For the experimentation conducted under car crash-like impact, it was discovered that the droplet undergoes changes in contact angles more readily compared to displacement to dissipate energy absorbed from impact. The droplet behaviour could be correlated to the Ohnesorge number which proposed a feasibility for this method to be used for determining fluid viscosity. It suggested that resistance to perturbation from impact is governed by viscosity of liquid where the resistance to perturbation increases with increasing viscosity.

In the last investigation of drop under gravitation impact revealed that the proposed experimental setup with moving gantry released from a constant height to an abrupt stop (impact) shows favourable characteristics that does not produce neither daughter drops nor air entrainment into drops and provides the ability for inspection of

bubble presence prior to using the droplet for other applications mentioned in Section 5.2 5.3

This understanding of drop mechanics in this chapter helps provides useful information for the design of automation of systems during transport as a constant inclined angle can be achieved to prevent droplet movement regardless of its mixture concentration. From the results, a suitable microplate surface can also be design to achieve highest level of stability. Finally, the findings in this chapter has provided feasibility of using experimental setups to help reduce or prevent sample loss during transport.

4 LIQUID PROCESSING FACTORS

4.1 Introduction

When conducting experiments using viscous liquids, certain processing factors can influence the reliability of the outcome. Therefore, in this chapter, investigations were conducted to analyse some of these factors in order to devise methods to eliminate or overcome its consequences. Section 4.2 presents the edge effect problem that arises when conducting experiments using microplates. This is followed by Section 4.3 which presents the investigations on bubble presence when dispensing viscous liquids from narrow tips.

4.2 Edge Effect (Microplating)

4.2.1 Introduction

In the biochemical experimentations, microplates continue to be one of the most universal tools for analytical research and clinical diagnostic screening. Maintaining the format of analyte handling to that of standard microplates in developing biochemical analysis instrumentation as it provides convenience of ready usage with existing readers therefore removes the cost for designing new readers. In addition, it also offers familiarity for users that have been accustomed to this widely established format. This format has been used to address various biochemical related needs [284-286] notwithstanding the availability of lab-on-a-chip alternatives [287]. The context of use of small volumes in current analyte handling was reported [288, 289]. More recently, studies have shown the ability to use transparencies (normally used with overhead projectors) in microplate instrumentation [136, 290]. The use of these transparencies will greatly improve cost effectiveness since they are cheap and easy to source.

The scale of testing required in modern biochemical analysis has driven the introduction of multiplexed formats using microplates [291, 292]. Multiplex testing,

however, presents analytical and quality control challenges. Among the controls that have been introduced include the use of blank areas, positive controls, negative controls, normalization controls, controls for nonspecific binding and to confirm sample addition, cross-reactivity controls, and controls to assess the activity of assay reagents such as the detection conjugate [293]. A factor that continues to complicate array-based tests in a microplate format is the regional variation in results of the outer against the inner wells of the plate, which is often described as the edge effect. The main culprit for this is widely believed to be the zonal differences in the rate of evaporation from the wells [165, 294]. Quite naturally, the use of plate seals [295] and tight closures [296] have been advanced to ameliorate the evaporation variation effect. A major cause of evaporation during microplate incubation is temperature. While the effect from temperature gradients have been alluded to [297], there have been no known studies made or approaches advanced to remedy the edge effect through reducing temperature gradients in microplates. In this section, the investigations on edge effect was conducted by providing an analytical link between temperature and evaporation rate, and conducting thermal simulation studies using finite elements (FEM).

Analysis of evaporation

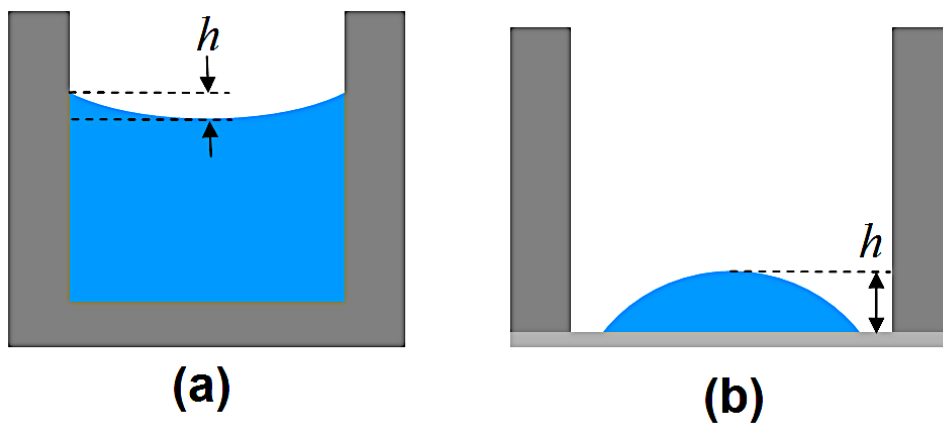


Figure 44: Illustration of liquid residence in a (a) standard microplate well, and (b) transparency microplate well.

Consider the evaporation mechanics involved for liquid residing in a standard microplate well (Figure 44a) and in a transparency microplate well that operates under reduced evaporation [137] (Figure 44b). The latter can be represented as a sessile drop in which efforts to characterize its evaporation have been attempted [155] by considering the adjacent air being saturated with vapor due to the rapid interchange of molecules between the liquid and vapor phases. The vapor phase is a thin saturated region that diffuses outward into the surrounding unsaturated air. Assuming a quasi-equilibrium process for slow evaporation in still air, the evaporation rate of the vapor Q can be taken to be represented by Fick's law given in Equation (24).

$$Q = \rho \frac{\partial V}{\partial t} = 4\pi D r (C_s - C_\infty) f(\theta) \quad (24)$$

Where D is the vapor diffusivity in still air,

r = radius of air-liquid surface curvature,

ρ = density of the liquid,

C_s = the saturated vapor concentration at drop surface,

C_∞ = the ambient vapor concentration determined by the relative humidity,

and $f(\theta)$ = the dependence of evaporation rate on the contact angle.

The evaporation process can be affected by many different factors [298, 299], but considering only a situation in time, Equation (24) can be simplified to Equation (25).

$$\frac{\partial V}{\partial t} = - \frac{2\pi D h M}{\rho R T} (P_s - P_\infty) \quad (25)$$

Where h = the height of drop,

R = gas constant,

M = molecular weight of the liquid,

Chapter 4: Liquid Processing Factors

T = temperature in Kelvins of the liquid,

P_s = the vapor pressure on the liquid surface,

P_∞ = the vapor pressure an infinite distance away (which can be assumed to be zero)

P_s is related to T using the Classius-Clayperon relation in Equation (26).

$$P_s = e^{\left(\frac{-\Delta H_V}{RT} + K\right)} \quad (26)$$

Where ΔH_V is the heat of vaporization of the liquid,

and K is the value for $\ln(P_s)$ when $\Delta H_V = 0$.

Hence, Equation (25) can be rewritten as Equation (27).

$$\frac{1}{h} \frac{\partial V}{\partial t} = - \left[\frac{2\pi DM}{\rho RT} e^{\left(\frac{-\Delta H_V}{RT} + K\right)} \right] \quad (27)$$

It can be assumed that this is the same in the case of liquid in standard microplate wells.

4.2.2 Materials and Methodology

ABAQUS FEA (Dassault Systemes) was used to conduct the simulations. The overall size of the standard microplate was 127.76 mm length, 85.48 mm wide, and 14.7 mm high, with the wells kept at a pitch of 9 mm from each other and having diameter and height of 6.5 mm and 11.45 mm respectively. The solid material used throughout was acrylic, while the liquid used was water. The transparency thickness of the transparency microplate was kept at 0.11 mm and the liquid droplets kept at 40 μL volume with a diameter of 5.34 mm in contact with the transparency. To achieve an

even mesh, the microplate section and the water section were meshed with tetrahedron elements due to their regular shapes, while the transparency section was meshed with rectangular element. The microplate sections in standard microplate model and transparency microplate model have about 720,000 nodes and 650,000 nodes respectively. The transparency sheet has approximately 58,000 nodes and each droplet has about 1,500 nodes in the transparency microplate model. The number of nodes in the water section in each well varies from 450 to 3300 depending on the filling ratio. All nodes in both models are approximately 1 mm apart. The boundary elements that were not affected by heating were fixed at 298 K (which corresponds to typical ambient temperature). The boundary elements subject to direct heating were set at 311 K (to correspond to the body incubation temperatures). The presence of strong temperature gradients within the liquid body will lead to convection flows that facilitate mass transfer. This effect was not included in the simulation as purpose of this investigation was to establish the average temperature of the liquid in each well.

4.2.3 Results & Discussion

Considering the relationship between temperature and evaporation rate, Equation (27) appears to portray an anomalous situation that the rate of evaporation is inversely proportional to temperature. However, in reality, there are only certain parameters in the equation are invariant with temperature. The properties for water are given in Table 3 and Table 4.

Table 3: Water properties that are invariant with temperature.

M (kgmol⁻¹)	0.018
R (JK⁻¹mol⁻¹)	8.314
K (Pa)	740.2943

Table 4: Water properties dependent on temperature.

T	298K (25°C)	311K (38°C)
ρ (kgm ⁻³)	997.15	992.97
ΔH_V (Jkg ⁻¹)	1814 x 10 ³	1891 x 10 ³
D (m ² s ⁻¹)	25.28 x 10 ⁻⁶	27.17 x 10 ⁻⁶

Consequently, through computing the right-hand side of Equation (27), the values obtained are $-3.91 \times 10^{-9} \text{ m}^2\text{s}^{-1}$ and $-9.23 \times 10^{-9} \text{ m}^2\text{s}^{-1}$ for temperatures of 25 °C and 38 °C respectively. This indicates that when the temperature is higher, the evaporation rate increases correspondingly. Hence, this confirms that the key to eliminating the edge effect will be to maintain a constant temperature of the liquid dispensed in all wells.

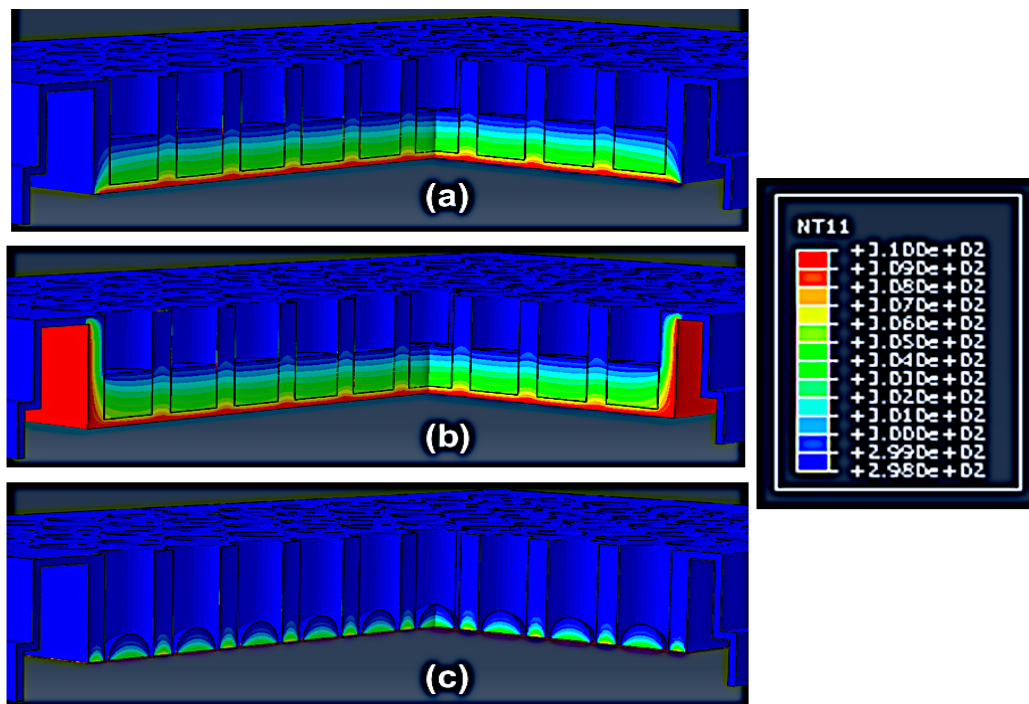


Figure 45: Results of the steady-state temperature distribution for finite element simulation in a (a) standard microplate with direct heating at the bottom, (b) standard microplate with direct heating at the bottom and sides, (c) transparency microplate with direct heating at the bottom.

Figure 45(a) presents the result of the FEM simulation with a standard microplate well in which only the bottom was heated. It can be seen that there is a considerable heat transfer via conduction from the side walls, causing the liquid in wells close to the edge to experience lower temperatures. Figure 46(a) present plots of the average liquid temperature sampled at the centre and corner wells of a standard microplate at different liquid filling ratios (height of liquid / height of well). The temperature difference trends evident confirm the edge effect through the influence of heat conduction. It can be seen that the temperature in the liquid is generally higher when the liquid filling ratio is increased. This is due to the thermal inertia offered by the liquid body.

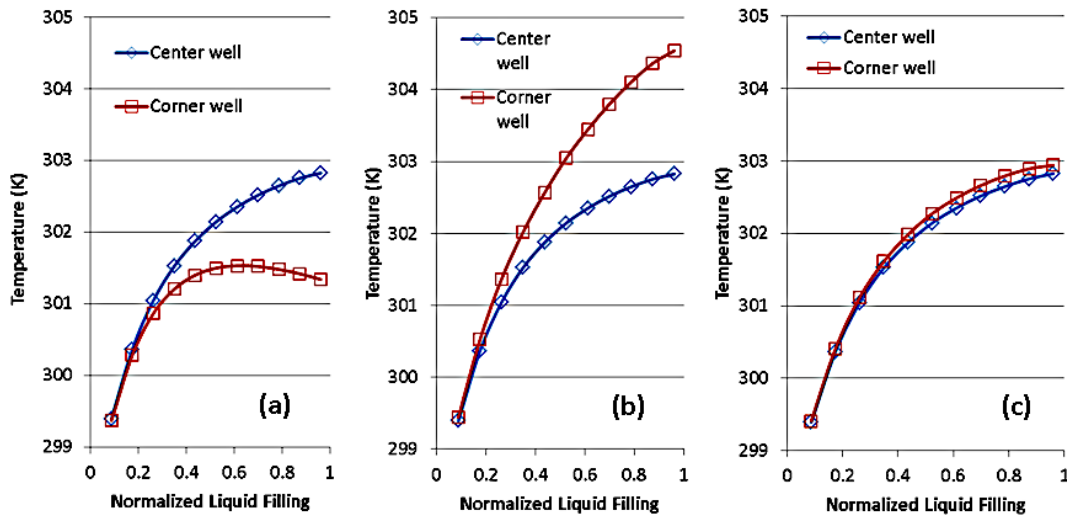


Figure 46: Average liquid temperature plots in a well at the centre and corner at different liquid filling ratios (height of liquid / height of well) of a standard microplate (a) directly heated only at the bottom at 310K, (b) directly heated at the bottom and sides at 310K, and (c) directly heated at the bottom at 310K and the sides at 304K.

In order to overcome the imbalance due to heat conductions, the case was simulated where the side walls were heated as well as the bottom at the same temperature. As shown in Figure 45(b), this cursorily indicates the capacity to eliminate the edge effect. On evaluating the average liquid temperature sampled at the centre and corner wells of a standard microplate at different liquid filling ratios however (Figure

46(b)), it can be seen that a reversed effect is attained, i.e. the temperature of the edge wells was higher than the centre wells. This is expected due to the contribution of heat from the side walls having a greater influence on the average temperature. Logically, a remedy will be to lower the temperature of the side walls relative to the bottom in order to counteract this imbalance. Figure 46(c) presents the case where a satisfactory outcome is achieved by keeping the temperature of the side walls at 304 K compared to 310 K at the bottom. It should be noted that different combinations will be needed if the ambient temperature is different.

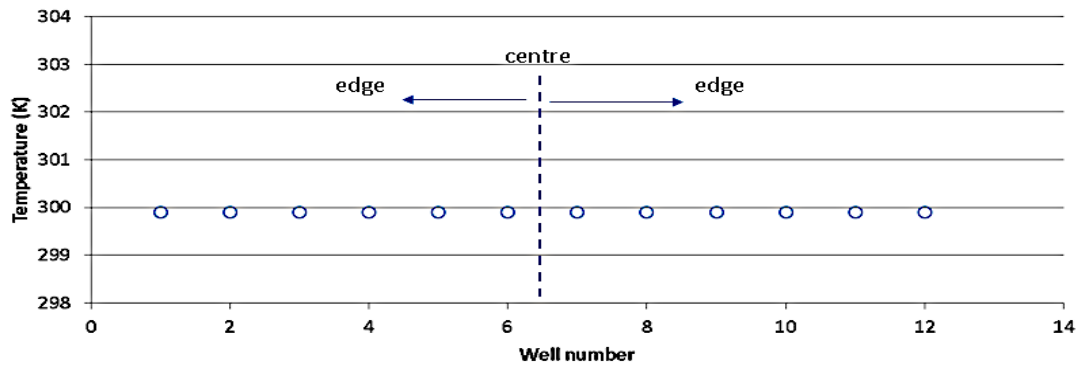


Figure 47: Distribution of temperature at different wells along the length of a transparency microplate, which show strong uniformity from centre to the edge.

The need to maintain a dual temperature heating mode can be a challenge in terms of instrumentation development. Since the heat loss due to conductivity is the main cause for the temperature disparity, a solution may be to use a material with very low thermal conductivity as manufacture for microplates applied in biochemical assays. Such an approach will likely not get much traction practically. In the early 1960s, microplates were primarily made of acrylic (thermal conductivity of $0.2 \text{ Wm}^{-1}\text{K}^{-1}$) until the appearance of polystyrene ($0.1 - 0.13 \text{ Wm}^{-1}\text{K}^{-1}$) plates in 1965 and has remained the mainstay of microplates to date. In recent times, materials like cyclo-olefins with superior optical properties have been used in microplate manufacture but they do not provide added advantage in terms of thermal conductivity ($0.16 \text{ Wm}^{-1}\text{K}^{-1}$) compared with polystyrene. It would be more convenient to place air between the liquid and solid

walls, since air has a thermal conductivity ($0.024 \text{ Wm}^{-1}\text{K}^{-1}$) that is about ten and five times lower than that of acrylic and polystyrene, respectively. A readily available solution is using adapted transparency microplates [137] in which the analyte does not contact the wall (see Figure 44(b)). This can be seen in the simulation result of Figure 45(c), as well as the uniform temperature distribution in different wells along the length of a transparency microplate from centre to the edge given in Figure 47. It should be noted that while the rate of evaporation is uniform, it does not imply that it is absent. One strategy that can be introduced to slow down the evaporation rate is to inject in silicone oil [149], although it is predicated that the oil does not affect the analyte. A more general approach would be to increase the humidity of the incubating environment as this will reduce the vapor pressure differences between the liquid and the air. While this is workable, it is important to mind the possibility of condensation occurring due to the high surface to volume ratios that are typically in place. Surfaces that are strongly hydrophobic encourage drops to condense on them more readily [300, 301], which can then dislodge more easily and mix with the analyte to alter its composition. This is particularly important when microplates are used in the context as cell incubators [302]. Finally, if convective heat dissipation modes are eliminated, the use of different solvents/liquids should have no influence on the results.

4.2.4 Conclusion

Analytical approach for the basis of the evaporation mechanics of a sessile drop was conducted. The evaporation rate was found to increase with increase in temperature due to the changes in heat of vaporization, density and diffusion coefficient with temperature. From simulations of direct heating of standard microplates at the bottom, the temperature in the liquid was generally higher when the liquid filling ratio was increased due to the thermal inertia effect offered by the liquid body. Considerable heat transfer via conduction from the side walls was found to be responsible for the liquid in wells close to the edge to experience lower temperatures. When the standard microplate was heated at equal temperatures at the bottom and sides, the temperature of the edge wells was higher than the centre wells. Applying a two-temperature heating

mode, 304 K at the side compared to 310 K at the bottom, allowed for a more uniform temperature distribution. Due to absence of direct liquid-solid wall contacts, transparency microplates were found to inherently possess immunity to the edge effect problem.

Results of this work were reported in the paper (LAU, C. Y., ZAHIDI, A. A. A., LIEW, O. W. & NG, T. W. 2015. A direct heating model to overcome the edge effect in microplates. *Journal of Pharmaceutical and Biomedical Analysis*, 102, 199-202) attached in Appendix E.

4.3 Bubble Formation (Dispensing)

4.3.1 Introduction

Loss of sample volume can be encountered when dispensing microvolumes of viscous liquids from tips due to the sticky nature of the liquid leaving some residue behind. Slow or reverse pipetting method is suggested to overcome this problem [303]. Another problem arising from working with viscous liquids is the presence of bubbles which will influence the imaging when using optical screening devices. Moreover, bubble formation when creating pendant drops from dispensing tips will affect the accuracy of the liquid volume generated. In this section, attempts were made to uncover the problem of air entrainment while dispensing viscous liquids from tips.

4.3.2 Materials and Methodology

A series of dispensation exercises were conducted where a pendant drop of specific volumes of liquid were created by delivering liquid via a flexible hose from a syringe pump to a 23-gauge stainless steel tip (with flat end) via syringe (see Figure 41). The pendant drop was inspected to identify any presence of bubbles. When bubbles were present, the dispensation was repeated to ensure there were no bubble presence in the pendant drop before continuing the next set of experiment that was previously

explained in Section 3.5. A 3D optical profilometer (Bruker, Veeco-Wyko) was used to characterise the stainless-steel tip based on a non-contact GT-1 interferometric system. The instrument was placed on a pneumatic vibration-isolation table (Newport) which was fitted with active high attenuation isolation and calibrated using step height standards (Bruker, Veeco). The instrument used phase-shifting and/or vertical scanning interferometry to resolve the topology of microscale surface structures. Both low and high magnifications were used for imaging to obtain optimal scanning results.

4.3.3 Results & Discussion

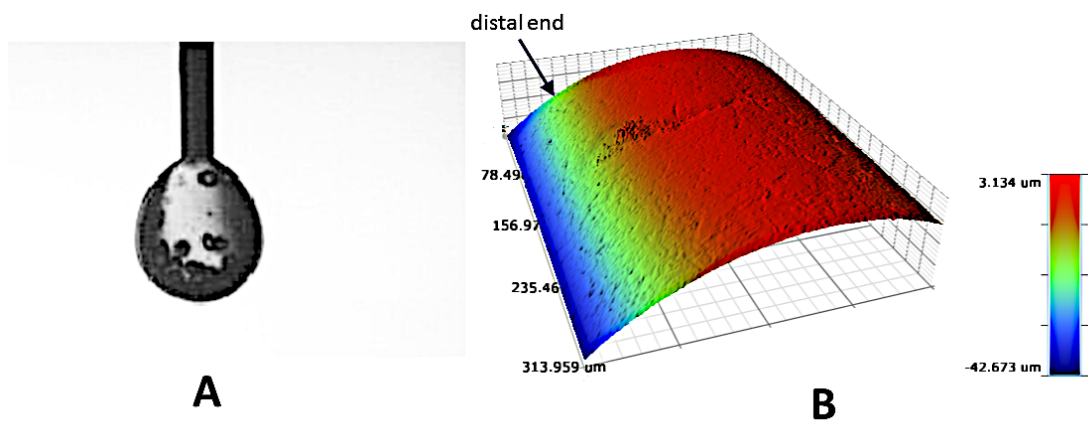


Figure 48: The presence of (A) air bubbles entrained in a pendant drop during liquid dispensation. These bubbles will degrade the image quality of the liquid lens. Imaging results (B) from optical profilometry of the tip do not reveal material accretion that would affect liquid pinning or facilitate bubble formation.

It was seen that the dispensation exercises developed small air bubbles within the pendant drop (see Figure 48A). If the pendant drop containing the presence of bubbles were used for creation of liquid lens, it is likely that this would disrupt the image fidelity of the liquid lens. In addition, the presence of bubbles in the pendant drop may also affect the visibility of immobilized insects in the microplate well if used as immobilizing medium. Evidently, formation of a pendant drop on the dispensing tip should be stable and secure to allow thorough inspection of bubble presence and then use appropriate interventions to prevent the delivery of drops containing bubbles onto

the substrate. After the pendant drops were confirmed to have no bubble presence, it is useful to implement the drop impact approach in Section 3.5 to dispense the pendant drop into the microplate wells and onto substrate to form the immobilization medium and liquid lens in Sections 5.1 and 5.3 respectively. The profile structure of the tip revealed using optical profilometry (Figure 48B) do not show presence of any material accretion or manufacturing defect (i.e. notch etc.) that could affect liquid pinning or allow air passage from the side that will cause bubble formation. Therefore, any enforced pinning ability resulted only from the regular edges of the tip [304].

4.3.4 Conclusion

Bubble presence occur during dispensation of viscous liquids from tips. The bubble presence will likely affect the image fidelity of liquid lens and also visibility of insects in immobilizing mediums. The stable and secure formation of a pendant drop on the dispensing tip prior to creation of liquid lens and immobilizing mediums is advantageous as this provides a thorough inspection of the pendant drop to be conducted and allow for appropriate interventions to prevent the delivery of drops containing bubbles onto the substrate.

Results of this work were reported in the paper (AHMAD ZAHIDI, A. A., CHUNG, D. C. K., KATARIYA, M., LIEW, O. W. & NG, T. W. 2019. Living specimens under field immobilization and smartphone microscopic observation. *Microscopy Research and Technique*, 0) attached in Appendix D.

4.4 Chapter Summary

This chapter discussed the factors affecting the efficiency of liquid processing. In the case of investigations to eliminate edge effect for standard microplates, it was found that applying a two-temperature heating mode, at the side (lower temperature) compared to at the bottom (higher temperature), resulted in a more uniform temperature distribution. From the absence of direct liquid-solid wall contacts, transparency

microplates were found to inherently possess immunity to the edge effect problem. The use of these transparencies will greatly improve cost effectiveness since they are cheap and easy to source. Maintaining the format of analyte handling to that of standard microplates in developing biochemical analysis instrumentation is important as it provides convenience of ready usage with existing readers therefore removes the cost for designing new readers. Therefore, the use of this strategy offers familiarity for users that have been accustomed to this widely established format.

From the investigations conducted for bubble formation while dispensing viscous liquids from tips, it was found that the bubble presence will likely affect the image fidelity of liquid lens and also visibility of insects in immobilizing mediums that will be discussed in Sections 5.3 and 5.2 respectively. The stable and secure formation of a pendant drop on the dispensing tip (from Section 3.5) prior to creation of liquid lens and immobilizing mediums is advantageous as this provides a thorough inspection of the pendant drop to be conducted and allow for appropriate interventions to prevent the delivery of drops containing bubbles onto the substrate. The profile structure of the dispensing tip revealed using optical profilometry did not show presence of any material accretion or manufacturing defect such as notch that could affect liquid pinning or allow air passage from the side that will cause bubble formation.

5 APPLICATIONS OF VISCOUS LIQUIDS

5.1 Introduction

There are many applications that require the use of viscous liquids. Glycerol, which is a type of viscous liquid was used for the investigations conducted in this chapter due to its favourable and advantageous optical properties as well as its compatibility with biochemical applications. This chapter presents the investigations on various viscous liquid applications using water-glycerol mixtures. Section 5.2 presents the investigations on methods for immobilisation of *Drosophila melanogaster* (fruit flies). This is followed by studies on liquid lens incorporated with smartphone for field microscopy application presented in Sections 5.3. Section 5.4 and 5.5 presents investigations of mixing methods for reagents and also blood centrifugations using UAV. Lastly, Section 5.6 presents the optical thermal immobilization of Bovine Serum Albumin using glycerol.

5.2 Field Immobilisation (Water-Glycerol)

5.2.1 Introduction

Sharp declines in insect population have resulted in the increased interest in studying their behaviour in their natural environment [305]. An approach would be to conduct preliminary open-field investigations to examine these specimens on-site to support a more comprehensive laboratory-based anatomical studies in later stages [306]. Sparse spatial data sampling in open-field investigations can be overcome with the availability of simple and cost-effective tools [307]. There is difficulty in developing non-destructive immobilization techniques for careful examination and preservation of active and living biological specimens. Many biological species can fly, swim or crawl actively which makes observations over long periods of time challenging. Various, chemical [308] and mechanical [309] immobilization methods exist. It is also popular to apply physical schemes based on the use of viscosity as it is

well-established. If the viscous substance is biologically inert, non-toxic, and non-osmotic, it is possible to minimize any detrimental effects on the specimen, although excessive viscosity can limit the ability to retrieve the specimen from the immobilizing medium post microscopic examination. Water-glycerol mixtures have shown promising results in preservation of biochemical samples as they are able to serve as cryo-protectants for stabilizing macromolecules, cells and tissues under cooling to sub-zero temperatures, and also suppress ice formation [310]. The experiment in this section reports the use of a single water-glycerol mixture composition that will serve as the immobilization medium for a model insect, *Drosophila melanogaster* (fruit fly), in the field setting.

5.2.2 Materials and Methodology

Live *Drosophila melanogaster* were commercially sourced (L7.3 Southern Biologicals) in a glass vial and then self-cultured to increase their population. Wells of a standard microplate were filled with varying percentages of water-glycerol mixtures. A funnel was placed over the mouth of a culture vial and inverted so that the stem of the funnel was positioned over one microplate well. When the foam plug covering the culture vial was removed, the vial was tapped so that some *Drosophila* flies fell into the liquid. This was repeated for the other microplate wells that contained different water-glycerol compositions.

5.2.3 Results & Discussion

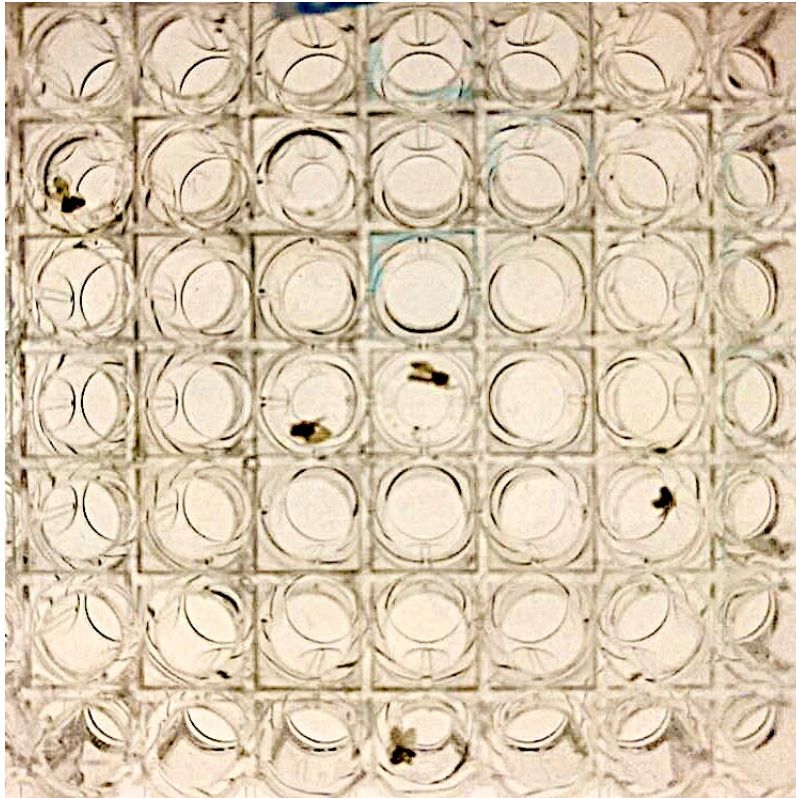


Figure 49: Images of a *Drosophila* sample immobilized in a microplate well using varying concentrations of water-glycerol mixtures. 30% (w/v) concentration was found sufficient for effective immobilization of live *Drosophila* flies.

It was found that 30% water-glycerol (w/v) provided effective immobilization of live *Drosophila* flies in microplate wells. This was the minimum concentration that was found sufficient to hold the *Drosophila* in the microplate well. Moreover, this concentration is practical in field operations as it is able to provide enough immobilization from the sticky viscous property of the water-glycerol mixture, but not too viscous that it will cause problems or inaccuracy in liquid dispensing as mentioned in Sections 3.5 and 4.3. This concentration of mixture can then be used to develop the liquid lens in Section 5.3. Interestingly, it was found that addition of some vinegar into the immobilizing medium helped to attract the insects better. This capturing process and immobilization method is harmless and minimizes mechanical or physical

distortion of the specimen. In addition, the *Drosophila* flies can be kept alive for further required analysis.

5.2.4 Conclusion

A minimum concentration of 30% water-glycerol (w/v) was of adequate viscosity to immobilize and hold the *Drosophila* in position within the microplate well. Hence, the efficacy of the water-glycerol mixture to hold the *Drosophila* in place is verified. Subsequently, the 30% water-glycerol mixture can be used to develop the liquid lens. This is due to the practicality of the concentration possessing enough viscosity to allow immobilization but not too viscous that it will cause problems during dispensing. Moreover, it was found that the inclusion of vinegar into the immobilizing medium improved the attraction of the insects. This process of capture and immobilization is harmless and minimizes mechanical or physical distortion of the specimen while continues to maintain a living captive specimen.

Results of this work were reported in the paper (AHMAD ZAHIDI, A. A., CHUNG, D. C. K., KATARIYA, M., LIEW, O. W. & NG, T. W. 2019. Living specimens under field immobilization and smartphone microscopic observation. *Microscopy Research and Technique*, 0) attached in Appendix D.

5.3 Smart Phone Microscopy (Water-Glycerol)

5.3.1 Introduction

One of the exciting functions that smartphones can offer is for it to be used as microscopes since they are easy to source and are designed with impressive high resolution camera sensors [311, 312]. Liquid lenses are typically made of optical grade liquids and are known for its versatility in altering its focal length for imaging applications. Varying the focal length requires manipulating the wetting properties of the liquid which involves designs that require significant construction and fabrication resources. This experiment investigates the relationship of the focal length relative to its shape of the liquid lens. Microscopic examination of actively moving specimens

raises real challenges [313]. Therefore, application of this smartphone/liquid lens-based setup with *Drosophila* as the target of interest was reported.

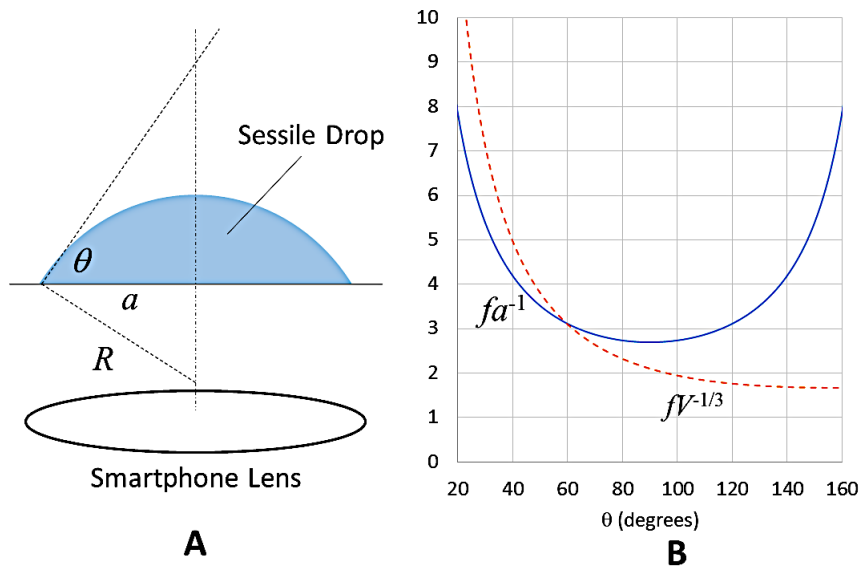


Figure 50: Sessile drop (A) placed on top of the lens of a smartphone creates a compound lens system with key parameters that increases magnification. Plots of $fV^{-1/3}$ and $f\alpha^{-1}$ (B) against θ showing that the focal length can be manipulating by keeping either values V or a as constant. This indicates that magnification adjustment can be achieved.

If gravity effects are ignored, a sessile drop forms a semi-spherical shape when it is placed on a surface (see Figure 50A). From geometry, the relationship governing the drop is radius of curvature, contact angle and radius of drop on the substrate surface given by Equation (28).

$$a = R\sin\theta \quad (28)$$

Where a is the radius of drop on the substrate surface,

R is the radius of curvature,

and θ is the contact angle.

The volume, V of the drop is related to θ and R via Equation (29) since it is typically known.

$$V = \frac{\pi R^3}{3} (\cos^3 \theta - 3 \cos \theta + 2) \quad (29)$$

Assuming that the sessile drop is taken as a plano-convex thick lens, then its focal length is related to R in Equation (30).

$$f = \frac{R}{(n-1)} \quad (30)$$

Where f is the focal length,

and n is the refractive index of the liquid.

Combining Equation (28) and (30), gives Equation (31).

$$f(a^{-1}) = \frac{1}{(n-1) \sin \theta} \quad (31)$$

Combining Equation (29) and (30), gives Equation (32).

$$f(V^{-1/3}) = \frac{1}{(n-1)} \left[\frac{3}{\pi(\cos^3\theta - 3\cos\theta + 2)} \right]^{1/3} \quad (32)$$

The smartphone lens has an existing focal length, f_s . When the liquid lens was placed on top of the smartphone lens, this creates a compound lens with a focal length f_t . The relationship of f_t and f_s is given in Equation (33).

$$f_t = \frac{f_s f}{f_s + f} \quad (33)$$

The magnification is given by Equation (34).

$$M = \frac{1}{f_t} \quad (34)$$

Therefore, a higher magnification can be achieved from keeping f small. The plot of $fV^{-1/3}$ against θ based on Equation (32) in Figure 50B, for $n = 1.37$ using 30% water-glycerol (w/v) and $20^\circ < \theta < 160^\circ$ (these range of values represent realistic situations) shows that the magnification will increase as a result of the decrease in value of f , from increasing the contact angle but keeping the volume constant. It will be difficult to implement this as it requires preparing surfaces with varying wettability. A more approachable option will be to use the method of scribing a circle on the substrate [137, 314] which keeps the drop radius, a on the substrate constant and the scribe groove provides additional pinning effect. Different volumes of liquid can be added within the confines of the scribe circle, resulting an increase in contact angle. The plot

of fa^{-1} against θ based on Equation (31) in Figure 50B also shows an increase in magnification is achievable from decreasing values of f through increasing the values of θ from 20° to 90° but keeping the drop radius constant.

5.3.2 Materials and Methodology

A lens testing chart (<http://www.normankoren.com/Tutorials/MTF5.html>) was created and attached to a translation stage. A transparent poly (methyl methacrylate) PMMA substrate of 1mm thickness was scribed using a punch wad tool to create a 3 mm diameter circles to create the groove that holds the drop sample. The liquid lens was formed on the scribed circles by dispensing drops of 30% water-glycerol (w/v) through an impact liquid delivery method using pendant drops (see Section 3.5) to ensure that the lens created was free of bubbles (see Section 4.3). The substrate was then placed over the smartphone (iPhone 7) camera aperture to create the microscope imager. The images of the lens testing chart were then analysed.

5.3.3 Results & Discussion

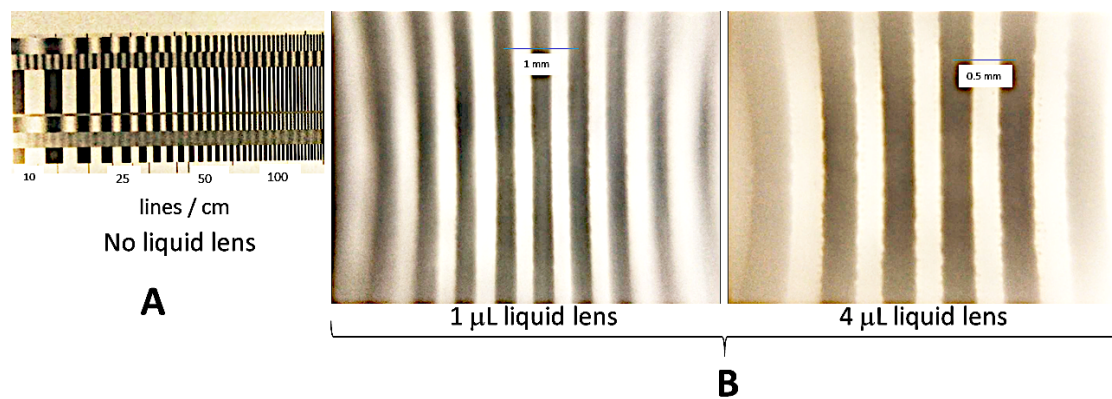


Figure 51: Images of the test chart obtained (A) without, and with (B) liquid lens of $1 \mu\text{L}$ and $4 \mu\text{L}$ created using different volumes dispensed onto a scribed transparent substrate of 3 mm diameter.

Target images up to 100 lines / cm were obtained and this was achieved solely using basic smartphone viewing without any aliasing (see Figure 51A). With liquid lens created on the smartphone, significant magnifications were achieved as the lines on the target images were identified to have 0.5 mm spacing (see Figure 51B). It is also clear that the use of higher liquid volumes, which would produce higher contact angles, resulted in higher magnifications (see Figure 51B). This demonstrates the tuneable feature of the liquid lens as discussed previously. After further analysis, the resolutions were found to be 5 $\mu\text{m}/\text{pixel}$ and 3.3 $\mu\text{m}/\text{pixel}$ with the 1 μL and 4 μL liquid lenses respectively. This is attained using the 12 mega-pixel camera of the smartphone. Some degree of pincushion distortion arising from the liquid lens used was observed. If corrections for these distortions were needed, image processing algorithms can be applied [315]. Using this same mixture, it was possible to obtain magnified images of the immobilized insects (from Section 5.1), which helps in the visual identification of the insect genus (see Figure 52). This demonstrated that this method of using liquid lens allows data to be collected in the field sampling and also eliminates the need of sending samples back to the laboratory.



Figure 52: Images of a *Drosophila* sample immobilized in a microplate well, recorded with liquid lens incorporated to a smartphone.

Experiments were conducted both outside and inside the laboratory, and found to work well in both modes. An effective immobilization and imaging technique, coupled with appropriate insect attraction methods for baiting the target is required to create an effective overall system. Existing research focuses more on investigations on methods for attracting insects, and leans towards finding effective species-specific attractants [316, 317]. Since the liquid lens is compatible with the performance of the optics to produce magnified images of the specimen [318], a fabrication facility is not necessary to create solid lenses for microscopy. However, using this simple set-up in the field has limitations to achievable magnification and resolution. Therefore, the approach described here is best applied for preliminary screening purposes. In the case where follow-up examination is needed, field samples can be collected and returned to the laboratory for high resolution imaging that are more refined.

It is anticipated that other biological specimens of suitable dimensions may also be examined noting the limitations of magnification and resolution with this method. Hence, there may even be potential to study soil-living biological organisms such as *Caenorhabditis elegans* or *Dictyostelium discoideum* depending on the stage of their life cycle as well as the availability of a suitable soil extraction method. In the case of *C. elegans* (~ 1 mm in length), it is possible to easily examine filtered Baermann funnel liquid extracts of nematode-infested soil in the field using this smartphone/liquid lens method. Nevertheless, the suitability of the immobilization medium should be investigated prior to conducting the experiment. It is recommended that auxiliary lighting be used for microscopic examination under low ambient light conditions. Colour-multiplexed illumination can be easily integrated into this simple setup if needed [319]. Lastly, faster power drainage of the battery occurs when using smartphones for applications such as imaging. Therefore, it is advisable to prepare battery banks on standby in the field to ensure that the battery can be recharged.

5.3.4 Conclusion

The ability to attain magnified views of *Drosophila* samples using liquid lens of 30% water-glycerol (w/v) mixture incorporated together with a smartphone was

demonstrated. The focal length tuning characteristic was confirmed and digital resolutions of up to 3.3 μm / pixel were achieved for 4 μL droplet volume. In order to eliminate bubbles formation in the liquid lens (in Section 4.3) which will affect imaging fidelity, the liquid transfer method which allows for inspection of a pendant drop as it is stably generated on a dispensing tip and dislodged from gravitational impact (in Section 3.5) onto the scribed surface, was implemented. This combined approach offers practicality in conducting preliminary open-field investigations by allowing specimens to be examined on-site, thus possibly removing the necessity for specimen collection for laboratory-based analysis.

Results of this work were reported in the paper (AHMAD ZAHIDI, A. A., CHUNG, D. C. K., KATARIYA, M., LIEW, O. W. & NG, T. W. 2019. Living specimens under field immobilization and smartphone microscopic observation. *Microscopy Research and Technique*, 0) attached in Appendix D.

5.4 Reagent Mixing with UAV (Water-Glycerol)

5.4.1 Introduction

The use of point-of-care testing (POCT) for biomarker measurements has been increasing in the research community. POCT offers numerous advantages in the clinical and non-clinical setting. This includes reduced delays in diagnosis and treatment, minimal sample handling and requirement for sophisticated equipment, and also user friendly. Centralized laboratory-based testing involves a hierarchy of steps beginning with specimen collection, handling, transport and storage; instrument set up; testing; and finally result reporting. POCT offers an opportunity to bypass these steps as pre- and post-analytical errors most commonly arise from them. However, cost burdens, analytical and clinical performances comparing POCT to laboratory-based testing [320-322], remain a concern despite the benefits that it can offer.

Timeliness and cost are the two important factors governing the transport of samples to the laboratory [323, 324]. It is more advantageous to use autonomous

systems to ensure sample viability. Pneumatic tubes are the main transport systems used in hospitals and are crucial to the function of most healthcare support systems [325, 326]. Since the up rise in of unmanned aerial vehicles (UAV) in commercial applications, they have been explored for outdoor delivery of biological specimen [327]. Although there were concerns raised due to some cases of malfunction [328], more robust electronics technologies can be used to overcome these problems. A major advantage of UAV is the ability to access remote areas and escape traffic congestion in urban areas. Although route planning strategies for conventional courier methods can be adapted, they offer limited improvements in timeliness of sample delivery [323, 324]. Pre-processing of the samples en-route during transport can help improve this timeliness factor.

In sample handling, appropriate mixing of samples is a vital step to attaining high quality specimens for laboratory testing. To achieve optimal downstream separation of serum or plasma when collecting blood into receptacles, appropriate mixing is essential for homogenous dispersion of silica particles, separator gels, clot activators or anti-coagulants. Haemolysis of red blood cells could cause the sample to be unfitting for testing. Therefore, it is important to minimize this effect by controlling the level of agitation applied during mixing. Automated mixing methods commonly rely on sustained and controlled agitation for specific periods of time. New methods have been developed to mix micro-litre range liquid samples in lab-on-chip devices [329], capillaries [289], liquid bridges [235], drops [330] in the laboratory. Most samples are transported to the laboratory in the millilitre volume range for the purpose of providing margins for repetitions when conducting experiments [331]. This usually arises from inconsistencies in process [332], assay [333] or substrate [334].

Typical quadcopters can be functional as a means to transport samples and also conduct mixing in tandem during transport. However, it would be unfeasible to attach mixing devices such as vortex mixers onto them do to the limited payload. Furthermore, the planned flight pattern of the quadcopter can be disrupted as a result from the forces generated by a vortex mixer in operation. A suggested solution would be to utilize the flight manoeuvring ability of the quadcopter itself. In contrast to fixed wing aircrafts, four vertically oriented propellers are responsible in producing the aerodynamic lift in

quadcopters. From this, it is convenient to generate lateral, longitudinal, and rotational movements. There is even an in-built program to perform flipping (looping) manoeuvres in the flight control of many quadcopters. The control schemes needed to attain the kinematics has been well studied [335] but is usually intended for showcasing their aerobatic abilities. This section examines the capability of this manoeuvre function to helpfully mix samples in-flight during transport.

5.4.2 Materials and Methodology

A Parrot Minidrone quadcopter was used having the mass of 63.5 g mass and dimensions measuring 15.2 x 15.2 x 3.8 mm. It was powered by a 550 mAh lithium battery and flight was controlled using a smartphone application (FreeFlight, Android or iOS). The liquid media used to illustrate the mixing capability were glycerol and deionized water. Red and blue food dye were added to glycerol and deionized water respectively to distinctly verify the mediums. Glycerol was chosen for this experiment as it is widely used in many pharmaceutical formulations for cryopreservation due to the capability of glycerol molecules to modify the hydrogen bonding ability of water molecules [336]. The mixing is not influenced by the relatively distinct viscosities of glycerol (1.414 Ns/m²) and water (0.001 Ns/m²) [337] at 20°C instead offers a suitable example for demonstrating the mixing capability of the quadcopter. The test sample was filled into a 2-mL glass vial (Verex) with plastic cap where 0.5 mL of glycerol and 0.5 mL water added sequentially to form two distinct aqueous layers. A fixture was designed to secure an array of test vials and fabricated using a 3D printer (Stratsys, UPrint SE Plus).

5.4.3 Results & Discussion

The fixture designed to be secured onto quadcopter was able to house 4 glass vials for transport (see Figure 53A). This design can also be adapted with the use of a larger quadcopter that will possibly hold a larger number of vials. The segregation of water (stained blue) and glycerol (stained red) is confirmed by the quantitative red,

green, and blue colour distribution as derived from the line profile (dashed line) prior to the manoeuvre test (see Figure 53B). After the quadcopter that was affixed with vials, it was made to perform the flipping manoeuvre 14 times. As illustrated in Figure 53C, a homogenous sample with uniform distribution of the colour components was achieved from mixing. Subsequently, the quadcopter was used to transport similar samples without any flipping manoeuvres. Both the liquid mediums remained in their respective layers as indicated by clear distinction of the bottom red and top blue colour distribution shown in Figure 53B. This demonstrates that the flipping manoeuvre was responsible for the mixing.

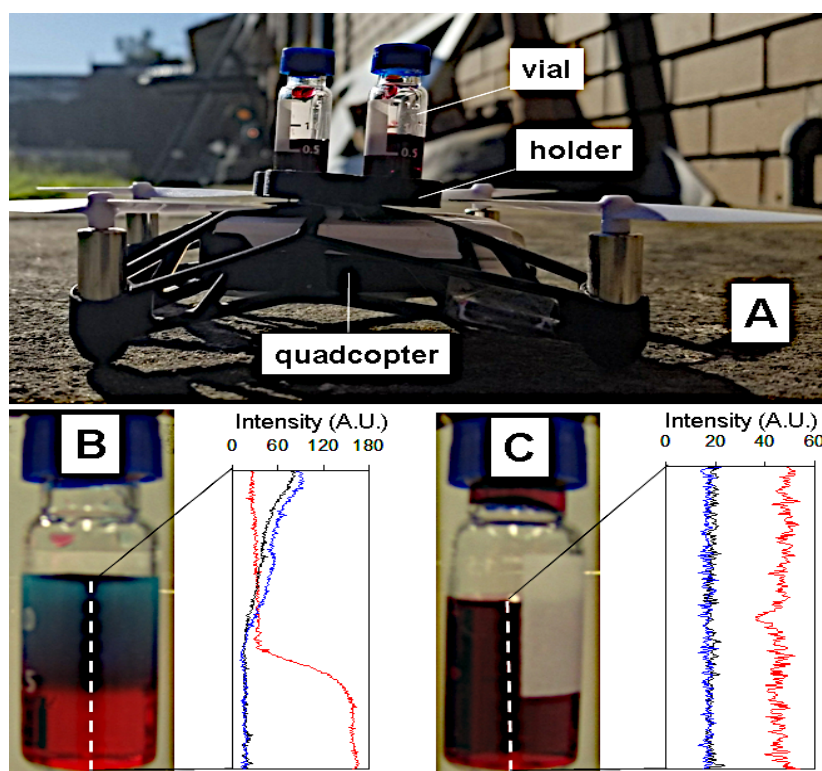


Figure 53: The quadcopter (A) affixed with 3D printed vial holder that is able to house up to four vials for transport. Before transport (B), the vial comprising of water (stained blue) and glycerol (stained red) showed clear segregation between liquid mediums, which was confirmed by the quantitative red, green, and blue colour distribution as derived from the line profile (dashed line). Uniform mixing was achieved upon transport and flipping on the quadcopter (C). Under transport conditions without flipping, the result shown in (B) was obtained.

It should be noted that the mixing mode follows that of a tumbling mode which is usually applied to the preparation of blended granular formulations [338]. This is a gentler approach compared to the method of aggressive shaking applied in vortex mixers which may help avoid causing cell damage [339]. The modification of this quadcopter is also cost effective and energy conserving as it omits any need to incorporate mixing devices onto it. This conservation of energy is advantageous as it can instead increase the range of travel distance which is essential for outdoor sample transport. It is anticipated that other type of manoeuvres can be performed to offer better mixing outcomes which will require hardware modifications to the quadcopter such as tilted rotors [340]. A fully autonomous operation should be developed in order to attain mixing consistency and to reduce frequency of flight crashes.

5.4.4 Conclusion

The quadcopter has demonstrated the ability to safely transport and mix samples using the simple flip manoeuvre feature. The mixing was able to produce a homogenous sample with uniform distribution. The flipping manoeuvre adapts a tumbling method which provides gentler mixing and prevents cell damage. The method of quadcopter modification is more cost effective and energy conserving. This promises to advance the timeliness and sample quality aspect in the transport of biochemical specimens for laboratory analysis.

Results of this work were reported in the paper (KATARIYA, M., CHUNG, D. C. K., MINIFE, T., GUPTA, H., **ZAHIDI, A. A. A.**, LIEW, O. W. & NG, T. W. 2018. Drone inflight mixing of biochemical samples. *Analytical Biochemistry*, 545, 1-3) attached in Appendix F.

5.5 Centrifugation with UAV (Blood-Milk)

5.5.1 Introduction

Controlling pre-analytical errors arising from sample handling and processing can help deliver more accurate test results that advances optimal medical care. When working with whole blood samples, separation of serum and plasma from contact with the cell components within a given time frame is necessary. This is due the test analyte levels being influenced by the time between collection and centrifugation [341]. Cellular components that are released by cell lysis may contaminate the serum that are not centrifuged within 60 minutes from collection [342]. In addition, some plasma-based assays require prompt centrifugation to prevent increased analyte levels as a result of platelet activation and degranulation [343]. Timeliness and cost are the two vital factors governing the transport of samples to the laboratory [344] to ensure sample viability.

It would be beneficial to use autonomous schemes such as drones which have recently been investigated for field biological specimen delivery [345]. Although drones can be subjected to malfunctions, more durable technologies are being developed to subdue them [346]. Drones can conveniently access remote venues and avoid in traffic-congested urban environments. The prospects of performing en-route mixing and even centrifugation is appealing as this will reduce the pre-analytical time at the destination laboratory and could significantly improve the timeliness aspect.

It would be unfeasible to attach a centrifuge device onto a typical quadcopter to transport and perform centrifugation in tandem due to the payload constraints. Instead, it would be more viable to adapt the propeller blades of quadcopters to perform the centrifugation of samples stored in capillary tubes. It is convenient to collect and store samples such as blood and milk in capillary tubes due to its ability to induce the self-filling of liquid [347, 348]. During flight, these propellers can spin up to 15,000 revolutions per minute (RPM). In studies conducted by Pearson [349], this speed was found sufficient to separate plasma from blood cell components held in glass capillary tubes. This section elaborates the functions of quadcopter aside from transporting samples and highlights the main challenges of achieving (a) unchanged drone flight

characteristics with adaptation of the propellers, (b) secure attachments of components despite the forces developed from high speed spinning, and (c) convenient installation and removal of the sample-containing capillary tubes.

5.5.2 Materials and Methodology

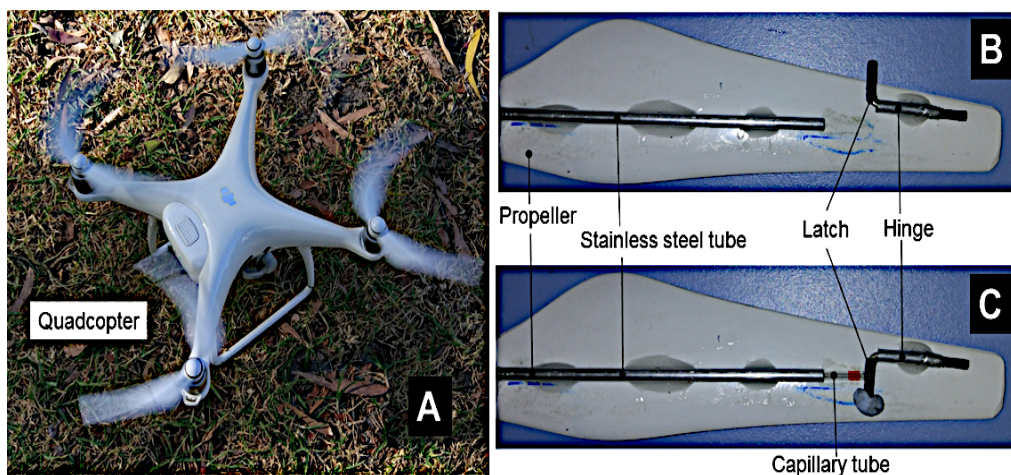


Figure 54: The propellers of the quadcopter (A) were adapted with stainless-steel tube and hinge affixed by strong adhesive on them (B) to allow en-route centrifugation of samples in capillary tubes. After the capillary tube was inserted into the stainless-steel tube (C), a bent rod that acts as a latch was moved to secure the capillary tube in place.

The quadcopter used was a DJI Phantom 4 Pro with a mass of 1388 g and diagonal length of 350 mm without the propellers (Figure 54A). It is powered by a 5870 mAh lithium battery and flights were controlled using a remote controller that supports smartphone and tablet interface. Each of the four (removable) propellers, were modified to incorporate a stainless-steel tube that was able to hold standard 75 μ L glass capillary tubes (Hirshmann). The fixture (Figure 54B and C) comprised of a hollow stainless-steel tube affixed using strong adhesive (Araldite Ultra Clear) rated at 12–15 MPa to the top surface of the propeller to fulfil the requirements (a)-(c) mentioned previously. A bent rod served to function like a latch which is located by a hinge and secured by adhesive to the propeller. This latch holds the capillary tube in place after it was placed into the steel tube. An initial series of tests notwithstanding standard manoeuvres were

conducted with the quadcopter to ensure that the fixture remained securely attached. There was a tendency for the propellers to flex since they were rotated at high speed which leads to potential failure by curved delamination [350].

The application of adhesives at three spots (Figure 54B & C) instead of along the full length of the stainless-steel tube was found effective in preventing this. After confirming that fixture was secure, tests were conducted using non-homogenized milk and blood samples. Blood samples was sourced from a healthy 34-year-old male volunteer with consent, was drawn directly into the capillary tube following finger prick with a lancet. The capillary tubes containing samples were sealed using a sealing clay (Hirshmann) to prevent any sample losses during centrifugation. In the test, the capillary tubes were spun for a total of 10 minutes using the adapted propellers. The tube was removed after specific time intervals to analyse the separation into regions containing red blood cells, buffy coat, and plasma. The tests were repeated with milk samples with a total spin time of 35 minutes. The tube was removed after specific time intervals to analyse the separation of milk.

5.5.3 Results & Discussion

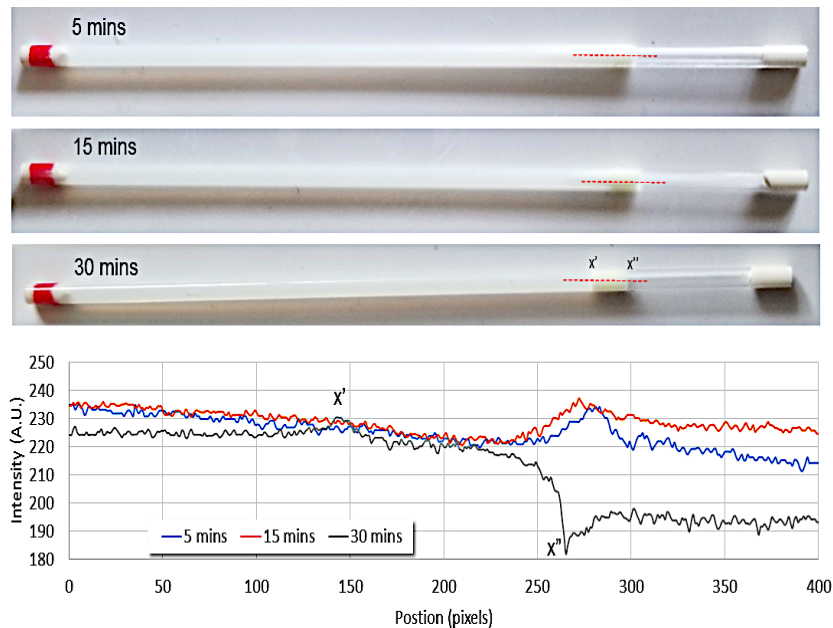


Figure 55: A non-homogeneous milk sample in a capillary tube when centrifuged developed a cream layer. Line plots were taken along the dashed red lines to analyse the cream layer. The separation is indicated by the positions marked x' and x'' and became sufficiently distinct after 30 minutes centrifugation.

Milk fat consists of fat globules which are primarily composed of a globule of triglyceride with a lipid bilayer membrane surrounding it. This membrane is similar to the apical membrane of the epithelial cells. Milk fat is typically secreted from mammary these epithelial cells. The lipid bilayer membrane helps to stabilize the fat globules in an emulsion within the aqueous environment of milk. When raw original feed milk is centrifuged, the fat component is displaced to develop a cream layer since the lipid has a lower buoyant density than water. Although this cream portion becomes visible after 5 minutes of centrifugation, it was found that 30 minutes of centrifugation with the quadcopter was required to achieve good separation (see Figure 55). In order to quantify the separation, a line profile plot (based on brightness level) feature in ImageJ was used to analyse the cream layer.

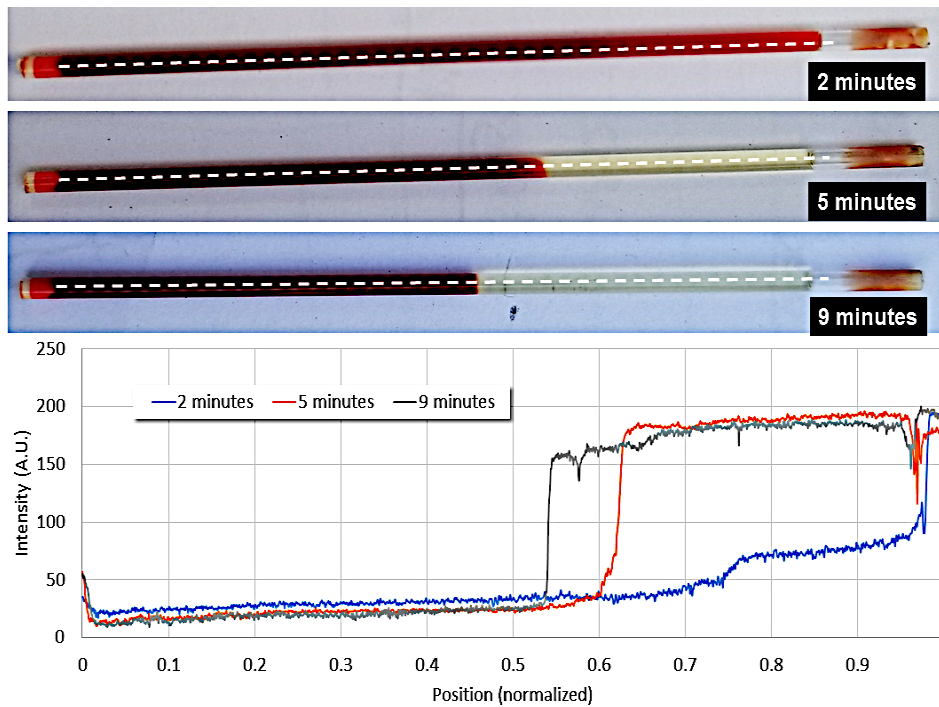


Figure 56: A human blood sample in a capillary tube when centrifuged developed separation into regions containing red blood cells, buffy coat, and plasma. Although analysis of line plots taken along the dashed white lines indicate separation becomes sufficiently distinct after only 2 minutes centrifugation, it was necessary to extend the centrifuge time longer to ensure that a complete process was achieved.

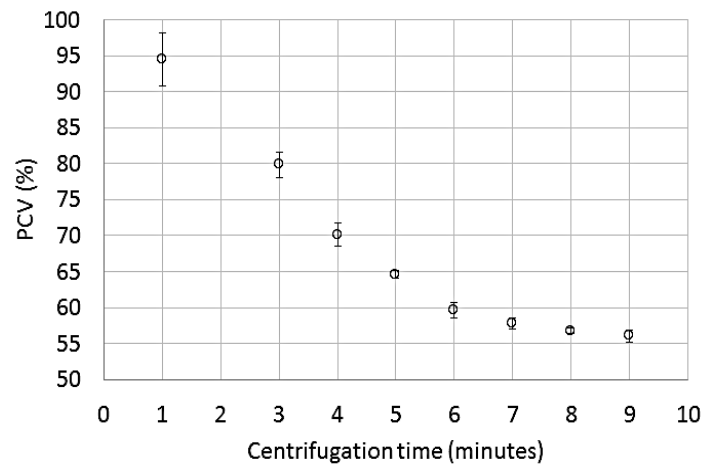


Figure 57: Calculations of the packed cell volume (PCV) as a function of centrifugation time from 5 blood samples. It can be seen that centrifugation of at least 8 minutes is needed to complete the separation process.

Figure 56 shows that component separations were distinctive after 5 minutes of centrifugation. However, longer centrifugation is necessary to pellet the cells and obtain

good yields of plasma. Packed Cell Volume (PCV) is the ratio of the volume occupied by the red blood cells to the volume of the whole blood by percentage which can be used as an indicator. From the plot in Figure 57, this value stabilizes after 8 minutes of centrifugation. Thus, the process is highly repeatable since there was low scatter in data (from 5 runs) after 8 minutes. It is also probable to use smaller capacity batteries (lighter and takes a shorter time to recharge) since the processing time is relatively short. It is recognized that there is a potential for safety threat such that possible breakage of these fragile glass capillary tubes may cause harm or infection from blood-borne pathogens. The breakage of this tube is likely to occur when applying some force to one end of the tube when inserting into the sealing clay [351] or perhaps during centrifugation. Nevertheless, after conducting many countless hours of tests, there was no observation of capillary tube breakage occurring during centrifugation with the quadcopter. Nonetheless, plastic capillary tubes can be used as a safety precaution where previous studies have revealed similar performance characteristics with glass capillary tubes [352]. Another alternative would be to wrap the glass capillary tubes in puncture-resistant film.

There are several practical advantages from using this en-route centrifugation approach. Firstly, there is prospective to use this approach for milk samples to advance human lactation investigations [353]. The deaths of 1.4 million and 10% of disease burden in less than 5 years old children were found to be caused by sub-optimal breastfeeding, especially non-exclusive breastfeeding in the first six months after birth [354]. The risks for this are even higher in remote areas where there is limited access to healthcare services [355]. Additionally, early detection of human immunodeficiency virus (HIV) can be done via paediatric blood tests screening that is conducted exclusively using capillary tube collection [356]. Although perinatal HIV is almost eradicated in high-income countries, the disease is highly prevalent in remote sub-Saharan African and Asian communities [357]. The method of modifying the quadcopter's original propellers for centrifugation, instead of substituting them with alternative fixtures [358], allows for the process to be conducted in tandem while transporting samples which improves the timeliness of pre-analytical sample processing. It is important for the quadcopter propellers to attain high thrust coefficients whilst not failing in the process. Thus, requires a careful design as well as thorough

testing analysis in order to prevent costly repercussions that may from flight crashes [359].

5.5.4 Conclusion

The modification of the original propellers of a drone to hold capillary tubes detailed in this experiment was found to satisfy all the requirements (a) of unchanged drone flight characteristics, (b) able to secure attachments of components despite the forces developed from high speed spinning, and (c) provide convenient installation and removal of the sample-containing capillary tubes. This method is different to substituting the propeller of the drone with a centrifuging device that holds fluid samples. At least 30 minutes of centrifugation was required to achieve distinct separation of non-homogenized milk into its creamy component while only 8 minutes was required to separate human blood into red blood cells, buffy coat, and plasma. This approach can help progress towards achieving optimal medical care through improved timeliness in diagnosis procedures requiring centrifugation and supplements en-route mixing ability of quadcopters previously mentioned in Section 5.4.

Results of this work were reported in the paper (KATARIYA, M., CHUNG, D. C. K., MINIFIE, T., GUPTA, H., **ZAHIDI, A. A. A.**, LIEW, O. W. & NG, T. W. 2018. Note: Biochemical samples centrifuged in-flight on drones. *Review of Scientific Instruments*, 89, 106102) attached in Appendix G.

5.6 Optical Characterization in the Thermal Immobilisation of BSA

5.6.1 Introduction

Bovine serum albumin (BSA) is a globular protein that is widely used in molecular biology, biochemistry and therapeutic applications because of its stability, lack of interference in many biochemical reactions, easy availability and relatively low

cost. BSA is commonly used as a protein and enzyme stabilizers against thermal inactivation [360]. PCR amplification is a technique for applications in cloning, gene expression studies, genetic analyses and diagnostics which can be enhanced using BSA and also glycerol [199, 200]. The function of BSA as a stabiliser can be optimized through investigation of thermal characteristics especially when applied in biochemical processes in the form of moveable drops on surfaces. The feasibility of BSA in the water-glycerol mixtures used were investigated in relation to extreme temperature changes where the findings will be useful for applications such as enhancing PCR amplifications [360].

5.6.2 Materials and Methodology

Materials

0.1 g of BSA lyophilized powder of $\geq 96\%$ purity (Sigma Aldrich) was weighed in using an electronic balance and transferred into an Eppendorf tube. 2.5 mL of distilled water was then pipetted into the tube and thoroughly mixed using a vortex mixer at low power to create 4% wt of BSA solution. 900 μL of 0%-100% water-glycerol mixtures were prepared in separate Eppendorf tubes. 6 μL of the BSA solution was pipetted into a quartz cuvette together with 294 μL of distilled water (0% water-glycerol). The two mixtures were mixed thoroughly using the vortex mixer at low power. The pH of the solution was 7.0.

Methods

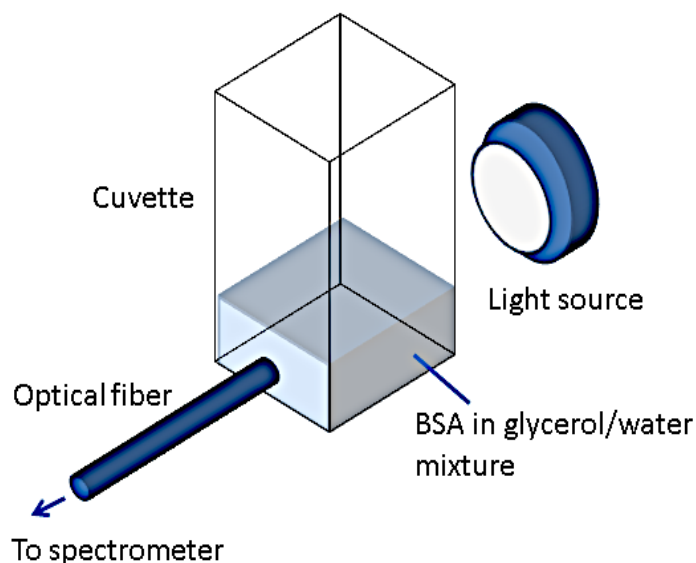


Figure 58: The experimental setup to examine the optical behaviour of BSA in water-glycerol mixtures. Both samples were added to a cuvette and were illuminated using broadband light. An optical fibre connected to a spectrometer was used to collect the transmitted light.

The setup used to conduct the optical measurements is shown in Figure 58. The cuvette containing both the BSA sample and water-glycerol mixture was placed on a

Peltier heater that was driven by a DC power supply with a constant voltage of 6.5V. The temperature on the surface of the Peltier heater was measured using a thermocouple. It was assumed that the thermocouple readings will be indicative of the temperature of the sample due to the relatively slow heating of heater and small volume of sample used. Heating signature of the system was identified by recording the temperature against time for one set of readings. Subsequently, the light spectrum was recorded using an optical fibre connected to a spectrometer (Ocean Optics) at every 5 °C temperature rise starting from 25 °C to 95 °C. The Peltier heater was allowed to cool down to room temperature by switching off the power supply in between readings. The experiment was repeated replacing the distilled water with water-glycerol mixtures ranging from 10% to 100% glycerol. The average relative humidity recorded during the experiment was 55%.

5.6.3 Results & Discussion

Investigation of glycerol influence on the thermal stability of BSA can provide insights to whether protein functionality in gels can be influenced by neutral co-solvents. Turbidity provides an indirect indication of aggregation. Therefore, the investigation was conducted by measuring the level of turbidity through calculating its absorbance. The reference intensity, I_0 was determined for a wavelength of light that passes through the sample at its original state into the spectrometer. Assuming adherence to the Beer-Lambert law such that it corresponds to the state of turbidity of the sample, the absorbance was calculated using Equation (35) using any intensity I that was subsequently measured.

$$A = \log_{10} \left(\frac{I_0}{I} \right) \quad (35)$$

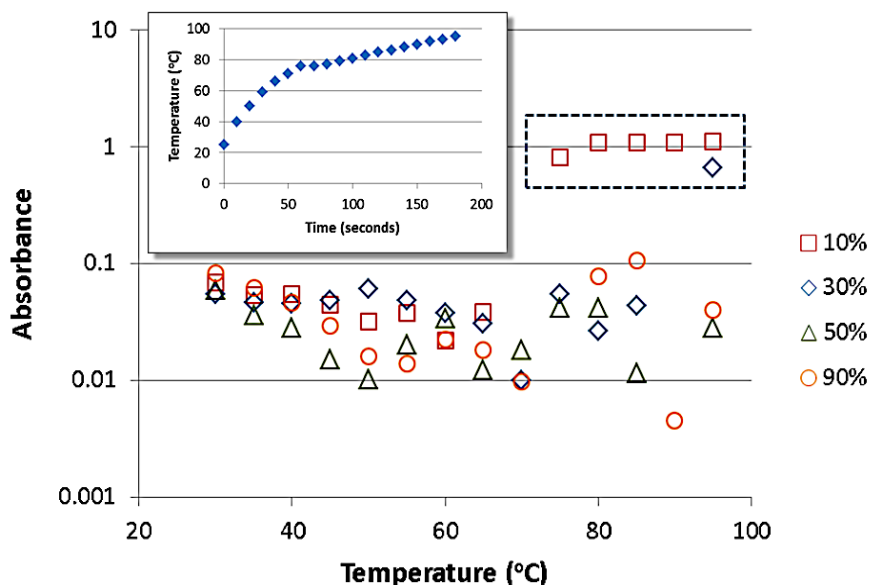


Figure 59: Plots of the absorbance changes in BSA dissolved in solutions containing varying water-glycerol compositions when heated from 25 °C to 95 °C. When aggregation occurs in response to temperature, the sample undergoes significant absorbance (at 600 nm) increase (see points grouped by dashed box). The inset graph indicates the heating rate of the samples.

The reference intensity, I_0 was the recorded intensity value at 25 °C. The results in Figure 59 shows the levels of absorbance recorded at 600 nm in relation to temperature as it was raised with time. In addition, the inset of Figure 59 shows the temperature-time trend during heating. With 10% glycerol, there is significant increase in turbidity observed when the temperature reached 75 °C. With 30% glycerol, the temperature corresponding to this increase was shifted to 95 °C. For mixtures with glycerol content above 50% no increase in turbidity was observed even when the temperature increased up to 95 °C. These results suggest the thermal stabilizing effect that increasing glycerol content can offer for BSA. However, it is important to note that both the size and concentration of protein aggregates formed can influence turbidity. Since the aggregate size may have changed with time and solution composition, cautions should be taken when using the results here to deduce the aggregation rate. These findings provide support in the design process of biochemical devices that

requires use of droplet movement as well as mass and heat transfer modes in applications as mentioned in Section 3.2.

5.6.4 Conclusion

Turbidity measurements indicate that higher glycerol content can be used to improve thermal stability. 50% glycerol content is sufficient to eliminate turbidity effects arising from heating. The findings from this experiment can help provide support in the feasibility for design of biochemical devices that applies the use of droplet movement as well as mass and heat transfer modes.

Results of this work were reported in the paper (ZAHIDI, A. A. A., CHEONG, B. H. P., HUYNH, S. H., VUONG, T., LIEW, O. W. & NG, T. W. 2015. Glycerol-water sessile drop elongation on PTFE inclines in relation to biochemical applications. *Colloids and Surfaces a-Physicochemical and Engineering Aspects*, 486, 21-28) attached in Appendix A.

5.7 Chapter Summary

This chapter discussed the many useful applications of viscous liquids in various biochemical and medical industry. Glycerol, blood and milk were the viscous liquids chosen for the purpose of investigating its characteristic, functionality and benefits. It was shown that aside from the known advantageous properties, glycerol managed to successfully capture *Drosophila* flies via the incorporation of a vinegar as an attractant and able to immobilize the flies while maintaining a living captive specimen. Moreover, glycerol was shown to be used as a liquid lens and successfully allowed magnification of actively moving specimens for microscopic observations. These applications were intended for preliminary open-field investigations by allowing specimens to be examined on-site, thus possibly removing the necessity for specimen collection for laboratory-based analysis. In addition, glycerol showed protein thermal stabilising capabilities through elimination of BSA turbidity that was a result of sample

heating which supports in the feasibility for design of biochemical devices that applies the use of droplet movement as well as mass and heat transfer modes. Since human blood and milk are vital sources in the medical field and scarce in remote areas, efforts were taken to improve the cost and timeliness factor to achieve optimal medical care. Since UAV are able to access remote areas and avoid urban traffic congestions, the new approach of using UAV to conduct en-route mixing and centrifugation of blood and milk samples in tandem with transporting the samples showed prospects in achieving this purpose.

6 OVERALL CONCLUSIONS

This project has been successful in achieving the objectives outlined. In terms of the experimentation on liquid stability under various physical conditions, it has been found that understanding of drop mechanics helps provides useful information for the design of transport systems as a constant inclined angle can be achieved to prevent droplet movement regardless of its mixture concentration. The results revealed that the wetting characteristics was influenced by the interaction of fluid with both the solid as well as the air entrapped within the surface microstructures and the contact angle hysteresis does not have any influence on the slip angle. Although Type III droplet condition (drop separates into mother and daughter drop) arising from the use of scribed transparency microplates should be avoided, it was found that it could instead provide feasibility of improved mixing during transportation. Furthermore, it was found that resistance to perturbation from impact is governed by viscosity of liquid where the resistance to perturbation increases with increasing viscosity. The experimental set up for drop dislodgement using gravitational impact shows favourable characteristics that does not produce neither daughter drops nor air entrainment into drops. This provides the ability for inspection of bubble presence prior to using the droplet for other applications.

With good knowledge gained on liquid stability, efforts to study liquid processing factors and its application problems has uncovered a way to eliminate the edge effect for standard microplates. This is achieved through a two-temperature heating mode, wherein heat losses at the side is lower compared to at the bottom (higher temperature). Transparency microplates were found to inherently possess immunity to the edge effect problem. The use of these transparencies will greatly improve cost effectiveness since they are cheap and easy to source. From the investigations conducted for bubble formation while dispensing viscous liquids from tips, it was found that the bubble presence will likely affect the image fidelity of liquid lens and also visibility of insects in immobilizing mediums

Chapter 6: Overall Conclusions

Finally, useful applications of viscous liquids in biomedical experimentation has been achieved. This include the use of glycerol liquid droplet in a three-fold function. Firstly, as a medium to capture via the incorporation of a chemical attractant. Next, as an immobilizing agent for actively moving specimens. Finally, to allow magnification for preliminary microscopic observation in field investigations. 30% water-glycerol concentration was found optimum in field applications as it is not too viscous or sticky that will raise dispensing problems but provide enough viscosity for trapping and also immobilization. Consequently, glycerol was able to prevent aggregation by increasing thermal stability of protein solutions such as BSA. It was found that 50% glycerol content is sufficient to eliminate turbidity effects arising from heating. These findings can help provide support in the feasibility for design of biochemical devices that applies the use of droplet movement as well as mass and heat transfer modes.

REFERENCES

1. Roger, H.P., *Protein denaturation*. Nature, 1979. **279**(5716): p. 824.
2. Arakawa, T., et al., *Factors affecting short-term and long-term stabilities of proteins*. Advanced Drug Delivery Reviews, 1993. **10**(1): p. 1-28.
3. Jaenicke, R., *Protein stability and molecular adaptation to extreme conditions*, in *EJB Reviews 1991*, P. Christen and E. Hofmann, Editors. 1992, Springer Berlin Heidelberg. p. 291-304.
4. Tworoger, S.S. and S.E. Hankinson, *Collection, Processing, and Storage of Biological Samples in Epidemiologic Studies: Sex Hormones, Carotenoids, Inflammatory Markers, and Proteomics as Examples*. Cancer Epidemiology Biomarkers & Prevention, 2006. **15**(9): p. 1578-1581.
5. Hellkamp, J., A. Carl, and K.P. Kohse, *Stability of Packed Red Blood Cell Units during Mechanical Transport Using a Modern Pneumatic Tube System*. Transfusion Medicine and Hemotherapy, 2002. **29**(5): p. 259-264.
6. Argos, P., et al., *Thermal stability and protein structure*. Biochemistry, 1979. **18**(25): p. 5698-5703.
7. Fágáin, C.Ó. and R. O'Kennedy, *Functionally-stabilized proteins — A review*. Biotechnology Advances, 1991. **9**(3): p. 351-409.
8. Elalouf, A., D. Tsadikovich, and S. Hovav, *Optimization of blood sample collection with timing and quality constraints*. Int. Trans. Oper. Res., 2018. **25**(1): p. 191-214.
9. Nge, P.N., C.I. Rogers, and A.T. Woolley, *Advances in microfluidic materials, functions, integration, and applications*. Chemical reviews, 2013. **113**(4): p. 2550.
10. Livak-Dahl, E., I. Sinn, and M. Burns, *Microfluidic Chemical Analysis Systems*. Annu. Rev. Chem. Biomol. Eng., 2011. **2**(1): p. 325-353.
11. Samiei, E., M. Tabrizian, and M. Hoorfar, *A review of digital microfluidics as portable platforms for lab-on a-chip applications*. Lab Chip, 2016. **16**(13): p. 2376-2396.
12. Shen, H.-H., et al., *EWOD microfluidic systems for biomedical applications*. Microfluidics and Nanofluidics, 2014. **16**(5): p. 965-987.
13. Vuong, T., et al., *Drop transfer between superhydrophobic wells using air logic control*. Lab on a Chip, 2015. **15**(4): p. 991-995.

References

14. Chaigneau, M., et al., *Plasmon resonance microsensors for droplet analysis*. Optics letters, 2007. **32**(16): p. 2435.
15. Bechhoefer, J., et al., *An Experimental-Study of the Onset of Parametrically Pumped Surface-Waves in Viscous Fluids*. Journal of Fluid Mechanics, 1995. **288**: p. 325-350.
16. Schroll, R.D., et al., *Impact of a viscous liquid drop*. Physical review letters, 2010. **104**(3): p. 034504.
17. Xu, L., *Instability development of a viscous liquid drop impacting a smooth substrate*. Phys. Rev. E, 2010. **82**(2).
18. Zhang, X., R.S. Padgett, and O.A. Basaran, *Nonlinear deformation and breakup of stretching liquid bridges*. Journal of Fluid Mechanics, 1996. **329**: p. 207-245.
19. Pagliaro, M., *The future of glycerol new uses of a versatile raw material*, ed. M. Rossi and C. Royal Society of. 2008, Cambridge: Cambridge : Royal Society of Chemistry.
20. Jahn, D.A., F.O. Akinkunmi, and N. Giovambattista, *Effects of Temperature on the Properties of Glycerol: A Computer Simulation Study of Five Different Force Fields*. Journal of Physical Chemistry B, 2014. **118**(38): p. 11284-11294.
21. da Silva, G.P., M. Mack, and J. Contiero, *Glycerol: A promising and abundant carbon source for industrial microbiology*. Biotechnology Advances, 2009. **27**(1): p. 30-39.
22. Leichus, B.N. and J.S. Blanchard, *Isotopic Analysis of the Reaction Catalyzed by Glycerol Dehydrogenase*. Biochemistry, 1994. **33**(48): p. 14642-14649.
23. Ramesh, K., et al., *A mild and expeditious synthesis of amides from aldehydes using bio glycerol-based carbon as a recyclable catalyst*. Tetrahedron Letters, 2012. **53**(21): p. 2636-2638.
24. Walborg, E.F. and R.S. Lantz, *Separation and Quantitation of Saccharides by Ion-Exchange Chromatography Utilizing Boric Acid/Glycerol Buffers*. Analytical Biochemistry, 1968. **22**(1): p. 123-&.
25. Weinhart, M., T. Becherer, and R. Haag, *Switchable, biocompatible surfaces based on glycerol copolymers*. Chemical Communications, 2011. **47**(5): p. 1553-1555.
26. Deshpande, A., J. Rane, and L. Jathar, *Effect of glycerol on the optical and physical properties of sol-gel glass matrices*. Journal of Sol-Gel Science and Technology, 2009. **49**(3): p. 268-276.
27. Robergs, R.A. and S.E. Griffin, *Glycerol - Biochemistry, pharmacokinetics and clinical and practical applications*. Sports Medicine, 1998. **26**(3): p. 145-167.

References

28. Knight, C., A. Braakhuis, and C. Paton, *The Effect of Glycerol Ingestion on Performance During Simulated Multisport Activity*. Research Quarterly for Exercise and Sport, 2010. **81**(2): p. 233-238.
29. Meng, F.-G., et al., *Osmophobic Effect of Glycerol on Irreversible Thermal Denaturation of Rabbit Creatine Kinase*. Biophysical Journal, 2004. **87**(4): p. 2247-2254.
30. Rariy, R.V., et al., *Thermobarostability of α -chymotrypsin in reversed micelles of aerosol OT in octane solvated by water-glycerol mixtures*. Biotechnology and Bioengineering, 1998. **57**(5): p. 552-556.
31. Esposito, A., et al., *Influence of Glycerol on the Structure and Thermal Stability of Lysozyme: A Dynamic Light Scattering and Circular Dichroism Study*. The Journal of Physical Chemistry B, 2009. **113**(51): p. 16420-16424.
32. Gekko, K. and S.N. Timasheff, *Mechanism of protein stabilization by glycerol: preferential hydration in glycerol-water mixtures*. Biochemistry, 1981. **20**(16): p. 4667-4676.
33. Baier, S.K., E.A. Decker, and D.J. McClements, *Impact of glycerol on thermostability and heat-induced gelation of bovine serum albumin*. Food Hydrocolloids, 2004. **18**(1): p. 91-100.
34. Bellavia, G., et al., *How Does Glycerol Enhance the Bioprotective Properties of Trehalose? Insight from Protein–Solvent Dynamics*. The Journal of Physical Chemistry B, 2014. **118**(30): p. 8928-8934.
35. Demuth, D., et al., *Effects of solvent concentration and composition on protein dynamics: ^{13}C MAS NMR studies of elastin in glycerol–water mixtures*. Biochimica et Biophysica Acta (BBA) - Proteins and Proteomics, 2015. **1854**(8): p. 995-1000.
36. Wang, W., *Instability, stabilization, and formulation of liquid protein pharmaceuticals*. International Journal of Pharmaceutics, 1999. **185**(2): p. 129-188.
37. von Bomhard, A., et al., *Cryopreservation of Endothelial Cells in Various Cryoprotective Agents and Media - Vitrification versus Slow Freezing Methods.(Report)*. 2016. **11**(2).
38. Werck-Reichhart, D., et al., *Glycerol allows low-temperature phase separation of membrane proteins solubilized in triton X-114: Application to the purification of plant cytochromes P-450 and b5*. Analytical Biochemistry, 1991. **197**(1): p. 125-131.
39. Yadav, S., S.J. Shire, and D.S. Kalonia, *Viscosity Analysis of High Concentration Bovine Serum Albumin Aqueous Solutions*. Pharmaceutical Research, 2011. **28**(8): p. 1973-1983.

References

40. Monkos, K., *Viscosity of bovine serum albumin aqueous solutions as a function of temperature and concentration*. International Journal of Biological Macromolecules, 1996. **18**(1): p. 61-68.
41. Bhamore, J.R., et al., *Tuning of gold nanoclusters sensing applications with bovine serum albumin and bromelain for detection of Hg(2+) ion and lambda-cyhalothrin via fluorescence turn-off and on mechanisms*. Anal Bioanal Chem, 2018. **410**(11): p. 2781-2791.
42. Nakane, Y., et al., *Bovine serum albumin-coated quantum dots as a cytoplasmic viscosity probe in a single living cell*. Analytical Methods, 2012. **4**(7): p. 1903-1905.
43. Liu, B. and L. Wang, *Fabrication of Bovine Serum Albumin Nanoparticles Loaded with Flavonoid Dyes for Long-term Bioimaging Applications*. Chemistry Letters, 2016. **45**(9): p. 1075-1077.
44. Pindrus, M.A., et al., *Effect of Aggregation on the Hydrodynamic Properties of Bovine Serum Albumin*. Pharmaceutical Research, 2017. **34**(11): p. 2250-2259.
45. Weiss, C. and W. Jelkmann, *Functions of the Blood*, in *Human Physiology*, R.F. Schmidt and G. Thews, Editors. 1989, Springer Berlin Heidelberg: Berlin, Heidelberg. p. 402-438.
46. Dormandy, J.A. *Measurement of Whole-blood Viscosity*. 1981. London: Springer London.
47. Irace, C., et al., *Blood viscosity but not shear stress associates with delayed flow-mediated dilation*. European Journal of Applied Physiology, 2015. **115**(4): p. 747-753.
48. Kim, B.J., et al., *Micro-Viscometer for Measuring Shear-Varying Blood Viscosity over a Wide-Ranging Shear Rate*. Sensors (Basel), 2017. **17**(6).
49. Pop, G.A.M., et al., *On-line blood viscosity monitoring in vivo with a central venous catheter, using electrical impedance technique*. Biosensors and Bioelectronics, 2013. **41**: p. 595-601.
50. Chen, G., et al., *Regulation of blood viscosity in disease prevention and treatment*. Chinese Science Bulletin, 2012. **57**(16): p. 1946-1952.
51. Yu, Z.T.F., et al., *Centrifugal microfluidics for sorting immune cells from whole blood*. Sensors and Actuators B: Chemical, 2017. **245**: p. 1050-1061.
52. Vonk, A.B., et al., *Residual blood processing by centrifugation, cell salvage or ultrafiltration in cardiac surgery: effects on clinical hemostatic and ex-vivo rheological parameters*. Blood Coagul. Fibrinolysis, 2012. **23**(7): p. 622-628.

References

53. Bernhardt, M., et al., *Detection of bacteria in blood by centrifugation and filtration*. Journal of Clinical Microbiology, 1991. **29**(3): p. 422.
54. Sun, Y. and P. Sethu, *Low-stress Microfluidic Density-gradient Centrifugation for Blood Cell Sorting*. Biomedical Microdevices, 2018. **20**(3): p. 77.
55. Tao, R. and K. Huang, *Reducing blood viscosity with magnetic fields*. Phys. Rev. E, 2011. **84**(1).
56. Phelan, J.P. and C.G. Bloore, *Viscosity and Non-Newtonian Behaviour of Concentrated Milk and Cream AU - Morison, Ken R*. International Journal of Food Properties, 2013. **16**(4): p. 882-894.
57. Stephani, R., et al., *Evaluation of the synergistic effects of milk proteins in a rapid viscosity analyzer*. Journal of Dairy Science, 2015. **98**(12): p. 8333-8347.
58. Velez-Ruiz, J. and G. Barbosa-Canovas, *Rheological properties of concentrated milk as a function of concentration, temperature and storage time*. J. Food Eng., 1998. **35**(2): p. 177-190.
59. Ho, Q.T., et al., *Effect of pH and heat treatment on viscosity and heat coagulation properties of milk protein concentrate*. International Dairy Journal, 2018. **85**: p. 219-224.
60. Zisu, B., M. Schleyer, and J. Chandrapala, *Application of ultrasound to reduce viscosity and control the rate of age thickening of concentrated skim milk*. International Dairy Journal, 2013. **31**(1): p. 41-43.
61. Troch, T., et al., *Cow milk coagulation: process description, variation factors and evaluation methodologies. A review*. Biotechnologie, Agronomie, Société et Environnement, 2017. **21**(4): p. 276-287.
62. Usov, N.A. and B.Y. Liubimov, *Dynamics of magnetic nanoparticle in a viscous liquid: Application to magnetic nanoparticle hyperthermia*. Journal of Applied Physics, 2012. **112**(2).
63. Kim, B.H., et al., *Effect of fluid viscosity on the liquid-feeding flow phenomena of a female mosquito*. Journal of Experimental Biology, 2013. **216**(6): p. 952-959.
64. Gadkari, S. and R. Thaokar, *Stability of immersed viscous liquid threads under electric field*. International Journal of Engineering Science, 2013. **62**: p. 9-21.
65. Cox, R., et al., *Characteristics of laterally vibrating resonant microcantilevers in viscous liquid media*. Journal of Applied Physics, 2012. **111**(1).
66. Dyre, J.C., *Solidity of viscous liquids*. Physical Review E, 1999. **59**(2): p. 2458-2459.

References

67. Martín, M., F.J. Montes, and M.A. Galán, *Mass transfer rates from bubbles in stirred tanks operating with viscous fluids*. Chemical Engineering Science, 2010. **65**(12): p. 3814-3824.
68. Wang, X., et al., *Energy Dissipation Rates of Newtonian and Non-Newtonian Fluids in a Stirred Vessel*. Chemical Engineering & Technology, 2014. **37**(9): p. 1575-1582.
69. Kido, L., M. Muller, and C. Russel, *The effect of viscosity on the kinetics of redox reactions in highly viscous silicate liquids*. Journal of Chemical Physics, 2012. **136**(22).
70. Lacey, M., *The air spora a manual for catching and identifying airborne biological particles*, ed. J.S. West and SpringerLink. 2006, Dordrecht: Dordrecht : Springer.
71. Zhang, X., et al., *Controllable and switchable capillary adhesion mechanism for bio-adhesive pads: Effect of micro patterns*. Chinese Science Bulletin, 2009. **54**(10): p. 1648-1654.
72. Favi, P.M., et al., *Inspiration from the natural world: from bio-adhesives to bio-inspired adhesives*. Journal of Adhesion Science and Technology, 2014. **28**(3-4): p. 290-319.
73. Heuzeroth, F., et al., *Viscous force — An important parameter for the modeling of deep bed filtration in liquid media*. Powder Technology, 2015. **283**(0): p. 190-198.
74. Santelices, B. and D. Aedo, *Evaluating substances that facilitate algal spore adhesion*. Hydrobiologia, 1999. **399**: p. 241-246.
75. Clauß, M., A.C. Springorum, and J. Hartung, *Effective Collection of Airborne Micro-Organisms by Direct Impaction on Silicone Sealants—Comparison of Different Adherent Surfaces*. Aerosol Science and Technology, 2010. **44**(11): p. 993-1004.
76. Thomas, G., *An Adhesive Surface Sampling Technique for Airborne Viruses*. Journal of Hygiene-Cambridge, 1970. **68**(2): p. 273-&.
77. Alcázar, P., et al., *A new adhesive for airborne pollen sampling in Spain*. Aerobiologia, 2003. **19**(1): p. 57-61.
78. Perrin, P.W., *Spore Trapping under Hot and Humid Conditions*. Mycologia, 1977. **69**(6): p. 1214-1218.
79. Sime, A.D., L.L. Abbott, and S.P. Abbott, *A mounting medium for use in Indoor Air Quality spore-trap analyses*. Mycologia, 2002. **94**(6): p. 1087-1088.

References

80. Kapyła, M., *Adhesives and Mounting Media in Aerobiological Sampling*. Grana, 1989. **28**(3): p. 215-218.
81. Finn, D., et al., *Sampling artifacts from the use of denuder tubes with glycerol based coatings in the measurement of atmospheric particulate matter*. Environmental Science & Technology, 2001. **35**(1): p. 40-44.
82. Bhat, M.M. and A.H. Rajasab, *Efficiency of Vertical Cylinder Spore Trap and Seven Day Volumetric Burkard Spore Trap in Monitoring Airborne Pollen and Fungal Spores*. Grana, 1989. **28**(2): p. 147-153.
83. Wenzel, R.N., *Resistance of solid surfaces to wetting by water*. Industrial and Engineering Chemistry, 1936. **28**: p. 988-994.
84. LIU, M.B., et al., *MODELING OF CONTACT ANGLES AND WETTING EFFECTS WITH PARTICLE METHODS*. International Journal of Computational Methods, 2011. **08**(04): p. 637-651.
85. Verheijen, H.J.J. and M.W.J. Prins, *Contact angles and wetting velocity measured electrically*. Review of Scientific Instruments, 1999. **70**(9): p. 3668-3673.
86. Vedantam, S. and M.V. Panchagnula, *Constitutive modeling of contact angle hysteresis*. Journal of Colloid and Interface Science, 2008. **321**(2): p. 393-400.
87. Wang, X.-S., et al., *A generalized Young's equation for contact angles of droplets on homogeneous and rough substrates*. Journal of Adhesion Science and Technology, 2013. **28**(2): p. 161-170.
88. McHale, G., N.J. Shirtcliffe, and M.I. Newton, *Contact-Angle Hysteresis on Super-Hydrophobic Surfaces*. Langmuir, 2004. **20**(23): p. 10146-10149.
89. Valsamis, J.-B., M.D. Volder, and P. Lambert, *Physical Background*, in *Surface Tension in Microsystems: Engineering Below the Capillary Length*, P. Lambert, Editor. 2013, Springer Berlin Heidelberg: Berlin, Heidelberg. p. 3-16.
90. Arjmandi-Tash, O., et al., *Kinetics of Wetting and Spreading of Droplets over Various Substrates*. Langmuir, 2017. **33**(18): p. 4367-4385.
91. Gołębek, M. and L. Hołysz, *Changes in wetting and energetic properties of glass caused by deposition of different lipid layers*. Applied Surface Science, 2010. **256**(17): p. 5463-5469.
92. Szymczyk, K., et al., *Wettability, adhesion, adsorption and interface tension in the polymer/surfactant aqueous solution system. I. Critical surface tension of polymer wetting and its surface tension*. Colloids and Surfaces A: Physicochemical and Engineering Aspects, 2012. **402**(0): p. 132-138.

References

93. Campos, R., et al., *Fluoroalkyl-Functionalized Silica Particles: Synthesis, Characterization, and Wetting Characteristics*. Langmuir, 2011. **27**(16): p. 10206-10215.
94. Leese, H., et al., *Wetting behaviour of hydrophilic and hydrophobic nanostructured porous anodic alumina*. Colloids and Surfaces A: Physicochemical and Engineering Aspects, 2013. **420**(0): p. 53-58.
95. Whyman, G. and E. Bormashenko, *How to Make the Cassie Wetting State Stable?* Langmuir, 2011. **27**(13): p. 8171-8176.
96. Rosen, M.J. and L.D. Song, *Superspreading, skein wetting, and dynamic surface tension*. Langmuir, 1996. **12**(20): p. 4945-4949.
97. Sibirev, N.V., M.V. Nazarenko, and V.G. Dubrovskii, *Wetting regime of semiconductor nanowhisker growth: Stability and shape of catalyst droplet*. Technical Physics Letters, 2012. **38**(3): p. 221-224.
98. Dorfler, F., M. Rauscher, and S. Dietrich, *Stability of thin liquid films and sessile droplets under confinement*. Phys. Rev. E, 2013. **88**(1).
99. Nuraje, N., et al., *Superhydrophobic electrospun nanofibers*. Journal of Materials Chemistry A, 2013. **1**(6): p. 1929-1946.
100. Gillies, G., et al., *Contact angles and wetting behaviour of single micron-sized particles*. Journal of Physics-Condensed Matter, 2005. **17**(9): p. S445-S464.
101. Krol, D.J., A. Wymyslowski, and K.N. Allaf, *Adhesion work analysis through molecular modeling and wetting angle measurement*. Microelectronics Reliability, 2015. **55**(5): p. 758-764.
102. Liu, Z.G., et al., *Modeling the Wetting Patterns in Cultivation Substrates under Drip Irrigation*. Journal of Coastal Research, 2015: p. 173-176.
103. Beresnev, I., W. Gaul, and R.D. Vigil, *Thickness of residual wetting film in liquid-liquid displacement*. Physical Review E, 2011. **84**(2).
104. Marino, B.M., et al., *Capillarity effects on viscous gravity spreadings of wetting liquids*. Journal of Colloid and Interface Science, 1996. **177**(1): p. 14-30.
105. Lin, C.-M., P. Neogi, and R.M. Ybarra, *Wetting Kinetics of a Drop on a Horizontal Solid Surface under a Viscous Ambient Liquid*. Industrial & Engineering Chemistry Research, 1998. **37**(1): p. 66-70.
106. Yi-Ling, H., H. Tsung-Yi, and K. Chakrabarty. *On-chip biochemical sample preparation using digital microfluidics*. in *Biomedical Circuits and Systems Conference (BioCAS), 2011 IEEE*. 2011.

References

107. de Gennes, P.-G., F. Brochard-Wyart, and D. Quéré, *Capillarity: Deformable Interfaces*, in *Capillarity and Wetting Phenomena: Drops, Bubbles, Pearls, Waves*. 2004, Springer New York: New York, NY. p. 1-31.
108. Drelich, J. and A. Marmur, *Physics and applications of superhydrophobic and superhydrophilic surfaces and coatings*. Surface Innovations, 2014. **2**(4): p. 211-227.
109. Hao, G.-P., et al., *Design of Hierarchically Porous Carbons with Interlinked Hydrophilic and Hydrophobic Surface and Their Capacitive Behavior*. Chemistry of Materials, 2016. **28**(23): p. 8715-8725.
110. Falde, E.J., et al., *Superhydrophobic Materials for Biomedical Applications*. Biomaterials, 2016. **104**: p. 87-103.
111. Nosonovsky, M. and B. Bhushan, *Superhydrophobic surfaces and emerging applications: Non-adhesion, energy, green engineering*. Current Opinion in Colloid & Interface Science, 2009. **14**(4): p. 270-280.
112. Crawford, R.J. and E.P. Ivanova, *Chapter Two - Natural Superhydrophobic Surfaces*, in *Superhydrophobic Surfaces*, R.J. Crawford and E.P. Ivanova, Editors. 2015, Elsevier: Amsterdam. p. 7-25.
113. Cassie, A.B.D. and S. Baxter, *Wettability of porous surfaces*. Transactions of the Faraday Society, 1944. **40**(0): p. 546-551.
114. Koishi, T., et al., *Coexistence and transition between Cassie and Wenzel state on pillared hydrophobic surface*. Proceedings of the National Academy of Sciences of the United States of America, 2009. **106**(21): p. 8435-8440.
115. Suzuki, S. and K. Ueno, *Apparent Contact Angle Calculated from a Water Repellent Model with Pinning Effect*. Langmuir, 2017. **33**(1): p. 138-143.
116. Kwon, M.H., H.S. Shin, and C.N. Chu, *Fabrication of a super-hydrophobic surface on metal using laser ablation and electrodeposition*. Applied Surface Science, 2014. **288**: p. 222-228.
117. Papadopoulou, S.K., et al., *Superhydrophobic surfaces from hydrophobic or hydrophilic polymers via nanophase separation or electrospinning/electrospraying*. Colloids and Surfaces A: Physicochemical and Engineering Aspects, 2011. **387**(1): p. 71-78.
118. Tsai, P.-S., Y.-M. Yang, and Y.-L. Lee, *Fabrication of Hydrophobic Surfaces by Coupling of Langmuir–Blodgett Deposition and a Self-Assembled Monolayer*. Langmuir, 2006. **22**(13): p. 5660-5665.
119. Kuo, C.-Y., et al., *Fabrication of a high hydrophobic PVDF membrane via nonsolvent induced phase separation*. Desalination, 2008. **233**(1): p. 40-47.

References

120. Balu, B., V. Breedveld, and D.W. Hess, *Fabrication of “Roll-off” and “Sticky” Superhydrophobic Cellulose Surfaces via Plasma Processing*. *Langmuir*, 2008. **24**(9): p. 4785-4790.
121. Raimondo, M., et al., *Superhydrophobic properties induced by sol-gel routes on copper surfaces*. *Applied Surface Science*, 2017. **422**: p. 1022-1029.
122. Jothi Prakash, C.G., C. Clement Raj, and R. Prasanth, *Fabrication of zero contact angle ultra-super hydrophilic surfaces*. *Journal of Colloid and Interface Science*, 2017. **496**: p. 300-310.
123. Tang, P., et al., *Preparation of hydrophobic surface on titanium by micro-rolling and laser diffusion carbonitriding*. *Journal of Wuhan University of Technology-Mater. Sci. Ed.*, 2016. **31**(3): p. 533-537.
124. Yilbas, B.S., et al., *Droplet dynamics on a hydrophobic surface coated with N-octadecane phase change material*. *Colloids and Surfaces A: Physicochemical and Engineering Aspects*, 2018. **546**: p. 28-39.
125. Tian, X., T. Verho, and R.H.A. Ras, *Moving superhydrophobic surfaces toward real-world applications*. *Science*, 2016. **352**(6282): p. 142.
126. Cira, N.J., A. Benusiglio, and M. Prakash, *Vapour-mediated sensing and motility in two-component droplets*. *Nature*, 2015. **519**: p. 446.
127. Shemesh, J., et al., *Stationary nanoliter droplet array with a substrate of choice for single adherent/nonadherent cell incubation and analysis*. *Proceedings of the National Academy of Sciences*, 2014. **111**: p. 11293-11298.
128. Miranda-Fuentes, A., et al., *Developing strategies to reduce spray drift in pneumatic spraying in vineyards: Assessment of the parameters affecting droplet size in pneumatic spraying*. *Science of The Total Environment*, 2018. **616-617**: p. 805-815.
129. Thorsen, T., et al., *Dynamic Pattern Formation in a Vesicle-Generating Microfluidic Device*. *Physical Review Letters*, 2001. **86**(18): p. 4163-4166.
130. Leibacher, I., P. Reichert, and J. Dual, *Microfluidic droplet handling by bulk acoustic wave (BAW) acoustophoresis*. *Lab on a Chip*, 2015. **15**(13): p. 2896-2905.
131. Nguyen, N.-T., et al., *Recent Advances and Future Perspectives on Microfluidic Liquid Handling*. *Micromachines*, 2017. **8**(6): p. 186.
132. Zhao, Y., et al., *Magnetic liquid marbles, their manipulation and application in optical probing*. *Microfluidics and Nanofluidics*, 2012. **13**(4): p. 1-10.

References

133. Lee, K.-M., et al., *Review of Salmonella detection and identification methods: Aspects of rapid emergency response and food safety*. Food Control, 2015. **47(C)**: p. 264-276.
134. Balouiri, M., M. Sadiki, and S.K. Ibnsouda, *Methods for in vitro evaluating antimicrobial activity: A review*. Journal of Pharmaceutical Analysis, 2016. **6(2)**: p. 71-79.
135. Lu, G., et al., *Liquid filling in standard circular well microplates*. Journal of Applied Physics, 2010. **108(12)**.
136. Li, X.Y., et al., *Surface-scribed transparency-based microplates*. Langmuir : the ACS journal of surfaces and colloids, 2013. **29(2)**: p. 849.
137. Cheong, B.H.P., et al., *Scribed transparency microplates mounted on a modified standard microplate*. Analytical Biochemistry, 2014. **458**: p. 40-42.
138. Thompson, B., et al., *High-throughput quantitation of Fc-containing recombinant proteins in cell culture supernatant by fluorescence polarization spectroscopy*. Analytical Biochemistry, 2017. **534**: p. 49-55.
139. Jones, E., S. Michael, and G.S. Sittampalam, *Basics of assay equipment and instrumentation for high throughput screening*. 2016.
140. Mehling, M. and S. Tay, *Microfluidic cell culture*. Current Opinion in Biotechnology, 2014. **25**: p. 95-102.
141. Xie, L. and D.I.C. Wang, *Integrated approaches to the design of media and feeding strategies for fed-batch cultures of animal cells*. Trends in Biotechnology, 1997. **15(3)**: p. 109-113.
142. Riebeling, C., et al., *Defined culture medium for stem cell differentiation: Applicability of serum-free conditions in the mouse embryonic stem cell test*. Toxicology in Vitro, 2011. **25(4)**: p. 914-921.
143. Poladyan, A., L. Baghdasaryan, and A. Trchounian, *Escherichia coli wild type and hydrogenase mutant cells growth and hydrogen production upon xylose and glycerol co-fermentation in media with different buffer capacities*. International Journal of Hydrogen Energy, 2018. **43(33)**: p. 15870-15879.
144. Zhai, Y., et al., *Physical Properties of Archaeal Tetraether Lipid Membranes As Revealed by Differential Scanning and Pressure Perturbation Calorimetry, Molecular Acoustics, and Neutron Reflectometry: Effects of Pressure and Cell Growth Temperature*. Langmuir, 2012. **28(11)**: p. 5211-5217.
145. Hernandez Vera, R., et al., *A Modular and Affordable Time-Lapse Imaging and Incubation System Based on 3D-Printed Parts, a Smartphone, and Off-The-Shelf Electronics.(Research Article)*. PLoS ONE, 2016. **11(12)**: p. e0167583.

References

146. Wardani, S., et al., *The effect of inoculum size and incubation temperature on cell growth, acid production and curd formation during milk fermentation by Lactobacillus plantarum Dad 13*. International Food Research Journal, 2017. **24**(3): p. 921-926.
147. Neeley, C. and S. Verna, *Abstract 3475: Negative impact of evaporation on cervical cancer cells during long term incubation is alleviated by Thermo Scientific Edge plate*. Cancer Research, 2014. **74**: p. 3475-3475.
148. Walzl, A., et al., *A Simple and Cost Efficient Method to Avoid Unequal Evaporation in Cellular Screening Assays, Which Restores Cellular Metabolic Activity*. International Journal of Applied Science and Technology 2012. **2**.
149. Gregory, K.J. and Y. Sun, *Reduction of sample evaporation in small volume microplate luminescence assays*. Analytical Biochemistry, 2009. **387**(2): p. 321-323.
150. Potter, S.M. and T.B. DeMarse, *A new approach to neural cell culture for long-term studies*. Journal of Neuroscience Methods, 2001. **110**(1): p. 17-24.
151. Talbot, E.L., et al., *Control of the particle distribution in inkjet printing through an evaporation-driven sol-gel transition*. ACS applied materials & interfaces, 2014. **6**(12): p. 9572.
152. Wang, C., et al., *Study on water droplet flash evaporation in vacuum spray cooling*. International Journal of Heat and Mass Transfer, 2017. **112**: p. 279-288.
153. Zhu, P., B. Liu, and L. Bao, *Evaporation-induced surface coating of poly(p-phenylene benzobisoxazole) fibers with polyetherimide encapsulated nano-TiO₂*. Progress in Organic Coatings, 2018. **116**: p. 43-50.
154. Ma, H.C., et al., *Nanoliter homogenous ultra-high throughput screening microarray for lead discoveries and IC50 profiling*. Assay and Drug Development Technologies, 2005. **3**(2): p. 177-187.
155. Picknett, R.G. and R. Bexon, *The evaporation of sessile or pendant drops in still air*. Journal of Colloid And Interface Science, 1977. **61**(2): p. 336-350.
156. Gunjan, M.R. and R. Raj, *Dynamic Roughness Ratio-Based Framework for Modeling Mixed Mode of Droplet Evaporation*. Langmuir : the ACS journal of surfaces and colloids, 2017. **33**(28): p. 7191.
157. Yuan, W.Z. and L.Z. Zhang, *Pinning-Depinning Mechanisms of the Contact Line during Evaporation of Microdroplets on Rough Surfaces: A Lattice Boltzmann Simulation*. Langmuir, 2018. **34**(26): p. 7906-7915.

References

158. Gleason, K. and S.A. Putnam, *Microdroplet evaporation with a forced pinned contact line*. Langmuir : the ACS journal of surfaces and colloids, 2014. **30**(34): p. 10548.
159. Rowan, S.M., et al., *Evaporation of Microdroplets of Azeotropic Liquids*. The Journal of Physical Chemistry B, 2000. **104**(34): p. 8217-8220.
160. Panwar, A.K., S.K. Barthwal, and S. Ray, *Effect of evaporation on the contact angle of a sessile drop on solid substrates*. Journal of Adhesion Science and Technology, 2003. **17**(10): p. 1321-1329.
161. Chhasatia, V.H., A.S. Joshi, and Y. Sun, *Effect of relative humidity on contact angle and particle deposition morphology of an evaporating colloidal drop*. Applied Physics Letters, 2010. **97**(23).
162. Patel, M.I., R. Tuckerman, and Q.H. Dong, *A pitfall of the 3-(4,5-dimethylthiazol-2-yl)-5(3-carboxymethoxyphenol)-2-(4-sulfophenyl)-2H-tetrazolium (MTS) assay due to evaporation in wells on the edge of a 96 well plate*. Biotechnology Letters, 2005. **27**(11): p. 805-808.
163. Burt, S.M., T.J.N. Carter, and L.J. Kricka, *Thermal characteristics of microtitre plates used in immunological assays*. Journal of Immunological Methods, 1979. **31**(3): p. 231-236.
164. Lau, C.Y., et al., *A direct heating model to overcome the edge effect in microplates*. Journal of Pharmaceutical and Biomedical Analysis, 2015. **102**: p. 199-202.
165. Hermann, R., M. Lehmann, and J. Büchs, *Characterization of gas-liquid mass transfer phenomena in microtiter plates*. Biotechnology and Bioengineering, 2003. **81**(2): p. 178-186.
166. Lundholt, B.K., K.M. Scudder, and L. Pagliaro, *A Simple Technique for Reducing Edge Effect in Cell-Based Assays*. Journal of Biomolecular Screening, 2003. **8**(5): p. 566-570.
167. *Thermo Fisher Scientific - New Cell Culture Plate Eliminates Edge Effect during Extended Incubation*, in ENP Newswire. 2016.
168. Felton, M.J., *Product Review: Liquid handling: Dispensing reliability*. Analytical Chemistry, 2003. **75**(17): p. 397 A-399 A.
169. Wang, T., et al., *A new method for producing uniform droplets by continuous-ink-jet technology*. Review of Scientific Instruments, 2018. **89**(8).
170. Jetha, N.N. and A. Marziali, *Liquid-Handling Technology and the Method of Electrostatic Drop Transfer to Improve Dispensing Performance*. JALA: Journal of the Association for Laboratory Automation, 2006. **11**(4): p. 278-280.

References

171. Elise Le, R., *Contamination-pipetting: relative efficiency of filter tips compared to Microman® positive displacement pipette*. Nature Methods, 2006. **3**(6).
172. Ohta, M., et al., *Robust numerical analysis of the dynamic bubble formation process in a viscous liquid*. International Journal of Multiphase Flow, 2011. **37**(9): p. 1059-1071.
173. Yamada, K., H. Emori, and K. Nakazawa, *Time-evolution of bubble formation in a viscous liquid*. Earth Planets and Space, 2008. **60**(6): p. 661-679.
174. Frank, X., et al., *Bubbles in a viscous liquid: lattice Boltzmann simulation and experimental validation*. Journal of Fluid Mechanics, 2006. **546**: p. 113-122.
175. Jomni, F., A. Denat, and F. Aitken, *The dynamics of microscopic bubbles in viscous insulating liquids*. Journal of Applied Physics, 2009. **105**(5).
176. Pancholi, K., E. Stride, and M. Edirisinghe, *Dynamics of Bubble Formation in Highly Viscous Liquids*. Langmuir, 2008. **24**(8): p. 4388-4393.
177. Watanabe, M. and T. Sanada, *In-line motion of a pair of bubbles in a viscous liquid*. Jsme International Journal Series B-Fluids and Thermal Engineering, 2006. **49**(2): p. 410-418.
178. Yang, G.Q., B. Du, and L.S. Fan, *Bubble formation and dynamics in gas-liquid-solid fluidization—A review*. Chemical Engineering Science, 2007. **62**(1-2): p. 2-27.
179. Huynh, S.H., et al., *Plastron-Mediated Growth of Captive Bubbles on Superhydrophobic Surfaces*. Langmuir, 2015.
180. Spinks, G.M., et al., *Pneumatic Carbon Nanotube Actuators*. Advanced Materials, 2002. **14**(23): p. 1728-1732.
181. Carpi, F., et al., *Millimetre-scale bubble-like dielectric elastomer actuators*. Polymer International, 2010. **59**(3): p. 407-414.
182. Sijl, J., et al., *Subharmonic behavior of phospholipid-coated ultrasound contrast agent microbubbles*. The Journal of the Acoustical Society of America, 2010. **128**(5): p. 3239-3252.
183. Scardina, P. and M. Edwards, *Practical implications of bubble formation IN CONVENTIONAL TREATMENT*. Journal (American Water Works Association), 2002. **94**(8): p. 85-94.
184. Abdelwahed, M.A.B., et al., *Bubble formation and transport in T-junction for application to Liquid Composite Molding: Wetting effect*. Journal of Composite Materials, 2014. **48**(1): p. 37-48.

References

185. Davidson, J.F. and B.O.G. Schüler, *Bubble formation at an orifice in a viscous liquid*. Chemical Engineering Research and Design, 1997. **75**: p. S105-S115.
186. Newcome, L.R., *Unmanned aviation : a brief history of unmanned aerial vehicles*, ed. A. American Institute of and Astronautics. 2004, Reston, Va. : [London]: Reston, Va. : American Institute of Aeronautics and Astronautics London : Eurospan, distributor.
187. Chetan Khemraj, J.K., Ashish Srivastava, Gaurav Srivastava, Dr., *Autonomous UAV (Unmanned Aerial Vehicle) For Navigation and Surveillance Purposes*. 2012. Vol. 12. 2012.
188. Rudol, P. and P. Doherty. *Human Body Detection and Geolocalization for UAV Search and Rescue Missions Using Color and Thermal Imagery*. in *Aerospace Conference, 2008 IEEE*. 2008.
189. Gu, D.L.H., et al., *UAV aided intelligent routing for ad-hoc wireless network in single-area theater*. Wcnc: 2000 Ieee Wireless Communications and Networking Conference, Vols 1-3, 2000: p. 1220-1225.
190. Lazarus, S.B., et al., *Unmanned aerial vehicle navigation and mapping*. Proc. Inst. Mech. Eng. Part G-J. Aersp. Eng., 2008. **222**(G4): p. 531-548.
191. Cobleigh, B.R., *Emergency Response Fire-Imaging UAS Missions over the Southern California Wildfire Disaster*. 2007.
192. Leonard, J., A. Savvaris, and A. Tsourdos. *Towards a fully autonomous swarm of unmanned aerial vehicles*. in *Control (CONTROL), 2012 UKACC International Conference on*. 2012.
193. Saari, H., et al., *Unmanned Aerial Vehicle (UAV) operated spectral camera system for forest and agriculture applications*. Remote Sensing for Agriculture, Ecosystems, and Hydrology Xiii, 2011. **8174**.
194. Primicerio, J., et al., *A flexible unmanned aerial vehicle for precision agriculture*. Precision Agriculture, 2012. **13**(4): p. 517-523.
195. Lucieer, A., et al., *Using an Unmanned Aerial Vehicle (UAV) to capture micro-topography of Antarctic moss beds*. International Journal of Applied Earth Observation and Geoinformation, 2014. **27**: p. 53-62.
196. Zarco-Tejada, P.J., et al., *Estimating leaf carotenoid content in vineyards using high resolution hyperspectral imagery acquired from an unmanned aerial vehicle (UAV)*. Agricultural and Forest Meteorology, 2013. **171-172**: p. 281-294.
197. Yue, J.W., et al., *THE APPLICATION OF UNMANNED AERIAL VEHICLE REMOTE SENSING IN QUICKLY MONITORING CROP PESTS*. Intell. Autom. Soft Comput., 2012. **18**(8): p. 1043-1052.

References

198. Huang, Y., et al., *UAV Low-Altitude Remote Sensing for Precision Weed Management*. Weed Technology, 2018. **32**(1): p. 2-6.
199. Ahmed, G., et al., *Modeling the spreading and sliding of power-law droplets*. Colloids and Surfaces A: Physicochemical and Engineering Aspects, 2013. **432**: p. 2-7.
200. Caffarelli, L. and A. Mellet, *Capillary Drops: Contact angle hysteresis and sticking drops*. Calculus of Variations and Partial Differential Equations, 2007. **29**(2): p. 141-160.
201. Ling, W.Y.L., T.W. Ng, and A. Neild, *Effect of an Encapsulated Bubble in Inhibiting Droplet Sliding*. Langmuir, 2010. **26**(22): p. 17695-17702.
202. Ling, W.Y.L., et al., *Sliding variability of droplets on a hydrophobic incline due to surface entrained air bubbles*. Journal of Colloid and Interface Science, 2011. **354**(2): p. 832-842.
203. Davidson, M.R. and J.J. Cooper-White, *Pendant drop formation of shear-thinning and yield stress fluids*. Applied Mathematical Modelling, 2006. **30**(11): p. 1392-1405.
204. Wang, F., et al., *Mechanically durable superhydrophobic surfaces prepared by abrading*. J. Appl. Phys., 2013. **114**(12).
205. Lau, C.Y., et al., *Hydrophobic to superhydrophobic surface modification using impacting particulate sprays*. Applied Surface Science, 2014.
206. Matthias, J.M., et al., *Measuring air layer volumes retained by submerged floating-ferns *Salvinia* and biomimetic superhydrophobic surfaces*. Beilstein Journal of Nanotechnology, 2014. **5**(1): p. 812.
207. Sheng, X.L. and J.H. Zhang, *Air layer on superhydrophobic surface underwater*. Colloids and Surfaces a-Physicochemical and Engineering Aspects, 2011. **377**(1-3): p. 374-378.
208. Ling, W., G. Lu, and T. Ng, *Increased Stability and Size of a Bubble on a Superhydrophobic Surface*. Langmuir, 2011. **27**(7): p. 3233-3237.
209. Ueda, M., et al., *Effect of glycerol on the solubilities of benzene and toluene in water*. Kolloid-Zeitschrift und Zeitschrift für Polymere., 1976. **254**(5): p. 532-533.
210. Egorov, A.V., A.P. Lyubartsev, and A. Laaksonen, *Molecular Dynamics Simulation Study of Glycerol-Water Liquid Mixtures*. Journal of Physical Chemistry B, 2011. **115**(49): p. 14572-14581.
211. Sanz, A. and I. Martinez, *Minimum Volume for a Liquid Bridge between Equal Disks*. Journal of Colloid and Interface Science, 1983. **93**(1): p. 235-240.

References

212. Petkov, P.V. and B.P. Radoev, *Statics and dynamics of capillary bridges*. Colloids and Surfaces A: Physicochemical and Engineering Aspects, 2014. **460**: p. 18-27.
213. Schwalb, W., et al., *Surface tension drawing of liquid from microplate capillary wells*. Journal of Colloid and Interface Science, 2012. **365**(1): p. 314-319.
214. Katariya, M. and T.W. Ng, *Drops transformed from a continuous flow on a superhydrophobic incline*. Journal of Physics D-Applied Physics, 2013. **46**(34).
215. Katariya, M., T. Vuong, and T. Ng, *Liquid Body Formation from a Semispherical Superhydrophobic Well on a Small Incline*. Langmuir, 2014. **30**(46): p. 13731-13736.
216. Lai, A., N. Bremond, and H.A. Stone, *Separation-driven coalescence of droplets: an analytical criterion for the approach to contact*. Journal of Fluid Mechanics, 2009. **632**: p. 97-107.
217. Le Grand, N., A. Daerr, and L. Limat, *Shape and motion of drops sliding down an inclined plane*. Journal of Fluid Mechanics, 2005. **541**: p. 293-315.
218. Hong, S.J., et al., *Droplet Compression and Relaxation by a Superhydrophobic Surface: Contact Angle Hysteresis*. Langmuir, 2012. **28**(13): p. 5606-5613.
219. Charron, C., et al., *Crystallization in the presence of glycerol displaces water molecules in the structure of thaumatin*. Acta Crystallographica Section D, 2002. **58**(12): p. 2060-2065.
220. Vagenende, V., M.G.S. Yap, and B.L. Trout, *Mechanisms of protein stabilization and prevention of protein aggregation by glycerol*. Biochemistry, 2009. **48**(46): p. 11084.
221. Sikarwar, B.S., S. Khandekar, and K. Muralidhar, *Simulation of flow and heat transfer in a liquid drop sliding underneath a hydrophobic surface*. International Journal of Heat and Mass Transfer, 2013. **57**(2): p. 786-811.
222. Lau, C.Y., et al., *Transparency microplates under impact*. Journal of Colloid and Interface Science, 2014. **426**: p. 56-63.
223. Suzuki, M., et al., *Mixing Phenomena Induced by Capillary Oscillations of a Sessile Drop*. Journal of Japan Society of Fluid Mechanics, 2005. **24**(2): p. 205-206.
224. Chaudhury, M. and P. Goohpattader, *Activated drops: Self-excited oscillation, critical speeding and noisy transport*. Soft Matter and Biological Physics, 2013. **36**(2): p. 1-14.
225. Chong, M.L.H., et al., *Liquid-body resonance while contacting a rotating superhydrophobic surface*. European Physical Journal E, 2015. **38**(11).

References

226. Katariya, M., et al., *Linear Stepper Actuation Driving Drop Resonance and Modifying Hysteresis*. Langmuir : the ACS journal of surfaces and colloids, 2016. **32**(33): p. 8550.
227. Bertola, V. and M. Wang, *Dynamic contact angle of dilute polymer solution drops impacting on a hydrophobic surface*. Colloids and Surfaces A: Physicochemical and Engineering Aspects, 2015. **481**(C): p. 600-608.
228. Yang, W. and J. Xu, *Drop spreading and penetrating on micro/nano particle sintering porous with multiscale structure*. Colloids and Surfaces A: Physicochemical and Engineering Aspects, 2017. **516**: p. 9-22.
229. Wu, J., J.J. Huang, and W.W. Yan, *Lattice Boltzmann investigation of droplets impact behaviors onto a solid substrate*. Colloids and Surfaces A: Physicochemical and Engineering Aspects, 2015. **484**: p. 318-328.
230. Megaridis, C.M., K. Boomsma, and I.S. Bayer, *Partial rebound of molten-metal droplets impacting on solid substrates*. AIChE Journal, 2004. **50**(7): p. 1356-1363.
231. Olsson, E. and G. Kreiss, *A conservative level set method for two phase flow*. Journal of Computational Physics, 2005. **210**(1): p. 225-246.
232. Di, Y., et al., *Level Set Calculations for Incompressible Two-Phase Flows on a Dynamically Adaptive Grid*. Journal of Scientific Computing, 2007. **31**(1): p. 75-98.
233. Eggers, J., *Nonlinear dynamics and breakup of free-surface flows*. Reviews of Modern Physics, 1997. **69**(3): p. 865-929.
234. Bayer, I.S. and C.M. Megaridis, *Contact angle dynamics in droplets impacting on flat surfaces with different wetting characteristics*. Journal of Fluid Mechanics, 2006. **558**: p. 415-449.
235. Vuong, T., et al., *Microplate well coverage mixing using superhydrophobic contact*. Analytical Biochemistry, 2012. **430**(1): p. 53-55.
236. Wan, S., X. Huanming, and P. Kumar, *Numerical analysis and characterization of a wankel pump as a miniaturized mixer*. Journal of Micromechanics and Microengineering, 2015. **25**(8): p. 084001.
237. Sarkar, S., et al., *Cfd simulations to study the effects of wall protrusions on microfluidic mixing*. Journal of Micromechanics and Microengineering, 2015. **25**(8): p. 084008.
238. Couder, Y., et al., *Dynamical phenomena: Walking and orbiting droplets*. Nature, 2005. **437**(7056): p. 208.

References

239. Berry, J.D. and R.R. Dagastine, *Mapping coalescence of micron-sized drops and bubbles*. Journal of Colloid And Interface Science, 2017. **487**: p. 513-522.
240. Korhonen, H.T. and P. Niemelä, *Water absorption and the drying and cooling rates in mink (*Mustela vison*) following simulated diving*. Animal Science, 2002. **74**(2): p. 277-283.
241. Dickerson, A.K., Z.G. Mills, and D.L. Hu, *Wet mammals shake at tuned frequencies to dry*. Journal of the Royal Society Interface, 2012. **9**(77): p. 3208-3218.
242. White, S.D., P.J. Bourdeau, and A. Meredith, *Dermatologic problems of rabbits*. Seminars in Avian and Exotic Pet Medicine, 2002. **11**(3): p. 141-150.
243. Roscoe, D.E., et al., *Spontaneous dermatophilosis in twin white-tailed deer fawns*. Journal of wildlife diseases, 1975. **11**(3): p. 398.
244. Ghasemi, H. and C. Ward, *Mechanism of Sessile Water Droplet Evaporation: Kapitza Resistance at the Solid-Liquid Interface*. J. Phys. Chem. C, 2011. **115**(43): p. 21311-21319.
245. Nguyen, T.A.H., S.R. Biggs, and A.V. Nguyen, *Analytical Model for Diffusive Evaporation of Sessile Droplets Coupled with Interfacial Cooling Effect*. Langmuir, 2018. **34**(23): p. 6955-6962.
246. Hennes, M., et al., *Active depinning of bacterial droplets: The collective surfing of *Bacillus subtilis**. Proceedings of the National Academy of Sciences of the United States of America, 2017. **114**(23): p. 5958-5963.
247. Durbin, P.A., *On the Wind Force Needed to Dislodge a Drop Adhered to a Surface*. Journal of Fluid Mechanics, 1988. **196**: p. 205-222.
248. Moghtadernejad, S., et al., *Shear Driven Droplet Shedding on Surfaces with Various Wettabilities*. SAE International Journal of Aerospace, 2013. **6**(2): p. 459-464.
249. Chung, D.C.K., et al., *Uphill airflow transport of drops on superhydrophobic inclines*. Colloid and Interface Science Communications, 2015. **6**: p. 1-4.
250. An, S., et al., *Wetting and Coalescence of Drops of Self-Healing Agents on Electrospun Nanofiber Mats*. Langmuir, 2017. **33**(40): p. 10663-10672.
251. Li, G., et al., *Poly(vinyl alcohol)-Poly(ethylene glycol) Double-Network Hydrogel: A General Approach to Shape Memory and Self-Healing Functionalities*. Langmuir : the ACS journal of surfaces and colloids, 2015. **31**(42): p. 11709.

References

252. Zhang, Y., et al., *Spreading Dynamics of Molten Polymer Drops on Glass Substrates*. Langmuir : the ACS journal of surfaces and colloids, 2017. **33**(34): p. 8447.
253. Subramani, N.K. and Siddaramaiah, *Opto-Electrical Characteristics of Poly(vinyl alcohol)/Cesium Zincate Nanodielectrics*. Journal of Physical Chemistry C, 2015. **119**(35): p. 20244-20255.
254. Tuval, I., et al., *Bacterial swimming and oxygen transport near contact lines*. Proceedings of the National Academy of Sciences of the United States of America, 2005. **102**(7): p. 2277-2282.
255. Ragoonanan, V. and A. Aksan, *Heterogeneity in desiccated solutions: Implications for biostabilization*. Biophysical Journal, 2008. **94**(6): p. 2212-2227.
256. Zahidi, A.A.A., et al., *Glycerol-water sessile drop elongation on PTFE inclines in relation to biochemical applications*. Colloids and Surfaces a-Physicochemical and Engineering Aspects, 2015. **486**: p. 21-28.
257. Andrade, R.D., O. Skurtys, and F. Osorio, *The impact of liquid drops on purple cabbage leaves (Brassica oleracea l. Var. Capitata)*. Ingenieria E Investigacion, 2012. **32**(2): p. 79-82.
258. Sharp, J.S., *Resonant properties of sessile droplets; contact angle dependence of the resonant frequency and width in glycerol/water mixtures*. Soft Matter, 2012. **8**(2): p. 399-407.
259. Joanny, J.F. and P.G. Degennes, *A Model for Contact-Angle Hysteresis*. Journal of Chemical Physics, 1984. **81**(1): p. 552-562.
260. Israelachvili, J.N., *Intermolecular and Surface Forces Preface to the First Edition*. Intermolecular and Surface Forces, 3rd Edition, 2011: p. Xxi-XXii.
261. Penn, L.S. and B. Miller, *A Study of the Primary Cause of Contact-Angle Hysteresis on Some Polymeric Solids*. Journal of Colloid and Interface Science, 1980. **78**(1): p. 238-241.
262. Extrand, C.W., *A thermodynamic model for contact angle hysteresis*. Journal of Colloid and Interface Science, 1998. **207**(1): p. 11-19.
263. Athukorallage, B. and R. Iyer, *Investigation of energy dissipation due to contact angle hysteresis in capillary effect*. Murphys-Hsfs-2014: 7th International Workshop on Multi-Rate Processes & Hysteresis (Murphys) & the 2nd International Workshop on Hysteresis and Slow-Fast Systems (Hsfs), 2016. **727**.
264. Hong, S.J., et al., *Anomalous Contact Angle Hysteresis of a Captive Bubble: Advancing Contact Line Pinning*. Langmuir, 2011. **27**(11): p. 6890-6896.

References

265. Qiao, S.S., et al., *Friction of Droplets Sliding on Microstructured Superhydrophobic Surfaces*. Langmuir, 2017. **33**(47): p. 13480-13489.
266. Butt, H.J., et al., *Energy Dissipation of Moving Drops on Superhydrophobic and Superoleophobic Surfaces*. Langmuir, 2017. **33**(1): p. 107-116.
267. Kozbial, A., et al., *Study on the Surface Energy of Graphene by Contact Angle Measurements*. Langmuir, 2014. **30**(28): p. 8598-8606.
268. Farmer, J.D. and J.J. Sidorowich, *Predicting Chaotic Time-Series*. Physical Review Letters, 1987. **59**(8): p. 845-848.
269. Eder, O.J. and T. Lackner, *Brownian-Motion in Phase-Space*. Physical Review A, 1984. **29**(2): p. 799-810.
270. Ling, W.Y.L., A. Neild, and T.W. Ng, *Effect of a Rupturing Encapsulated Bubble in Inducing the Detachment of a Drop*. Langmuir, 2012. **28**(51): p. 17656-17665.
271. Krasovitski, B. and A. Marmur, *Drops down the hill: Theoretical study of limiting contact angles and the hysteresis range on a tilted plate*. Langmuir, 2005. **21**(9): p. 3881-3885.
272. Derby, B., *Inkjet Printing of Functional and Structural Materials: Fluid Property Requirements, Feature Stability, and Resolution*. Annual Review of Materials Research, Vol 40, 2010. **40**: p. 395-414.
273. Staat, H.J.J., et al., *Ultrafast imaging method to measure surface tension and viscosity of inkjet-printed droplets in flight*. Experiments in Fluids, 2017. **58**(1).
274. Vacek, V., *Determination of the shape of pendant drops*. The Chemical Engineering Journal, 1975. **9**(2): p. 167-169.
275. Sumesh, P.T. and R. Govindarajan, *The possible equilibrium shapes of static pendant drops*. Journal of Chemical Physics, 2010. **133**(14).
276. Fordham, S., *On the Calculation of Surface Tension from Measurements of Pendant Drops*. Proceedings of the Royal Society of London Series a-Mathematical and Physical Sciences, 1948. **194**(1036): p. 1-16.
277. Bacri, J.C. and D. Salin, *Instability of Ferrofluid Magnetic Drops under Magnetic-Field*. Journal De Physique Lettres, 1982. **43**(17): p. L649-L654.
278. Lenard, P., *Uber Regen*. Meteor Z, 1904. **21**: p. 248-262.
279. Moore, D.W., *The velocity of rise of distorted gas bubbles in a liquid of small viscosity*. Journal of Fluid Mechanics, 1965. **23**(4): p. 749-766.
280. Beard, K.V., *On the Acceleration of Large Water Drops to Terminal Velocity*. Journal of Applied Meteorology (1962-1982), 1977. **16**(10): p. 1068-1071.

References

281. Zhang, X.G. and O.A. Basaran, *An Experimental-Study of Dynamics of Drop Formation*. *Physics of Fluids*, 1995. **7**(6): p. 1184-1203.
282. Scheele, G.F. and B.J. Meister, *Drop Formation at Low Velocities in Liquid-Liquid Systems .I. Prediction of Drop Volume .2. Prediction of Jetting Velocity*. *Aiche Journal*, 1968. **14**(1): p. 9-&.
283. Che, Z.Z., et al., *Formation and breakup of compound pendant drops at the tip of a capillary and its effect on upstream velocity fluctuations*. *International Journal of Heat and Mass Transfer*, 2012. **55**(4): p. 1022-1029.
284. Szeto, K., et al., *High-throughput binding characterization of RNA aptamer selections using a microplate-based multiplex microcolumn device.(NOTE)(Report)*. *Analytical and Bioanalytical Chemistry*, 2014. **406**(11): p. 2727.
285. Zhu, M., et al., *Analysis of low level radioactive metabolites in biological fluids using high-performance liquid chromatography with microplate scintillation counting: Method validation and application*. *Journal of Pharmaceutical and Biomedical Analysis*, 2005. **39**(1 2): p. 233.
286. Liu, Y.Y.B., et al., *A functional dual-coated (FDC) microtiter plate method to replace the botulinum toxin LD50 test*. *Analytical Biochemistry*, 2012. **425**(1): p. 28-35.
287. Pavel, N., et al., *Revisiting lab-on-a-chip technology for drug discovery*. *Nature Reviews Drug Discovery*, 2012. **11**(8): p. 620.
288. Seemann, R., et al., *Droplet based microfluidics*, in *Rep. Prog. Phys.* 2012.
289. Lye, J.K.K., et al., *A capacity for mixing in capillary wells for microplates*. *Analytical Biochemistry*, 2011. **410**(1): p. 152-154.
290. Cheong, B.H.-P., et al., *Transparency-based microplates for fluorescence quantification*. *Analytical Biochemistry*, 2012. **422**(1): p. 39-45.
291. Eastman, P.S., et al., *Characterization of a multiplex, 12-biomarker test for rheumatoid arthritis*. *Journal of Pharmaceutical and Biomedical Analysis*, 2012. **70**: p. 415-424.
292. Xu, K., et al., *Multiplex chemiluminescent immunoassay for screening of mycotoxins using photonic crystal microsphere suspension array*. *Analyst*, 2014. **139**(4): p. 771-777.
293. Ellington, A.A., et al., *Measurement and quality control issues in multiplex protein assays: a case study*. *Clinical chemistry*, 2009. **55**(6): p. 1092.
294. Patel, M., R. Tuckerman, and Q. Dong, *A Pitfall of the 3-(4,5-dimethylthiazol-2-yl)-5-(3-carboxymethoxyphenyl)-2-(4-sulfophenyl)-2H-tetrazolium (MTS)*

References

- Assay due to Evaporation in wells on the Edge of a 96 well Plate*. Biotechnology Letters, 2005. **27**(11): p. 805-808.
295. Zimmermann, H.F., et al., *Rapid Evaluation of Oxygen and Water Permeation through Microplate Sealing Tapes*. Biotechnology Progress, 2003. **19**(3): p. 1061-1063.
296. Duetz, W.A., Minas, W., Kuhner, M., Clerval, R., Fjallman, A.H.M., Witholt, B., *Miniaturized microbial growth systems in screening*. Bioworld 2, 2001: p. 8–10.
297. Maddox, C.B., L. Rasmussen, and E.L. White, *Adapting Cell-Based Assays to the High-Throughput Screening Platform: Problems Encountered and Lessons Learned*. Journal of the Association for Laboratory Automation, 2008. **13**(3): p. 168-173.
298. Fang, X., et al., *Factors controlling the drop evaporation constant*. Journal of Physical Chemistry B, 2005. **109**(43): p. 20554-20557.
299. Hunyh, T., et al., *Contact angle and volume retention effects from capillary bridge evaporation in biochemical microplating*. Colloids and Surfaces A: Physicochemical and Engineering Aspects, 2013. **436**: p. 647-655.
300. Torresin, D., et al., *Flow condensation on copper-based nanotextured superhydrophobic surfaces*. Langmuir : the ACS journal of surfaces and colloids, 2013. **29**(2): p. 840.
301. Vuong, T., et al., *Precise drop dispensation on superhydrophobic surfaces using acoustic nebulization*. Soft Matter, 2013. **9**(13): p. 3631-3639.
302. Triaud, F., et al., *Evaluation of automated cell culture incubators*. Journal of the Association for Laboratory Automation, 2003. **8**(6): p. 82-86.
303. Vivien, M., *Pouring over liquid handling*. Nature Methods, 2013. **11**(1): p. 33.
304. Oliver, J.F., C. Huh, and S.G. Mason, *Resistance to Spreading of Liquids by Sharp Edges*. Journal of Colloid and Interface Science, 1977. **59**(3): p. 568-581.
305. Hallmann, C.A., et al., *More than 75 percent decline over 27 years in total flying insect biomass in protected areas*. Plos One, 2017. **12**(10).
306. Boeve, J.L., et al., *Field Method for Testing Repellency of an Icaridin-Containing Skin Lotion against Vespidae Wasps*. Insects, 2016. **7**(2).
307. Petrovskaya, N., S. Petrovskii, and A.K. Murchie, *Challenges of ecological monitoring: estimating population abundance from sparse trap counts*. Journal of the Royal Society Interface, 2012. **9**(68): p. 420-435.

References

308. Delly, J.G., *Narcosis and preservation of freshwater animals*. Am. Lab, 1985. **17**: p. 31-40.
309. Taylor, H.L., *The Taylor microcompressor, Mark II*. The Microscope, 1993. **41**: p. 19-20.
310. Kirichek, O., et al., *Segregated water observed in a putative fish embryo cryopreservative*. Royal Society Open Science, 2016. **3**(3): p. 150655.
311. Cesaretti, M., et al., *Testing feasibility of an accurate microscopic assessment of macrovesicular steatosis in liver allograft biopsies by smartphone add - on lenses*. Microscopy Research and Technique, 2018. **81**(1): p. 58-63.
312. Baek, D., et al., *Time - lapse microscopy using smartphone with augmented reality markers*. Microscopy Research and Technique, 2014. **77**(4): p. 243-249.
313. Aufderheide, K.J. and C. Janetopoulos, *Immobilization of living specimens for microscopic observation*. 2012.
314. Li, X.Y., et al., *Surface-Scribed Transparency-Based Microplates*. Langmuir, 2013. **29**(2): p. 849-855.
315. Park, J., S.C. Byun, and B.U. Lee, *Lens Distortion Correction Using Ideal Image Coordinates*. Ieee Transactions on Consumer Electronics, 2009. **55**(3): p. 987-991.
316. Lasa, R., et al., *Improved capture of Drosophila suzukii by a trap baited with two attractants in the same device.(Research Article)(Report)*. PLoS ONE, 2017. **12**(11): p. e0188350.
317. Huang, J., L. Gut, and M. Grieshop, *Evaluation of food-based attractants for drosophila suzukii (diptera: Drosophilidae)*. Environmental Entomology, 2017. **46**(4): p. 878-884.
318. Sung, Y.-L., et al., *Fabricating optical lenses by inkjet printing and heat-assisted in situ curing of polydimethylsiloxane for smartphone microscopy*. Journal of Biomedical Optics, 2015. **20**(4): p. 047005-047005.
319. Jung, D., et al., *Smartphone-based multi-contrast microscope using color-multiplexed illumination*. Sci Rep, 2017. **7**(1): p. 7564-7564.
320. Gavala, A. and P. Myrianthefs, *Comparison of point-of-care versus central laboratory measurement of hematocrit, hemoglobin, and electrolyte concentrations*. Heart & Lung - The Journal of Acute and Critical Care, 2017. **46**(4): p. 246-250.
321. Clark, J.L. and L.V. Rao, *Retrospective Analysis of Point-of-Care and Laboratory-Based Hemoglobin A_{1c} Testing*. The

References

- Journal of Applied Laboratory Medicine: An AACC Publication, 2017. **1**(5): p. 502.
322. Moreno, M., A. Schwartz, and R. Dvorkin, *The Accuracy of Point-of-Care Creatinine Testing in the Emergency Department*. Vol. 2015. 2015. 5.
323. Grasas, A., et al., *On the improvement of blood sample collection at clinical laboratories*. BMC Health Services Research, 2014. **14**: p. 12.
324. Doerner, K.F., et al., *Exact and heuristic algorithms for the vehicle routing problem with multiple interdependent time windows*. Computers and Operations Research, 2008. **35**(9): p. 3034-3048.
325. Fernandes, C.M.B., et al., *Pneumatic Tube Delivery System for Blood Samples Reduces Turnaround Times Without Affecting Sample Quality*. Journal of Emergency Nursing, 2006. **32**(2): p. 139-143.
326. Shibani, W.M., M.F. Zulkafli, and B. Basuno, *Methods of Transport Technologies: A Review on Using Tube/Tunnel Systems*. 2016. p. <xocs:firstpage xmlns:xocs=""/>.
327. Amukele, T., et al., *Can Unmanned Aerial Systems (Drones) Be Used for the Routine Transport of Chemistry, Hematology, and Coagulation Laboratory Specimens?* PLoS One, 2015. **10**(7): p. e0134020.
328. Lippi, G. and C. Mattiuzzi, *Biological samples transportation by drones: ready for prime time?* Annals of translational medicine, 2016. **4**(5): p. 92-92.
329. Mitic, S., et al., *Design of turbulent tangential micro-mixers that mix liquids on the nanosecond time scale*. Analytical Biochemistry, 2015. **469**: p. 19-26.
330. Karpitschka, S., et al., *Coalescence and noncoalescence of sessile drops: impact of surface forces*. Langmuir : the ACS journal of surfaces and colloids, 2014. **30**(23): p. 6826.
331. Deetz, C.O., D.K. Nolan, and M.G. Scott, *An examination of the usefulness of repeat testing practices in a large hospital clinical chemistry laboratory*. American journal of clinical pathology, 2012. **137**(1): p. 20.
332. Neubauer, J.C., et al., *Towards standardized automated immunomonitoring: an automated ELISpot assay for safe and parallelized functionality analysis of immune cells.(Report)*. Cytotechnology, 2017. **69**(1): p. 57.
333. Nett, J.E., et al., *Optimizing a Candida Biofilm Microtiter Plate Model for Measurement of Antifungal Susceptibility by Tetrazolium Salt Assay*. Journal of Clinical Microbiology, 2011. **49**(4): p. 1426.

References

334. Lilyanna, S., et al., *Variability in Microplate Surface Properties and Its Impact on ELISA*. The Journal of Applied Laboratory Medicine: An AACC Publication, 2017: p. jalm.2017.023952.
335. El-Badawy, A.A. and M.A. Bakr, *Quadcopter Aggressive Maneuvers along Singular Configurations: An Energy-Quaternion Based Approach*. Journal of Control Science and Engineering, 2016. **2016**.
336. Towey, J.J. and L. Dougan, *Structural examination of the impact of glycerol on water structure.(Report)*. Journal of Physical Chemistry B, 2012. **116**(5): p. 1633-1641.
337. Cheng, N.S., *Formula for the viscosity of a glycerol-water mixture*. Industrial and Engineering Chemistry Research, 2008. **47**(9): p. 3285-3288.
338. Metcalfe, G., et al., *Measurement of particle motions within tumbling granular flows*. Chaos: An Interdisciplinary Journal of Nonlinear Science, 1999. **9**(3): p. 581-593.
339. Chalmers, J.J., *Mixing, aeration and cell damage, 30+ years later: what we learned, how it affected the cell culture industry and what we would like to know more about*. Current Opinion in Chemical Engineering, 2015. **10**: p. 94-102.
340. Kumar, R., et al., *Tilting-rotor quadcopter for aggressive flight maneuvers using differential flatness based flight controller*. 2017. p. <xocs:firstpage xmlns:xocs=""/>.
341. Boyanton, B.L. and K.E. Blick, *Stability Studies of Twenty-Four Analytes in Human Plasma and Serum*. Clinical Chemistry, 2002. **48**(12): p. 2242.
342. Tuck, M.K., et al., *Standard operating procedures for serum and plasma collection: early detection research network consensus statement standard operating procedure integration working group*. Journal of proteome research, 2009. **8**(1): p. 113.
343. Brouwers, J., et al., *Platelet Activation Determines Angiopoietin-1 and VEGF Levels in Malaria: Implications for Their Use as Biomarkers.(Research Article)(Vascular endothelial growth factor)(Report)*. PLoS ONE, 2013. **8**(6): p. e64850.
344. Wexler, C., et al., *Evaluating turnaround times for early infant diagnosis samples in Kenya from 2011-2014: A retrospective analysis of HITSystem program data.(Research Article)(Report)*. PLoS ONE, 2017. **12**(8): p. e0181005.
345. Amukele, T.K., et al., *Drone Transport of Microbes in Blood and Sputum Laboratory Specimens*. Journal of clinical microbiology, 2016. **54**(10): p. 2622.

References

346. Eresen, A., N. AmamoAlu, and M.O. Efe, *Autonomous quadrotor flight with vision-based obstacle avoidance in virtual environment.(Report)*. Expert Systems With Applications, 2012. **39**(1): p. 894.
347. Brittin, W.E., *Liquid Rise in a Capillary Tube*. Journal of Applied Physics, 1946. **17**(1): p. 37-44.
348. Schwalb, W., et al., *Surface tension drawing of liquid from microplate capillary wells*. Journal of Colloid And Interface Science, 2011. **365**(1).
349. Pearson, T.C. and D.L. Guthrie, *Trapped plasma in the microhematocrit*. Am J Clin Pathol, 1982. **78**(5): p. 770-2.
350. Jiang, Z., et al., *Effect of curved delamination front on mode-I fracture toughness of adhesively bonded joints*. Engineering Fracture Mechanics, 2015. **138**: p. 73-91.
351. Jagger, J. and S. Deitchman, *Hazards of Glass Capillary Tubes to Health Care Workers*. JAMA, 1998. **280**(1): p. 31-31.
352. Wongkrajang, P., et al., *Accuracy and precision evaluation of Thai plastic microhematocrit tubes: the first product from Thailand*. Journal of the Medical Association of Thailand, 2012. **95**(6): p. 809.
353. Meier, P.P., et al., *Accuracy of a User-Friendly Centrifuge for Measuring Creamatocrits on Mothers' Milk in the Clinical Setting*. Breastfeed. Med., 2006. **1**(2): p. 79-87.
354. Black, R.E., et al., *Maternal and child undernutrition: global and regional exposures and health consequences*. The Lancet, 2008. **371**(9608): p. 243-260.
355. Ayawine, A. and K.A. Ae-Ngibise, *Determinants of exclusive breastfeeding: a study of two sub-districts in the Atwima Nwabiagya District of Ghana*. Pan Afr Med J, 2015. **22**: p. 248.
356. Sutcu, M., et al., *Clinical Findings of Pediatric HIV Infection in a Tertiary Center in Turkey*. Balkan Med J, 2017. **34**(3): p. 239-245.
357. Lallemand, M., et al., *Pediatric HIV--a neglected disease?* N Engl J Med, 2011. **365**(7): p. 581-3.
358. Priye, A., et al., *Lab-on-a-Drone: Toward Pinpoint Deployment of Smartphone-Enabled Nucleic Acid-Based Diagnostics for Mobile Health Care*. Anal Chem, 2016. **88**(9): p. 4651-60.
359. Kuantama, E., et al., *Quadcopter propeller design and performance analysis*. 2017. p. 269-277.

References

360. Farrell, E. and G. Alexandre, *Bovine serum albumin further enhances the effects of organic solvents on increased yield of polymerase chain reaction of GC-rich templates*. BMC Research Notes, 2012. **5**(1): p. 257-257.

APPENDICES

Appendix A

Colloids and Surfaces A: Physicochem. Eng. Aspects 486 (2015) 21–28



ELSEVIER

Contents lists available at ScienceDirect

Colloids and Surfaces A: Physicochemical and Engineering Aspects

journal homepage: www.elsevier.com/locate/colsurfa



Glycerol–water sessile drop elongation on PTFE inclines in relation to biochemical applications



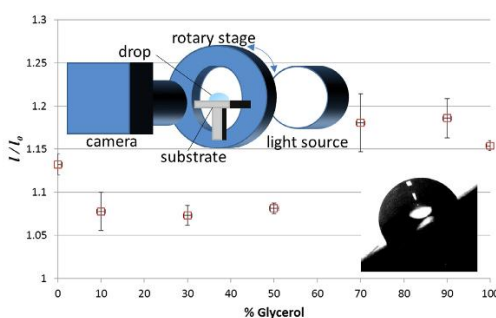
Alifa Afiah Ahmad Zahidi^a, Brandon Huey-Ping Cheong^a, So Hung Huynh^a, Thach Vuong^a, Oi Wah Liew^b, Tuck Wah Ng^{a,*}

^a Laboratory for Optics and Applied Mechanics, Department of Mechanical and Aerospace Engineering, Monash University, Clayton, Victoria 3800 Australia
^b Cardiovascular Research Institute, Yong Loo Lin School of Medicine, National University of Singapore, National University Health System, Centre for Translational Medicine, 14 Medical Drive, 117599, Singapore

HIGHLIGHTS

- Slip angles of 6 μL drops on tilted PTFE had complex trends to varying glycerol–water compositions.
- As the front contact line breached first, levels of contact angle hysteresis did not match slip angle trends.
- The ratios of lengths at detachment against equilibrium corresponded with slip angle trends.
- The drops elongated in relation to angle of tilt in two distinct stages.
- Turbidity measurements show higher glycerol contents improving thermal stability of bovine serum albumin.

GRAPHICAL ABSTRACT



ARTICLE INFO

Article history:
 Received 31 May 2015
 Received in revised form 24 August 2015
 Accepted 4 September 2015
 Available online 8 September 2015

Keywords:
 Drop
 Incline
 Elongation
 Contact angle
 Glycerol
 PTFE

ABSTRACT

The movement behavior of glycerol–water mixtures as sessile drops on a tilted PTFE incline is investigated here. The slip angles found showed complex relationships in relation to the mixture composition. Since the drop was found to breach its front contact line first, the levels of contact angle hysteresis did not have corresponding trends with the slip angles. However, the ratios of the drop lengths (at the point of detachment against that at equilibrium) had corresponding trends with the slip angle. The drop elongated in a two-stage manner as it was tilted progressively. Since this could not be ascribed to a sudden change in the gravitational force acting, it implied that the drop extended first as a single body before attempting to split into two. In considering the energetics involved, the change in the solid–liquid area was mainly used by the drop to adjust to the energy supplied by gravity. Comparative experiments done with drop compression and extension on the same surface eliminated the contribution from specific characteristics associated with the liquid and solid, and inaccuracies in the contact angle measurement method used. Turbidity measurements indicate the viability of using higher glycerol content to improve thermal stability of bovine serum albumin. The findings have important implications on the manner of how heat and mass transfer occurs for drops on inclines for biochemical applications.

© 2015 Elsevier B.V. All rights reserved.

* Corresponding author. Fax: +61 3 99051825.
 E-mail address: engngtw@gmail.com (T.W. Ng).

<http://dx.doi.org/10.1016/j.colsurfa.2015.09.007>
 0927-7757/© 2015 Elsevier B.V. All rights reserved.

1. Introduction

Drops on surfaces are widely encountered in nature and in a broad range of applications. There has been recent keen interest to apply drops in microfluidic batch-wise or discrete volume processes for biochemical analysis, where a precisely known volume of liquid is added to another and the mixture undergoes a series of unit operations, such as mixing, separation, and detection phases [1–4]. It also plays a role in the ability of droplets to fill capillaries, for instance, which is vital in new schemes of microplate instrumentation [5,6], and particle harvesting [7]. The obvious challenge in designing a working microfluidic device for such a purpose is to allow a discrete liquid drop to move on a surface. In this context, the use of gravitational forces via altering the surface's incline is arguably most convenient. In terms of the liquid media, there is wide interest to apply glycerol mixtures. Glycerol is a simple colorless, odorless, polyol (sugar alcohol) compound that is widely used in pharmaceutical formulations [8,9] due to its high solubility in water [10]. The important advantageous features that it has in biochemical applications are low evaporation [11] and the capacity to lower damage to cells during cryopreservation [12]. Bovine serum albumin (BSA) is a globular protein that is widely used in molecular biology, biochemistry and therapeutic applications because of its stability, lack of interference in many biochemical reactions, easy availability and relatively low cost. BSA is well known as a stabilizer of proteins and enzymes against thermal inactivation [13]. Both BSA and glycerol have also been shown to enhance polymerase chain reaction (PCR) amplification, a technique that has broad applications in cloning, gene expression studies, genetic analyses and diagnostics [14]. Increased understanding of thermal characteristics will facilitate optimization of BSA as a stabilizer, in particular when applied in the form of moveable drops on surfaces to conduct various biochemical processes and interrogations.

It is crucial to note that glycerol has higher viscosity (~1.4 Pa s) than water (~0.001 Pa s), which presents challenges such as clogging when used in conjunction with closed channel microfluidic devices. However, its application on open surfaces in the

form of droplets may overcome these problems. Many analytical, experimental and numerical studies have explored drop motion on an incline. The most widely used relationship to account for this is based on Young's equation in which the liquid–vapor, liquid–solid, and solid–vapor forces dictate the contact angle. When the drop is static, it is able to exhibit both advancing and receding contact angles (Fig. 1b). Many models, some with high degrees of mathematical complexity, have been devised to account for this effect [15,16]. This is in contrast to the cases where the drop is compressed (Fig. 1c) or extended (Fig. 1d) in an axis-symmetric manner, where it will exhibit exclusive advancing or receding angles respectively.

It has been observed that when a drop placed on a surface is subjected to increasing and gradual inclination relative to the horizontal, its front contact line breaches first [17,18]. Hence, the drop is able to exist in an extended shape in one direction before a high enough incline is able to cause its total detachment from the surface (Fig. 1b). To some extent, such a behavior is akin to a pendant drop dripping from a faucet [19]. From an application perspective, it will be instructive to be able to predict the extent in which the drop is able to withstand the degree of inclination of the surface, especially on surfaces that are weakly wetting. Based on the models developed [15,16], monitoring the contact angles should be a possibility, albeit this has not been confirmed conclusively from experiments. In this work, we conduct tests on glycerol–water mixture drops dispensed on a polytetrafluoroethylene (PTFE) surface which is hydrophobic (equilibrium contact angle >90°). In the main set of experiments, these drops will be quasi-statically tilted to the point where they displace from the surface. The contact angle behavior will be compared using experiments in which the drops are subjected to compression and extension. The viability of BSA in the glycerol–water mixtures used will be also examined in relation to extreme temperature changes with implications for useful applications, for example, in the enhancement of PCR amplifications [14].

The action of surface tension can be viewed from the perspective of surface energy (energy per unit area of the surface). When a liquid body touches a solid surface, it can spread out due to the

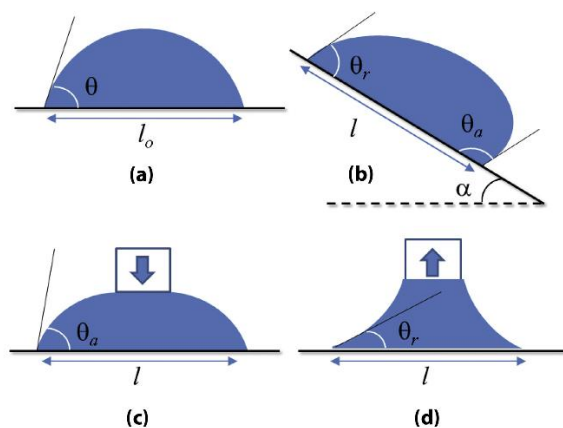


Fig. 1. The placement of a drop on a (a) horizontal surface will typically result in an equilibrium contact angle θ with width l_o , based on a semi-spherical shape. When (b) tilted at an angle α to the horizontal, the drop will assume an advancing θ_a and receding θ_r contact angles. It is often the case that the drop will breach at the advancing ahead of the receding contact line. Consequently, the drop is elongated in one direction such that $l > l_o$. The situation is different when the drop is compressed (c) and extended (d), where it will solely exhibit advancing and receding contact angles respectively.

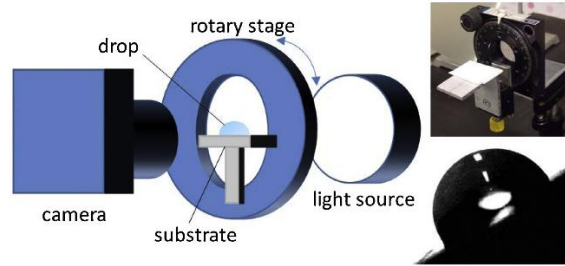


Fig. 2. The experimental setup to observe the drop change to detachment. In using a rotary stage with a through hole, and positioning the drop at the gimbal point, it was possible to rotate the drop through a wide range of inclines, and eschewing the need to reposition the camera each time. The inset pictures show the setup without the camera and light source, as well as an example image of the drop recorded.

interfacial energies in the system, comprising the surface–liquid interfacial tension (γ_{SL}), the surface–vapor interfacial tension (γ_{SV}), and the liquid–vapor interfacial tension (γ_{LV}). In this process, the flat area between the drop and the surface, A_{SL} , increases, while the exposed-to-the-air substrate surface flat area, A_{SV} , decreases. Depending on the shape development, changes to the liquid-to-vapor area A_{LV} may also vary. The spreading will stop when equilibrium is reached such that the work done by spreading δ_w goes to zero. In the process, it will also be necessary to include the contribution of work done by change in total volume of liquid dV as well as the Laplace pressure change ΔP between the inside and outside of the drop. Hence, it will be possible to express the whole process as

$$\delta_w = \gamma_{LV}dA_{LV} + \gamma_{SL}dA_{SL} + \gamma_{SV}dA_{SV} + dV\Delta P \quad (1)$$

In the general sense, it is possible to assume that $dA_{SL} = -dA_{SV}$. In addition, $dV = 0$ since the liquid can generally be taken as incompressible. Consequently, Eq. (1) can be simplified to

$$\delta_w = \gamma_{LV}dA_{LV} + (\gamma_{SL} - \gamma_{SV})dA_{SL} \quad (2)$$

If the drop is tilted quasi-statically on an incline, the incremental work done is asserted by the gravitational acceleration g such that the elongation drop is displaced through its center of mass by Δx in which

$$\rho V g \sin(\alpha) \Delta x = \gamma_{LV}dA_{LV} + (\gamma_{SL} - \gamma_{SV})dA_{SL} \quad (3)$$

where ρ is the fluid density and V its volume.

2. Methods

2.1. Materials

The substrate used in the experiments was a hydrophobic PTFE block. The characteristics of the substrate surface was verified using an optical profiler (Bruker Contour GT-1). It is based on employing phase-shifting and/or vertical scanning interferometry to resolve the topology of complex 3D structures. The technique is able to marry precision z-axis control with interference based techniques to resolve features from the angstrom to millimetre scale.

Glycerol/water mixtures ranging from 0 to 100% glycerol by volume, were prepared by adding glycerol (Sigma–Aldrich, G5516) to Milli-Q water. These solutions were prepared in polypropylene centrifuge tubes and mixed to homogeneity using a vortex mixer (Proscitech EVM80). The mixtures were allowed to settle for 1 h before use. For all experiments associated with drop on an incline, the temperature and relative humidity ranges were 20–22 °C, and 50–56% respectively.

0.1 g of BSA lyophilized powder of $\geq 96\%$ purity (Sigma–Aldrich) was weighed in using an electronic balance and placed into an Eppendorf tube. 2.5 mL of distilled water was then pipetted into the tube and mixed thoroughly with a vortex mixer at low power to create 4% wt of BSA solution. 900 μ L of 0–100% water–glycerol mixtures were prepared in separate Eppendorf tubes. 6 μ L of the BSA solution was pipetted into a quartz cuvette together with 294 μ L of distilled water. The two mixtures were mixed thoroughly using the vortex mixer at low power. The pH of the solution was 7.0.

2.2. Drop on incline experimentation

The experimental setup is depicted in Fig. 2 in which an opto-mechanical rotary stage (Edmund Optics, 52-572) with 1° resolution was adapted to permit a drop to be located on the PTFE substrate to correspond to the gimbal position. This circumvents the need to move the camera when different amounts of tilts are applied and also to allow the substrate to tilt over a large angular range. A bright LED lamp with diffuser was used to provide the lighting for recording. A video camera attached to an InfiniVar CFM-2/S microscope lens was used to image the drop. A manual pipette (VITLAB, 1641000) was used to accurately dispense a 10 μ L volume of the mixture on the substrate surface. The stage was tilted at intervals of 1°. In between each tilt, a delay of 30 s was introduced to permit the drop to acquire a quasi-static equilibrium state. Six readings were made for each drop mixture to confirm the drop characteristics. Since the images recorded had high contrast, we did not perform any post-processing operations on them. The geometrical values of the drop (angles and lengths) were derived using the software Tracker (<https://www.cabrillo.edu/~dbrown/tracker/>).

2.3. Drop compression and extension experimentation

In this set of experiments, a manual pipette (VITLAB, 1641000) was used to accurately dispense a 10 μ L volume of the mixture on the substrate surface. In assessing compression, a solid stainless steel rod of diameter 1.270 mm was then lowered slowly at a speed of 0.00001 mm/s onto the center of drop towards the substrate. A sequence of images was recorded to establish the contact angle development. In assessing extension, the same stainless steel rod was lowered until it just contacted the center of drop. It was then raised slowly away from the substrate. A sequence of images was again recorded to establish the contact angle development using Tracker.

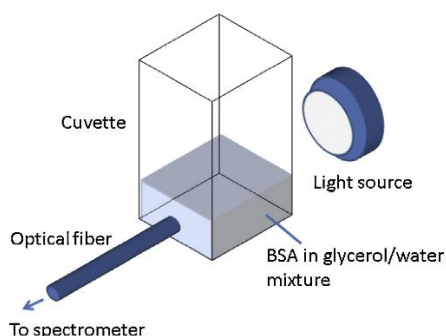


Fig. 3. The experimental setup to examine the optical behavior of BSA in glycerol–water mixtures. The samples were added to a cuvette in which a broadband light illuminated it and the transmitted light collected using an optical fiber that connects to a spectrometer.

2.4. Optical behavior of BSA in glycerol–water mixtures with temperature changes

The setup used to conduct the optical measurements is shown in Fig. 3. The cuvette containing the BSA sample in glycerol–water mixture was placed on a Peltier heater that was driven by a DC power supply. The voltage was kept constant at 6.5 V while a thermocouple was used to measure the temperature on the surface of the Peltier heater. Due to the relatively slow heating and small volume of sample used, it is assumed that the thermocouple readings will be indicative of the temperature of the sample. For one set of readings, the temperature against time was recorded to obtain the heating signature of the system. Following this, experiments were conducted to record the light spectrum using an optical fiber connected to a spectrometer (Ocean Optics) at every 5 °C temperature rise from 25 °C to 95 °C. In between each set of readings, the power supply was switched off to allow the Peltier heater to cool down to room temperature. The experiment was repeated by replacing the distilled water with water–glycerol mixtures ranging from 10% to 100% glycerol. During this experiment, the average relative humidity was recorded at 55%.

3. Results and discussion

The optical profilometry scans conducted do not reveal extraordinary structures of the PTFE sample used (Fig. 4). In addition, no anisotropy was found that would suggest that there would be directional influences on the drop in terms of surface wetting behavior. From a typical scan comprising 298512 data sampling points, the peak-to-peak value and root mean squared roughness parameters were measured to be 11.819 μm and 0.571 μm , respectively.

In the plots given in Fig. 5, it can be seen that the equilibrium contact angle (with zero incline) distribution was relatively similar regardless of the mixture composition. When tilted to the extent just before total detachment from the surface, there was a general trend of the advancing contact angle being larger than the receding contact angle. This represents the contact angle hysteresis that is often used to account for the added ability of drops to stay on inclines. However, it can be seen that the level of hysteresis does not appear to have any bearing on angle of incline (slip) in which the drop completely detaches from the surface. What is also noteworthy is the advancing contact angle even being generally smaller than the equilibrium contact angle.

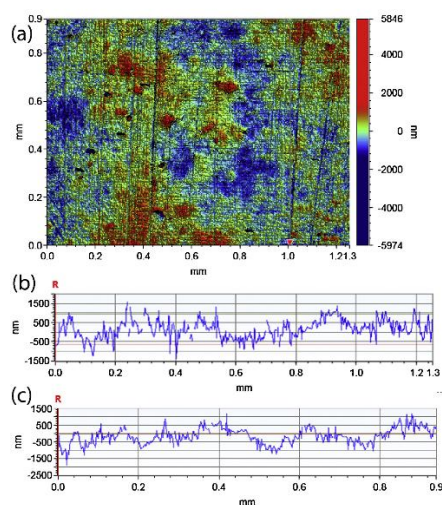


Fig. 4. Typical (a) area topographic scan from an area on the PTFE substrate using optical profilometry. Horizontal (b) and vertical (c) line sections taken from the scan do not reveal any anisotropy in the topographic distributions.

This seemingly anomalous behavior with the contact angle can be explained by the ability of the drop to breach its front contact line first [17,18]. With the back contact line still pinned to the surface, the drop is able to undergo a transient elongation. In making comparisons to solid mechanics, one could classify this elongation as plastic since the drop will not resume its original length even if the incline was set back to horizontal. Due to the quasi-static manner in which the incline was tilted, it was possible for us to rule out any flow dominated effects. Instead, it is a relaxation mechanism due to this elongation that allows the drops to assume contact angles that are smaller at advancing than at equilibrium.

The trend of the slip angle in Fig. 5 indicates a complex relationship between the adhesion forces of mixture-dependent composition of glycerol and water to the PTFE surface. This relationship is likely governed by the capacity of the surface to retain bubbles on the surface. Surfaces that are inherently hydrophobic, such as PTFE, if treated to have substantial micro and nanostructures, have the capacity to be highly non-wetting and exhibit very high equilibrium contact angles ($>120^\circ$) to render them superhydrophobic (SH) [20,21]. When immersed in water, SH surfaces have been shown to develop a stable thin film of air called a plastron [22,23]. Plastrons are also believed to be responsible for the ability of sessile bubbles to exist on the SH surfaces at volumes much larger than anticipated [24]. On non-SH PTFE, it is conceivable that regions of non-visible surface air entrapment may continue to exist even when the larger bubbles dissipate through diffusion [17]. In aqueous solutions, glycerol is well known to be able to disrupt the hydrogen-bonded structure of water, thereby making the solution more compact [25]. Molecular dynamics simulations conducted on glycerol–water liquid mixtures with higher weight percentages of glycerol, revealed the existence of heterogenous systems wherein surrounding water molecules have a large influence on the populations of glycerol conformational isomers (or conformers) [26]. While the local structure of water in the mixture can appear close to its counterpart in the pure state, the glycerol structure can exist

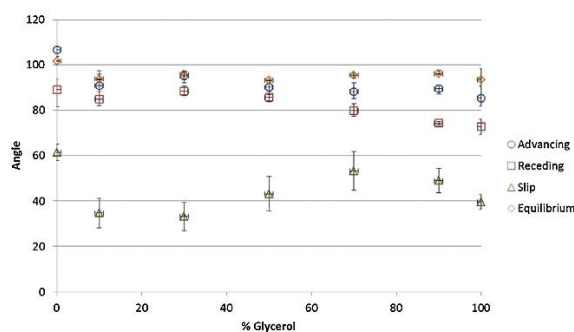


Fig. 5. Plots showing the distributions of drop equilibrium contact angle (when the drop was on a horizontal surface) as well as the slip angle, advancing and receding contact angles recorded for glycerol–water mixtures (ranging from 0 to 100% glycerol) on the PTFE substrate that was slowly tilted to the point just before detachment of the drop from the surface. The slip angle distributions were irregular, and do not follow the trends of the advancing and receding contact angles. Advancing and receding contact angles tend to decrease with increase in the proportion of glycerol in the mixture. The error bars indicate one standard deviation from 5 readings.

in three different forms; as molecules occurring in an environment reflective of pure glycerol, as monomers solvated by water, and as mixtures of H-bonded clusters connected in a 3-D glycerol H-bond network with water molecules. It is highly likely that in the presence of these micro-heterogeneities in the water–glycerol mixture, a capacity to develop complex wetting characteristics arose as the liquid interacted with the solid PTFE surface. This in turn, had an effect on the extent of air bubble entrapment on the surface. When these air bubbles interacted with the contact line, they had the ability to affect the ability of the drop to be retained on the inclined surface.

Notwithstanding, it will be useful to be able to relate the slip angle to a physical parameter of the drop. Fig. 6 provides a plot of the distributions of l/l_0 ratios (at the point of detachment of the drop) in relation to the glycerol–water mixture used. It can be seen that the trends mimic closely with the trend of slip angles presented in Fig. 5. The relatively large spread in values of the slip angles and l/l_0 ratios found can be attributed to the readiness of the PTFE surface to trap air bubbles randomly on surfaces. Better insight into the correlation between slip angle and l/l_0 ratio can be obtained by tracing the important parameters of the drop with increase in the angle of incline up to the point of its slippage from the surface. Fig. 7 provides the case in which the advancing and receding contact angles were traced with a drop of water and another with a drop containing 30% glycerol (inset). From the plots, it can be seen that the contact angles do not provide any indication of the tendency of the drops to either elongate or slip from the surface. This is to be expected if one considers that contact angles are mere manifestations of how the drop assumes shapes in order to minimize its surface energy in response to the increasing perturbation by gravity.

However, tracing the length of the drops (Fig. 8) provided a very different outcome. Here it can be seen that in both pure water and with 30% glycerol, the drops yielded a two-stage manifestation of elongation. Such a behavior cannot be ascribed to a sudden change in the gravitational force acting on the drops, which is a function of the sine of the tilt angle (see inset of Fig. 7). This implies that in the initial stage, the drop was extending as single body. In the second stage, however, the drop was attempting to initiate a process of splitting into two, in which the heightened extension rate is caused by the front end of the liquid body having a greater motive force compared with the rear end that seeks to stay. Due to the limited surface energy change that the drop is able to withstand

before slippage, it is unable to proceed to the point of rupture, which would have caused a daughter droplet to develop at the rear and remain on the surface. In some way, it is possible to conceptualize the mechanics to be somewhat similar to a liquid bridge that is quasi-statically stretched [27] or evaporated [28] between two solid surfaces. In particular, the ability of the liquid body to displace has been seen when one of the surfaces is a nozzle where the liquid contained in it could be “pulled” out [29]. The situation of drops undergoing frustrated attempts to separate is typically encountered in highly dynamical conditions but typically on surfaces that have low adhesion forces [30,31] which is similar to the situation here. This is not surprising as the liquid body then has higher freedom to undergo shape adjustments more readily. Why then will the drop not proceed to rupture immediately? We contend that this is due to a reverse process reported in which drops have shown to have a tendency to coalesce even when attempting to separate [32].

We consider the energetics involved. If we make the assumption that Δx in Eq. (3) corresponds to a change in l , it can be argued that a substantial portion of work done by the drop to account for the energy change due to gravitational increase may in fact be supported by dA_{SL} . Such an assumption is reasonable since the extent of shape deformation for drops on a hydrophobic surface is not as extensive as drops on more hydrophilic surfaces, where corners, which can lead to pinching, have been known to develop [33]. Since the extent of shape deformation is more restrained on hydrophobic surfaces, it is possible for dA_{SV} to be more limited, thus allowing dA_{SL} to dominate when the drop attempts to energetically adjust to the energy supplied by gravity. It is also conceivable that the limited extent of dA_{SV} may then permit the drop to assume advancing contact angles that do not deviate much from equilibrium, since less work is needed to achieve the limiting condition at the front contact line.

Fig. 9 presents traces of contact angle development with time for a liquid drop that was compressed and extended respectively. During the compression process (a), the contact angle can be seen to be moving towards an advancing state before reaching a limiting value of $\sim 102^\circ$. When extended (b), the contact angle alternatively reduced to a receding state before arriving at a limiting value of $\sim 85^\circ$. Both these behaviors are typical of that reported previously in the literature with non-wetting surfaces [34] and thus show that the behavior with drops on the incline are neither caused by surface or liquid characteristics, but on the manner in which the liquid body

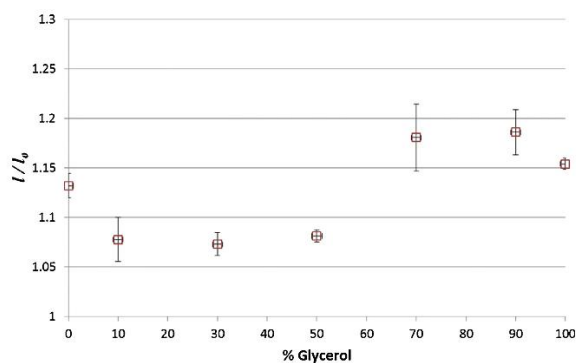


Fig. 6. Plots of l/l_0 ratios with varying glycerol–water composition where drops are placed on PTFE (Teflon). The distribution of the latter show similar trends to the slip angles in Fig. 4. This indicates a relationship between the extent of elongation of the drop and its capacity resist detachment as the PTFE surface is slowly but increasingly tilted. The error bars indicate one standard deviation from 5 readings.

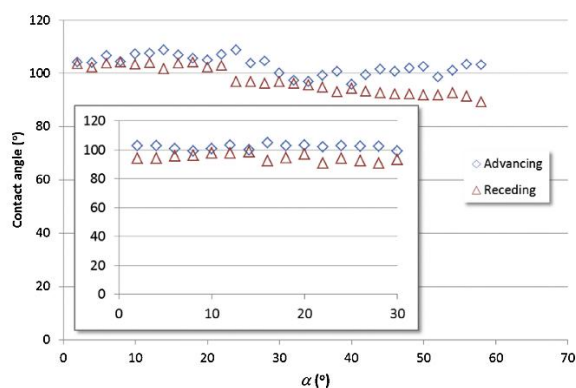


Fig. 7. Traces of the advancing and receding contact angles of a water drop with various tilting of the incline. The inset gives the case with 30% glycerol in a mixture with water. In all cases, the contact angle does not provide information on the propensity of the drop to slip or to deform on the incline prior to slipping.

tries to minimize its energy on the surface. Specifically for a drop on an incline, the three phase contact line is essentially unbalanced, compared to the case where it is compressed or extended. The effect of using the length of the drop to accommodate for this imbalance will not be significant when the surface is wetting, as the higher adhesion forces will restrict extension whilst allowing the drop to undergo angular distortions (resulting in contact angle changes). The low adhesion forces on a poorly wetting surface alternatively permits the contact width extension and thus does not need the angular distortion to accommodate for the additional energy. The results in Fig. 9 also infer that the somewhat invariant contact angle trends in Fig. 7 are not caused by inaccuracies in the manner in which they are measured.

We make some comments on applications. While superhydrophobic surfaces promise the capacity of liquid transfer with low amounts of sample loss (i.e. from low levels of adhesions) and contamination in biochemical analysis, the control of drop movement will expectedly be difficult in systems that apply simple tilting unless the surfaces can be shaped to provide gravitational

potential wells and movement achieved by external perturbation. It is envisaged that regions on a surface that are both hydrophobic and superhydrophobic will be needed to create a practicable system. The manner in which the drop elongates, offers the capacity to match the hydrophobic region to the extent of extension within the first stage. Logically then, a consistent tilt angle to drop detachment, notwithstanding the mixture composition, may be achievable, thus facilitating automation. Apart from the low evaporation characteristics offered, drop movement using water–glycerol mixtures is useful due to their protein stabilizing properties in biochemical processes such as protein crystallization and pharmaceutical protein formulation [35] which is derived from its ability to preserve protein stability and functionality [36]. It should also be noted that once drop movement commences, mass and heat transfer can be facilitated due to the wall shear stresses developing [37]. However, there are other advantages offered in the use of glycerol as the medium for which proteins are able to remain in.

An examination of the influence of glycerol on the thermal stability of BSA can provide insights into the influence of neutral

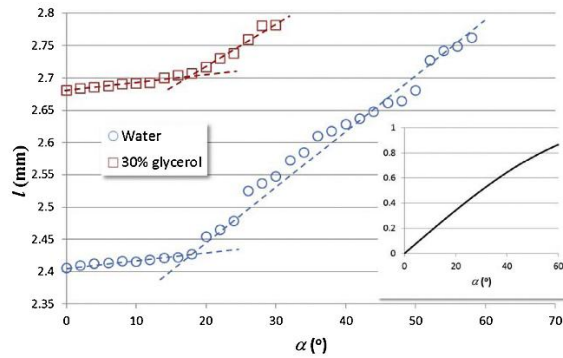


Fig. 8. Traces of the length of drop with progressive change in the tilt angle of incline for a drop of water and a mixture containing 30% glycerol. A two-stage elongation process is observed for the drops. The inset provides a plot of the sine of α in relation to the change in α , which provides a scaling of progressive force due to gravity acting on the drop.

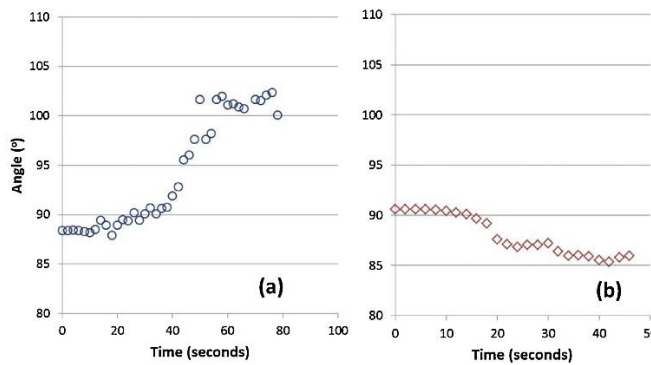


Fig. 9. Traces of the (a) advancing contact angle when a drop of glycerol–water liquid mixture (50% glycerol) was slowly compressed, and the (b) receding contact angle when it was slowly extended with time. The substrate was also PTFE.

co-solvents on protein functionality in gels. One method to do this is to trace the level of turbidity since it provides an indirect indication of aggregation. A metric to determine the level of turbidity is to calculate its absorbance. For a wavelength of light that passes through the sample at its original state into the spectrometer, it is possible to determine the intensity I_0 which is useable as reference. Any intensity I that is subsequently measured can then be used to determine the absorbance by assuming adherence to the Beer–Lambert law, such that it corresponds to the state of turbidity of the sample, via

$$A = \log_{10} \left(\frac{I_0}{I} \right) \quad (4)$$

In our measurements, we use the intensity recorded at 25 °C as the value for I_0 . The results, as depicted in Fig. 10, indicate the levels of absorbance recorded at 600 nm in relation to temperature as it was raised with time (the temperature–time trend associated with the heating is given in the inset graph). With 10% glycerol, it can be seen that a significant increase in turbidity occurred when the temperature reached 75 °C. With 30% glycerol, alternatively, the temperature corresponding to this increase was shifted to 95 °C.

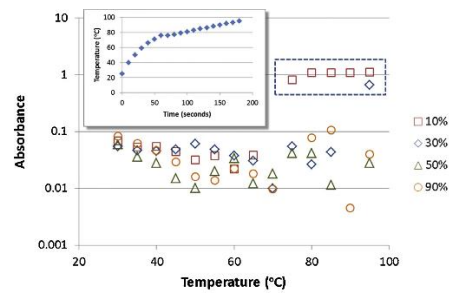


Fig. 10. Plots of the absorbance changes in BSA dissolved in solutions containing varying glycerol–water compositions when heated from 25 °C to 95 °C. When aggregation occurs in response to temperature, the sample undergoes significant absorbance (at 600 nm) increase (see points grouped by dashed box). The inset graph indicates the heating rate of the samples.

Not surprisingly then, mixtures with glycerol content above 50% exhibited no increase in turbidity as the temperature was raised up to 95 °C. These results indicate the thermal stabilizing effect that increasing glycerol content offers for BSA. It should be noted that turbidity depends on both the size and concentration of protein aggregates formed. Hence, any attempt to use the results here to infer the aggregation rate should be treated with caution, since the aggregate size may have changed with time and solution composition.

The findings here portend the ability to assist in the creation of biochemical devices that seeks to make use of droplet movement as well as mass and heat transfer modes in applications.

4. Conclusions

The equilibrium contact angle (with zero incline) distribution of a drop on a PTFE surface was found to be relatively similar with various glycerol–water mixture compositions. However, the slip angle trend was complex as it is governed by the capacity of the surface to retain bubbles on the surface. In aqueous solutions, glycerol is known to be able to disrupt the hydrogen-bonded structure of water, thereby making the glycerol structure able to develop micro-heterogeneities, which would then cause the wetting characteristics to be determined by how the liquid interacts with both the solid as well as the air entrapped within the surface microstructures. When tilted to the extent just before total detachment from the surface, the drop was found to breach its front contact line first. This caused the levels of advancing and receding contact angles not to have any bearing on the slip angle, in fact the advancing contact angle was found to be generally smaller than the equilibrium contact angle. Alternatively, the l/l_0 ratios (at the point of detachment of the drop) showed trends that closely followed that of the slip angles. In tracing the length of the drops, a two-stage elongation was found. Since such a behavior could not be ascribed to a sudden change in the gravitational force acting on the drops, it implied that the drop was extending as single body initially, but then attempted to initiate a process of splitting into two. In considering the energetics involved, it could be surmised that dA_{SL} was main factor used by the drop adjust to the energy supplied by gravity, while dA_{SV} was limited. Comparative experiments using drop compression and extension eliminate the possibility that specific characteristics associated with the liquid and solid could be responsible for this behavior. Turbidity measurements indicate the viability of using higher glycerol content to improve thermal stability.

Acknowledgements

T.W. and O.W. acknowledge funding support from the Australian Research Council through DP120100583. This work was performed in part at the Melbourne Centre for Nanofabrication (MCN) in the Victorian Node of the Australian National Fabrication Facility (ANFF). The assistance of Hemayet Uddin, Melbourne Centre for Nanofabrication, in obtaining the optical profilometry traces of the PTFE surface is appreciated.

References

- [1] W. Bou-Zeid, D. Brutin, Effect of relative humidity on the spreading dynamics of sessile drops of blood, *Colloids Surf. A: Physicochem. Eng. Aspects* 456 (2014) 273–285.
- [2] Y. Wang, Y. Zhao, S.K. Cho, Efficient in-droplet separation of magnetic particles for digital microfluidics, *J. Micromech. Microeng.* 17 (2007) 2148–2156.
- [3] C. Planchettea, E. Lorenceaua, G. Brenn, Liquid encapsulation by binary collisions of immiscible liquid drops, *Colloids Surf. A: Physicochem. Eng. Aspects* 365 (2010) 89–94.
- [4] L. Mazutis, J. Gilbert, W.L. Ung, D.A. Weitz, A.D. Griffiths, J.A. Heyman, Single-cell analysis and sorting using droplet-based microfluidics, *Nat. Protocols* 8 (2013) 870–891.

- [5] X.Y. Li, B.H.-P. Cheong, A. Somers, O.W. Liew, T.W. Ng, Surface-scribed transparency based microplates, *Langmuir* 29 (2013) 849–855.
- [6] B.H.-P. Cheong, V. Diep, T.W. Ng, O.W. Liew, Transparency based microplates for fluorescence quantification, *Anal. Biochem.* 422 (2012) 39–45.
- [7] B.H.-P. Cheong, M. Muradoglu, O.W. Liew, T.W. Ng, Concentrating nanoparticles in environmental monitoring, *Environ. Toxicol. Pharmacol.* 40 (2015) 187–190.
- [8] M. Lexis, N. Willenbacher, Yield stress and elasticity of aqueous foams from protein and surfactant solutions—The role of continuous phase viscosity and interfacial properties, *Colloids Surf. A: Physicochem. Eng. Aspects* 459 (2014) 177–185.
- [9] H. Zhang, M.W. Grinstaff, Synthesis of atactic and isotactic poly(1,2-glycerol carbonate)s: degradable polymers for biomedical and pharmaceutical applications, *J. Am. Chem. Soc.* 135 (2013) 6806–6809.
- [10] A. Madeira, M. Camps, A. Zorzano, T.F. Moura, G. Soveral, Biophysical assessment of human Aquaporin-7 as a water and glycerol channel in 3T3-L1 Adipocytes, *PLoS One* 8 (2013) e83442.
- [11] G. MacBeath, S.L. Schreiber, Printing proteins as microarrays for high-throughput function determination, *Science* 289 (2000) 1760–1763.
- [12] J.G. Baust, D. Gao, J.M. Baust, Cryopreservation an emerging paradigm change, *Organogenesis* 5 (2009) 90–96.
- [13] B.S. Chang, R.R. Mahoney, Enzyme thermostabilization by bovine serum albumin and other proteins: evidence for hydrophobic interactions, *Biotechnol. Appl. Biochem.* 22 (1995) 203–214.
- [14] E.M. Farrell, G. Alexandre, Bovine serum albumin further enhances the effects of organic solvents on increase yield of polymerase chain reaction of GC-rich templates, *BMC Res. Notes* 5 (2012) 257.
- [15] G. Ahmed, M. Sellier, Y.C. Lee, M. Jermy, M. Taylor, Modelling the spreading and sliding of power-law droplets, *Colloids Surf. A: Physicochem. Eng. Aspects* 432 (2013) 2–7.
- [16] L.A. Caffarelli, A. Mellet, Capillary drops: contact angle hysteresis and sticking drops, *Calc. Var. Part. Differ. Equ.* 29 (2007) 141–160.
- [17] W.Y.L. Ling, T.W. Ng, A. Neild, Effect of an encapsulated bubble in inhibiting droplet sliding, *Langmuir* 26 (2010) 17695.
- [18] W.Y.L. Ling, T.W. Ng, A. Neild, Q. Zheng, Sliding variability of droplets on a hydrophobic incline due to surface entrained air bubbles, *J. Colloid Interface Sci.* 354 (2010) 832–842.
- [19] M.R. Davidson, J.J. Cooper-White, Pendant drop formation of shear-thinning and yield stress fluids, *Appl. Math. Modell.* 30 (2006) 1392–1405.
- [20] F. Wang, S. Yu, J. Ou, M. Xue, W. Li, Mechanically durable superhydrophobic surfaces prepared by abrading, *J. Appl. Phys.* 114 (2013) 124902.
- [21] C.V. Lau, T. Vuong, J. Wang, M. Muradoglu, O.W. Liew, T.W. Ng, Hydrophobic to superhydrophobic surface modification using impacting particulate sprays, *Appl. Surf. Sci.* 311 (2014) 89–94.
- [22] M.J. Maysner, H.F. Bohn, M. Reker, W. Barthlott, Measuring air-layer volumes retained by submerged floating-ferns *Salvinia* and biomimetic superhydrophobic surfaces, *Beilstein J. Nanotechnol.* 5 (2014) 812–821.
- [23] X. Sheng, J. Zhang, Air layer on superhydrophobic surface underwater, *Colloids Surf. A: Physicochem. Eng. Aspects* 377 (2011) 374–378.
- [24] W.Y.L. Ling, G. Lu, T.W. Ng, Increased stability and size of a bubble on a superhydrophobic surface, *Langmuir* 27 (2011) 3233–3237.
- [25] M. Ueda, A. Katayama, N. Kuroki, T. Urabata, Effect of glycerol on the solubilities of benzene and toluene in water, *Colloid Polym. Sci.* 254 (1976) 532–533.
- [26] A.V. Egorov, A.P. Lyubartsev, A. Laaksonen, Molecular dynamics simulation study of glycerol–water liquid mixtures, *J. Phys. Chem. B* 115 (2011) 14572–14581.
- [27] A. Sanz, J. Martinez, Minimum volume for a liquid bridge between equal disks, *J. Colloid Interface Sci.* 93 (1983) 235–240.
- [28] P.V. Petkov, B.P. Radoev, Statics and dynamics of capillary bridges, *Colloids Surf. A: Physicochem. Eng. Aspects* 460 (2014) 18–27.
- [29] W. Schwab, T.W. Ng, J.K.K. Lye, O.W. Liew, B.H.-P. Cheong, Surface tension drawing of liquid from microplate capillary wells, *J. Colloid Interface Sci.* 365 (2012) 314–319.
- [30] M. Kataraya, T.W. Ng, Drops transformed from a continuous flow on a superhydrophobic incline, *J. Phys. D: Appl. Phys.* 46 (2013) 345302.
- [31] M. Kataraya, T. Vuong, T.W. Ng, Liquid body formation from a semi-spherical superhydrophobic well on a small incline, *Langmuir* 30 (2014) 13731–13736.
- [32] A. Lai, N. Bremond, H.A. Stone, Separation-driven coalescence of droplets: an analytical criterion for the approach to contact, *J. Fluid. Mech.* 632 (2009) 97–107.
- [33] N. Le Grand, A. Daerr, L. Limat, Shape and motion of drops sliding down an inclined plane, *J. Fluid Mech.* 541 (2005) 293–315.
- [34] S.-J. Hong, T.-H. Chou, S.H. Chan, Y.-J. Sheng, H.-K. Tsao, Droplet compression and relaxation by a superhydrophobic surface: contact angle hysteresis, *Langmuir* 28 (2012) 5606–5613.
- [35] C. Charron, A. Kadri, M.-C. Robert, R. Geigé, B. Lorber, Crystallization in the presence of glycerol displaces water molecules in the structure of thaumatin, *Acta Crystallogr.* 58 (2002) 2060–2065.
- [36] V. Vagenende, M.G.S. Yap, B.L. Trout, Mechanisms of protein stabilization and prevention of protein aggregation by glycerol, *Biochemistry* 48 (2009) 11084–11096.
- [37] B.S. Sikarwar, S. Khandekar, K. Muralidhar, Simulation of flow and heat transfer in a liquid drop sliding underneath a hydrophobic surface, *Int. J. Heat Mass Transfer* 57 (2013) 786–811.

Appendix B

Colloids and Surfaces A: Physicochem. Eng. Aspects 522 (2017) 74–82



Contents lists available at ScienceDirect

Colloids and Surfaces A: Physicochemical and Engineering Aspects

journal homepage: www.elsevier.com/locate/colsurfa

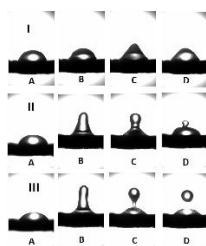
Characteristics of drops on flat microplating surfaces from controlled upward longitudinal impact

Alifa Afiah Ahmadi^a, Chun Yat Lau^a, Mayur Katariya^a, Oi Wah Liew^b, Tuck Wah Ng^{a,*}^a Laboratory for Optics and Applied Mechanics, Department of Mechanical & Aerospace Engineering, Monash University, VIC3800 Clayton, Australia^b Cardiovascular Research Institute, Yong Loo Lin School of Medicine, National University of Singapore, National University Health System, Centre for Translational Medicine, 14 Medical Drive, 117599 Singapore, Singapore

HIGHLIGHTS

- Repeatable upward impact momentums of up to 4.31×10^{-3} Ns on glycerol–water sessile drops was achieved.
- The propensity for the sessile drop to separate diminished with greater glycerol content in the mixture.
- The sessile drops were found to separate more readily when placed on scribed flat microplating surfaces.
- Additional pinning during the phase when the contact angle moved from receding to advancing facilitated separation.
- Finite element analysis indicated enhanced mixing when the separated liquid bodies coalesced.

GRAPHICAL ABSTRACT



ARTICLE INFO

Article history:
Received 16 January 2017
Received in revised form 22 February 2017
Accepted 23 February 2017
Available online 27 February 2017

Keywords:
Impact
Microplate
Water–glycerol
Necking
Drops
Mixing

ABSTRACT

Sessile drops, based on water–glycerol mixtures at 40 μ L, deposited on solid substrates were studied as they were accelerated upwards and then stopped suddenly to create an upward longitudinal impact effect. By varying the initial start positions of the platform in the setup, controlled impact momentums of up to 4.31×10^{-3} Ns could be attained. Three categories of drop behavior, labeled I to III, were uncovered. On the non-scribed substrate types I and II drop behavior were found, whereas all types of demeanor were exhibited by the scribed surface. On the scribed surface, the contact angle is able to recede more (by 20°) than on the non-scribed surface (by 15°). This is primarily due to the strong contact line pinning offered by the parapet and steep scarp formed around the groove. Since the liquid body is able to attain a lower receding contact angle on the scribed surface, this will allow higher adhesion effect of its lower portion even as the upper portion seeks to separate. This manifests in a greater propensity for the liquid body to neck and thus for separation to occur. Numerical simulations reveal the tendency of the separated drops to develop circulations that change direction as they coalesce. There is therefore potential for increased mixing using this mode.

© 2017 Elsevier B.V. All rights reserved.

* Corresponding author.
E-mail address: engngtw@gmail.com (T.W. Ng).
<http://dx.doi.org/10.1016/j.colsurfa.2017.02.064>
0927-7757/© 2017 Elsevier B.V. All rights reserved.

1. Introduction

Biochemical analysis using microfluidic technology continues to enjoy high levels of interest and development since its advent

over a decade ago [1,2]. There is now increasing interest to adopt alternative approaches that are easier to integrate and scale, and overcomes the issue of flow at any one location being dependent on the flow properties of the entire system that are endemic of continuous and closed flow devices. The use of discrete, independently controllable sample volumes [3], in particular with drops on open surfaces [4–6], is one option that is actively investigated. It has the advantage of having the microfluidic function assume a set of basic repeated operations, whereby one unit of fluid can be precisely moved over one unit of distance, thus facilitating the use of hierarchical and modular approaches that then make up flexible and scalable system architectures with high fault tolerance capabilities. Moreover, because sample volumes can be controlled independently, such systems offer greater potential to be reconfigured to change their functionality.

Standard microplates (micro titers) continue to be the tool of choice for liquid handling in analytical research and clinical diagnostic screening [7,8]. Their parallel architecture and standardized formats offer the ability for high throughput processing and easy instrumentation development, respectively. One aspect of microplate advancement has been to find more effective ways to dispense and manage the testing of increasingly smaller liquid volumes where poor well filling is a demonstrated problem [9]. An approach of using scribed transparency-based versions has been shown to overcome this problem [10,11]. They are also demonstrated to be able to sustain an appreciable degree of inadvertent sidelong impact without liquid sample spilling or displacement despite their seemingly less robust appearance in terms of handling stability [12]. In the process of this sidelong impact, capillary waves were found to travel toward the contact line at the opposite end. The scribed edges on the surface, through heightened pinning, could increase the amplitude of the wave to some extent, and would also multiply its resistance to spreading if the advancing contact angle condition was not exceeded [12]. These capillary waves are formed as a means to dissipate the mechanical energy supplied to the system. These perturbations understandably are not of the extent that they are able to offer strong bulk mixing of the liquid sample.

There are however, specific driving forces that can cause sessile drops to clearly exhibit resonance. In such a case, it may be possible for bulk mixing and even particle assembly to occur [13]. The need to provide a driving excitation to match the sessile drop's resonant frequency necessitates the availability of precision equipment to do so. However, if stochastic excitation is introduced such that it falls within the range the resonant frequency resides in, it is possible for the system to be set into resonance. This has been demonstrated with drops (i) rolling down a surface with asperities lithographically produced using fibrils of well-defined lengths, cross-sections and spacing [14], (ii) placed on a stationary tip coming in contact with a rotating SH drum, such that resonance is maintained primarily from stochastic stick-slip events between the liquid and SH surface [15], and (iii) dispensed on substrates that are created to have a circular hydrophilic region bound by superhydrophobicity so that they exhibited high contact angles, and then translated by a linear stepper actuator [16]. Yet, the extent of mechanical energy transferred from actuation of the liquid body will facilitate enhanced diffusion but not likely to the extent of significant bulk mixing.

In this work, we report findings in which sessile drops are accelerated upwards and then stopped suddenly to create a longitudinal impact effect. This contrasts sharply with previous studies made of drops released from heights and then impacted on solid substrates [17–20]. The tests were conducted on water–glycerol mixtures at varying volumes. These mixtures are routinely used to preserve the functionality of biological molecules during cooling and thawing processes, and to suppress intracellular ice formation, which

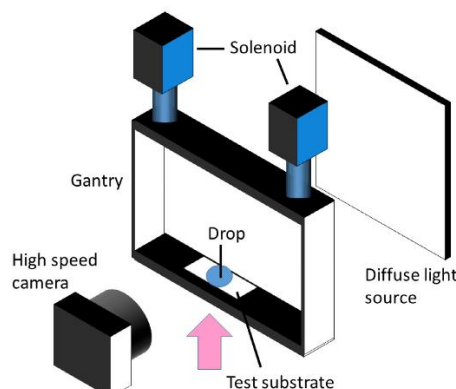


Fig. 1. Schematic description of the setup to conduct the experiments in which a pair of identical solenoids activated simultaneously actuates a gantry containing a substrate with drop dispensed on it. With diffuse illumination from the rear, high-speed camera video sequences of the drop as it was raised and stopped suddenly could be recorded for analysis.

can be harmful to cells and tissues [21,22]. Efforts are made to categorize the range of behaviors exhibited up to the point of liquid body separation. Careful attention is paid to the effects arising from the scribed or non-scribed scheme of the transparency. In the case of the liquid body detachment, numerical simulation is used to assess the liquid flow characteristics in order to deduce the extent of coalescent mixing.

2. Methods

The setup shown in Fig. 1 was used to conduct the experiments. Two pull-only solenoids (Techbrands, SS0902) are used to translate a gantry uniformly upwards. This is made possible by a 12 Volt DC power supply providing an electrical current to them simultaneously via a latching switch. The gantry is made by sawing off a rectangular 50–50 mm aluminum channel of 2.5 mm thickness with a depth of 20 mm. Aluminum was chosen because of its lightweight and rigid features. The test substrate is affixed to the lower surface of the gantry. During tests, specific volumes of liquid are dispensed using a manual pipette (Eppendorf) on the test substrate. Due to the architecture of the gantry, a diffused light source can be used to provide the background illumination to obtain good contrast images on a high-speed camera as the solenoid moves the gantry and stops at the end of each stroke. The movement stroke of the solenoid was adjusted to specific values to obtain different impact effects.

Prior to the experiments with drops being conducted, the gantry movement in relation to the stroke of the solenoids was characterized. This was done by tracking a selected position on the gantry using the high-speed camera video sequences recorded from the moment the gantry started to move to the time that it stopped. The impact momentum can be determined via this analysis. Its maximum value will be limited by the pulling power of the solenoid actuators and the frame rate of the high-speed camera. For the latter, the ability to accurately deduce higher impact momentums will be curbed if the frame-sampling rate is not rapid enough.

Glycerol–water mixtures (0–70% v/v) of 40 μ L volume were used as test liquid drop samples. Glycerol is a simple colorless, odorless; polyol (sugar alcohol) compound widely used in agri-

Table 1
Listing of viscosity and surface tensions of glycerol–water mixtures used.

Glycerol mixture % (v/v)	Viscosity (Ns/m ²) at 20° C	Surface tension (N/m) at 20° C
0	0.001790	0.0728
10	0.002564	0.0717
20	0.003900	0.0707
30	0.006371	0.0697
40	0.011331	0.0688
50	0.022363	0.0679
60	0.050223	0.0670
70	0.13286	0.0662

cultural, chemical, biotechnological, clinical and pharmaceutical industries. Glycerol possesses unique physical and chemical properties that make it particularly advantageous for biological and biotechnological applications in enhancing protein stability, folding and conformational integrity [21,23] and in lowering damage to cells during cryopreservation [22] with new advance applications reported in the development of tissue scaffolds [24] and contrast agent for tumor-targeted magnetic resonance imaging [25]. Glycerol preparations ranging between 10 and 40% are typically used for the preservation of protein activity and stability while high concentrations at 60% have been shown to result in protein destabilization. Hence, glycerol–water mixtures between 0 and 70% v/v was studied and from a physical property perspective, the use of glycerol–water mixtures offers the ability to alter the surface tension and viscosity of samples. The values of these in relation to the mixtures used are shown in Table 1.

All parameters associated with the drop following impact were obtained from the high-speed video sequences. They were derived by selecting specific locations on an initial image followed by frame-by-frame software processing (Tracker).

The substrate used was cellulose acetate film of 0.5 mm thickness. In the case of scribed substrates, samples wells of diameter 6.96 mm reminiscent of standard 96-well microplate well diameter were scribed on the substrate. This was done by placing the cellulose acetate film in a desktop cutter plotter (Wentai, JK361) which had a 90° cutting tip. The force of the needle on the cutter plotter was chosen to ensure that the transparency was not completely cut through. The setting of 500 N was used for best results. Furthermore a speed of 50 mm/s was chosen so that the accuracy of the shape of the design was well preserved.

The scribed substrate was characterized using a 3D optical profilometer (Bruker, Veeco-Wyko) based on a non-contact GT-1 interferometric system. The instrument was located on a pneumatic vibration-isolation table (Newport) which was fitted with active high attenuation isolation and calibrated using step height standards (Bruker, Veeco). The instrument uses phase-shifting and/or vertical scanning interferometry to resolve the topology of structures. Imaging was done using both low and high magnifications in order to derive optimal scanning results.

The capacity of drop mixing was interrogated using numerical simulation. They were based on the finite element method and performed using COMSOL Multiphysics 5.0 based on the geometries of two typical drop sizes coming together. The package allows for an interactive environment to model many scientific and engineering problems based on partial differential equations (PDE) by the finite element method. It is particularly attractive to develop models that require accounting for interconnected physical phenomena. In order to simulate the merging and deformation of the droplets, the model needed to simulate a two phase flow (the flow of liquid and flow of the surrounding air) using the level-set method [26,27]. A two-dimensional mesh model was used since it will sufficiently account for axis-symmetry coalescence. To define the boundary conditions, we assumed the bottom boundary to be a wetted wall

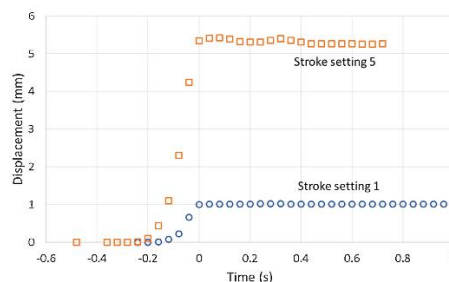


Fig. 2. Displacement versus time traces for two stroke settings of the solenoid used in the experiment. A higher stroke generally produced higher maximum velocities prior to impact.

Table 2
Listing of maximum velocity and impact momentum obtained using the different stroke settings on the solenoid.

Stroke setting	Maximum velocity (mm/s)	Impact momentum (Ns × 10 ⁻³)
1	12.00	1.28
2	20.00	2.13
3	33.60	3.57
4	35.70	3.79
5	40.55	4.31

with a contact angle of 90°, the boundary tangent to the axis symmetry surrounding the droplet was assumed to be an outlet for the airflow and the top boundary was assumed to be a free inlet for airflow. In the simulations, the total elements used ranged from 1.31 × 10⁻⁵ to 3.34 × 10⁻⁵, in which the minimum and maximum element sizes of the fluid phase were 1.31 × 10⁻⁵ and 3.31 × 10⁻⁵, respectively. The absolute tolerances on every model were 5 × 10⁻⁴ to minimize errors. These conditions were arrived from a mesh convergence process conducted. This was also used to confirm that the results obtained were not an artifact of under-resolved geometries.

3. Results and discussion

Fig. 2 provides displacement versus time traces for two stroke settings on the solenoid. While the use of a longer stroke generally provided higher maximum velocities (gradient in the traces), the relationship is non-linear. The maximum velocities determined when multiplied with the moving mass (0.1062 kg) yielded the momentum at impact. These values are listed in Table 2.

There were three general types of drop behavior following impact uncovered. In type I (see Fig. 3), the drop undergoes some axial displacement immediately after impact, but essentially behaves as one single entity throughout. At its highest extension, the drop resembles a cone (C) and before the drop returns to its original semi-spherical shape (A), it takes on an initial pancake-like shape (E).

In type II behavior (see Fig. 4), the drop extends axially to a much greater extent (B). However, being unable to extend further, it begins to experience some instability [28], and the upper section takes on a globular shape with the development of a necking region maintaining a liquid bridge with the main body (C). Subsequently, the upper drop portion collapses downward to the main liquid body with reduction in size of the globular and neck region (D). Finally, the globular and neck region completely disappears and the drop assumes the initial pancake-like shape (E) as observed in type I behavior before returning to its original shape (A).

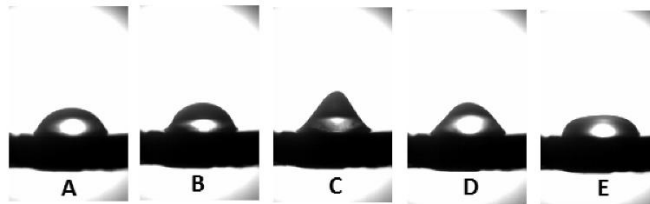


Fig. 3. Type I classification of drop behavior on impact observed in which there is no necking nor separation of the liquid body. This example was based on 10% glycerol–water (v/v).

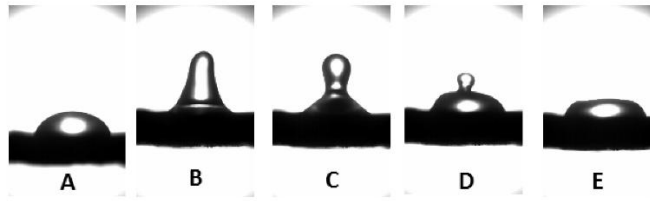


Fig. 4. Type II classification of drop behavior on impact observed in which there is necking but no separation of the liquid body. This example was based on 10% glycerol–water (v/v).

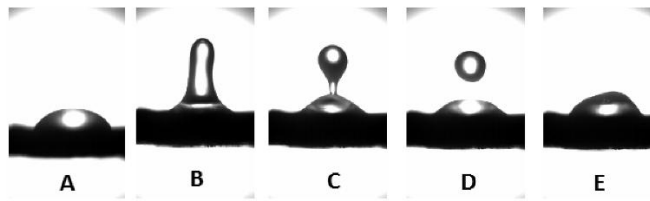


Fig. 5. Type III classification of drop behavior on impact observed in which there is separation of the liquid body. This example was based on 10% glycerol–water (v/v).

Drop separation occurs in type III behavior (see Fig. 5), wherein the wavelength caused by the perturbation exceeds its circumference. In contrast with type II, the drop experiences an even greater extension and narrowing whereby the formation of the globular upper region is accompanied by a very narrow neck (B and C). Consequently, complete pinching off at the neck region results in the detachment of the upper globular region to form two separate bodies. The top liquid body assumes a sphere whereas the bottom liquid body returns to a semi-spherical shape. The former then falls back onto and merges with the latter to reform a single liquid body (E).

On inspecting the region plot for the non-scribed substrate in Fig. 6, only types I and II behaviors were observed, with the latter emerging when higher impact momentum was introduced. This is accounted for by the drop being able to assume a smaller cross-sectional width, and thus being able to approach the Rayleigh instability condition more readily. Increasing the glycerol percentage in the mixture with concomitant increase in viscosity results in enhanced energy dissipation and any perturbations are rapidly damped from the thread. For this reason, there is lower propensity for manifestation of type II behavior with higher glycerol–water mixtures.

In contrast, all three types of drop behavior were observed in the circularly scribed substrate (Fig. 7). Since the composition of

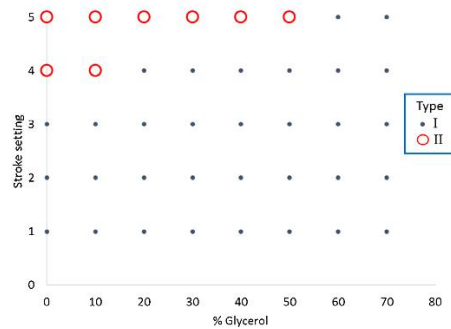


Fig. 6. Region plot of the types of drop behavior observed with varied solenoid stroke settings and percentage of glycerol in the glycerol–water mixture by volume with a non-scribed substrate. The type of behavior is deemed after taking the most prevalent one observed out of 10 recordings at each stroke and glycerol percentage setting.

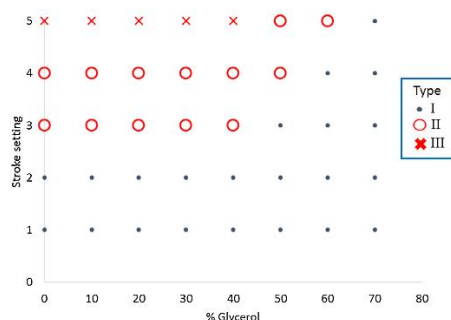


Fig. 7. Region plot of the types of drop behavior observed with varied solenoid stroke settings and percentage of glycerol in the glycerol–water mixture by volume with a circularly scribed substrate. The type of behavior is deemed after taking the most prevalent one observed out of 10 recordings at each stroke and glycerol percentage setting.

the substrate used was the same, and all test conditions were unchanged, it is clear that the action afforded by the scribed surface structure at the three-phase contact line provided the impetus toward the liquid body attaining the instability condition more readily. Inspection of the topography of the scribed region reveals the formation of grooves whereby the inability to remove substrate material resulted in structures resembling parapets and scarps (Fig. 8). These structures are not symmetrical which then has implications on the directional pinning of three phase contact lines.

An approach to present the physics explaining this phenomenon is to compare the time evolution traces of key parameters of the drop. Fig. 9 gives the situation with the normalized (to the value prior to motion) width of the drop. In both the non-scribed and scribed substrates, the width increased at the phase just before impact. This is due to the forces from deceleration causing the drop to flatten out. As soon as impact is made, the width then starts to shrink, a mechanism that allows the liquid body to harness the momentum transferred from the gantry to try to propel itself upwards. Following this, there is a series of oscillations in the width, which is used by the liquid body to dissipate the mechanical energy. These are the result of capillary waves formed that typically accompany severe free-surface deformations in drops when they impact on surfaces [12,29]. It is noteworthy, however, that in the case of the scribed surface, the width does not decrease beyond the width of the well. This indicates a stronger pinning effect at the three-phase contact line as the liquid tries to move toward the center of the well. Interestingly, the extent of this pinning is not as

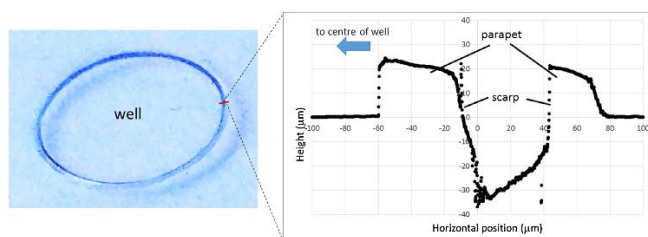


Fig. 8. The cross section topography of the scribed region of the substrate. There is clear presence of a groove due to the cutter used, with structures resembling parapets and scarps on either side. These were not symmetrical.

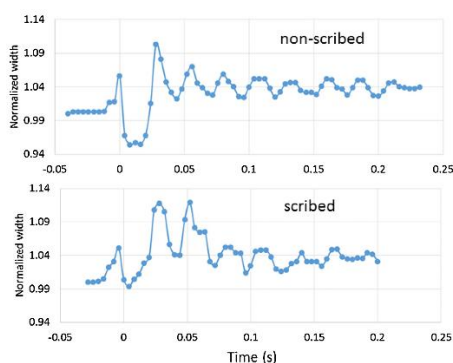


Fig. 9. Time traces of the width of a water drop on the non-scribed and scribed substrates, normalized to their starting values (non-scribed = 2.3 mm, scribed = 2.5 mm) taken from the point of impact ($t = 0$ s) under stroke setting 4. In both cases, oscillations in the width after impact are used by the liquid body to dissipate energy. For the non-scribed case, the diameter of the scribed well is the minimum to which the drop could reduce its width to.

strong in inhibiting the increase of the width over the extent of the scribed well. This is attributed to the asymmetrical geometry of the scribed groove, where the less steep scarp further from the center of the well imbues a relatively lower degree of pinning on the three phase contact lines as it tries to move over (see Fig. 8).

The height of the drop on the scribed surface (= 2.5 mm) was marginally higher than on the non-scribed surface (= 2.3 mm) initially. This is to be expected due to the width constraint on the former. During the deceleration phase prior to impact, the drop in both cases experienced a reduction in height (Fig. 10). This is essentially to accommodate the increase in width during this phase. As soon as impact occurs, there is a sudden increase in height, followed by its decrease and then cycles of height fluctuations behind tapering off. As in the case of width, this mechanism is used by the liquid body to dissipate mechanical energy. The maximum height achieved is about the same, notwithstanding the drop in the non-scribed surface exhibiting type I behavior as opposed to the drop on the scribed surface manifesting type II behavior. This result appears to indicate the height achieved is dependent only on the upward momentum transferred from the impact, while the changes in shape is dictated by the manner in which surface tension is used to deal with redistribution of mass within the body.

The greatest insight is perhaps offered by comparing the traces of the contact angle with time (Fig. 11). The constraint in width

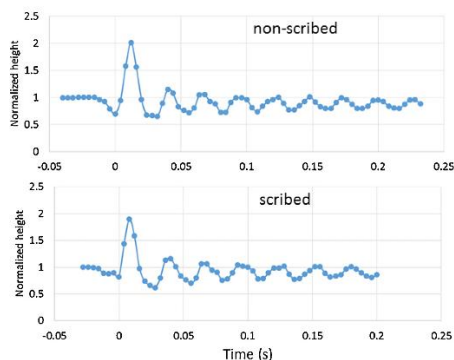


Fig. 10. Time traces of the height of a water drop on the non-scribed and scribed substrates, normalized to their starting values (non-scribed = 7.2 mm, scribed = 6.86 mm) taken from the point of impact ($t = 0$ s) using stroke setting 4. The trends are similar, although types I and II behavior are found for the non-scribed and non-scribed substrates, respectively.

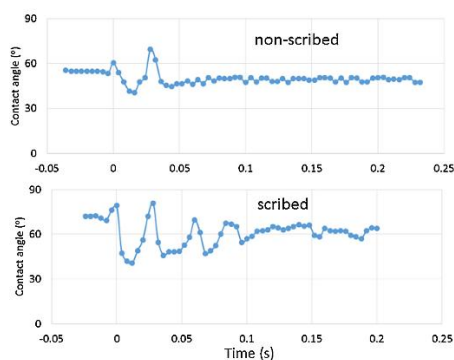


Fig. 11. Time traces of the contact angle of the drop on the non-scribed and scribed substrates taken from the point of impact ($t = 0$ s) using stroke setting 4. With the scribed substrate, the contact angle is able to exhibit a higher extent of reduction (up to 30° from the original condition) than on the non-scribed substrate (15° from start condition).

of the drop on the scribed surface naturally incurs a higher initial contact angle ($=80^\circ$) than the non-scribed surface ($=55^\circ$). At the point of impact, the contact angle increases for a short fraction of time (~ 8 ms) before the drop begins its increase in height (Fig. 10) or reduction in width (Fig. 9). This indicates contact angle change as the first mechanism for adjusting mechanical energy changes in the drop. As the liquid body becomes extended, it brings the contact angle to a receding state, which is used to help maintain adhesion to the substrate. It is noteworthy that on the scribed surface the contact angle is able to recede more (by 20°) than on the non-scribed surface (by 15°). This is primarily due to the strong contact line pinning offered by the parapet and steep scarp formed around the scribed groove. With the non-scribed surface, it can be seen that any contact angle oscillations arising from the impact are quickly suppressed. This is because the drop is able to use changes in both the height and width to do so. Since the liquid body is able

to attain a lower receding contact angle on the scribed surface, the higher adhesion effect on its main body in conjunction with greater propensity of the upper portion to detach is manifested by the ability for the drop to neck to a greater extent, thus allowing complete pinching off and type III behavior to be exhibited.

The occurrence of type III behavior (where the two separate liquid bodies are formed) instinctively suggests that it should be eschewed if possible. It should be noted, however, that the platform movement characteristics is reasonably repeatable. This suggests the possibility of harnessing enhanced mixing when the two liquid bodies coalesce. Better insights can be gleaned from finite element modeling. To reduce computational time, only half the drops were simulated. The graded mesh models of the two liquid bodies are depicted in Fig. 12; A for the liquid phase, and B for the gaseous phase. The meshing densities have been kept high and roughly constant throughout in order to track the spatial changes faithfully. Fig. 13A–D provides the flow outcomes arising from the coalescence at various stages in time. The shape changes follow the trends of the experimental results, indicating correctness of the modeling. In general, the flow unifies at time around 67 ms from start into a downwards and outwards position as a result of the droplet expanding. This results in a capillary wave that bounces back roughly at 78 ms to create an inward flow. Circulation begins to appear circa 79 ms whilst the merged drop starts to regain its height at 0.83 ms. What follows then is a downward flow that reappears as drop height is decreased. The capillary wave then appears in a back and forth fashion, causing circulations to form in the process.

It can be seen that throughout the process circulations develop in the merged liquid body, and this indicates good mixing [30–32]. In order to interrogate the nature of these circulations better, an area was selected (depicted as z in Fig. 13A) where the magnitude of circulatory flows were traced. This is simply the magnitude of the expression $C = \oint V \cdot dl$, where V is the velocity and dl the differential length. The result, shown in Fig. 14, indicates an initial high positive peak (indicative of anti-clockwise circulation) followed by a cyclical characteristic with time. It is important to note that the cycling phase has positive and negative values, which indicates that the circulation alternates between the clockwise and anti-clockwise senses. Interestingly, this happens within the process of coalescence without the need to either move physical contacts in different directions [30] or implement reversals in flow [32]. This can reasonably be taken to imbue enhanced mixing. It can be also noted from Fig. 13A–D that multiple centers of circulation of the liquid body can result throughout the duration when the two liquid bodies coalesce. These centers are difficult to locate precisely, yet the spatial shifting implies that the mixing distributes itself across the liquid body rather than being centered at one location. While this does not suggest uniform mixing throughout, it does suggest that the process should significantly aid overall mixing.

The correctness of the simulation results can be inferred indirectly by the liquid shapes at specific phases of the coalescence during experimentation (Fig. 15). Despite the apparent skewness (to the left), the correspondences are compelling. It is important to highlight that the use of the drop separation followed by coalescence can yield some unexpected situations. We have found in some rare instances where the separated bodies would bounce off each other rather than to merge (Fig. 16). Since the coalescence occurs during the post-receding process, it is clear that the dynamics of primary drop (sticking with the substrate) should be partly governed by the pinning characteristics of this drop. There is, then, reason to expect that this should strongly influence the subsequent coalescence between the primary and secondary drops. The inability to completely control the symmetry of the manner with which the liquid bodies coalesce (see Fig. 15) using the existing setup has unfortunately not engendered an ability to experimentally verify this. Another possible cause for the non-coalescence behavior may

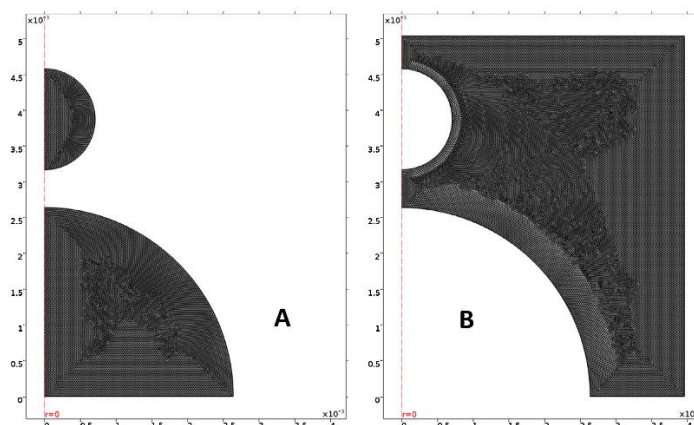


Fig. 12. Graded meshes of drop coalescence behavior under finite element analysis, in which the (A) liquid and (B) gaseous phases are depicted. The dense meshes enable the interaction changes to be well described.

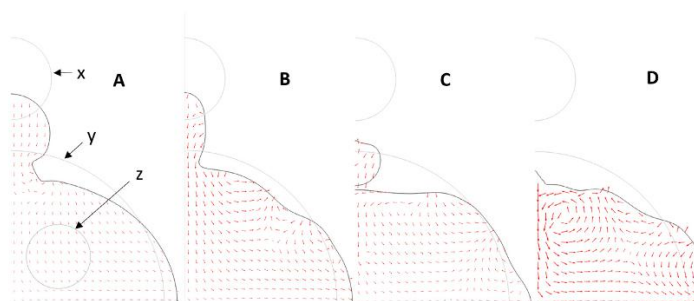


Fig. 13. Sequence of simulation results (A) to (D) depicting the flow field generated as the two liquid bodies began to merge. The original positions are described using x and y in (A). A region, depicted by z , was selected to interrogate the circulation flow strength.

lie with the development of an increasingly compressed entrapped air film between the two liquid bodies which would then keep them separate notwithstanding their motions toward each other. This effect, however, has only been observed previously with highly viscous liquids that are vibrated [33]. From a collision perspective, non-coalescence is essentially a manifestation of a stable collision developing. Recent studies have indicated that there are parameter spaces (i.e. interaction velocity, drop deformation, interfacial tension, etc.) at which hydrodynamic effects can stabilize collisions that are intrinsically unstable [34]. It is conceivable then that more nuanced control schemes incorporated may ensure that the non-coalescence occurrences can be altogether eliminated.

4. Conclusions

A method to cause sessile drops, based on water–glycerol mixtures at $40\ \mu\text{L}$ volume, deposited on solid substrates, to accelerate upwards and then stopped suddenly to create a longitudinal impact effect was devised. At impact momentums of up to $4.31 \times 10^{-3}\ \text{Ns}$, three categories of drop behavior were uncovered. On the scribed

substrate, the drop was found to be able to separate, but not on the non-scribed substrate. This can be explained by the ability of the contact angle on the scribed substrate to be able to recede more compared with the non-scribed substrate. With stronger adhesion of the main liquid body to the substrate, greater necking could then ensue with complete pinching off possible. Rather than consider this mode as disadvantageous, numerical simulations of the separated drops coalescing together showed circulations that change direction with time. This portended improved mixing if the experimentation could be well controlled.

Acknowledgments

This work was performed in part at the Melbourne Centre for Nanofabrication (MCN) in the Victorian Node of the Australian National Fabrication Facility (ANFF).

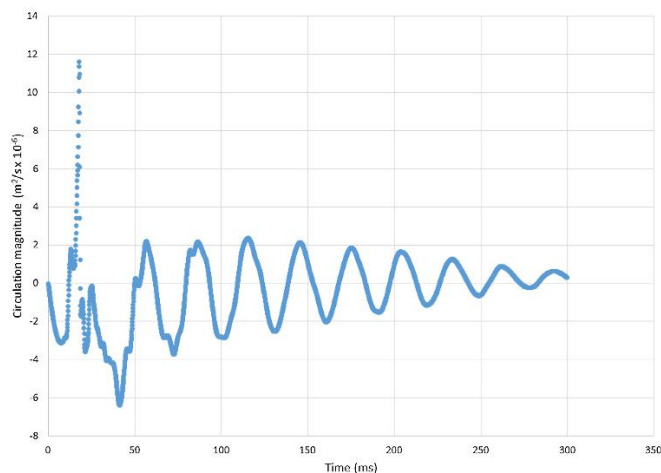


Fig. 14. The circulation flow strength developed in the region z in Fig. 13(A) traced with time in which positive values indicate a counter-clockwise flow. There was an initial peak followed by a cycle of positive and negative values that suggest good liquid mixing.



Fig. 15. Sequence of high-speed camera images of the coalescence phase (A) to (D) in the Type III behavior. They show the merging liquid shape to experimentally correspond with the simulation images results of Fig. 13 (A) to (D).

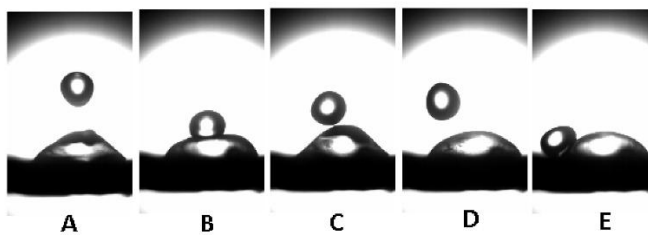


Fig. 16. Sequence of images showing the separated bodies not merging together on rare occasions.

References

[1] P.N. Nge, C.I. Rogers, A.T. Woolley, Advances in microfluidic materials, functions, integration, and applications, *Chem. Rev.* 113 (2013) 2550–2583.

[2] E. Livak-Dahl, I. Sinn, M. Burns, Microfluidic chemical analysis systems, *Ann. Rev. Chem. Biomol. Eng.* 2 (2011) 325–353.

[3] E. Samiei, M. Tabrizian, M. Hoorfar, A review of digital microfluidics as portable platforms for lab-on-a-chip applications, *Lab Chip* 16 (2016) 2376–2396.

[4] H.-H. Shen, S.-K. Fan, C.-J. Kim, D.-J. Yao, EWOD microfluidic systems for biomedical applications, *Microfluid. Nanofluid.* 16 (2014) 965–987.

[5] T. Vuong, B.H.-P. Cheong, S.H. Huynh, M. Muradoglu, O.W. Liew, T.W. Ng, Drop transfer between superhydrophobic wells using air logic control, *Lab Chip* 15 (2015) 991–995.

[6] M. Chaigneau, K. Balaa, T. Minea, G. Louarn, Plasmon resonance microsensor for droplet analysis, *Opt. Lett.* 32 (2007) 2435–2437.

[7] K.-M. Lee, M. Runyon, T.J. Herrman, R. Phillips, J. Hsieh, Review of Salmonella detection and identification methods: aspects of rapid emergency response and food safety, *Food Control* 47 (2015) 264–276.

[8] M. Balouiri, M. Sadiki, S.K. Ibsouda, Methods for in vitro evaluating antimicrobial activity: a review, *J. Pharm. Anal.* 6 (2016) 71–79.

[9] G. Lu, H.Y. Tan, A. Neild, O.W. Liew, Y. Yu, T.W. Ng, Liquid filling in standard circular well microplates, *J. Appl. Phys.* 108 (2010) 124701.

[10] X.Y. Li, B.H.-P. Cheong, A. Somers, O.W. Liew, T.W. Ng, Surface-scribed transparency based microplates, *Langmuir* 29 (2013) 849–855.

[11] B.H.-P. Cheong, W.S. Chua, O.W. Liew, T.W. Ng, Scribed transparency microplates mounted on a modified standard microplate, *Anal. Biochem.* 458 (2014) 40–42.

[12] C.Y. Lau, Z. Roslan, B.H.-P. Cheong, W.S. Chua, O.W. Liew, T.W. Ng, Transparency microplates under impact, *J. Colloid Interface Sci.* 426 (2014) 56–66.

[13] M. Suzuki, N. Takahashi, T. Miyazaki, H. Aoyama, Mixing phenomena induced by capillary oscillations of a sessile drop, *J. Jap. Soc. Fluid Mech.* 24 (2005) 205–206.

- [14] M.K. Chaudhury, P.S. Goohpattader, Activated drops: self-excited oscillation, critical speeding and noisy transport, *Eur. Phys. J. E Soft Matter* 36 (2013) 15.
- [15] M.L.H. Chong, M. Cheng, M. Katariya, M. Muradoglu, B.H.-P. Cheong, A.A. Ahmad Zahidi, Y. Yu, O.W. Liew, T.W. Ng, Liquid body resonance while contacting a rotating superhydrophobic surface, *Eur. Phys. J. E Soft Matter* 38 (2015) 119.
- [16] M. Katariya, S.H. Huynh, D. McMorran, C.Y. Lau, M. Muradoglu, T.W. Ng, Linear stepper actuation driving drop resonance and modifying hysteresis, *Langmuir* 32 (2016) 8550–8556.
- [17] V. Bertola, M. Wang, Dynamic contact angle of dilute polymer solution drops impacting on a hydrophobic surface, *Colloid Surf. A Physicochem. Eng. Asp.* 481 (2015) 600–608.
- [18] W. Yang, J. Xu, Drop spreading and penetrating on micro/nano particle sintering porous with multiscale structure, *Colloid Surf. A Physicochem. Eng. Asp.* 516 (2017) 9–22.
- [19] J. Wu, J.J. Huang, W.W. Yan, Lattice Boltzmann investigation of droplets impact behaviors onto a solid substrate, *Colloid Surf. A Physicochem. Eng. Asp.* 484 (2015) 318–328.
- [20] C.M. Megaridis, K. Boomsma, I.S. Bayer, Partial rebound of molten-metal droplets impacting on solid substrates, *AIChE J.* 50 (2004) 1356–1363.
- [21] W. Wang, Instability, stabilization, and formulation of liquid protein pharmaceuticals, *Int. J. Pharm.* 185 (1999) 129–188.
- [22] A. von Bomhard, A. Elsässer, L.M. Ritsch, S. Schwarz, N. Rotter, Cryopreservation of endothelial cells in various cryoprotective agents and media – vitrification versus slow freezing methods, *PLoS One* 11 (2016) e0149660.
- [23] V. Vagenende, M.S.G. Yap, B.L. Trout, Mechanisms of protein stabilization and prevention of protein aggregation by glycerol, *Biochemistry* 48 (2009) 11084–11096.
- [24] X.J. Loh, A.A. Karim, C. Owh, Poly(glycerol sebacate) biomaterial: synthesis and biomedical applications, *J. Mater. Chem. B* 3 (2015) 7641–7652.
- [25] Y. Cao, M. Liu, K. Zhang, J. Dong, G. Zu, Y. Chen, T. Zhang, D. Xiong, R. Pei, Preparation of linear poly(glycerol) as a T1 contrast agent for tumor-targeted magnetic resonance imaging, *J. Mater. Chem. B* 4 (2016) 6716–6725.
- [26] E. Olsson, G. Kreiss, A conservative level set method for two phase flow, *J. Comp. Phys.* 210 (2005) 225–246.
- [27] Y. Di, R. Li, T. Tang, P. Zhang, Level set calculations for incompressible two-phase flows on a dynamically adaptive grid, *J. Sci. Comp.* 31 (2007) 75–98.
- [28] J. Eggers, Nonlinear dynamics and breakup of free-surface flows, *Rev. Mod. Phys.* 69 (1995) 865–929.
- [29] I.S. Bayer, C. Megaridis, Contact angle dynamics in droplets impacting on flat surfaces with different wetting characteristics, *J. Fluid Mech.* 558 (2006) 415–449.
- [30] T. Vuong, B.H.-P. Cheong, J.K.K. Lye, O.W. Liew, T.W. Ng, Microplate well coverage-mixing using superhydrophobic contact, *Anal. Biochem.* 430 (2012) 53–55.
- [31] S. Wan, X. Huanming, P. Kumar, Numerical analysis and characterization of a Wankel pump as a miniaturized mixer, *J. Micromech. Microeng.* 25 (2015) 084001.
- [32] S. Sarkar, K.K. Singh, V. Shankar, K.T. Shenoy, CFD simulations to study the effects of wall protrusions on microfluidic mixing, *J. Micromech. Microeng.* 25 (2015) 084008.
- [33] Y. Couder, S. Protière, E. Fort, A boudaoud, dynamical phenomena: walking and orbiting droplets, *Nature* 437 (2005) 208.
- [34] J.D. Berry, R.R. Dagastine, Mapping coalescence of micron-sized drops and bubbles, *J. Colloid Interface Sci.* 487 (2017) 513–522.

Appendix C

Colloids and Surfaces A 579 (2019) 123661



Contents lists available at ScienceDirect

Colloids and Surfaces A

journal homepage: www.elsevier.com/locate/colsurfa

Behaviour of sessile drops revealed in ‘car crash’ like impact



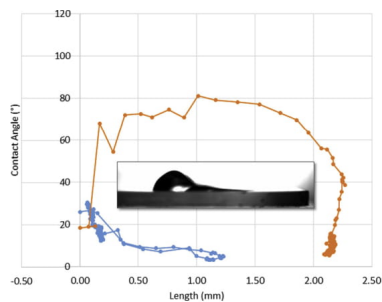
Alifa Afiah Ahmad Zahidi^a, Kamal Mohammad Salleh^a, Sewminda Kalana Samarasinghe^a,
Dwayne Chung Kim Chung^a, Ushan Dantarayanara^a, Md Hemayet Uddin^b, Oi Wah Liew^c,
Tuck Wah Ng^{a,*}

^aLaboratory for Optics and Applied Mechanics, Department of Mechanical & Aerospace Engineering, Monash University Clayton, VIC, 3800, Australia

^bMelbourne Centre for Nanofabrication, 151 Wellington Road, Clayton, VIC, 3168, Australia

^cCardiovascular Research Institute, Yong Loo Lin School of Medicine, National University of Singapore, National University Health System, Centre for Translational Medicine, 14 Medical Drive, 117599, Singapore

GRAPHICAL ABSTRACT



ARTICLE INFO

Keywords:
Impact
Drop
Pinning
Contact angle
Energy dissipation

ABSTRACT

This study reports the effect of impact forces on the behaviour of sessile drops when their rapid horizontal displacement is abruptly abrogated. The experimental setup is akin to “car crash” simulation, wherein an object is moved linearly at a predetermined speed and then brought to a complete stop by colliding with a stationary obstacle. The mechanical translator used allowed drops to attain consistent speeds prior to imposition of an impact force. In investigations on binary mixtures comprising glycerol-water (0–100% vv) and polyvinyl alcohol – water (0–10% vv), it was found that the positions as well as the contact angles of the advancing and receding contact lines could alter in tandem. The trajectories from a new phase-space representation for binary mixtures of varied compositions indicated that drop behaviour as a function of contact angle and positional displacement differed between the advancing and receding contact lines in order to dissipate the impact energy applied. The experimental results scaled well with Ohnesorge numbers but not Bond or Weber numbers, indicating a dominant effect played by viscosity. The approach here offers new vistas in viscosity determination of fluids, and in the study of drops subjected to evaporation and freezing conditions.

* Corresponding author.

E-mail address: engngtw@gmail.com (T.W. Ng).

<https://doi.org/10.1016/j.colsurfa.2019.123661>

Received 23 January 2019; Received in revised form 8 July 2019; Accepted 8 July 2019

Available online 09 July 2019

0927-7757/ © 2019 Elsevier B.V. All rights reserved.

1. Introduction

The evaporation from and the freezing of sessile drops on surfaces have many practical implications in industry. For this reason, various aspects of these have been studied and reported in the literature [1–5]. When sessile drops on surfaces are subjected to strong airflow their evaporation characteristics are altered [6]. Similarly, the imposition of impact affects the freezing processes of sessile drops on cooled surfaces [7].

Studies on the dislodgement of single sessile drops from surfaces through the action of airflow have been conducted [8]. Clearly, the retention behaviour of sessile drops on surfaces have practical implications in relation to the ability for evaporative cooling as well as the propensity for icicle formation on surfaces when the temperature is low. In recent times, the ready creation of self-cleaning superhydrophobic surfaces have provided the means to ameliorate problems when dealing with cooled surfaces, and even offers other new potential applications as well [9,10]. However, a vast majority of surfaces are not superhydrophobic in nature, and as such sidelong impact offers another mechanism for sessile drop dislodgement. This has been shown to be relevant in investigations to ascertain the ability of pinned drops in maintaining positional stability notwithstanding the imposition of these forces [11]. In biochemical applications, for instance, strong movements of drops away from the areas where they are meant to be held at can result in sample loss and contamination. In many instances, care is often exercised to eschew inadvertent impacts in the transport of liquids due to the heightened problem that their spillage can cause, in particular if the samples are biohazardous in nature. In addition, if impact forces can be applied in a more controlled fashion, it arguably facilitates better characterization of the retention behaviour of sessile drops on surfaces to such perturbations.

In a previous work, a swinging pendulum setup was used to provide the sidelong impact on sessile drops [11]. If the striker is carefully aligned to hit the object at the centre of percussion, such that the striker is positioned directly below the pivot when it contacts the object to generate a perpendicular impact. Ideally, no reaction force is produced at the pivot and the object should only receive a purely sidelong force component. This is, however, difficult to ensure in practice. A more reliable way of delivering a controlled sidelong impact force would be to create a setup that mimics a “car crash” test, wherein an object is moved linearly to reach a predetermined speed and then brought to an abrupt stop by collision with a stationary obstacle.

A table-top version of this setup is developed and described here. From this, the effect of impact on the behaviour of glycerol–water and polyvinyl alcohol (PVA)–water sessile drops deposited on a glass substrate are investigated. These binary liquid systems allow for viscosity and density to be varied by altering their compositions. In addition, PVA-water systems find use as nanofluids to improve heat transfer characteristics [12,13] or as drug releasing biocompatible agents [14,15]. Glycerol-water systems alternatively are widely used in biomass to chemical conversion [16,17], as surfactant stabilizer [18], and as the medium to handle biological samples without freezing damage [19,20]. A new method of using phase-space diagrams to depict the advancing and receding points of the three-phase contact lines with the onset of impact is also presented.

2. Theoretical considerations

A drop on a horizontal surface (Fig. 1A) that is in equilibrium is governed by the well-established laws of Laplace and Young. At the three-phase contact line

$$\gamma_{LS} + \gamma_{LV} \cos\theta = \gamma_{SV} \quad (1)$$

where θ is the equilibrium contact angle, and the interfacial tensions between the liquid–solid, liquid–vapour, and solid–vapour interfaces are γ_{LS} , γ_{LV} , γ_{SV} respectively. The theoretical thermodynamic contact angle

is based on the assumption that a droplet is at rest on an ideal homogeneous surface and has reached equilibrium. In reality where non-equilibrium and usually heterogeneous surface presents distinct complexities, mechanical pinning [21] or adhesion hysteresis [22] could occur and the many possible metastable states result in a range of contact angles that can be assumed. Essentially, this implies that there may be more than one value that exist for γ_{LS} [23]. A drop that is placed on an incline support this notion (Fig. 1B) as it clearly manifests advancing and receding contact lines and angles. Under the condition that the advancing and receding contact angles are known, it follows that the interfacial energy of the solid–liquid phase should assume values that are different and they correspond to the varied contact angles [24]. This phenomenon in part explains why energy dissipation arising from liquid travel in a capillary tube exists [25].

A drop that is moved together with a substrate (Fig. 2A) will experience an air drag effect that is similar to that of air flowing towards a drop on a stationary substrate. If the rate of displacement of the substrate is moderate, and if adhesion to the substrate is sufficiently strong, this air drag effect is expected to be small. When the substrate is brought to a sudden stop via collision, the drop has to develop energy dissipation mechanisms to deal with this sudden momentum change. It can harness the ability of the contact angles to alter as well as the contact line to move in order to accommodate this [20,26,27]. The energetics associated with the latter can be estimated provided that the extent of adhesion on the surface is not significant, as in the case of superhydrophobic surfaces. Even so, an approach to perform energy calculations would require obtaining the complete three-dimensional shape of the liquid body as it is deformed. Such data is difficult to obtain especially when there is significant free-form deformation of the liquid body.

The analysis here is based on a simpler characterization approach whereby the contact angles and positions of points associated with advancing and receding contact line (*AL* and *RL* in Fig. 2A and B) are considered. Contact angles have been used as indications of surface energy when the propensity of drops to move is altered albeit while they are still stationary. Prior to impact (Fig. 2A), the positions of the contact line are relatively invariant, as with the corresponding contact angles, θ_a and θ_r , associated with them. Following impact (Fig. 2B), these parameters will change. While θ_a and θ_r can be tracked easily, the displaced positions of *AL* and *RL* need to be established from a reference point on the rigid reference. With the progress of time t after impact, they are obtained via

$$\delta_a(t) = L_a(t) - L_a(0) \quad (2a)$$

$$\delta_r(t) = L_r(t) - L_r(0) \quad (2b)$$

Since the displacements and contact angles of *AL* and *RL* are two vital parameters used by the liquid body to dissipate energy, it is possible to introduce a phase-space plot for depiction. Phase-space diagrams have been successfully utilized in many mathematical and physics problems to describe dynamical systems. It is essentially a collective depiction of states of a system, wherein every point contains the unique state of the properties that define how the system is behaving. Phase space diagrams have been applied to characterize signals from real systems subjected to chaos [28] or driven by Brownian perturbations [29].

3. Materials and methods

3.1. Liquid samples

Glycerol (Sigma, G9012-1 L) and PVA (Sigma, 9002-89-5) were obtained from commercial sources to prepare the binary mixtures for testing. Mixtures of different viscosities and densities were prepared by mixing appropriate volumes of glycerol or PVA with deionized (DI) water in plastic centrifuge tubes. These tubes were agitated in a vortex

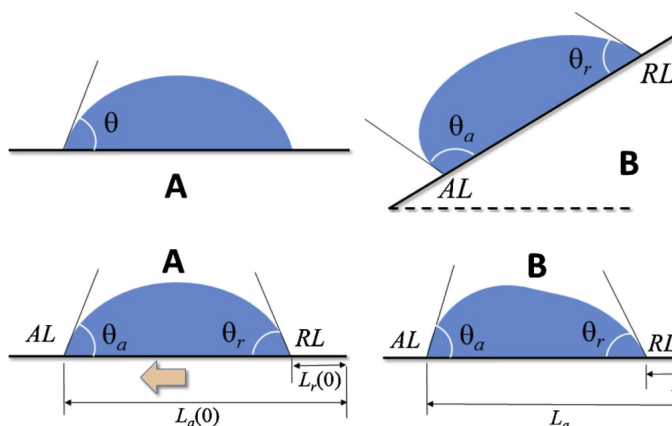


Fig. 1. (A) Schematic depiction of a sessile drop on a horizontal substrate which results in an axis-symmetric shape with contact angle θ . (B) When the substrate is inclined, the axis-symmetric nature vanishes such that advancing line AL develops with advancing contact angle θ_a . Similarly, a receding line RL develops with receding contact angle θ_r .

Fig. 2. (A) As a sessile drop resting on a substrate is moved (in the direction of the arrow), the distances of the advancing (AL) and receding (RL) contact lines from a reference point on the rigid substrate, $L_a(0)$ and $L_r(0)$ respectively, are almost invariant up to the point of impact. (B) Following impact, the changes in L_a , L_r , θ_a and θ_r with time characterizes the response of the drop to the force applied.

mixer (VELP Scientifica, Wizard IR) for 2 min and allowed to settle for at least 1 h before use.

3.2. Surface characterization

The characteristics of the substrate surface was first verified using an optical profiler (Bruker, Contour GT-I). A vertical scanning interferometry mode was used to resolve the topology of the 3D structures. The sampling area was kept at $125 \times 95 \mu\text{m}$ in order to adequately observe the microstructures. Following this, the same substrate was placed in an atomic force microscope (Bruker, Dimension Icon) to obtain more detailed characterization. For this, a smaller sampling area of $50 \times 25 \mu\text{m}$ was implemented due to slower imaging scan rates.

3.3. Impact setup

A slider mechanism (Fig. 3) with travel length of 860 mm was constructed using 3D printed and standard metal components. A motorized belt drive enables the slider to move when electricity is supplied to the high speed direct current (DC) motor. The setup is affixed to the table using sturdy clamps. During operation, the slider is made to translate at a constant speed, and then allowed to collide with a heavy block where the slider is brought to a complete stop. Videos of the sidelong impact are recorded using a high speed camera (Fastec) operating at 1000 frames per second. To obtain high quality images, a fibre optic light source provides illumination that is diffused via a ground glass screen at the opposite end of the camera. For additional characterization of the impact, a logging accelerometer (GCDC, X200-4) was located close to the location where the drops are positioned.

3.4. Experimentation

A ground glass microscopic slide of thickness 1.02 mm is attached using strong adhesive to the slider. It is located such that its thickness and trailing edge are both visible and can thus be used provide scale and positional reference respectively from the sequence of high speed camera images obtained. In all the tests, the motor in the setup was driven at the same voltage and current so that the slider is moved reproducibly at a predetermined speed prior to impact. An initial test was conducted with ten runs without liquid drops to verify consistent attainment of slider speed. In tests conducted with liquid drops, 15 μL of varying compositions of glycerol-water (0–100% v/v) and PVA-water

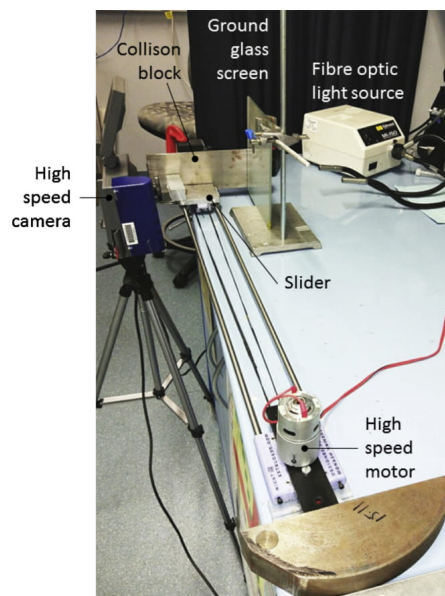


Fig. 3. Picture of table-top setup developed to simulate “car crash” investigations of sessile drops. The drops are deposited on substrates attached to the slider which is then moved to specific speeds where it comes to an abrupt stop when it hits the collision block. The video sequence is captured using a high speed camera.

(0–10% v/v) were dispensed using a manual pipette (Eppendorf) onto a microscope slide. The slide was cleaned with alcohol and dried by heating for at least 2 min to remove all traces of the liquid sample before the next impact test was conducted.

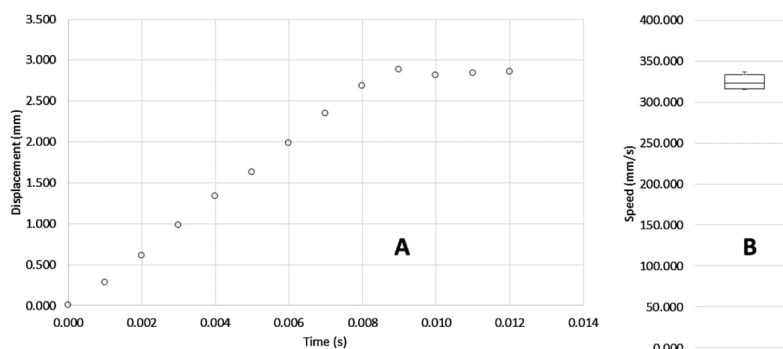


Fig. 4. (A) The displacement versus time trace of the slider shows a uniform speed achieved before impact. (B) The spread of slider speeds obtained from 10 repeated tests indicating that a reproducible and consistent speed was achieved by the experimental set up.

4. Results and discussion

A typical positional displacement versus time trace of the slider is shown in Fig. 4A. Prior to impact, it can be seen that the trace shows a linear gradient which implies that the slider attained a constant velocity. Upon impact, the slider is shown to be brought to an abrupt halt as indicated by the horizontal plateau of the trace. The box plot of readings taken from 10 repeated experiments in Fig. 4B show a small spread, indicating that the velocity attained is consistent. The average speed prior to impact is 0.323 m/s.

Fig. 5A furnishes a typical acceleration (taken from the accelerometer mounted on the slider) versus time trace of the slider. Prior to impact, it can be seen that acceleration is limited, confirming that the slider was travelling close to constant speed in the lead up to collision. Following impact, typical peak accelerations were attained which died down within 100 ms. Similar to the case with the video camera recordings, the box plot of readings taken from 10 repeated experiments show a small spread in the peak acceleration attained, suggesting good

levels of repeatability. By equating the impulse to the change in momentum during collision, the impulse time is estimated to be 3.6 ms. Such short durations account for “hard” collisions that imbue maximal perturbations on the drop. In crash studies, crumple zones are typically implemented to ameliorate this effect.

The sequence of images of the drops moved on the slider, and after an impact force is applied when the slider is brought to a complete stop by a stationary obstruction. The shape of water (Fig. 6A) and 70% glycerol-water (Fig. 6B) drops exhibited important and distinct characteristics. Firstly, there were no changes to the position and shape of the drops prior to impact. This implies that the drag force resulting from the flow of air generated by predetermined speed of the slider (movement to the left) did not have any significant effect on the drops. Upon impact of the slider with the block (from the second image onwards), the contact angles at the left and right three-phase contact lines, moved into advancing and receding states respectively. As long as the drops were not positionally displaced, monitoring the contact angle values alone should suffice in characterizing the mechanics. Inspection of the

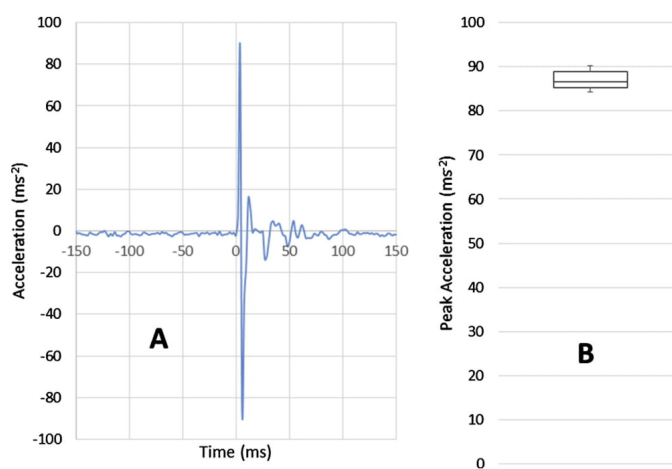


Fig. 5. (A) The acceleration versus time (value set at zero at the point of impact) trace of the slider shows typical mirror image maximum peaks and troughs. (B) The spread of the maximum accelerations obtained from 10 repeated tests show low levels of spread.

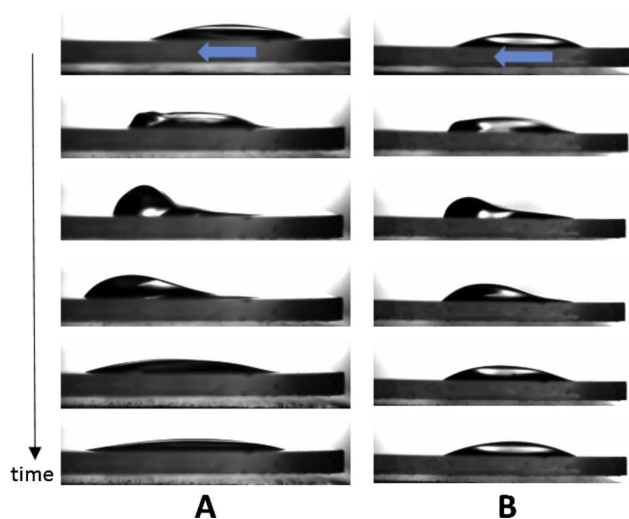


Fig. 6. Sequence of high speed images (from top to bottom) recorded as sessile drops of (A) water, and (B) 70% glycerol-water (v/v) were subjected to sidelong impact when movement of slider (direction according to blue arrow) was abrogated abruptly. Impact with the block occurred from the second image onwards. There are clear differences in drop behaviour in terms of displacement and contact angles at the advancing (left) and receding (right) contact points. (For interpretation of the references to colour in this figure legend, the reader is referred to the web version of this article).

image sequences, however, revealed that there was motion and shape deformation of the drop after impact, implying that this mechanism was used by the drop as means to dissipate the energy accrued from impact. Clearly, the ability to depict the movement and the contact angle changes of the drop in tandem should provide better insights into the processes used for energy dissipation. This is also made possible by the nature of collision of the slider with the block in the setup, which ensures that force applied to the drop is restricted to only one axis (in the direction of the slider).

The phase-space plots of the attendant contact angles and position of the advancing (*AL*) and receding (*RL*) three-phase contact lines of varied glycerol-water mixtures following impact are given in Fig. 7. The utility of the phase-space plot is illustrated in the Supplementary video for the case with water. With water (0% glycerol-water), the trace of *AL* (indicated in orange) manifested significant increases in its contact angle and position. While contact angle was eventually restored close to its initial equilibrium condition, this was not the case for its position. The traces of *RL* (indicated in blue) showed marginal reductions in the contact angle but significant displacement in position, albeit not as much as for *AL*. Interestingly, the *RL* line was eventually restored to its original position. With increasing glycerol content in the binary mixture, rapid reduction in positional displacement of *RL* was observed to the point where it remained virtually unchanged at 50% composition. The behaviour of *AL* with increasing glycerol content showed the same trend of attenuation but positional displacement is only unchanged above 60% glycerol while contact angle continue to vary even above 80% composition. These results indicate that contact angle change is more readily used to adapt to energy changes than contact line movement. While the nature of contact angle change is somewhat uniform, it is noted that some extent of positional restoration of *AL* is exhibited at 20% and 30% compositions. This indicated that position displacement of *AL* is sensitive to local pinning strengths which tend to be random in nature. That *AL* is more susceptible to more extensive contact angle and positional changes than *RL* in order to adapt to the energy applied from impact corroborates with the behaviour exhibited with static perturbations such as the action of gravity via gradual tilting of the surface, where the advancing contact line has been shown to breach more readily than the receding contact line [30]. It can be also seen that the

contact angle in *AL* is limited to below 100°. This supports the view that overall heterogeneity of the surface, which has been kept somewhat constant throughout, plays an important role in determining this value [31].

The trend of behaviour with PVA-water mixtures (Fig. 8) follows that of glycerol-water mixtures in which higher compositions (of PVA or glycerol) reduced the extent of changes to contact angles and positions in *RL* and *AL*. Similarities observed for the trajectory profiles of the phase-space diagram offers the opportunities to query if the behaviours are scaled by non-dimensional parameters such as the Bond (*Bo*), Weber (*We*) or Ohnesorge numbers (*Oh*) which are respectively given by

$$Bo = \frac{(\rho_l - \rho_v)gw^2}{\gamma} \quad (3)$$

$$We = \frac{\rho_l wv^2}{\gamma} \quad (4)$$

$$Oh = \frac{\mu}{\sqrt{\gamma w \rho_l}} \quad (5)$$

where ρ is the density (of the liquid or gaseous phase), γ the surface tension, μ the viscosity, g the gravitational acceleration, v the velocity of the slider just before impact, and w the characteristic length (in this case the contact length of the liquid drop with the solid substrate just before impact). From the plots of these numbers, taken as a function of drop compositional attribute, it can be seen that only the Ohnesorge number correlated with the v/v percentage of the polyols in the binary mixtures (see Fig. 9). This dimensionless parameter relates viscous forces to inertial and surface tension forces. With varying glycerol-water and PVA-water composition mixtures, the density differences can affect inertia significantly despite the volume remaining the same. Hence using the Ohnesorge number is more appropriate than the capillary number, as the latter only relates viscous to surface tension forces. This observation implies that under the condition where the drop volume is 15 μL and speed before impact is 0.323 m/s, the ability of the sessile drop on a typical hydrophilic surface (ground glass) to be unperturbed by impact is dominated by the viscosity of the fluid; i.e. the

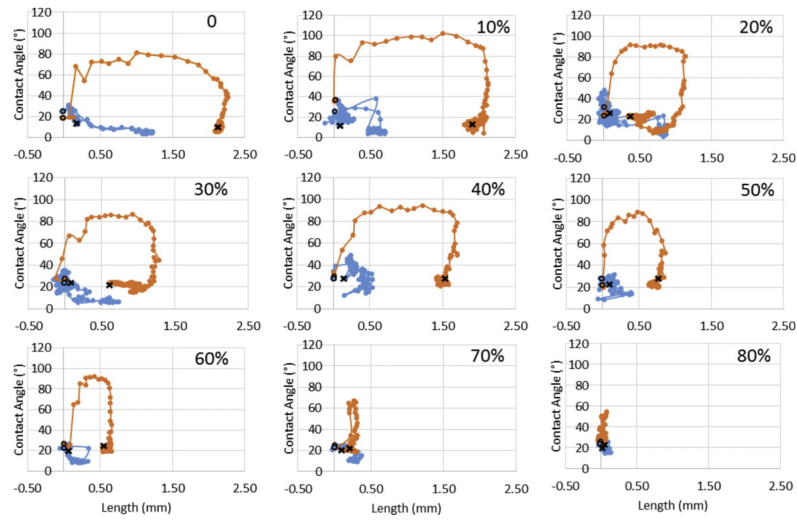


Fig. 7. Phase-space plots of drop advancing (orange) and receding (blue) contact line angles and positions following impact. The composition of the drop as a volume/volume percentage of glycerol in water is shown for each plot. The start and end conditions are indicated as circles and crosses respectively. (For interpretation of the references to colour in this figure legend, the reader is referred to the web version of this article).

higher the viscosity the lower the changes in contact angle and position in AL and RL . In fact, imperceptible changes were observed when $Oh \sim 0.005$, which corresponded to 90% and 5% glycerol and PVA respectively. This value is significantly lower than that required for creating jets in inkjet printing (permissible only when $0.1 < Oh < 1$) [32]. Since inkjet printing has also been advanced as a means of estimating viscosity [33] (possible only when jetting has occurred), the use of the impact approach described here offers a viable alternative method to do so without the attendant limitations of jetting. As the drops are relatively static, there is also potential to use arguably more economical setups (e.g. lasers and photodiodes) that eschew high speed imaging for droplet characterization. It is important to note that changing the speed

of impact will alter the viscosity range manifested in the phase-space trajectories. Consequently, there is potentially greater adaptability in studying the behaviour of drops over a wider range of viscosities. It is important to note that when two or more sessile drops are located on the slider, the forces applied on each following impact are exactly the same. This is not the case with applying airflows over sessile drops, wherein the drops upstream will experience different forces than those downstream. Thus, the approach described here offers versatility in studies into the behaviour of sessile drops subjected to cooling or freezing conditions, which have important industrial applications.

It is noteworthy that drops released from heights to impact on surfaces manifest highly observable vibrations [34]. These vibrations

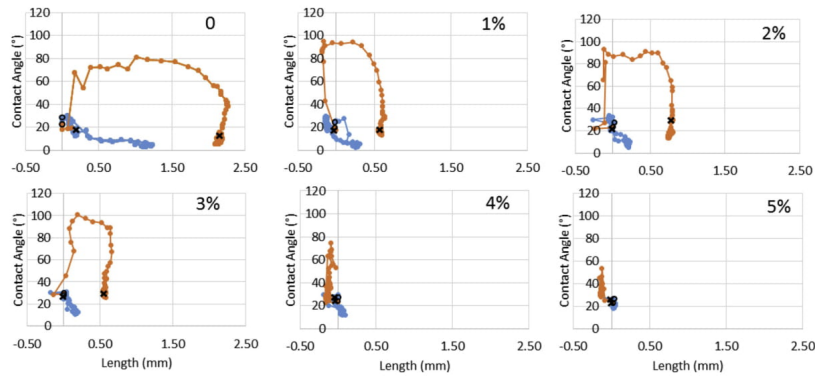


Fig. 8. Phase-space plots of drop advancing (orange) and receding (blue) contact line angles and positions following impact. The composition of the drop as a volume/volume percentage of polyvinyl alcohol in water is shown for each plot. The start and end conditions are indicated as circles and crosses respectively. (For interpretation of the references to colour in this figure legend, the reader is referred to the web version of this article).

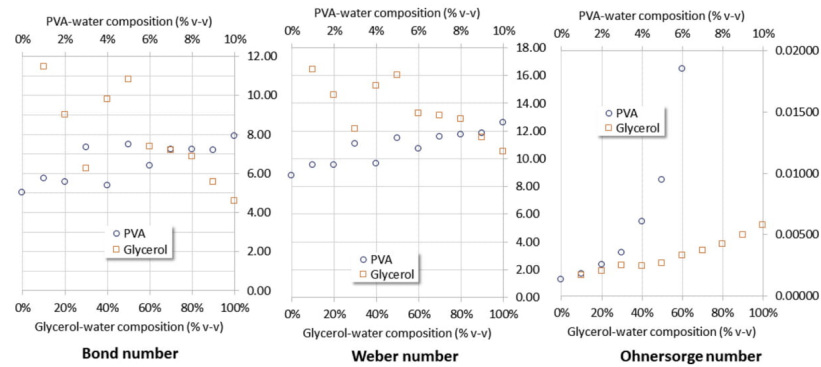


Fig. 9. Plots of the Bond, Weber, and Ohnesorge numbers for the various compositions of PVA-water and glycerol-water mixtures used in the experiment. Good correlation is only observed with the Ohnesorge numbers.

are also noticeable if the substrate that holds a drop is struck sidelong by a pendulum striker [11], since the impact can possess an upward vertical force component to engender them. That such vibrations are muted in their manifestation here, with a setup that tends to limit any vertical upward force component from developing, confirms the earlier thesis that the use of vibrations by drops to dissipate energy occurs primarily when axial perturbations are present [11].

The ability of the substrate to pin the liquid drop to some extent imparts strong influence by structures that are present on the surface. Results obtained using optical profilometry and atomic force microscopy (AFM), provided in Fig. 10 A and B respectively, show similar granulated structures that are approximately of the same size spatially. The peaks are however higher under optical profilometry imaging, and can be attributed to inaccuracies that inevitably occur when this technique is used to measure from the flattened peaks of transparent surfaces. It is pertinent to note that ground glass is typically created from standard glass using either particulate spraying or acid etching. As the former tends to create random indentations [35], it is clear that the latter process had been used to create the substrate here. Despite the high measuring resolutions that it is capable of, the AFM imaging did not reveal significant nanometer scale features on the substrate. Coupled with the uniform distribution of the granulated structures, this imputes a tendency towards strong Wenzel wetting which in turn accounts for the heightened adhesion of the drop to the surface

notwithstanding impact.

5. Conclusions

The experimental setup here has been shown to allow drops to attain constant speeds prior to impact. When the advancing and receding contact point lines of a sessile drop are displaced, they have been shown to occur only along one axis. This allowed the phase-space trajectories to be plotted to trace responses from binary mixtures in terms of changes in contact angle and positional displacement of the contact lines. A scaling dependence to the Ohnesorge number is uncovered revealing a possibility of the method to be used to determine the viscosities of fluids. New vistas into the study of drops subjected to evaporation and freezing are also expected.

Declarations of Interest

The authors declare no conflicts of interests related to this work.

Acknowledgements

The PVA samples provided by D. Li and Z. Xiong, Department of Chemical Engineering, University of Melbourne, are appreciated.

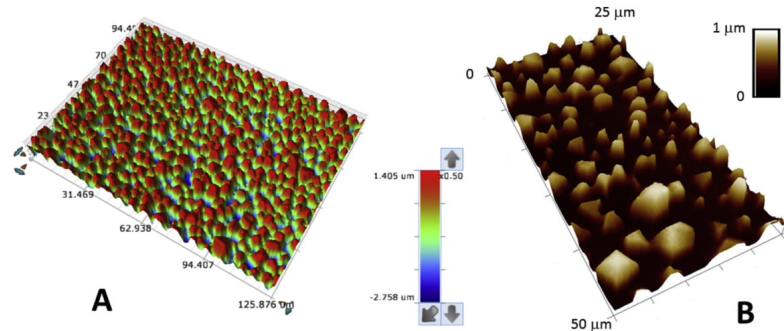


Fig. 10. Imaging plots of the substrate obtained using (A) optical profilometry and (B) atomic force microscopy reveal similar granulated structures.

Appendix A. Supplementary data

Supplementary material related to this article can be found, in the online version, at doi:<https://doi.org/10.1016/j.colsurfa.2019.123661>.

References

- [1] W.-Y. Shi, K.-Y. Tang, J.-N. Ma, Y.-W. Jia, H.-M. Li, L. Feng, Marangoni convection instability in a sessile droplet with low volatility on heated substrate, *Int. J. Therm. Sci.* 117 (2017) 274–286.
- [2] F. Wang, Z. Hu, C. Abarca, M. Fefer, J. Liu, M.A. Brook, R. Pelton, Factors influencing agricultural spray deposit structures on hydrophobic surfaces, *Colloids Surf. A Physicochem. Eng. Asp.* 553 (2018) 288–294.
- [3] X. Jiang, L. Tian, X. Liu, T. Li, Micro-patterning of titanium surface and its effect on droplet evaporation, *Colloids Surf. A Physicochem. Eng. Asp.* 545 (2018) 31–38.
- [4] Z. Jin, X. Cheng, Z. Yang, Experimental investigation of the successive freezing processes of water droplets on an ice surface, *Int. J. Heat Mass Transf.* 107 (2017) 906–915.
- [5] S. Ozbay, H.Y. Erbil, Ice accretion by spraying supercooled droplets is not dependent on wettability and surface free energy of substrates, *Colloids Surf. A Physicochem. Eng. Asp.* 504 (2016) 210–218.
- [6] H.K. Navaz, E. Chan, B. Markicevic, Convective evaporation model of sessile droplets in a turbulent flow—comparison with wind tunnel data, *Int. J. Therm. Sci.* 47 (2008) 963–971.
- [7] H. Zhang, Z. Jin, M. Jiao, Z. Yang, Experimental investigation of the impact and freezing processes of a water droplet on an ice surface, *Int. J. Heat Mass Transf.* 109 (2017) 716–724.
- [8] P.A. Durbin, On the wind force needed to dislodge a drop adhered to a surface, *J. Fluid Mech.* 196 (1988) 205–222.
- [9] D.C.K. Chung, M. Katariya, S.H. Huynh, B.H.-P. Cheong, O.W. Liew, M. Muradoglu, T.W. Ng, Uphill airflow transport of drops on superhydrophobic inclines, *Colloids Interface Sci. Commun.* 6 (2015) 1–4.
- [10] T. Vuong, B.H.-P. Cheong, S.H. Huynh, M. Muradoglu, O.W. Liew, T.W. Ng, Drop transfer between superhydrophobic wells using air logic control, *Lab Chip* 15 (2015) 991–995.
- [11] C.Y. Lau, Z. Roslan, B.H.P. Cheong, W.S. Chua, O.W. Liew, T.W. Ng, Transparency microplates under impact, *J. Colloid Interface Sci.* 426 (2014) 56–63.
- [12] L.R. Oliveira, A.C.A. Silva, N.O. Dantas, E.P.B. Filho, Thermophysical properties of TiO₂-PVA/water nanofluids, *Int. J. Heat Mass Transf.* 115 (2017) 795–808.
- [13] M. Hassan, A. Faisal, M.M. Bhatti, Interaction of aluminum oxide nanoparticles with flow of polyvinyl alcohol solutions base nanofluids over a wedge, *Appl. Nanosci.* 8 (2018) 53–60.
- [14] D.S. Muggli, A.K. Burkoth, K.S. Anseth, Crosslinked polyanhydrides for use in orthopedic applications: degradation behavior and mechanics, *J. Biomed. Mater. Res.* 46 (1998) 271–278.
- [15] C. Brough, D.A. Miller, J.M. Keen, S.A. Kucera, D. Lubda, R.O. Williams III, Use of polyvinyl alcohol as a solubility-enhancing polymer for poorly water soluble drug delivery (Part 1), *AAPS Pharm. Sci. Tech.* 17 (2016) 167–179.
- [16] A. Corma, G.W. Huber, L. Suwannaud, P. O'Connor, Biomass to chemicals: catalytic conversion of glycerol/water mixtures into acrolein, reaction network, *J. Catal.* 257 (2008) 163–171.
- [17] Z. Yamani, Z.N. Aishah, S. Amina, J. Linnekoski, Thermodynamic analysis of glycerol conversion to olefins, *Energy Procedia* 61 (2014) 2489–2492.
- [18] L. Zhang, X. Zhang, P. Zhang, Z. Zhang, S. Liu, B. Han, Efficient emulsifying properties of glycerol-based surfactant, *Colloids Surf. A Physicochem. Eng. Asp.* 553 (2018) 225–229.
- [19] P. Moffett, G. Fors, J.K. Graham, Cryopreservation of stallion sperm in freezing diluents containing glycerol alone or a combination of cryoprotectants, *J. Equine Vet. Sci.* 43 (2016) S69.
- [20] A.A. Ahmad Zahidi, B.H.-P. Cheong, S.H. Huynh, T. Vuong, O.W. Liew, T.W. Ng, Glycerol–water sessile drop elongation on PTFE inclines in relation to biochemical applications, *Colloids Surf. A Physicochem. Eng. Asp.* 486 (2015) 21–28.
- [21] J.F. Joanny, P.G. de Gennes, A model for contact angle hysteresis, *J. Chem. Phys.* 81 (1984) 552–562.
- [22] J.N. Israelachvili, *Intermolecular and Surface Forces*, Academic Press, New York, 1985.
- [23] L. Penn, B. Miller, A study of the primary cause of contact angle hysteresis on some polymeric solids, *J. Colloid Interface Sci.* 78 (1980) 238–241.
- [24] C.W. Extrand, A thermodynamic model for contact angle hysteresis, *J. Colloid Interface Sci.* 207 (1998) 11–19.
- [25] B. Athukorallage, R. Iyer, Investigation of energy dissipation due to contact angle hysteresis in capillary effect, *J. Phys. Conf. Ser.* 727 (2016) 012003.
- [26] X. Ye, X. Zhang, M. Li, C. Li, S. Dong, Contact line dynamics of two-dimensional evaporating drops on heated surfaces with temperature-dependent wettabilities, *Int. J. Heat Mass Transf.* 128 (2019) 1263–1279.
- [27] H.-J. Butt, N. Gao, P. Papadopoulos, W. Steffen, M. Kappel, R. Berger, Energy dissipation of moving drops on superhydrophobic and superoleophobic surfaces, *Langmuir* 33 (2017) 107–116.
- [28] J.D. Farmer, J.J. Sidorowich, Predicting chaotic time series, *Phys. Rev. Lett.* 59 (1987) 845–848.
- [29] O.J. Eder, T. Lackner, Brownian motion in phase space, *Phys. Rev. A* 29 (1984) 799–810.
- [30] W.Y. Ling, A. Neild, T.W. Ng, Effect of a rupturing encapsulated bubble in inducing the detachment of a drop, *Langmuir* 28 (2014) 17656–17665.
- [31] B. Krasovitski, A. Marmur, Drops down the hill: theoretical study of limiting contact angles and the hysteresis range on a tilted plate, *Langmuir* 21 (2005) 3881–3885.
- [32] B. Derby, Inkjet printing of functional and structural materials: fluid property requirements, feature stability, and resolution, *Ann. Rev. Mater. Res.* 40 (2010) 395–414.
- [33] S.D. Hoath, D.C. Vaddilo, O.G. Harlen, C. Mellroy, N.F. Morrison, W.-K. Hsiao, T.R. Tuladhar, S. Jung, G.D. Martin, I.M. Hutchings, Inkjet printing of weakly elastic polymer solutions, *J. Non-Newtonian Fluid Mech.* 205 (2014) 1–10.
- [34] F. Wang, T. Fang, Post-impact drop vibration on a hydrophilic surface, *Exp. Therm. Fluid Sci.* 98 (2018) 420–428.
- [35] C.Y. Lau, T. Vuong, J. Wang, M. Muradoglu, O.W. Liew, T.W. Ng, Hydrophobic to superhydrophobic surface modification using impacting particulate sprays, *Appl. Surf. Sci.* 311 (2014) 89–94.

Appendix D

Received: 10 January 2019 | Revised: 20 February 2019 | Accepted: 24 June 2019
 DOI: 10.1002/jemt.23340

RESEARCH ARTICLE



Living specimens under field immobilization and smartphone microscopic observation

Alifa A. Ahmad Zahidi¹ | Dwayne C. K. Chung¹ | Mayur Katariya¹ | Oi Wah Liew² | Tuck Wah Ng¹ 

¹Laboratory for Optics and Applied Mechanics, Department of Mechanical & Aerospace Engineering, Monash University, Clayton, Victoria, Australia

²Centre for Translational Medicine, Cardiovascular Research Institute, Yong Loo Lin School of Medicine, National University of Singapore, National University Health System, Singapore

Correspondence

Tuck Wah Ng, Laboratory for Optics and Applied Mechanics, Department of Mechanical and Aerospace Engineering, Monash University, Clayton, VIC 3800, Australia.
 Email: engngtw@gmail.com

Review Editor: Paolo Bianchini

Abstract

In this work a single glycerol–water mixture, determined to be most apt at 30% (wt/vol), was used to immobilize *Drosophila* samples as well as to create a liquid lens for smartphone magnification viewing. This provides the advantage of being able to observe immobilized insects directly in the field rather than in the laboratory. In order to avoid having bubbles in the liquid lens and immobilizing medium that hinder visibility, an approach was developed where a stable pendant drop is moved in tandem with the dispensing tip by gravity and stopped abruptly so that sufficient momentum is transferred to the drop for its dislodgement. With 30% glycerol–water (wt/vol) mixtures, applying a minimal stroke of 10 mm with longitudinal impact delivered a momentum of 0.1464 N/s that allowed transfer of a preselected liquid volume for the processes.

KEYWORDS

dislodgement, drops, glycerol-water, impact, insect, smartphone

1 | INTRODUCTION

There is strong interest to study the behavior of insects in their natural environment more carefully due to a palpable sharp decline in their populations (Hallmann et al., 2017). A strategy to do this is via open-field investigations to examine these specimens on-site in order to augment more in-depth laboratory-based anatomical studies at a later stage (Boevé, Eertmans, Adriaens, & Rossel, 2016). The availability of simple and cost-effective tools helps to overcome the problem of sparse spatial data sampling in open-field investigations (Petrovskaya, Petrovskii, & Murchie, 2012). A major challenge has been the development of nondestructive immobilization techniques for careful examination of active, living biological specimens. Although some biological species are sessile, a great many can fly, swim, or crawl actively, making observations over extended periods of time difficult or even impossible. Immobilization methods that have been applied can be broadly classified as chemical (Delly, 1985), mechanical (Taylor, 1993), and physical. Physical schemes based on the use of viscosity are well-established and popular. If the viscous substance is biologically inert, nontoxic, and

nonosmotic, it is possible to minimize any detrimental effects on the specimen, although excessive viscosity can limit the ability to retrieve the specimen from the immobilizing medium post microscopic examination. As smartphones are ubiquitous and are equipped with high resolution camera sensors, they offer exciting vistas as use as microscopes (Baek, Cho, Yun, Youn, & Bang, 2014; Cesaretti et al., 2017). While the focal length can be altered in liquid lenses by manipulating the wetting properties, they typically involve designs that require significant resources in construction and in fabrication.

In this work, we report the use of a single glycerol–water mixture composition that will serve both as the liquid lens for a smartphone microscope as well as the immobilization medium for a model insect, *Drosophila melanogaster* (fruit fly), in the field setting. There is enduring interest in studying glycerol–water mixtures due to their ability to serve as cryoprotectants for stabilizing macromolecules, cells, and tissues under cooling to subzero temperatures, along with the suppression of ice formation (Kiriker, Soper, Dzyuba, & Holt, 2016). The focal length relationship of the liquid lens relative to its shape is investigated and an impact liquid delivery method using pendant

drops developed to ensure that the lens is free of bubbles. For the immobilization aspect, the efficacy of the glycerol-water mixture to hold the *Drosophila* in place is verified.

2 | LIQUID LENS SHAPE RELATION TO FOCAL LENGTH

When a sessile drop is placed on the surface, it develops a semi-spherical shape if the effects of gravity are ignored (see Figure 1a). From geometry, the radius of curvature R is related to the contact angle θ and radius of drop on the substrate surface a via

$$a = R \sin \theta \quad (1)$$

As the volume V of the drop is typically known, it is related to θ and R via

$$V = \frac{\pi R^3}{3} (\cos^3 \theta - 3 \cos \theta + 2) \quad (2)$$

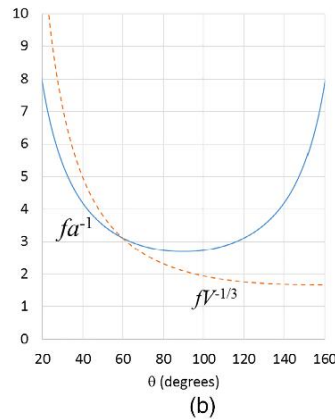
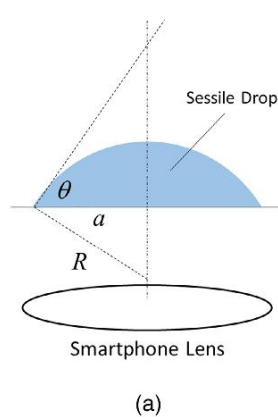
If the sessile drop is taken as a plano-convex thick lens, then its focal length f is taken to be

$$f = \frac{R}{(n-1)} \quad (3)$$

where n is the refractive index of the liquid. Combining Equations (1) and (3), we have

$$f(a^{-1}) = \frac{1}{(n-1) \sin \theta} \quad (4)$$

Combining Equations (1) and (2), we have



$$f(V^{-1/3}) = \frac{1}{(n-1)} \left[\frac{3}{\pi(\cos^3 \theta - 3 \cos \theta + 2)} \right]^{1/3} \quad (5)$$

As the liquid lens is typically placed above the smartphone lens with focal length f_s , this creates a compound lens with a focal length f_t given by

$$f_t = \frac{f_s f}{f_s + f} \quad (6)$$

As the magnification $M = 1/f_t$, keeping f small will result in higher magnification. Based on Equation (5), the plot of $fV^{-1/3}$ against θ for $n = 1.37$ (corresponding to 30% glycerol-water [wt/vol]) and $20^\circ < \theta < 160^\circ$ (these range of values depict realistic situations) in Figure 1b, shows that if the volume is kept constant and contact angle increased, the value of f decreases and the magnification increases. This will require preparing surfaces with varying wettabilities, which in practice can be difficult to achieve. A more practicable option will be to use the approach of scribing a circle on the substrate (Cheong, Chua, Liew, & Ng, 2014; Li, Cheong, Somers, Liew, & Ng, 2013) which then fixes the value of drop radius a on the substrate and affords an added pinning effect. As seen in the plot of fa^{-1} against θ based on Equation (4) in Figure 1b, increasing the values of θ from 20° to 90° (by applying different volumes within the confines of the scribed circle) should allow f to decrease and the magnification to increase as well.

3 | METHODS

3.1 | *Drosophila* trapping

Live *D. melanogaster* were obtained commercially (L7.3 Southern Biologicals, Knoxfield, Victoria, Australia) in a glass vial and cultured to increase their population. When the insects were ready for testing,

FIGURE 1 Sessile drop (a) with key parameters such that it is located on top of the lens of a smartphone creates a compound lens system that increases magnification. Plots of (b) $fV^{-1/3}$ and fa^{-1} against θ which indicate the ability of the focal length to be altered by keeping either V or a constant. This imbues magnification adjustment if a few of sessile drops are selectively placed on top of the smartphone lens [Color figure can be viewed at wileyonlinelibrary.com]

wells of a standard microplate were filled with varying percentages of glycerol–water mixtures. A funnel was placed over the mouth of a culture vial and inverted so that the stem of the funnel is positioned over one microplate well. When the foam plug covering the culture vial was removed, the vial was tapped so that some *Drosophila* flies fell into the liquid. This was repeated for the other microplate wells that contained different glycerol–water compositions. It was found that a minimum concentration of 30% glycerol–water (wt/vol) was of adequate viscosity to immobilize and hold the *Drosophila* in position within the microplate well. Hence, the 30% glycerol–water mixture was also used to develop the liquid lens.

3.2 | Liquid lens behavior

A lens testing chart (<http://www.normankoren.com/Tutorials/MTF5.html>) was created and attached to a translation stage. A transparent poly(methyl methacrylate) substrate of 1 mm thickness was scribed using a punch wad tool to create a 3 mm diameter circles to hold the drop sample. The liquid lens was formed on the scribed circles by dispensing drops of 30% glycerol–water (wt/vol) either by use of a syringe for direct delivery or via the impact dislodgement method as described in the next section. The substrate was then located over the smartphone (iPhone 7) camera aperture to create the microscope imager. The images of the lens testing chart were then analyzed.

3.3 | Impact dislodgement method

Figure 2 presents the setup used to conduct the experiments. A gantry is made by sawing off a rectangular 50 × 50 mm aluminum channel of 2.5 mm thickness with a depth of 20 mm. It was then attached to a linear sliding stage. The test substrate is affixed to the lower surface of the gantry. During tests, specific volumes of liquid are delivered via a flexible hose from a syringe pump to a 23 gauge stainless steel tip (with flat end) via syringe to create a pendant drop. The architecture of the gantry is such that a diffused light source could be incorporated to provide the necessary background illumination to obtain good contrast images from a high speed camera (Fastec Imaging, Troubleshooter TS1000ME, San Diego, California, USA). With the amount of movement of the gantry kept constant at 9.5 mm, and suddenly released, it was able to supply a fixed impact force that dislodges the drop from the tip.

Prior to the experiments with drops being conducted, the momentum generated by the gantry system was characterized. This was done by tracking the falling positions of the gantry using the high speed camera video sequences recorded just before impact. Preceding this, the mass of all the moveable parts was measured and found to be 0.4 kg. The momentum of the impact was determined by multiplying this mass with the velocity just before impact.

The stainless steel tip was characterized using a 3D optical profilometer (Bruker, Veeco-Wyko, Plainview, New York, USA) based on a noncontact GT-1 interferometric system. The instrument was located on a pneumatic vibration-isolation table (Newport) which was fitted with active high attenuation isolation and calibrated using step height standards (Bruker, Veeco). The instrument uses phase-shifting

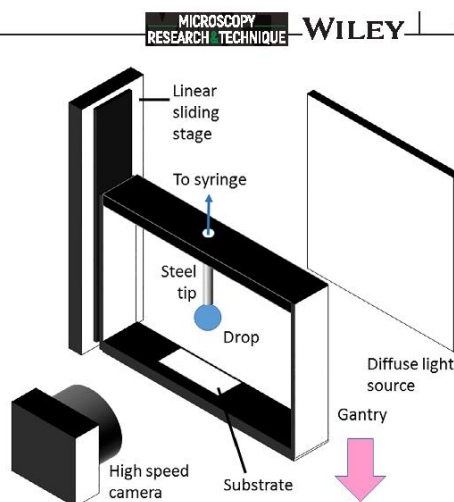


FIGURE 2 Schematic description of the setup to conduct the experiments in which a gantry containing a steel tip with a pendant drop is kept at a height. With diffuse illumination from the rear, high speed camera video sequences of the drop as the gantry fell and stopped suddenly could be recorded for analysis [Color figure can be viewed at wileyonlinelibrary.com]

and/or vertical scanning interferometry to resolve the topology of microscale surface structures. Imaging was done using both low and high magnifications to obtain optimal scanning results.

4 | RESULTS AND DISCUSSION

It was found that 30% glycerol–water (wt/vol) provided effective immobilization of live *Drosophila* flies in microplate wells. Using this same mixture (which is advantageous in field operations), it was possible to obtain magnified images of the insects, facilitating visual identification of the genus (see Figure 3). This demonstrated the ability of the liquid lens method to gather data in the field sans the need of sending samples back to the laboratory.

Using basic smartphone viewing alone, it was possible to obtain target images up to 100 lines/cm without aliasing (Figure 4a). With liquid lens created on the smartphone, significant magnifications were achieved, as seen from images of lines on the target having 0.5 mm spacing (see Figure 4b). It is clear that the use of higher liquid volumes, which would result in higher contact angles, produced higher magnifications. This attests to the tunable feature of the liquid lens as discussed previously. On analyzing the images further, it was found that the resolutions were 5 $\mu\text{m}/\text{pixel}$ and 3.3 $\mu\text{m}/\text{pixel}$ with the 1 and 4 μL liquid lenses, respectively. This is attained using the smartphone's 12 mega-pixel camera. Some degree of pincushion distortion arising from the liquid lens used was observed. Image processing algorithms can be applied to correct for these distortions if needed (Park, Byun, & Lee, 2009).

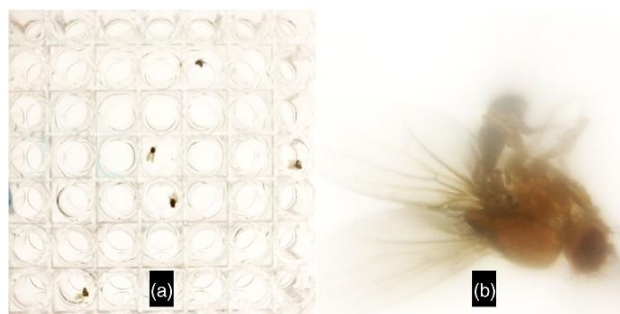


FIGURE 3 Images of a *Drosophila* sample immobilized in a microplate well, recorded (a) without, and (b) with liquid lens incorporated to a smartphone [Color figure can be viewed at wileyonlinelibrary.com]

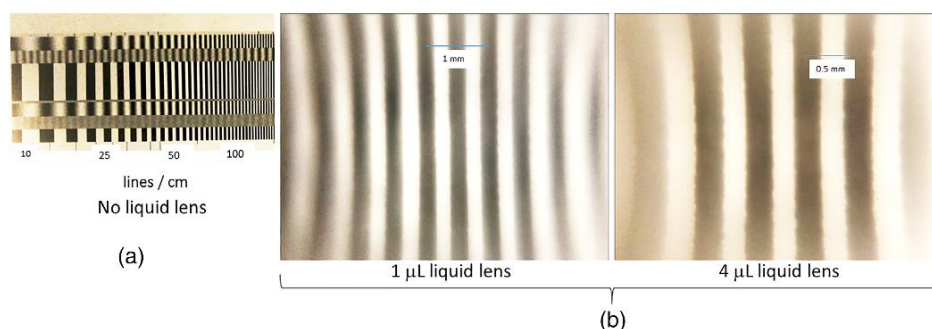


FIGURE 4 Images of the test chart obtained (a) without, and with (b) liquid lens of 1 μL and 4 μL created using different volumes dispensed onto a scribed transparent substrate of 3 mm diameter [Color figure can be viewed at wileyonlinelibrary.com]

Attempts were made to uncover the problem of air entrainment while dispensing viscous liquids from tips. Occurrences of this were found following a series of dispensation exercises conducted, leading to typical cases where small air bubbles were developed within the pendant drop (see Figure 5a and Video S1). These bubbles will adversely impact image fidelity of the liquid lens created. Bubbles in the immobilizing medium will also affect, to some extent, the visibility of immobilized insects in the microplate well. Clearly, stable formation of a pendant drop on the dispensing tip is advantageous as this allows careful inspection of the pendant drop to be made and appropriate interventions can then be taken to prevent the delivery of drops containing bubbles onto the substrate. Once bubbles in the pendant drop are confirmed not to be present, it is possible then to use a drop impact approach to dispense the pendant drop onto the substrate to form the liquid lens, as well as into the respective microplate wells. The profile structure of the tip uncovered using optical profilometry (Figure 5b) do not show presence of any material accretion or manufacturing defect (i.e., notch, etc.) that could affect liquid pinning or permit the passage of air from the side that will facilitate bubble formation. Any enhanced pinning ability is

hence offered only by the regular edges of the tip (Oliver, Huh, & Mason, 1977).

The trace of gantry position against time (Figure 6a) indicated that gravity was the sole dominant force involved and that the contributions from air resistance can be neglected. The fall velocity is determined by the slope at the point of impact and was found to be 366 mm/s. A fall time of 0.038 s from rest as determined from the trace equates to 373 mm/s based on Newton's law. The close correspondence between experimentally and theoretically derived velocities indicated that airflow drag was not a significant factor affecting the travel of the gantry. Taking into consideration the mass of all moving parts, the momentum at the point of impact was thus determined to be 0.1464 N/s. When free fall of the gantry was initiated (Figure 6b), the dispensing tip moves downward in tandem with the spherical drop which assumes a somewhat flattened shape as would be expected from the upward-acting force of the laminar air flow. Upon impact, the evolution of drop shape at the point of detachment is reminiscent of the characteristics of a pendant drop generated from slow flow rates and pinched-off from a stationary tip under its own weight.

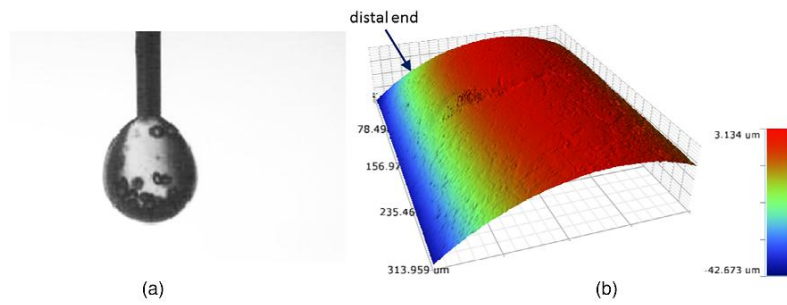


FIGURE 5 The presence of (a) air bubbles entrained in a pendant drop during liquid dispensation. These bubbles will degrade the image quality of the liquid lens. Imaging results (b) from optical profilometry of the tip do not reveal material accretion that would affect liquid pinning or facilitate bubble formation [Color figure can be viewed at wileyonlinelibrary.com]

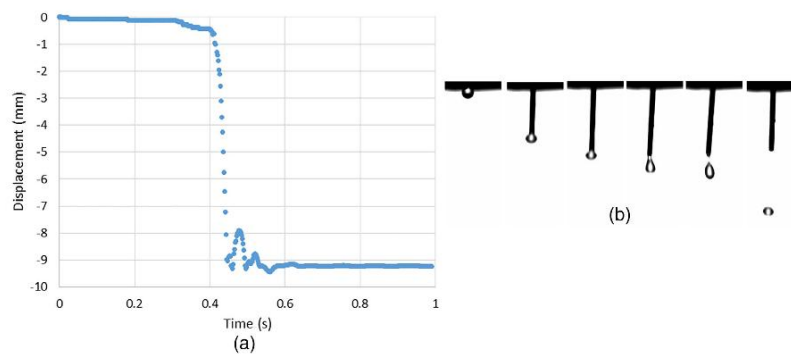


FIGURE 6 Plot of (a) distance of tip displacement versus time trace of the tip (and thus the gantry based on rigid body assumption). This allowed the velocity at the point of impact to be determined. The sequence (b) of high speed images (from left to right) show changes in the morphology of a drop stably maintained initially at the dispensing tip and then accelerated downwards by gravity to an abrupt stop before terminal velocity can be reached. The resulting impact force triggers detachment of the drop from the tip where it resumes its flattened spherical shape [Color figure can be viewed at wileyonlinelibrary.com]

Overall, the approach can be practically implemented in the field as it only comprises the impact dislodgement device, a microplate well, a vial of 30% glycerol–water (wt/vol) mixture, and a smartphone with scribed transparent sheet over the lens. As the only electronic device in the mix, the smartphone offers possibilities of processing the magnified images on site or this could be achieved by making use of varied electronic cloud-based resources when those on the smartphone are limited. There is also potential of combining this approach with smartphone applications that estimate physical cloud coverage in the field (Paris, Downs, Igoe, & Turner, 2016) as ambient lighting is a known factor that affects insect trapping (Yela & Holyoak, 1997).

Application of this smartphone/liquid lens-based setup was illustrated here with *Drosophila* as the target of interest where

microscopic examination of actively moving specimens presents a real challenge (Aufderheide & Janetopoulos, 2012). Experiments have been conducted outside and inside the laboratory, and found to work well in both modes. An effective overall method requires not only an effective immobilization and imaging technique, but also an appropriate insect attraction scheme for baiting the target. The latter has been the focus of the research community geared toward identifying effective species-specific attractants (Huang, Gut, & Grieshop, 2017; Lasa et al., 2017). Thus, the liquid droplet used in this scheme can have a threefold function: to capture via the incorporation of a chemical attractant, to immobilize by the use of a viscous substance and to allow magnification of actively moving specimens for microscopic observations. For *Drosophila*, we have found that addition of some vinegar into the immobilizing medium helped to attract the insects

better. This process of capture and immobilization is benign and minimizes mechanical or physical distortion of the specimen. In addition, we are able to keep the *Drosophila* alive with this method for further analysis if necessary. Furthermore, the use of a liquid lens is compatible with the performance of the optics to produce magnified images of the specimen without the need for any fabrication facility to create solid lenses suited for microscopy (Sung, Jeang, Lee, & Shih, 2015).

It should be noted that the tool described here is best applied for preliminary screening purposes in the field as there are limits to achievable magnification and resolution with this simple set-up. Where follow-up examination is deemed necessary, field samples can be collected for high resolution imaging using more sophisticated instruments in the laboratory. We also envisage that other biological specimens of suitable dimensions may also be examined bearing in mind the limitations of magnification and resolution with this method. Hence, even soil-living biological organisms such as *Caenorhabditis elegans* or *Dictyostelium discoideum* may potentially be studied depending on the stage of their life cycle as well as the availability of a suitable soil extraction method. In the case of *C. elegans* (typically about 1 mm in length), we envisage that filtered Baermann funnel liquid extracts of nematode-infested soil can easily be examined in the field using this smartphone/liquid lens method. However, the suitability of the immobilization medium should be investigated first. Intuitively, if microscopic examination is required under conditions of low ambient light, the use of auxiliary lighting is recommended. The simple setup of our method allows color-multiplexed illumination to be easily incorporated if needed (Jung et al., 2017). Finally, when using smartphones for applications such as imaging, faster power drainage of the battery should be noted. Hence, having a few power banks on standby is always advisable in the field.

5 | CONCLUSIONS

The ability to immobilize *Drosophila* samples using 30% glycerol-water (wt/vol) and obtaining magnified views of them using liquid lens of the same mixture and a smartphone is demonstrated. In the latter, the focal length tuning characteristic was confirmed and digital resolutions of up to 3.3 $\mu\text{m}/\text{pixel}$ could be attained. In order to circumvent the problem of bubbles that will affect imaging fidelity, a method of liquid transfer, wherein a pendant drop is stably generated on a dispensing tip and moved in tandem in the direction of gravity by a gantry displacement method such that sufficient momentum is transferred to dislodge the drop, was introduced. This method of precise drop delivery onto a destination substrate uses a relatively small movement stroke of 10 mm with no daughter drops or air entrained into the liquid. This approach offers the practical means to conduct open-field investigations by allowing specimens to be examined on-site, thus possibly obviating the need for specimen collection for laboratory-based analysis.

ACKNOWLEDGMENTS

This work was performed in part at the Melbourne Centre for Nanofabrication (MCN) in the Victorian Node of the Australian

National Fabrication Facility (ANFF). The assistance of H. Uddin in optical topography imaging is appreciated. Information provided by the Victorian Institute of Invertebrate Sciences is appreciated.

ORCID

Tuck Wah Ng  <https://orcid.org/0000-0001-5592-1390>

REFERENCES

- Aufderheide, K. J., & Janetopoulos, C. (2012). Immobilization of living specimens for microscopic observation. In A. Méndez-Vilas (Ed.), *Current microscopy contributions to advances in science and technology* (Vol. 2, pp. 833–838). Badajoz, Spain: Formatex Research Centre.
- Baek, D., Cho, S., Yun, K., Youn, K., & Bang, H. (2014). Time-lapse microscopy using smartphone with augmented reality markers. *Microscopy Research and Technique*, 77, 243–249.
- Boevé, J. L., Eertmans, F., Adriaens, E., & Rossel, B. (2016). Field method for testing repellency of an Icaridin-containing skin lotion against Vespidae wasps. *Insects*, 7, 22.
- Cesaretti, M., Poté, N., Dondero, F., Cauchy, F., Schneck, A. S., Soubrane, O., ... Antonini, A. (2017). Testing feasibility of an accurate microscopic assessment of macrovesicular steatosis in liver allograft biopsies by smartphone add-on lenses. *Microscopy Research and Technique*, 81, 58–63.
- Cheong, B. H.-P., Chua, W. S., Liew, O. W., & Ng, T. W. (2014). Scribed transparency microplates mounted on a modified standard microplate. *Analytical Biochemistry*, 458, 40–42.
- Delly, J. G. (1985). Narcosis and preservation of freshwater animals. *American Laboratory*, 17, 31–40.
- Hallmann, C. A., Sorg, M., Jongejans, E., Siepel, H., Hofland, N., Schwan, H., ... de Kroon, H. (2017). More than 75 percent decline over 27 years in total flying insect biomass in protected areas. *PLoS One*, 12, e0185809.
- Huang, J., Gut, L., & Grieshop, M. (2017). Evaluation of food-based attractants for *Drosophila suzukii* (Diptera: Drosophilidae). *Environmental Entomology*, 46, 878–884.
- Jung, D., Choi, J.-H., Kim, S., Ryu, S., Lee, W., Lee, J.-S., & Joo, C. (2017). Smartphone-based multi-contrast microscope using color-multiplexed illumination. *Scientific Reports*, 7, 7564.
- Kiriker, O., Soper, A. K., Dzyuba, B., & Holt, H. V. (2016). Segregated water observed in a putative fish embryo cryopreservative. *Royal Society Open Science*, 3, 150655.
- Lasa, R., Tadeo, E., Toledo-Hernández, R. A., Carmona, L., Lima, I., & Williams, T. (2017). Improved capture of *Drosophila suzukii* by a trap baited with two attractants in the same device. *PLoS One*, 12(11), e0188350.
- Li, X. Y., Cheong, B. H.-P., Somers, A., Liew, O. W., & Ng, T. W. (2013). Surface-scribed transparency based microplates. *Langmuir*, 29, 849–855.
- Oliver, J. F., Huh, C., & Mason, S. G. (1977). Resistance to spreading of liquids by sharp edges. *Journal of Colloid and Interface Science*, 59, 568–581.
- Parisi, A. V., Downs, N., Iggoe, D., & Turner, J. (2016). Characterization of cloud cover with a smartphone camera. *Instrumentation Science and Technology*, 44, 23–34.
- Park, J., Byun, S.-C., & Lee, B.-U. (2009). Lens distortion correction using ideal image coordinates. *IEEE Transactions on Consumer Electronics*, 55, 987–991.

- Petrovskaya, N., Petrovskii, S., & Murchie, A. K. (2012). Challenges of ecological monitoring: Estimating population abundance from sparse trap counts. *Journal of the Royal Society Interface*, 9, 420–435.
- Sung, Y.-L., Jeang, J., Lee, C.-H., & Shih, W.-C. (2015). Fabricating optical lenses by inkjet printing and heat-assisted in-situ curing of polydimethylsiloxane for smartphone microscopy. *Journal of Biomedical Optics*, 20, 047005.
- Taylor, H. L. (1993). The Taylor microcompressor, mark II. *The Microscope*, 41, 19–20.
- Yela, J. L., & Holyoak, M. (1997). Effects of moonlight and meteorological factors on light and bait trap catches of noctuid moths (Lepidoptera: Noctuidae). *Environmental Entomology*, 26, 1283–1290.

SUPPORTING INFORMATION

Additional supporting information may be found online in the Supporting Information section at the end of this article.

How to cite this article: Ahmad Zahidi AA, Chung DCK, Katariya M, Liew OW, Ng TW. Living specimens under field immobilization and smartphone microscopic observation. *Microsc Res Tech*. 2019;1–7. <https://doi.org/10.1002/jemt.23340>

Appendix E

Journal of Pharmaceutical and Biomedical Analysis 102 (2015) 199–202



Contents lists available at ScienceDirect

Journal of Pharmaceutical and Biomedical Analysis

journal homepage: www.elsevier.com/locate/jpba

Short communication

A direct heating model to overcome the edge effect in microplates

Chun Yat Lau^a, Alifa Afiah Ahmad Zahidi^a, Oi Wah Liew^b, Tuck Wah Ng^{a,*}

^a Laboratory for Optics and Applied Mechanics, Department of Mechanical & Aerospace Engineering, Monash University, Clayton, Victoria 3800, Australia
^b Cardiovascular Research Institute, Yong Loo Lin School of Medicine, National University of Singapore, National University Health System, Centre for Translational Medicine, 14 Medical Drive, Singapore 117599, Singapore

ARTICLE INFO

Article history:

Received 7 August 2014
 Received in revised form
 10 September 2014
 Accepted 13 September 2014
 Available online 22 September 2014

Keywords:

Edge effect
 Finite element
 Heating
 Microplate
 Transparency

ABSTRACT

Array-based tests in a microplate format are complicated by the regional variation in results of the outer against the inner wells of the plate. Analysis of the evaporation mechanics of sessile drops showed that evaporation rate increase with temperature was due to changes in the heat of vaporization, density and diffusion coefficient. In simulations of direct bottom heating of standard microplates, considerable heat transfer via conduction from the side walls was found to be responsible for lower temperatures in the liquid in wells close to the edge. Applying a two temperature heating mode, 304 K at the side compared to 310 K at the bottom, allowed for a more uniform temperature distribution. Transparency microplates were found to inherently possess immunity to the edge effect problem due to the presence of air between the liquid and solid wall.

© 2014 Elsevier B.V. All rights reserved.

1. Introduction

In the biochemical laboratory, microplates (or microtiter plates) remain as arguably the most ubiquitous tools in analyte handling for analytical research and clinical diagnostic screening. Keeping the format of analyte handling implements to follow that of standard microplates in developing biochemical analysis instrumentation has the advantage of ready usage with existing readers, thus eliminating the costs associated with developing new readers. It also offers practitioners with familiarity in employing a widely established format. Such a strategy has been harnessed to address various biochemical related needs [1–3] despite the advent of lab-on-a-chip alternatives [4]. Some developments in analyte handling itself to function in this vein have been reported in the context of small volumes [5,6]. More recently, we have advanced the ability to use transparencies, normally applied in conjunction with overhead projectors, in microplate instrumentation [7,8]. The immense cost effectiveness here offers the possibility of application even in resource-limited laboratories.

The scale of testing required in modern biochemical analysis has driven the introduction of multiplexed formats using microplates [9,10]. Multiplex testing, however, presents analytical and quality control challenges. Among the controls that have been introduced

include the use of blank areas, positive controls, negative controls, normalization controls, controls for nonspecific binding and to confirm sample addition, cross-reactivity controls, and controls to assess the activity of assay reagents such as the detection conjugate [11]. A factor that continues to complicate array-based tests in a microplate format is the regional variation in results of the outer against the inner wells of the plate, which is often described as the edge effect. The main culprit for this is widely believed to be the zonal differences in the rate of evaporation from the wells [12,13]. Quite naturally, the use of plate seals [14] and tight closures [15] has been advanced to ameliorate the evaporation variation effect. A major cause of evaporation during microplate incubation is temperature. While the effect from temperature gradients have been alluded to [16], there have been no known studies made or approaches advanced to remedy the edge effect through reducing temperature gradients in microplates. Here, we investigate this aspect by providing an analytical link between temperature and evaporation rate, and conducting thermal simulation studies using finite elements (FEM).

2. Analysis of evaporation

Let us consider the evaporation mechanics involved for liquid residing in a standard microplate well (Fig. 1a) and in a transparency microplate well that operates under reduced evaporation [17] (Fig. 1b). Essentially, the latter is a sessile drop in which efforts to characterize its evaporation have been attempted [18]

* Corresponding author. Tel.: +61 3 99054647.
 E-mail address: engngtw@gmail.com (T.W. Ng).

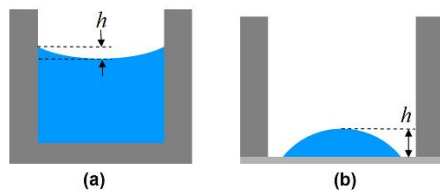


Fig. 1. Schematic depiction of liquid residence in (a) a standard microplate well, and (b) transparency microplate well.

by considering the adjacent air being saturated with vapor due to the rapid interchange of molecules between the liquid and vapor phases. The vapor phase is essentially then a thin saturated region that diffuses outward into the surrounding unsaturated air. Assuming a quasi-equilibrium process for slow evaporation in still air, the evaporation rate of the vapor Q can be taken to be represented by Fick's law such that

$$Q = \rho \frac{dV}{dt} = 4\pi Dr(C_s - C_\infty)f(\theta) \quad (1)$$

where D is the vapor diffusivity in still air, r = radius of air-liquid surface curvature, ρ = density of the liquid, C_s = the saturated vapor concentration at drop surface, C_∞ = the ambient vapor concentration determined by the relative humidity, and $f(\theta)$ = the dependence of evaporation rate on the contact angle. Various factors can affect the evaporation process [19,20], albeit if we consider only a situation in time, Eq. (1) can be simplified to

$$\frac{dV}{dt} = -\frac{2\pi DhM}{\rho RT}(P_s - P_\infty) \quad (2)$$

where h = the height of drop, R = gas constant, M = molecular weight of the liquid, T = temperature in Kelvins of the liquid, P_s = the vapor pressure on the liquid surface, P_∞ = the vapor pressure an infinite distance away (which can be assumed to be zero). P_s is related to T using the Clausius-Clayperon relation

$$P_s = \exp\left(\frac{-\Delta H_V}{RT} + K\right) \quad (3)$$

where ΔH_V is the heat of vaporization of the liquid, and K is the value for $\ln(P_s)$ when $\Delta H_V = 0$. Hence Eq. (2) can be rewritten as

$$\frac{1}{h} \frac{dV}{dt} = -\left[\frac{2\pi DM}{\rho RT} \exp\left(\frac{-\Delta H_V}{RT} + K\right)\right] \quad (4)$$

We can assume this to be the same in the case of liquid in standard microplate wells.

3. Simulation details

The simulations were conducted using ABAQUS FEA (Dassault Systemes). For the standard microplate, its overall size was 127.76 mm length, 85.48 mm wide, and 14.7 mm high, with the wells kept at a pitch of 9 mm from each other and having diameter and height of 6.5 mm and 11.45 mm respectively. The solid material used throughout was acrylic, while the liquid used was water. In the case of transparency microplates, the transparency thickness was kept at 0.11 mm and the liquid droplets kept at 40 μ L volume with a diameter of 5.34 mm in contact with the transparency. The microplate section and the water section were meshed with tetrahedron elements due to their regular shapes, while the transparency section was meshed with rectangular element to achieve an even mesh. The microplate sections in standard microplate model and transparency microplate model have about 720,000 nodes and 650,000 nodes respectively. The transparency

sheet has approximately 58,000 nodes and each droplet has about 1500 nodes in the transparency microplate model. The number of nodes in the water section in each well varies from 450 to 3300 depending on the filling ratio. All nodes in both models are approximately 1 mm apart. In the simulations, the boundary elements not affected by heating were fixed at 298 K (which corresponds to typical ambient temperature). The boundary elements subject to direct heating were set at 311 K (to correspond to the body incubation temperatures typically used in biochemical and immunoassays when heating is required). The presence of strong temperature gradients within the liquid body will lead to convection flows that facilitate mass transfer. In our simulations we do not include this effect as our purpose is to establish the average temperature of the liquid in each well.

4. Results and discussion

We start by considering the relationship between temperature and evaporation rate. Eq. (4) appears to portray an anomalous situation that the rate of evaporation is inversely proportional to temperature. In reality, however, only certain parameters in the equation are invariant with temperature, i.e. for water $M = 0.018 \text{ kg mol}^{-1}$, $R = 8.314 \text{ J K}^{-1} \text{ mol}^{-1}$, $K = 740.2943 \text{ Pa}$. At $T = 298 \text{ K}$ (25°C), $\rho = 997.15 \text{ kg m}^{-3}$, $\Delta H_V = 1814 \times 10^3 \text{ J kg}^{-1}$, $D = 25.28 \times 10^{-6} \text{ m}^2 \text{ s}^{-1}$; while at $T = 311 \text{ K}$ (38°C), $\rho = 992.97 \text{ kg m}^{-3}$, $\Delta H_V = 1891 \times 10^3 \text{ J kg}^{-1}$, $D = 27.17 \times 10^{-6} \text{ m}^2 \text{ s}^{-1}$. Consequently, if we compute the right hand side of Eq. (4), we have values of $-3.91 \times 10^{-9} \text{ m}^2 \text{ s}^{-1}$ and $-9.23 \times 10^{-9} \text{ m}^2 \text{ s}^{-1}$ for temperatures of 25°C and 38°C respectively. This indicates that when the temperature is higher, the evaporation rate increases correspondingly. Hence, this confirms that the key to eliminating the edge effect will be to maintain a constant temperature of the liquid dispensed in all wells.

Fig. 2(a) presents the result of the FEM simulation with a standard microplate well in which only the bottom was heated. It can be seen that there is a considerable heat transfer via conduction from the side walls, causing the liquid in wells close to the edge to experience lower temperatures. Fig. 3(a) present plots of the average liquid temperature sampled at the center and corner wells of a standard microplate at different liquid filling ratios (height of liquid/height of well). The temperature difference trends evident confirm the edge effect through the influence of heat conduction. It can be seen that the temperature in the liquid is generally higher when the liquid filling ratio is increased. This is due to the thermal inertia offered by the liquid body.

In order to overcome the imbalance due to heat conductions, we have simulated the case where the side walls were heated as well as the bottom at the same temperature. As shown in Fig. 2(b), this cursorily portends the capacity to ameliorate the edge effect. On evaluating the average liquid temperature sampled at the center and corner wells of a standard microplate at different liquid filling ratios however (Fig. 3(b)), it can be seen that a reversed effect is attained, i.e. the temperature of the edge wells were higher than the center wells. This is expected due to the contribution of heat from the side walls having a greater influence on the average temperature. Logically, a remedy will be to lower the temperature of the side walls relative to the bottom in order to counteract this imbalance. Fig. 3(c) presents the case where a satisfactory outcome is achieved by keeping the temperature of the side walls at 304 K compared to 310 K at the bottom. It should be noted that different combinations will be needed if the ambient temperature is different.

The need to maintain a dual temperature heating mode can be a challenge in terms of instrumentation development. Since the heat loss due to conductivity is the main culprit for the temperature disparity, a remedy may be to use a material with very low thermal

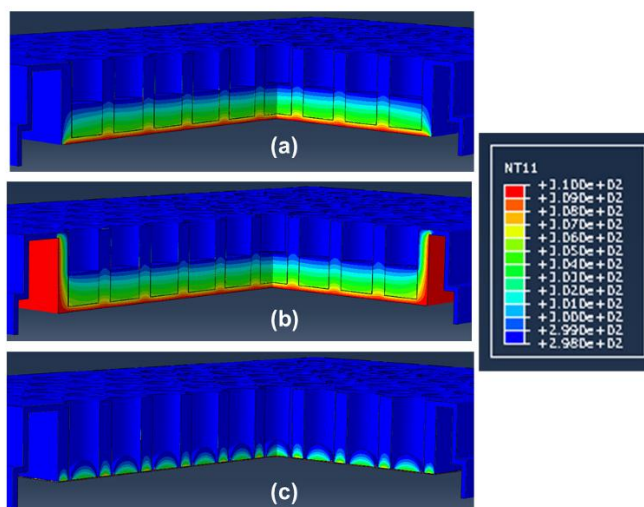


Fig. 2. Finite element simulation results of the steady-state temperature distribution in a (a) standard microplate with direct heating at the bottom, (b) standard microplate with direct heating at the bottom and sides, (c) transparency microplate with direct heating at the bottom.

conductivity as manufacture for microplates applied in biochemical assays. Such an approach will likely not get much traction practically. In the early 1960s, microplates were primarily made of acrylic (thermal conductivity of $0.2 \text{ W m}^{-1} \text{ K}^{-1}$) until the appearance of polystyrene ($0.1\text{--}0.13 \text{ W m}^{-1} \text{ K}^{-1}$) plates in 1965 and has remained the mainstay of microplates to date. In recent times, materials like cyclo-olefins with superior optical properties have been used in microplate manufacture but they do not provide added advantage in terms of thermal conductivity ($0.16 \text{ W m}^{-1} \text{ K}^{-1}$) compared with

polystyrene. A more convenient remedy is attainable by placing air between the liquid and solid walls, since air has a thermal conductivity ($0.024 \text{ W m}^{-1} \text{ K}^{-1}$) that is about ten and five times lower than that of acrylic and polystyrene, respectively. As it turns out, a ready solution is available via the use of adapted transparency microplates [17] in which the analyte does not contact the wall (see Fig. 1(b)). This can be seen in the simulation result of Fig. 2(c), as well as the uniform temperature distribution in different wells along the length of a transparency microplate from center to the

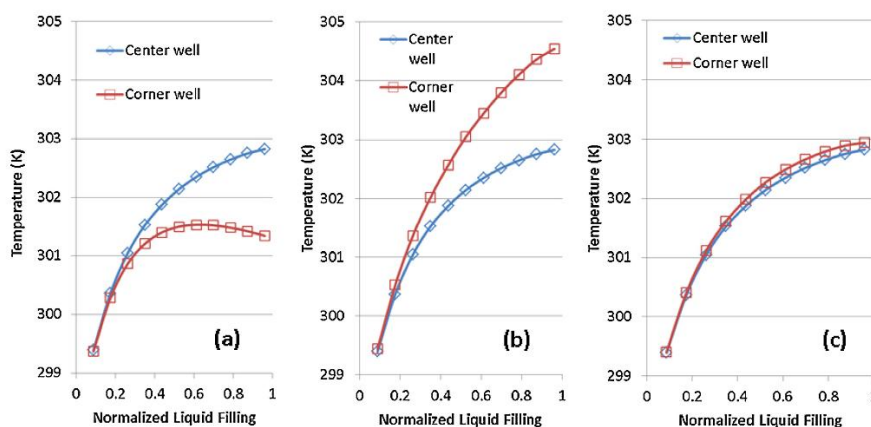


Fig. 3. Plots of the average liquid temperature in a well at the center and corner at different liquid filling ratios (height of liquid/height of well) of a standard microplate (a) directly heated only at the bottom at 310K, (b) directly heated at the bottom and sides at 310K, and (c) directly heated at the bottom at 310K and the sides at 304K.

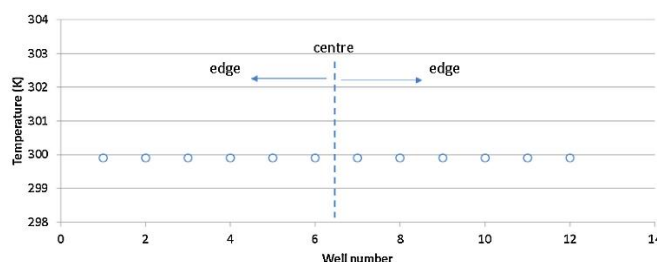


Fig. 4. Temperature distribution at different wells along the length of a transparency microplate, which show strong uniformity from center to the edge.

edge given in Fig. 4. It should be noted that while the rate of evaporation is uniform, it does not mean that it is absent. One strategy that can be introduced to slow down the evaporation rate is to inject in silicone oil [21], albeit it is predicated that the oil does not affect the analyte. A more general approach would be to increase the humidity of the incubating environment as this will reduce the vapor pressure differences between the liquid and the air. While this is workable, it is important to mind the possibility of condensation occurring due to the high surface to volume ratios that are typically in place. Surfaces that are strongly hydrophobic encourage drops to condense on them more readily [22,23], which can then dislodge more easily and mix with the analyte to alter its composition. This is particularly important when microplates are used in the context as cell incubators [24]. We also make a final comment that if convective heat dissipation modes are eliminated, the use of different solvents/liquids should have no bearing on the results.

5. Conclusions

The basis of the evaporation mechanics of a sessile drop was considered analytically. The evaporation rate was found to increase with increase in temperature due to the changes in heat of vaporization, density and diffusion coefficient with temperature. From simulations of direct heating of standard microplates at the bottom, the temperature in the liquid was generally higher when the liquid filling ratio was increased due to the thermal inertia effect offered by the liquid body. Considerable heat transfer via conduction from the side walls was found to be responsible for the liquid in wells close to the edge to experience lower temperatures. When the standard microplate was heated at equal temperatures at the bottom and sides, the temperature of the edge wells were higher than the center wells. Applying a two temperature heating mode, 304 K at the side compared to 310 K at the bottom, allowed for a more uniform temperature distribution. Due to absence of direct liquid–solid wall contacts, transparency microplates were found to inherently possess immunity to the edge effect problem.

Acknowledgement

This work was supported in part through the Australian Research Council Grant DP120100583.

References

- [1] K. Szeto, S.J. Reinholt, F.M. Duarte, J.M. Pagano, A. Ozer, L. Yao, J.T. Lis, H.G. Craighead, High-throughput binding characterization of RNA aptamer selections using a microplate-based multiplex microcolumn device, *Anal. Bioanal. Chem.* 406 (2014) 2727–2732.

- [2] M. Zhu, W. Zhao, N. Vazquez, J.G. Mitroka, Analysis of low level radioactive metabolites in biological fluids using high-performance liquid chromatography with microplate scintillation counting: method validation and application, *J. Pharm. Biomed. Anal.* 39 (2005) 233–245.
- [3] Y.Y.B. Liu, P. Rigsby, D. Searidic, J.D. Marks, R.G.A. Jones, A functional dual-coated (FDC) microtiter plate method to replace the botulinum toxin LD50 test, *Anal. Biochem.* 425 (2013) 28–35.
- [4] P. Neuzil, S. Gieselbrecht, K. Lange, T.J. Huang, A. Manz, Revisiting lab-on-a-chip technology for drug discovery, *Nat. Rev. Drug Discov.* 11 (2012) 620–632.
- [5] R. Seemann, M. Brinkmann, T. Pohl, S. Herminghaus, Droplet based microfluidics, *Rep. Prog. Phys.* 75 (2012) 016601.
- [6] J.K.K. Lye, T.W. Ng, A. Neild, O.W. Liew, A capacity for mixing in capillary wells for microplates, *Anal. Biochem.* 410 (2011) 152–154.
- [7] B.H.-P. Cheong, V. Diep, T.W. Ng, O.W. Liew, Transparency based microplates for fluorescence quantification, *Anal. Biochem.* 422 (2012) 39–45.
- [8] X.Y. Li, B.H.-P. Cheong, A. Somers, O.W. Liew, T.W. Ng, Surface-scribed transparency based microplates, *Langmuir* 29 (2013) 849–855.
- [9] P.S. Eastman, W.C. Manning, F. Qureshi, D. Haney, C. Cavet, C. Alexander, L.K. Hesterberg, Characterization of a multiplex, 12-biomarker test for rheumatoid arthritis, *J. Pharm. Biomed. Anal.* 70 (2012) 415–424.
- [10] K. Xu, Y. Sun, W. Li, J. Xu, B. Cao, Y. Jiang, T. Zheng, J. Li, D. Pan, Multiplex chemiluminescent immunoassay for screening of mycotoxins using photonic crystal microsphere suspension array, *Analyst* 139 (2014) 771–777.
- [11] A.A. Ellington, I.J. Kullo, K.R. Bailey, G.G. Klee, Measurement and quality control issues in multiplex protein assays: a case study, *Clin. Chem.* 55 (2009) 1092–1099.
- [12] M.J. Patel, R. Tuckerman, Q. Dong, A pitfall of the 3-(4,5-dimethylthiazol-2-yl)-5-(3-carboxymethylphenyl)-2-(4-sulfonylphenyl)-2H-tetrazolium (MTS) assay due to evaporation in wells on the edge of a 96 well plate, *Biotechnol. Lett.* 27 (2005) 805–808.
- [13] R. Hermann, M. Lehmann, J. Buchs, Characterization of gas–liquid mass transfer phenomena in microtitre plates, *Biotechnol. Bioeng.* 81 (2003) 178–186.
- [14] H. Zimmermann, G. John, H. Trauthwein, U. Dingemissen, K. Huthmacher, Rapid evaluation of oxygen and water permeation through microplate sealing tapes, *Biotechnol. Prog.* 19 (2003) 1061–1063.
- [15] W.A. Duetz, W. Minas, M. Kuhner, R. Clerval, A.H.M. Fjalman, B. Witholt, Miniaturized microbial growth systems in screening, *Bioworld* 2 (2001) 8–10.
- [16] C.B. Maddox, L. Rasmussen, E.L. White, Adapting cell-based assays to the high throughput screening platform: problems encountered and lessons learned, *J. Assoc. Lab. Autom.* 13 (2008) 168–173.
- [17] B.H.P. Cheong, W.S. Chua, O.W. Liew, T.W. Ng, Scribed transparency microplates mounted on a modified standard microplate, *Anal. Biochem.* 458 (2014) 40–42.
- [18] R.G. Picknett, R. Bexon, The evaporation of pendant and sessile drops in still air, *J. Colloid Interface Sci.* 61 (1977) 336–350.
- [19] X. Fang, B. Li, E. Petersen, Y. Ji, J.C. Sokolow, M.H. Rafailovich, Factors controlling the drop evaporation constant, *J. Phys. Chem. B* 109 (2005) 20554–20557.
- [20] T. Hunyh, M. Muradoglu, O.W. Liew, T.W. Ng, Contact angle and volume retention effects from capillary bridge evaporation in biochemical microplating, *Colloids Surf. A* 436 (2013) 647–655.
- [21] K.J. Gregory, Y. Sun, Reduction of sample evaporation in small volume microplate luminescence assays, *Anal. Biochem.* 387 (2009) 321–323.
- [22] D. Torresin, M.K. Tiwari, D. Del Col, D. Poulikakos, Flow condensation on copper-based nanotextured superhydrophobic surfaces, *Langmuir* 29 (2013) 840–848.
- [23] T. Vuong, A. Qi, M. Muradoglu, B.H.-P. Cheong, O.W. Liew, C.X. Ang, J. Fu, L. Yeo, J. Friend, T.W. Ng, Precise drop dispensation on superhydrophobic surfaces using acoustic nebulization, *Soft Matter* 9 (2013) 3631–3639.
- [24] F. Triaud, D.-H. Clenet, Y. Cariou, T.L. Neel, D. Morin, A. Truchaud, Evaluation of automated cell culture incubators, *J. Assoc. Lab. Autom.* 8 (2003) 82–86.

Appendix F

Analytical Biochemistry 545 (2018) 1–3



Contents lists available at ScienceDirect

Analytical Biochemistry

journal homepage: www.elsevier.com/locate/yabio

Drone inflight mixing of biochemical samples

Mayur Katariya^a, Dwayne Chung Kim Chung^a, Tristan Minife^a, Harshit Gupta^a, Alifa Afiah Ahmad Zahidi^a, Oi Wah Liew^b, Tuck Wah Ng^{a,*}^a Laboratory for Optics and Applied Mechanics, Department of Mechanical & Aerospace Engineering, Monash University, Clayton, Victoria, 3800, Australia^b Cardiovascular Research Institute, Yong Loo Lin School of Medicine, National University of Singapore, National University Health System, Centre for Translational Medicine, 14 Medical Drive, 117599, Singapore

ARTICLE INFO

Keywords:
Drone
UAV
Quadcopter
Mixing
Transport

ABSTRACT

Autonomous systems for sample transport to the laboratory for analysis can be improved in terms of timeliness, cost and error mitigation in the pre-analytical testing phase. Drones have been reported for outdoor sample transport but incorporating devices on them to attain homogenous mixing of reagents during flight to enhance sample processing timeliness is limited by payload issues. It is shown here that flipping maneuvers conducted with quadcopters are able to facilitate complete and gentle mixing. This capability incorporated during automated sample transport serves to address an important factor contributing to pre-analytical variability which ultimately impacts on test result reliability.

There is understandable interest towards increasing use of point-of-care testing (POCT) for biomarker measurements with associated advantages of reduced delays in diagnosis and treatment, minimal sample handling and requirement for sophisticated equipment, ease-of-use with lower staff training burdens to maintain formal accreditation, as well as opportunity for broad applications both in the clinical and non-clinical setting. POCT offers to bypass many steps where pre- and post-analytical errors most commonly arise in centralized laboratory-based testing, which include appropriate specimen collection, handling, transport and storage; instrument set up; testing; and result reporting. Although significant advances in POCT technologies in terms of improved test reliability and increasing spectrum of available POCT menus, there remains issues of relative cost burdens, analytical and clinical performances compared to laboratory-based testing that continue to require sustained efforts to address [1–3]. Clearly, the role of laboratory testing remains a core pillar for disease management where rapid diagnosis, timely and appropriate intervention are central to quality healthcare.

The transport of samples to the laboratory is strongly governed by the twin factors of timeliness (to ensure their viability) and cost [4,5], where the use of autonomous schemes have clear advantages. In hospitals, pneumatic tubes have long been implemented in this vein, to the extent that they are now indispensable to the function of most healthcare support systems [6,7]. More recently, the use of drones, or unmanned aerial vehicles (UAV), has been explored for outdoor biological specimen delivery [8]. While some instances of malfunctions have been

highlighted as issues of concern [9], these glitches will likely be overcome through the use of more robust electronics technologies, thus enabling their potential use not only in remote venues but also in traffic congested urban environments, where route planning strategies can only offer limited improvements in timeliness of sample delivery [4,5]. The timeliness aspect can be further augmented if some parts of the pre-processing of samples are done en-route during transport. Appropriate mixing of samples is arguably the most common sample handling step which is key to obtaining quality specimens for laboratory testing. In the case of blood collection into receptacles, proper mixing for homogenous dispersion of silica particles, separator gels, clot activators or anti-coagulants is vital for optimal downstream separation of serum or plasma. Controlling the level of agitation applied during mixing is also important for minimizing hemolysis of red blood cells which could render the sample unsuitable for testing. Automated methods for mixing are generally based on sustained and controlled agitation for specific periods of time. Novel schemes have been devised to mix volumes of liquid samples in lab-on-chip devices [10], capillaries [11], and liquid bridges [12], and drops [13] in the micro-liter range in the laboratory. Samples that are transported to the laboratory are mostly in the milliliter volume range in order to provide margins for repeat testing procedures [14] which occasionally can be due to process [15], assay [16] or substrate [17] inconsistencies. The limited payload of a typical quadcopter drone will render it unfeasible to attach devices such as vortex mixers onto it for sample transport and mixing in tandem. In addition, the forces generated by a vortex mixer in operation can

* Corresponding author.
E-mail address: engngtw@gmail.com (T.W. Ng).

<https://doi.org/10.1016/j.ab.2018.01.004>

Received 12 December 2017; Received in revised form 29 December 2017; Accepted 2 January 2018

Available online 04 January 2018

0003-2697 / © 2018 Elsevier Inc. All rights reserved.

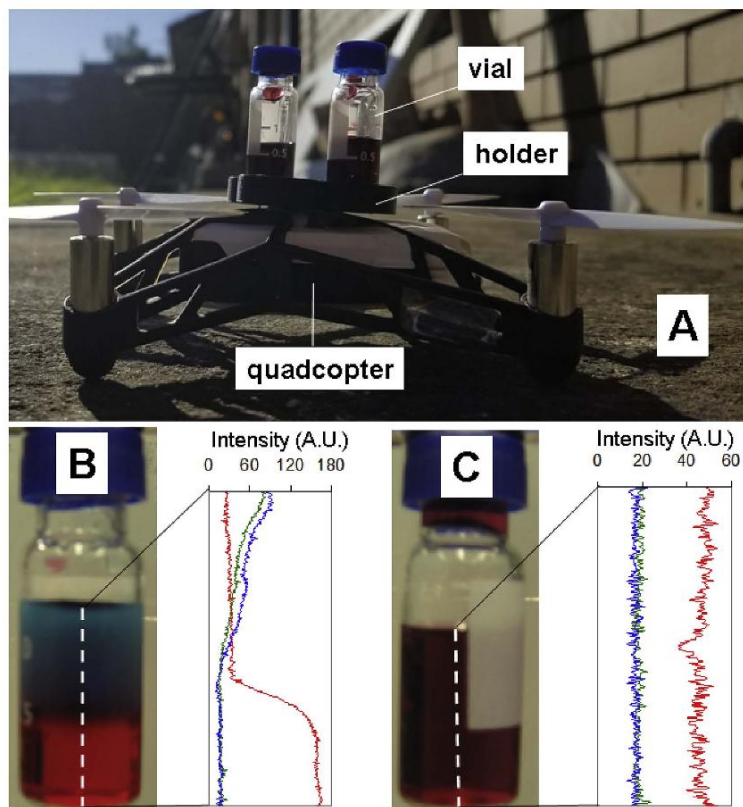


Fig. 1. The quadcopter drone (A) with 3D printed holder attached on that is able to hold up to four vials for transport. Prior to transport with the quadcopter (B), the vial containing water (stained blue) and glycerol (stained red) showed limited mixing, which was confirmed by the quantitative red, green, and blue color distribution as derived from the line profile (dashed line). Complete mixing is achieved following transport and flipping on the quadcopter (C). Under transport and no flipping, the result shown in (B) is obtained. (For interpretation of the references to colour in this figure legend, the reader is referred to the Web version of this article.)

disrupt the planned flight pattern of a quadcopter. A solution however may be offered by the flight maneuvering capability of the quadcopter itself. The aerodynamic lift in quadcopters, as opposed to fixed-wing aircraft, is generated by four vertically oriented propellers. This allows movements to be generated laterally, longitudinally, and rotationally with ease. In the flight control of many quadcopters, there is an in-built capability for them to perform flipping (looping) maneuvers. This is generally offered as a means of showcasing their aerobatic abilities, where the control schemes needed to attain the kinematics has been well studied [18]. In this work, the ability of this maneuver to helpfully mix samples in-flight is investigated.

The quadcopter used was a Parrot Minidrone with mass of 63.5 g mass and dimensions measuring $15.2 \times 15.2 \times 3.8$ mm. It is powered by a 550 mAh lithium battery wherein flight can be controlled using a smartphone application (FreeFlight, Android or iOS). The liquid media used to illustrate the mixing capability were glycerol and deionized water to which red and blue food dye, respectively, were added to afford visual distinction. Glycerol is widely used in many pharmaceutical formulations for cryopreservation, which is believed to be attributed to

glycerol molecules acting to modify the hydrogen bonding ability of water molecules [19]. The highly disparate viscosities of glycerol (1.414Ns/m^2) and water (0.001Ns/m^2) [20] at 20°C however do not engender their easy mixing and offers a suitable test bed for demonstrating the mixing capability of the quadcopter. The test sample comprise 0.5 mL of glycerol and 0.5 mL water added sequentially to form two distinct aqueous layers in a 2-mL glass vial (Vorex) with plastic cap. A fixture to hold an array of vials was designed and fabricated using a 3D printer (Stratsys, UPrint SE Plus).

Fig. 1A shows the quadcopter that was modified to house 4 glass vials for transport. With a larger quadcopter, it will be possible to adapt this to haul a larger number of vials. The vial that contains water (top) and glycerol (bottom) prior to the maneuver clearly shows segregation that is confirmed by quantitative color analysis (Fig. 1B). After the quadcopter (with vials) was made to perform the flipping maneuver 14 times (see example in video provided), a good extent of mixing was attained to obtain a homogenous sample with uniform distribution of the colour components (see Fig. 1C). To ensure that the maneuver was responsible for the mixing, similar samples were transported without

flipping where glycerol and water in the glass vials remain in their respective layers as indicated by clear demarcation of the bottom red and top blue colour distribution shown in Fig. 1B.

Supplementary video related to this article can be found at <http://dx.doi.org/10.1016/j.ab.2018.01.004>.

It is important to note that the manner of mixing here follows more of a tumbling mode which is normally applied to the preparation of blended granular formulations [21]. This is unlike the reliance on aggressive shaking utilized in vortex mixers. This gentler mixing action may overcome problems associated with cell damage [22]. The lack of any need to incorporate devices to the quadcopter is also cost effective and energy conserving. The latter offers to increase the range of travel distance that is crucial for outdoor sample transport. It is foreseeable that maneuvers aside from flipping can be performed to optimize mixing. Hardware modifications to the quadcopter, such as tilted rotors, may offer better outcomes in this respect [23]. It should be noted that fully autonomous operation should be pursued in order to ensure mixing consistency and to lower the possibility of flight crashes.

In summary, the ability to transport and mix samples using the simple flip maneuver offered in quadcopters is demonstrated. This promises to advance the timeliness and sample quality aspect in the transport of biochemical specimens for laboratory analysis.

Acknowledgements

Discussions with Y.T. Png, Pel-Air Aviation Pty Ltd are appreciated.

References

- [1] A. Gavala, P. Myriantheis, Comparison of point-of-care versus central laboratory measurement of hematocrit, hemoglobin, and electrolyte concentrations, *Heart Lung: J. Acute Crit. Care* 46 (2017) 246–250.
- [2] J.L. Clark, L.V. Rao, Retrospective analysis of point-of-care and laboratory-based hemoglobin A1c testing, *J. Appl. Lab. Med.* DOI: 10.1373/jalm.2016.021493.
- [3] M. Moreno, A. Schwartz, R. Dvorkin, The accuracy of point-of-care creatinine testing in the emergency department, *Adv. Emerg. Med.* 2015 (2015) 965368.
- [4] A. Grasso, H. Ramalinho, L.S. Pessoa, M.G.C. Resende, I. Caballé, N. Barba, On the improvement of blood sample collection at clinical laboratories, *BMC Health Serv. Res.* 14 (2014) 12.
- [5] K. Doerner, M. Gronalt, R.F. Hartl, G. Kiechle, M. Reimann, Exact and heuristic algorithms for the vehicle routing problem with multiple interdependent time windows, *Comput. Oper. Res.* 35 (2008) 3034–3048.
- [6] C.M. Fernandes, A. Worster, K. Eva, S. Hill, C. McCallum, Pneumatic tube delivery system for blood samples reduces turnaround times without affecting sample quality, *J. Emerg. Nurs.* 32 (2006) 139–143.
- [7] W.M. Shibani, M.F. Zulkafli, B. Basuno, Methods of transport technologies: a review on using tube/tunnel systems, *IOP Conf. Ser. Mater. Sci. Eng.* 160 (2016) 012042.
- [8] T.K. Amukele, L.J. Sokoll, D. Pepper, D.P. Howard, J. Street, Can unmanned aerial systems (drones) be used for the routine transport of chemistry, hematology, and coagulation laboratory specimens? *PLoS One* 10 (2015) e0134020.
- [9] G. Lippi, C. Mattiuzzi, Biological samples transportation by drones: ready for prime time? *Ann. Transl. Med.* 4 (2016) 92.
- [10] S. Mitic, J.W. van Nieuwkastele, A. van den Berg, S. de Vries, Design of turbulent tangential micro-mixers that mix liquids on the nanosecond time scale, *Anal. Biochem.* 469 (2015) 19–26.
- [11] J.K.K. Lye, T.W. Ng, A. Neild, O.W. Liew, A capacity for mixing in capillary wells for microplates, *Anal. Biochem.* 410 (2011) 152–154.
- [12] T. Vuong, B.H.-P. Cheong, J.K.K. Lye, O.W. Liew, T.W. Ng, Microplate well coverage mixing using superhydrophobic contact, *Anal. Biochem.* 430 (2012) 53–55.
- [13] S. Karpitschka, C. Hanske, A. Fery, H. Riegler, Coalescence and noncoalescence of sessile drops: impact of surface forces, *Langmuir* 30 (2014) 6826–6830.
- [14] C.O. Deetz, D.K. Nolan, M.G. Scott, An examination of the usefulness of repeat testing practices in a large hospital clinical chemistry laboratory, *Am. J. Clin. Pathol.* 137 (2012) 20–25.
- [15] J.C. Neubauer, I. Sébastien, A. Germann, S.C. Müller, A. Meyerhans, H. von Briesen, H. Zimmermann, Towards standardized automated immunomonitoring: an automated ELISpot assay for safe and parallelized functionality analysis of immune cells, *Cytotechnology* 69 (2017) 57–73.
- [16] J.E. Nett, M.T. Cain, K. Crawford, D.R. Andes, Optimizing a Candida biofilm microtiter plate model for measurement of antifungal susceptibility by tetrazolium salt assay, *J. Clin. Microbiol.* 49 (2011) 1426–1433.
- [17] S. Lilyanna, E.M.W. Ng, S. Moriguchi, S.P. Chan, R. Kokawa, S.H. Huynh, P.C.J. Chong, Y.X. Ng, A.M. Richards, T.W. Ng, O.W. Liew, Variability in microplate surface properties and its impact on ELISA, *J. Appl. Lab. Med.* DOI: 10.1373/jalm.2017.023952.
- [18] A.A. El-Badawy, M.A. Bakr, Quadcopter aggressive maneuvers along singular configurations: an energy-quaternion based approach, *J. Contr. Sci. Eng.* 2016 (2016) 7324540.
- [19] J.J. Towey, L. Dougan, Structural examination of the impact of glycerol on water structure, *J. Phys. Chem. B* 116 (2012) 1633–1641.
- [20] N.-S. Cheng, Formula for the viscosity of a glycerol–water mixture, *Ind. Eng. Chem. Res.* 47 (2008) 3285–3288.
- [21] G. Metcalfe, L. Graham, J. Zhou, K. Liffman, Measurement of particle motions within tumbling granular flows, *Chaos* 9 (1999) 581–593.
- [22] J.J. Chalmers, Mixing, aeration and cell damage, 30+ years later: what we learned, how it affected the cell culture industry and what we would like to know more about, *Curr. Opin. Chem. Engin* 10 (2015) 94–102.
- [23] R. Kumar, A. Nemati, M. Kumar, R. Sharma, K. Cohen, F. Cazaurang, Tilting-rotor quadcopter for aggressive flight maneuvers using differential flatness based flight controller, *In ASME Dynamic Sys. Control Conf.* (2017), October 11–13, Virginia (USA). V003T39A006.

Appendix G

Note: Biochemical samples centrifuged in-flight on drones

Mayur Katariya, Dwayne Chung Kim Chung, Tristan Minifie, Harshit Gupta, Alifa Afiah Ahmad Zahidi, Oi Wah Liew, and Tuck Wah Ng

Citation: *Review of Scientific Instruments* **89**, 106102 (2018); doi: 10.1063/1.5031039

View online: <https://doi.org/10.1063/1.5031039>

View Table of Contents: <http://aip.scitation.org/toc/rsi/89/10>

Published by the [American Institute of Physics](#)

Articles you may be interested in

[Development of a scanning electron microscopy with polarization analysis system for magnetic imaging with ns time resolution and phase-sensitive detection](#)

Review of Scientific Instruments **89**, 083703 (2018); 10.1063/1.5037528

[Note: A compact low-vibration high-performance optical shutter for precision measurement experiments](#)

Review of Scientific Instruments **89**, 096111 (2018); 10.1063/1.5046445

[SIESTA: A high current ion source for erosion and retention studies](#)

Review of Scientific Instruments **89**, 103501 (2018); 10.1063/1.5039156

[Unsupervised learning about 4D features of microparticle motion](#)

Review of Scientific Instruments **89**, 10K109 (2018); 10.1063/1.5037462

[Development of a triple probe array for mode conversion study of electron cyclotron wave](#)

Review of Scientific Instruments **89**, 10J121 (2018); 10.1063/1.5038852

[Simultaneous measurement of C VI, Ne X, and Li III charge exchange lines on EAST](#)

Review of Scientific Instruments **89**, 10D119 (2018); 10.1063/1.5036835



PFEIFFER VACUUM

VACUUM SOLUTIONS FROM A SINGLE SOURCE

Pfeiffer Vacuum stands for innovative and custom vacuum solutions worldwide, technological perfection, competent advice and reliable service.

[Learn more!](#)



Note: Biochemical samples centrifuged in-flight on drones

Mayur Katariya,¹ Dwayne Chung Kim Chung,¹ Tristan Minifie,¹ Harshit Gupta,¹ Alifa Afiah Ahmad Zahidi,¹ Oi Wah Liew,² and Tuck Wah Ng^{1(a)}

¹Laboratory for Optics and Applied Mechanics, Department of Mechanical and Aerospace Engineering, Monash University, Clayton, Victoria 3800, Australia

²Cardiovascular Research Institute, Yong Loo Lin School of Medicine, National University of Singapore, National University Health System, Centre for Translational Medicine, 14 Medical Drive, Singapore 117599

(Received 27 March 2018; accepted 17 September 2018; published online 1 October 2018)

The ability to conduct en-route centrifugation of samples improves quality and timeliness in the pre-analytical phase. This is demonstrated here on a quadcopter whereby the propellers were adapted to house and apply centrifugal forces to sample-containing capillary tubes instead of incorporating a centrifuge. Tests revealed the ability of the method to separate non-homogenized milk into a cream portion and a skim milk portion, and human whole blood into plasma, buffy coat, and red blood cell components. *Published by AIP Publishing.* <https://doi.org/10.1063/1.5031039>

In the clinical laboratory, testing must deliver quality results that are timely and reliable in order to advance optimal medical care. Controlling pre-analytical errors arising from sample handling and processing contributes to the validity and diagnostic value of the test results. In the case of whole blood samples, it is vital to separate serum and plasma from contact with the cell components within a given time frame as some test analyte levels are significantly influenced by the time between collection and centrifugation.^{1,2} Serum that is not centrifuged within 60 min from collection may be contaminated by cellular components that are released by cell lysis,³ while some plasma-based assays require prompt centrifugation to avoid spurious elevated analyte levels arising from platelet activation and degranulation.⁴

The transport of samples to the laboratory is strongly governed by the twin factors of timeliness (to ensure sample viability) and cost.⁵ For both factors, the use of autonomous schemes has clear advantages. Drones, or unmanned aerial vehicles (UAV), have recently been explored for outdoor biological specimen delivery.⁶ With robust technologies increasingly being developed to overcome possible malfunctions,⁷ drones can potentially be used not only in remote venues but also in traffic-congested urban environments. In the latter, route planning strategies can only offer limited improvements in the timeliness of samples being delivered.⁸ The timeliness improvement can be further extended if some parts of pre-processing of samples, such as mixing,⁹ are done en-route during transport. The ability to perform en-route mixing and even centrifugation is highly attractive as this will reduce the pre-analytical time at the destination laboratory, thus reducing turn-around-times for sample testing. The payload constraint of a typical quadcopter drone renders it unfeasible to attach a centrifuge onto it for sample transport and centrifugation in tandem. This limitation can be circumvented by adapting the propeller blades of quadcopters to perform the centrifugation of samples collected in capillary tubes. The ability of capillary

tubes to permit the self-filling of liquid^{10,11} makes them attractive for the collection of samples such as blood and milk. During flight, these propellers can spin up to 15 000 revolutions per minute (RPM) which has been experimentally demonstrated to be sufficient to separate plasma from blood cell components held in glass capillary tubes.¹² The work described here addresses the main challenges of having (a) the drone flight characteristics unchanged with adaptation of the propellers, (b) no dislodgment of components notwithstanding the forces developed from high speed spinning, and (c) easy installation and removal of the sample-containing capillary tubes.

The quadcopter used was a DJI Phantom 4 Pro with 1388 g mass and a diagonal size of 350 mm without the propellers [Fig. 1(a)]. It is powered by a 5870 mA h lithium battery wherein flight can be controlled using a remote controller that supports smartphone and tablet interfacing. Each of the four propellers, which are removable from the quadcopter, was adapted to contain a fixture that will hold standard 75 μ l glass capillary tubes (Hirschman). In order to achieve the characteristics [(a)-(c)] mentioned earlier, a fixture was devised [Figs. 1(b) and 1(c)] that comprised a hollow stainless steel tube affixed using strong adhesive (Araldite Ultra Clear) rated at 12–15 MPa to the top surface of the propeller. When the capillary tube is slid into the steel tube, it can be held in place by a bent rod fashioned to operate like a latch which is located by a hinge that is also affixed by adhesive to the propeller.

An initial series of tests were conducted to ensure that the fixture could be retained notwithstanding standard manoeuvres conducted with the quadcopter. As the propellers were rotated at a high speed, there was a tendency for them to flex, leading to a possibility of failure by curved delamination.¹³ It was found that the application of adhesives at three spots [Figs. 1(b) and 1(c)], rather than continuously, along the length of the stainless steel tube was effective in preventing this.

Once integrity was assured, tests were conducted with non-homogenized milk and blood samples. The blood sample, obtained from a healthy 34 yr old male volunteer with consent, was directly drawn into the capillary tube after a finger prick with a lancet. The capillary tubes with samples were

^{a)} Author to whom correspondence should be addressed: engngtw@gmail.com

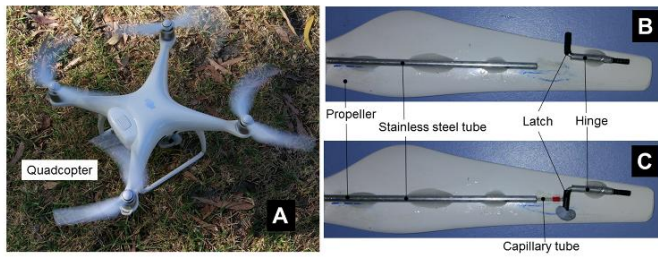


FIG. 1. To enable en-route centrifugation of samples in capillary tubes, the propellers of the quadcopter (a) were modified to have a stainless steel tube and hinge affixed by strong adhesive on them (b). When the capillary tube is inserted into the stainless steel tube (c), a bent rod serving as a latch, when flipped into position helped us to keep the capillary tube in place.

inserted into sealing clay (Hirschman) to ensure no losses during centrifugation. In the test with milk samples, the capillary tube was spun for a total of 35 min. The tube was removed after specific time intervals to query the separation of milk. Milk fat is typically secreted from mammary epithelial cells as fat globules which are primarily composed of a globule of triglyceride surrounded by a lipid bilayer membrane similar to the apical membrane of the epithelial cells. This membrane helps us to stabilize the fat globules in an emulsion within the aqueous environment of milk. Lipid has a lower buoyant density than water, so when raw original feed milk is centrifuged, the fat

component is displaced to develop a cream layer. Although this cream portion becomes visible after 5 min of centrifugation, the ability to measure it quantitatively requires using the line profile plot (based on the brightness level) feature in ImageJ. It was established that 30 min of centrifugation with the quadcopter was necessary to ensure good separation (see Fig. 2).

In the test with blood samples, the capillary tubes were spun for a total of 10 min using the adapted propellers. The tube was removed after specific time intervals to query the separation into regions containing red blood cells, buffy coat, and plasma. As shown in Fig. 3, component separations are

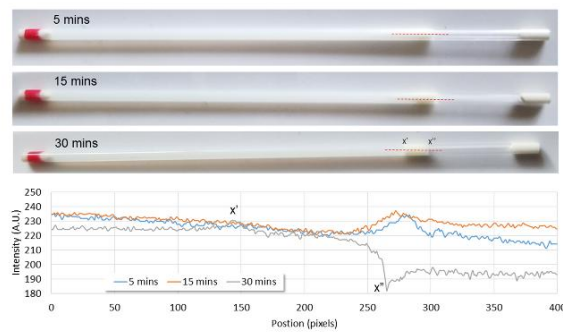


FIG. 2. A sample of non-homogeneous milk in a capillary tube when centrifuged develops a cream layer. This layer can be evaluated by analyzing line plots taken along the dashed red lines. The separation becomes sufficiently distinct after 30 min centrifugation, as indicated by the positions marked x' and x'' .

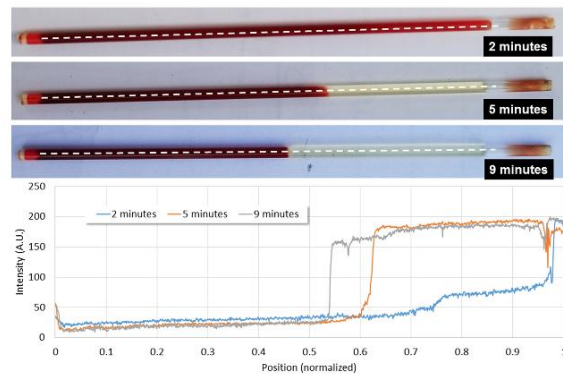


FIG. 3. A sample of human blood in a capillary tube when centrifuged develops separation into regions containing red blood cells, buffy coat, and plasma. While separation becomes sufficiently distinct after only 2 min centrifugation, as analysis of line plots taken along the dashed white lines indicate, it is necessary to do so for longer to ensure that the process is complete.

distinct from 5 min of centrifugation onwards. However, longer centrifugation is needed to pellet the cells and obtain good yields of plasma. A convenient indicator will be to determine the Packed Cell Volume (PCV), which is essentially the ratio of the volume occupied by the red blood cells to the volume of the whole blood by percentage. As indicated in Fig. 4, this value stabilizes after 8 min of centrifugation. The low scatter in data (from 5 runs) after this time imputes high repeatability in the process. This relatively short processing time offers the ability to use smaller capacity batteries, which are lighter and take a shorter time to recharge, for en-route centrifugation while delivering in traffic congested urban environments. It is acknowledged that the use of glass capillary tubes for blood collection poses a potential safety threat as possible breakage of these fragile tubes can cause injury or infection from blood-borne pathogens. The likelihood of tube breakage occurs when some force is applied to one end of the tube for insertion into the sealing clay¹⁴ or possibly during centrifugation. However, we did not observe capillary tube breakage during centrifugation with the quadcopter even after many countless hours of testing. Nonetheless, a safe alternative to reduce potential injury risks is to use plastic capillary tubes where previous studies have demonstrated comparable performance characteristics with glass capillary tubes.¹⁵ Other possible compatible products include glass capillary tubes wrapped in puncture-resistant film.

There is potential to apply the milk sample centrifugation approach here to advance human lactation investigations.¹⁶ Sub-optimal breastfeeding, especially non-exclusive breastfeeding in the first six months of life, has been found to be responsible for 1.4×10^6 deaths and 10% of disease burden in children younger than 5 yr.¹⁷ These concerns are accentuated in areas where access to healthcare services is more limited.¹⁸ On a similar vein, pediatric blood tests, conducted exclusively using capillary tube collection, remain a vital tool in the early detection of human immunodeficiency virus (HIV).¹⁹ While perinatal HIV has been virtually eliminated in high-income countries, the situation in remote sub-Saharan African and Asian communities remains highly challenging.²⁰

The approach here of using the quadcopter's original propellers for centrifugation, rather than replacing them with alternative fixtures,²¹ ensures that the process is conducted

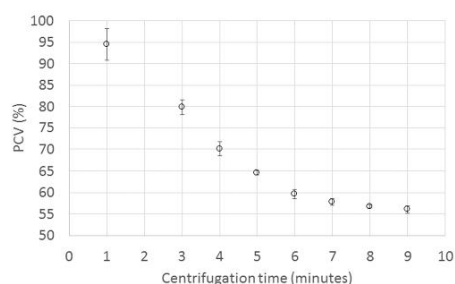


FIG. 4. Calculations of the packed cell volume (PCV) as a function of centrifugation time from 5 blood samples. It can be seen that centrifugation of at least 8 min is needed to complete the separation process.

in-flight, thus improving the timeliness of pre-analytical sample processing. It should be noted that the quadcopter propellers need to attain high thrust coefficients whilst not failing in the process. This necessitates their careful design and testing in order to prevent costly damages arising from flight crashes.²²

In summary, the adaptation of the propellers of a quadcopter to house capillary tubes detailed in this work was shown not to affect flight characteristics, operate notwithstanding the forces that develop from high speed spinning, and allow the capillary tube to be easily introduced and removed. This is unlike an approach of replacing the propeller of the drone with a device that holds fluid samples for centrifugation.²¹ Distinct separation of non-homogenized milk into its creamy component required 30 min of centrifugation, while only 8 min was needed to separate human blood into red blood cells, buffy coat, and plasma. This approach offers to advance optimal medical care through improved timeliness in diagnosis procedures requiring centrifugation and complements the recent uncovered ability to conduct en-route mixing.⁹

T.W.N. acknowledges the assistance by Christine H.P.C. (registered nurse) in blood collection, N. De Rose for help on adhesive attachment, and discussions with Y. T. Png, Pel-Air Pty Ltd.

- ¹S. Blonshine, K. D. Fallon, C. M. Lehman, and S. Sittig, *Procedures for Handling and Processing Blood Specimens for Common Laboratory Tests: Approved Guideline*, 4th ed. [Clinical and Laboratory Standards Institute (CLSI), Wayne, PA, 2004], GP43-A4.
- ²B. L. Boyanton, Jr. and K. E. Blick, *Clin. Chem.* **48**, 2242 (2002).
- ³M. K. Tuck, D. W. Chan, D. Chia, A. K. Godwin, W. E. Grizzle, K. E. Krueger, W. Rom, M. Sanda, L. Sorbara, S. Stass, W. Wang, and D. E. Brenner, *J. Proteome Res.* **8**, 113 (2009).
- ⁴J. Brouwers, R. Noviyanti, R. Fijnheer, P. G. de Groot, L. Trianty, S. Mudaliana, M. Roest, D. Syafruddin, A. van der Ven, and Q. de Mast, *PLoS One* **8**, e64850 (2013).
- ⁵C. Wexler, A.-L. Cheng, B. Gautney, S. Finocchiaro-Kessler, K. Goggin, and S. Khamadi, *PLoS One* **12**, e0181005 (2018).
- ⁶T. K. Amukele, J. Street, K. Carroll, H. Miller, and S. X. Zhang, *J. Clin. Microbiol.* **54**, 2622 (2016).
- ⁷A. Eresen, N. Imamoglu, and M. Efe, *Expert Syst. Appl.* **39**, 894 (2012).
- ⁸A. Grasa, H. Ramalhinho, L. S. Pessoa, M. G. C. Resende, I. Caballé, and N. Barba, *BMC Health Serv. Res.* **14**, 12 (2014).
- ⁹M. Katarlya, D. C. K. Chung, T. Minife, H. Gupta, A. A. A. Zahidi, O. W. Liew, and T. W. Ng, *Anal. Biochem.* **545**, 1 (2018).
- ¹⁰W. E. Brittin, *J. Appl. Phys.* **17**, 37 (1946).
- ¹¹W. Schwab, T. W. Ng, J. K. K. Lye, O. W. Liew, and B. H.-P. Cheong, *J. Colloid Interface Sci.* **365**, 314 (2012).
- ¹²T. C. Pearson and D. L. Guthrie, *Am. J. Clin. Pathol.* **78**, 770 (1982).
- ¹³Z. Jiang, S. Wan, Z. Zhong, S. Li, and K. Shen, *Eng. Fract. Mech.* **138**, 73 (2015).
- ¹⁴J. Jagger and S. Deitchman, *JAMA, J. Am. Med. Assoc.* **280**, 31 (1998).
- ¹⁵P. Wongkrjang, N. Opartkiattikul, W. Chinswangwatanakul, and S. Areewatanana, *J. Med. Assoc. Thailand* **95**, 809-815 (2012).
- ¹⁶P. P. Meier, J. L. Engstrom, J. L. Zuliger, J. E. Motykowski, U. Vasan, W. A. Meier, P. E. Hartmann, and T. M. Williams, *Breastfeed. Med.* **1**, 79 (2006).
- ¹⁷J. T. Black, N. Terrieri, and C. J. Victora, *Lancet* **371**, 243 (2008).
- ¹⁸A. Ayawine and K. A. Ae-Ngibise, *Pan Afr. Med. J.* **22**, 248 (2015).
- ¹⁹M. Sirtçi, M. Acar, H. Aktürk, S. H. Torun, H. Beka, A. Ağaçfidan, N. Salman, and A. Somer, *Balk. Med. J.* **34**, 239 (2017).
- ²⁰M. Lallemand, S. Chang, R. Cohen, and B. Pecoul, *N. Engl. J. Med.* **365**, 581 (2011).
- ²¹A. Priye, S. Wong, Y. Bi et al., *Anal. Chem.* **88**, 4651 (2016).
- ²²E. Kuantama, D. Craciun, I. Tarca, and R. Tarca in *New Advances in Mechanisms, Mechanical Transmissions and Robotics*, edited by B. Corves, E. C. Lovasz, M. Hüsing, I. Maniu, and C. Gruescu (Springer Verlag, 2016), pp. 269-277.